

Copyright is owned by the Author of the thesis. Permission is given for a copy to be downloaded by an individual for the purpose of research and private study only. The thesis may not be reproduced elsewhere without the permission of the Author.

**Unravelling magma generation, storage, and ascent
processes from the crystal cargo and their host lavas:**

A case study of Taranaki Volcano, New Zealand

A dissertation presented in partial fulfilment of the
requirements for the degree of

Doctor of Philosophy

in

Earth Sciences

at Massey University (Manawatū campus)

Palmerston North, New Zealand

Nessa D'Mello

2021



Copyright is owned by the Author of the thesis. Permission is given for a copy to be downloaded by an individual for the purpose of research and private study only. The thesis may not be reproduced elsewhere without the permission of the Author.

Acknowledgements

I would first like to thank my chief-supervisor Prof. Georg Zellmer for being an exceptional mentor and providing continual academic support throughout the project. His enthusiasm, knowledge, and work ethic created a very positive work environment. I am thankful to work with an excellent supervisory team- Prof. Jonathan Procter, Dr. Gabor Kereszturi, and Dr. Geoff Kilgour, who have always made the time to provide crucial input and feedback and offer their perspectives on the progress of the research.

The help of the following has been essential for the completion of this thesis: Teresa Ubide and John Caulfield at the University of Queensland, Amanda French (University of Waikato), Ian Schipper and Juergen Kuepper (Victoria University of Wellington), and Masako Uzuki and Yoshiyuki Iizuka (Academia Sinica, Taiwan). Tenille Hancock, Anke Zernack, and Daniel Coulthard Jr. are much appreciated for their help in the field; Anja Moebis, James Ardo, Mallory McAteer, and Hannah Harvey in the lab; and Kate Arentsen, who has always been prompt with addressing administrative concerns.

I would like to thank the geochemistry group- Raimundo Brahm, Carlos Corella Santa Cruz, Charline Lormand and Daniel Coulthard Jr, for their constructive discussions and coffee. A special thank you to my MSc supervisor Prof. N. R. Karmalkar and Dr. A. Mudholkar for introducing me to the world of geochemistry.

I owe much to my family, for their constant support, encouragement for keeping me motivated. I am sincerely thankful for Romana Mbinya, Ambika Rethinavelu, Kudzai Mvare, Michelle Musakwa, and Denise Gray for being great friends. Most of all, I thank God for his love, patience, and faithfulness.

This thesis is dedicated to my father,

Nelson E. D'Mello

Abstract

Mt. Taranaki is a back-arc stratovolcano situated in the North Island of New Zealand, *c.* 400 km west of the Hikurangi trench. This thesis investigates the Holocene lavas of Taranaki volcano to constrain the processes of melt generation and evolution before these magmas were erupted. The crystal cargo carried in these eruptives is dominated by plagioclase, clinopyroxene, and amphibole, which with exception of the crystal rims are in chemical disequilibrium with the carrier melt represented by the groundmass. Compositional overlap of mineral data between the crystals in lavas and from xenoliths, along with numerous glomerocrysts and fractured crystals, indicate an antecrystic or xenocrystic origin of the crystals. Thermohygrometric data derived from chemical equilibrium between crystal rims and groundmass reveal hot and occasionally H₂O-undersaturated felsic melts (55–68 SiO₂ wt%). These cannot be related to deep crustal hot zones and are thus interpreted to be sourced from subduction melange diapirs that rise through the mantle wedge. Repeated, heterogeneous intrusion of these diverse melts into the crust, dominated by plutonic rocks of the 120 Ma Median Batholith, results in a subvolcanic crystal mush zone. The melts entrain mafic crystals in various proportions (40–55 vol.%), reducing magmatic silica contents by 5–11 wt%. Mineral phases display a complex and varied history observed through elemental concentration maps that suggest repeated resorption and recrystallisation in varied environments. These crystals are not exclusive to lavas of any stratigraphic unit and can be found within the same sample over very short length scales (within centimetres from each other). Eruption-triggering injections pick up this complex crystal cargo. Amphiboles break down during ascent and develop distinct reaction rims that vary little in width ($\pm 20\%$, 1σ , on average) within individual thin sections but show a large variation between samples from different lava flows, from less than 5 to more than 450 μm . The combined

evidence indicates that Taranaki lavas are a product of high temperature, aphyric to sparsely phyric subduction melange partial melts, and remobilised colder, mafic mush zone crystals. Together they ascend through the shallow crust on timescales of the order of hours to days.

Contents

Abstract **iii**

List of Tables **ix**

List of Figures..... **x**

Chapter 1.: Introduction..... **1**

1.1. Research introduction and motivation..... 1

1.2. Research Objectives 6

1.3. Aims 7

Chapter 2.: Geological Background..... **9**

2.1. North Island of New Zealand 9

2.1.1. Taupo Volcanic Zone (TVZ) 11

2.1.2. The Taranaki Basin 13

2.1.3. Taranaki Volcanic Lineament 15

2.2. Mount Taranaki 17

2.3. Stratigraphy and Age of Rocks of present Taranaki cone 20

2.4. Petrology, mineralogy, and geochemistry 23

2.4.1. Whole Rock Classification..... 23

2.4.2. Whole Rock Geochemistry 24

2.4.3. Mineral Assemblages 27

2.5. Previous Petrological Model for Taranaki Eruptives 29

Chapter 3.: Methodology **33**

3.1. Sample Site Selection and Mapping..... 33

3.2. Field Work..... 35

3.3. Laboratory Analyses..... 36

3.3.1. Petrographic glass mounted sections 36

3.3.2. Back-scattered electron (BSE) imaging 36

3.3.3. X-ray fluorescence (XRF)..... 36

3.3.4. Electron microprobe analysis (EPMA) 37

3.3.5. Laser ablation inductively coupled plasma mass spectrometry (LA-ICP-MS) 38

3.3.6. Electron back scatter diffraction (EBSD) 39

3.4. Data Processing 39

3.4.1. Calculation of true thickness of reaction rims..... 39

3.4.2. Thermobarometry and Hygrometry 40

3.4.3. Major element mass balance calculations 41

3.4.4.	Calibration of EPMA major element maps	42
Chapter 4.:	Remobilization of cool mafic mushes by hot felsic melts: diverse primary melt compositions at Taranaki volcano, New Zealand.....	43
4.1.	Introduction	45
4.2.	Geological background.....	46
4.3.	Method.....	48
4.3.1.	Sampling and sample preparation	48
4.3.2.	X-ray fluorescence (XRF) analysis	48
4.3.3.	Electron probe microanalysis (EPMA)	49
4.3.4.	Mass balance calculations for groundmass compositions.....	50
4.4.	Results	50
4.4.1.	Mineral chemistry	50
4.4.2.	Whole Rock Chemistry	54
4.5.	Discussion	57
4.5.1.	The nature of the crystal cargo.....	57
4.5.2.	Thermobarometry and Hygrometry	59
4.5.3.	Origin of microcrysts of Taranaki.....	62
4.5.4.	Influence of antecrysts on the whole rock compositions	63
4.5.5.	Generation of felsic, aphyric to sparsely phyrlic parental melts at Mt. Taranaki	65
4.6.	Conclusions	67
Chapter 5.:	The crystal cargo of Taranaki lavas: exploring intrusive processes through the crystal cargo of volcanic rocks.....	71
5.1.	Introduction	73
5.2.	Geological background and petrology	74
5.3.	Methodology	76
5.4.	Results	77
5.4.1.	Plagioclase	78
5.4.2.	Pyroxene.....	81
5.4.3.	Amphibole.....	85
5.5.	Discussion	87
5.5.1.	Mineral- melt equilibrium.....	87
5.5.2.	Interpretation of zoning textures	89
5.5.3.	Crystallization environments	93
5.5.4.	The source of crystals and the Median Batholith.....	99
5.5.5.	Model for Taranaki	100

5.6. Conclusions	103
Chapter 6.: Deciphering magma storage and ascent processes of Taranaki, New Zealand, from the complexity of amphibole breakdown textures.....	105
6.1. Introduction	107
6.2. Geological and petrological background.....	110
6.3. Materials and methods.....	114
6.3.1. X-ray fluorescence	115
6.3.2. Backscatter imaging	116
6.3.3. Electron probe microanalysis.....	116
6.3.4. Electron backscatter diffraction analyses.....	117
6.3.5. Calculation of true thickness of reaction rims.....	117
6.3.6. P-T conditions	118
6.4. Results	118
6.4.1. Whole rock and melt chemistry	118
6.4.2. Petrographic observations and mineral chemistry	119
6.4.3. Amphibole.....	121
6.4.4. Breakdown textures.....	124
6.4.5. Rim thicknesses.....	130
6.5. Discussion	131
6.5.1. Amphibole stability field for Taranaki.....	131
6.5.2. Magmatic processes and breakdown textures	134
6.5.3. Stability Conditions.....	139
6.5.4. Progression of amphibole breakdown.....	140
6.5.5. Extent of amphibole breakdown	142
6.5.6. Magma ascent times from reaction rim thicknesses	143
6.5.7. A model for magma ascent at Taranaki	146
6.6. Conclusions	148
Chapter 7.: Synthesis.....	151
7.1. Introduction	151
7.2. Role of mafic antecrysts in Taranaki lavas	151
7.3. The case for ‘Subduction Melanges’	152
7.4. Summit and Satellite vents	155
7.5. A simple three (?) member mixing system	157
7.6. Testing and applying the subduction melange model	159
Chapter 8.: Conclusions	161

8.1. From melt generation to extrusion	161
8.2. Outlook.....	163
References	167
Appendix A	191
Appendix B	192
Appendix C	193
Appendix D	194
Appendix E	195

List of Tables

Table 2.1: Summarised stratigraphy of the last 10 kyrs of Taranaki eruptions modified from previous studies	22
Table 3.1: Table shows the samples of this study w.r.t. their location, stratigraphic unit, age, and lithology.....	35
Table 3.2: Geothermometers, barometers and hygrometers employed in this study, along with equilibrium tests.....	41
Table 4.1: Whole rock chemistry of samples in this study (oxides in wt% and trace and minor elements in ppm).	55
Table 4.2: Groundmass compositions determined through mass balance calculations and EPMA measurements.....	57
Table 6.1: Stratigraphy of the Taranaki volcano modified from Stewart et al. (1996), Platz et al. (2012), and Zernack et al. (2012).....	112
Table 6.2: Normalised major element oxide concentrations for the amphibole samples in this study.	121
Table 6.3: Comparison of amphibole (A), reaction rim (RR) and melt compositions (M)	127
Table 6.4: Reaction rim thicknesses of amphiboles sampled.	130

List of Figures

Figure 1.1: Schematic figures of andesite genesis at arc volcanoes.	2
Figure 2.1: Tectonic framework of New Zealand and the principal volcanic centres in the North Island.....	10
Figure 2.2: A subcrustal illustration of subduction beneath the North Island of New Zealand with the crust thickening below the Taranaki-Ruapehu Line (TR Line). Along the Hikurangi Trench, westward subduction of the Pacific Plate (including the Hikurangi Plateau) occurs beneath the North Island of New Zealand. Modified from Dimech et al. (2017).....	11
Figure 2.3 The evolution of the Taranaki basin and southward migration of Taranaki volcanism through time. Modified from Giba et al. (2010).....	14
Figure 2.4 Tectonics and location of the Taranaki Volcanic Lineament in the western peninsula of the North Island of New Zealand.	16
Figure 2.5: Major and minor element chemistry of the volcanic products of Taranaki over time.....	25
Figure 2.6: Trace element and isotopic data for Taranaki lavas with respect to age and vent.....	26
Figure 2.7: Illustration showing the petrological model for Taranaki volcano with metasomatized mantle releasing basaltic parental melts that partially melt an amphibolitic underplate.....	30
Figure 3.1: Mosaic image of Taranaki volcano with 60% overlap between flightpaths. This image was then imported into ArcGIS software to trace the lava flows.	34
Figure 4.1 (A) Regional geology of the North Island of New Zealand showing the primary zone of subduction (Hikurangi Margin) and the location of the Taupo Volcanic Zone (TVZ).	47
Figure 4.2 Panels showing glomerocrysts and fractured crystals and the relative proportions of phases.	51
Figure 4.3 Chemical classification and nomenclature of dominant mineral phases.....	52
Figure 4.4 Major element variations between mineral phases in comparison to the whole rock compositions and measured groundmass compositions. The plots indicate simple mixing of mineral and groundmass to form whole rock compositions.....	53
Figure 4.5 (A) Total Alkali vs Silica classification of the whole rock (WR) and groundmass (Le Maitre et al., 2002).	56
Figure 4.6 Major element chemistry of minerals from Taranaki lava flows (this work) in comparison with mineral data of xenoliths (cumulates, gabbros and diorites) entrained in Taranaki lavas (Gruender et al., 2010; Price et al., 2016). This shows complete compositional overlap of crystals entrained in Taranaki lavas and crystals from xenoliths.	58
Figure 4.7 Equilibrium conditions between plagioclase and clinopyroxene minerals and melt.....	60
Figure 4.8 (A) Thermobarometry of amphibole and clinopyroxene.....	61

Figure 4.9 Mixing model for crystals and groundmass to produce whole rock compositions	64
Figure 4.10 Silica-temperature relation of Taranaki lavas.....	66
Figure 4.11 Schematic diagram showing melt generation in Taranaki.....	68
Figure 5.1 Geological Map of New Zealand.....	75
Figure 5.2 Total Alkali vs Silica diagram for samples from this study with major mineral phase data superimposed.....	76
Figure 5.3: Panel 1 show the different types of textures of crystal phases	78
Figure 5.4 Chemical classification of plagioclase crystals based on the scheme of (Earnshaw and Greenwood, 1997) for cores, mantles and rims.	79
Figure 5.5 Types of zoning seen in plagioclases of Taranaki lavas.....	80
Figure 5.6 Classification of clinopyroxenes based on the scheme of Morimoto (1988). All cores, mantles and rims plot in the augite-diopside field.....	82
Figure 5.7 Types of zoning seen in clinopyroxenes of Taranaki lavas.....	83
Figure 5.8 Sector zoned clinopyroxenes from samples (A) L2; (B) L18; (C) L5 and (D) L16.	84
Figure 5.9 Amphibole classification based on the scheme of Hawthorne et al., (2012).	85
Figure 5.10 Types of zoning seen in amphiboles of Taranaki lavas.....	86
Figure 5.11 Equilibrium conditions for plagioclase and clinopyroxene.....	88
Figure 5.12 Histogram showing at least 2 populations of plagioclase with distinct An contents for all Taranaki crystals.	94
Figure 5.13 Cr zonation patterns in clinopyroxene.....	97
Figure 5.14 Panels illustrating the various zoning patterns seen in plagioclase, clinopyroxene and amphibole. Variations in greyscale indicate crystallisation in different environments resulting in chemical zoning. Clinopyroxene crystal clots are also represented.	101
Figure 5.15 Model for Taranaki eruptives.	102
Figure 6.1 Location of Mt. Taranaki and the Taranaki Volcanic Lineament with respect to the North Island of New Zealand (inset) and the western peninsula	110
Figure 6.2 Map showing the Holocene lava flows that form the current day edifice of Taranaki.....	114
Figure 6.3 Geochemical classification according to Le Maitre (2002) of whole rocks, groundmasses, and amphiboles of Taranaki. The shaded region encompasses the whole rock composition of Taranaki lavas from literature (Stewart et al., 1996; Zernack et al., 2012).	119
Figure 6.4 Petrographic images of Taranaki crystal assemblage.....	120
Figure 6.5 Mineral chemistry of amphiboles of Taranaki.....	122
Figure 6.6 Binary plots of oxide compositions of Taranaki amphiboles in comparison to the natural composition of amphibole from the Crater Flat volcanic zone near Yucca Mountain, Nevada (Nicholis and Rutherford, 2004).	123

Figure 6.7 Summary diagram of the types and appearance of the breakdown products seen in Taranaki	124
Figure 6.8: Graphical representation of the types of rims and their abundance for each sample considered for this study.....	125
Figure 6.9 Variation in amphibole reaction rim types seen in Taranaki eruptives	126
Figure 6.10 Volumetric decomposition as a result of amphibole breakdown.	129
Figure 6.11 P-T stability field for Taranaki amphiboles using various thermobarometers.	133
Figure 6.12 (a) Amphibole zonation with evidence of reaction at zone boundary (ES Amp4); (b) BSE image of a lighter reacted core and reverse zoned mantle (ES3 Amp1)	140
Figure 6.13 Amphibole zonation seen in sample ES3. Points mark locations of EPMA analysis from core to rim. Graphs show the variation in major oxides with approximate distances in μm	141
Figure 6.14 Magma ascent times based on the experimental runs.....	145
Figure 6.15 Model of magma storage and ascent of magmas at Taranaki.....	147
Figure 7.1: Comparison of Taranaki subduction components with the Mariana Arc illustrating the predominance of mixing processes over partial melting.	154
Figure 7.2: Comparison of summit and satellite eruptives based on whole rock chemistry	156
Figure 7.3: A schematic illustration of the three key mixing endmembers that contribute in forming the lava flows seen in Taranaki.....	158

Chapter 1.: Introduction

1.1. Research introduction and motivation

Subduction zones are the regions where sediments, oceanic crust and mantle lithosphere are recycled into and re-equilibrated with the ambient mantle ([Stern, 2002](#)). The associated volcanism represents one of the most common forms of volcanic activity on Earth, constituting about 15% of the total global output ([Crisp, 1984](#)), and it encompasses a wide range of compositions from basaltic to rhyolitic, low-to-high K, low-to-high Mg# and low-to-high Al content ([Pearce and Peate, 1995](#); [Zellmer et al., 2016](#)).

Many geochemical studies have focused on the andesite generation at volcanic arcs because of its implications on the composition of the Earth's crust, and numerous models for the generation of these magmas have been proposed. These include (i) partial melting of harzburgite in the mantle wedge fluxed by H₂O rich fluids or melts liberated from the subducting slab (e.g., [Blatter and Carmichael, 2001](#); [Carmichael, 2002, 2004](#); [Hirose, 1997](#); [Tatsumi and Ishizaka, 1982](#)); (ii) crystallization of mantle derived basalts or basaltic andesite in shallow crustal magma reservoirs (e.g., [Grove et al., 1997](#); [Pichavant et al., 2002](#); [Sisson and Grove, 1993](#)); (iii) crystallization of mantle derived basalts or basaltic andesite in the deep arc crust at or close to the Moho in a deep crustal hot zone (e.g., [Annen et al., 2006](#); [Annen and Sparks, 2002](#); [Mortazavi and Sparks, 2004](#); [Müntener et al., 2001](#); [Müntener and Ulmer, 2018](#); [Prouteau and Scaillet, 2003](#); [Solano et al., 2012](#)); (iv) dehydration partial melting of meta-basalts (amphibolites) in the lower or middle crust by intrusions of hot, mantle derived magma (e.g., [Jackson et al., 2003](#); [Petford and Atherton, 1996](#); [Price et al., 2021](#); [Smith and Leeman, 1987](#)); (v) mixing of silicic magmas and mantle derived mafic magmas, with the silicic component being derived from the crustal rocks in some cases (e.g., [Druitt and Bacon, 1989](#); [Heiken and](#)

[Eichelberger, 1980](#); [Kent, 2014](#)); (vi) generation of primary melts from the subducted slab or the sub arc mantle, or a mixture of both ([e.g.,Errázuriz-Henao et al., 2019](#); [Parolari et al., 2021](#); [Straub et al., 2011](#); [Straub et al., 2020](#); [Straub et al., 2008](#)); and (vii) melting of sediment-rich mélangé ([e.g.,Castro et al., 2010](#); [Codillo et al., 2018](#); [Hao et al., 2016](#); [Marschall and Schumacher, 2012](#)); or a combination of several of these processes.

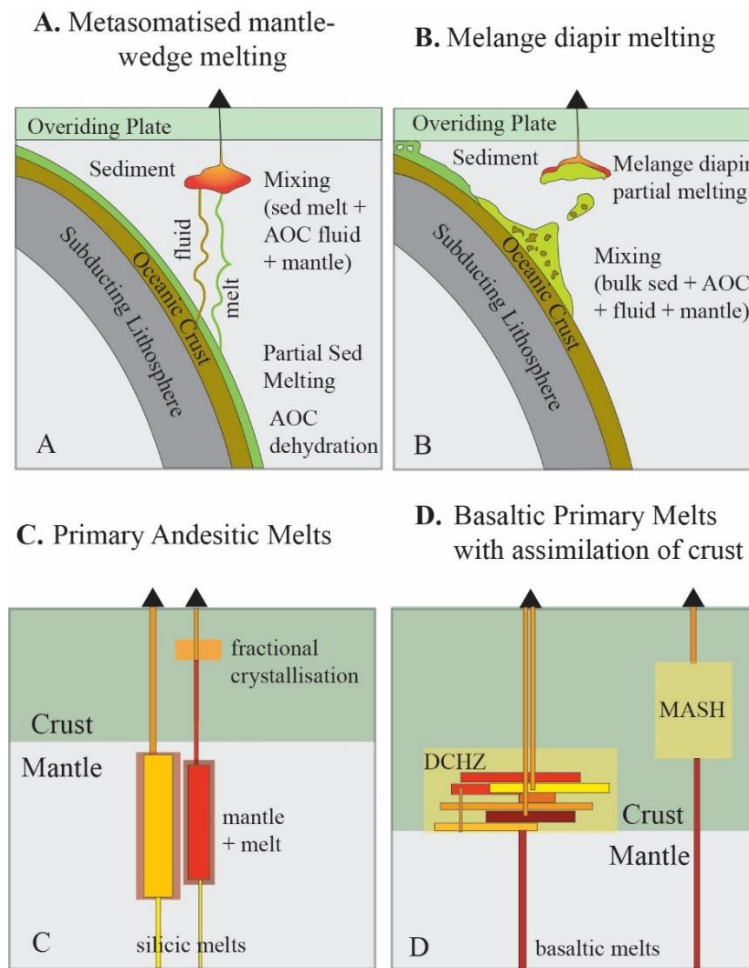


Figure 1.1: Schematic figures of andesite genesis at arc volcanoes. (A) primary melts resulting from metasomatisation of the mantle from subducted slab derived melts and fluids. Partial melting of the metasomatized mantle generates primary melts that feed arc volcanoes. (B) Partial melting of subduction melanges (sediment + altered oceanic crust) in the mantle wedge to form primary melts (C) Genesis of ‘hybridised’ melts in the mantle through the interaction of large or small volume silica rich melts with the peridotitic mantle and minor fractional crystallisation in the crust (D) Genesis of hybridised melts in the crust through the repeated injection of basaltic melts into a Deep Crustal Hot Zone (DCHZ) where the crust is assimilated. Thus, Mixing, Assimilation, Storage and Hybridisation (MASH) of basaltic melts in a silica rich crust results in andesite formation. Modified from [Nielsen et al. \(2020\)](#) and [Straub et al. \(2011\)](#).

It is evident that processes that occur during magma storage can play an important role in the generation of andesitic magmas. Magma is stored in reservoirs defined as regions of partially or wholly molten rock with varying proportions of melt, crystals and exsolved

volatiles ([Bachmann and Bergantz, 2008](#)), or as the domains of the magmatic system that contain melt (\pm exsolved fluids) and are above solidus ([Sparks et al., 2019](#)). However, it has also been suggested that a part of the magma reservoir is entirely below the solidus temperature, in cold storage, and is later rejuvenated ([Cooper and Kent, 2014](#)). Depending on the proportion of components, magma reservoirs are identified either as ‘magma chambers’ with a large proportion of melt, or as ‘mushes’ which can be defined as a semi-rigid framework of crystals and melt ([Sparks et al., 2019](#); [Wager et al., 1960](#)). Geochronology suggests that magmas can be stored in such mush systems from tens to thousands of years ([Cooper and Kent, 2014](#)) Magma reservoirs, in some systems, span the vertical extent of the crust and are termed as trans-crustal-magmatic-systems ([Edmonds et al., 2019](#); [Sparks and Cashman, 2017](#)). This system extends from the lower crust (and even the upper mantle) to the shallow reservoirs, with partially molten rock, with a low-volume intergranular melt phase that cannot be identified through geophysical studies ([Sparks et al., 2019](#)). The interstitial melt is extracted and locally accumulates, through percolative flow, in sufficient volume to become eruptible ([Cashman et al., 2017](#)).

These can provide data on the homogeneity of the magmatic system, temporal changes of magma composition, the extent to which eruptive activity is influenced by the ascent of discrete magma batches and potentially the physical structure of the magmatic systems ([Barclay et al., 2010](#); [Coombs et al., 2013](#); [Larsen et al., 2010](#); [Martel et al., 2017](#); [Neave et al., 2019b](#); [Petrelli and Zellmer, 2020](#); [Scott, 2013](#); [Sheldrake et al., 2016](#); [Turner et al., 2013](#); [Turner et al., 2017](#); [Zellmer et al., 2016](#)).

It is impossible to observe these processes directly and they can only be inferred through geophysical monitoring and, to inform the interpretation of geophysical data, through petrological observations of previously erupted products.

The genesis of the crystal population is indicated through equilibrium or disequilibrium with the matrix/groundmass. Most arc magmas typically contain a significant proportion of entrained crystals that are not in equilibrium with the melts and show disequilibrium textures, including reaction rims, multiple resorption zones, partial resorption zones and changes in mineral chemistry ([Mollo and Hammer, 2017](#); [Nixon and Pearce, 1987](#); [Umino and Horio, 1998](#); [Wallace and Carmichael, 1994](#); [Zellmer et al., 2016](#)). These crystals indicate open system processes and complex magma plumbing systems with episodes of contamination, assimilation, metasomatism, recharge, reheating and mixing or mingling between magmas or between magmas and crystal mush ([Costa et al., 2008](#); [Martel et al., 2017](#); [Zellmer et al., 2016](#)). Crystal populations within volcanic products comprise three principal components that indicate their genesis: autocrysts, crystallized from the melt they are entrained in ; xenocrysts, foreign to the magmatic host and magma system , and antecrysts, recycled one or several times before inclusion in the host magma, but having an origin within the same magmatic system ([Zellmer, 2021](#)). The crystal cargo is sensitive to variations in conditions such as pressure, temperature, fO_2 , composition of the host melt and volatile content, and preserves information of past magmatic processes and compositions as chemical zonation in crystal transects ([Costa et al., 2013](#); [Elardo and Shearer, 2014](#); [Humphreys et al., 2006](#); [Nakamura, 1995a](#); [Streck, 2008](#); [Welsch et al., 2016](#); [Zellmer et al., 2003](#)). Due to the potent influence of crystal chemistry on whole rock geochemistry, assumptions of their origins could lead to incorrect interpretations and mislead inferences of the fundamental processes underpinning arc magmatism ([Larrea et al., 2013](#); [Sakya et al., 2012](#)). Thus, an independent study of crystal cargo and its influence on rock chemistry is required.

Upwelling melts interact with crystal mush zones, remobilizing and reacting with the crystal cargo and interacting with the wall rock and interstitial melts ([Beier et al., 2017](#);

[Hildreth and Moorbath, 1988](#); [Holness et al., 2019](#)). As magma (melt + crystals) ascend from the storage region, volatiles that were once dissolved in the melt begin to exsolve and result in the degassing of magmas ([Rutherford, 2008](#)). Degassing depends on several factors, including the rate of magma ascent, the permeability of the wall rocks and the physical and chemical properties of the magma in question ([Gonnermann and Manga, 2013](#); [Sparks, 2003](#)).

Petrological observations of hydrous mineral crystals within lava domes have provided insights into the rates of magma ascent ([Devine et al., 1998](#); [Nicholis and Rutherford, 2004](#); [Rutherford, 2008](#); [Rutherford and Devine, 2003](#); [Rutherford and Hill, 1993](#)).

Minerals, such as amphiboles (e.g., hornblende), react with the increasingly volatile-depleted melt during degassing, resulting in the formation of reaction rims in the contact with melt, indicative of changes in the conditions of the host melt during storage and ascent. The reaction begins once the melt H₂O content is sufficiently decreased to destabilize amphibole. The breakdown of amphibole taking place during depressurization follows the reaction amphibole + melt₁ ↔ orthopyroxene + clinopyroxene + plagioclase + ilmenite + melt₂ ([Rutherford and Hill, 1993](#)).

Amphibole reaction rims are often used to unravel complex magma ascent and mixing processes. Ascent-driven dehydration and decomposition of amphibole were used to calibrate models for assessing magma ascent timescales in intermediate arc magmas ([Browne and Gardner, 2006](#); [Rutherford and Devine, 2003](#); [Rutherford and Hill, 1993](#)).

However, other factors also trigger amphibole breakdown, such as oxidation, fluxing of the melt with a CO₂ rich fluid, or heating ([Rutherford and Hill, 1993](#)).

1.2. Research Objectives

Constraining the petrogenesis of andesites is key to understanding the evolution of the crust, as well as the assessment of volcanic hazards at subduction zones. Whether the andesites are generated within the crust or in the mantle is a matter of much discussion. Intermediate magmas are conventionally viewed as originating from primary basaltic melts, released from the mantle into the overlying crust, where they are hybridised in a polybaric (mid-to lower crustal) storage region (e.g., [Annen et al., 2006](#); [Hildreth and Moorbath, 1988](#)). More recently, it has been proposed that melt differentiation can occur in the mantle wedge through incorporating crustal (eroded forearc) and sedimentary components into the subduction channel through high-silica melanges (e.g., [Straub et al., 2020](#)). The first objective of this thesis is to gain insight into the generation of intermediate magmas at back-arc volcanoes through the study of whole rock, melt, and mineral compositions.

Arc magmas can contain a significant proportion of crystals with disequilibrium textures, which indicate variations in magmatic conditions ([Gill, 1981](#); [Zellmer et al., 2016](#)). The phenocrysts can be autocrystic, i.e., crystallised from the melt they are entrained in ([Miller et al., 2007](#)), xenocrystic, i.e., foreign to the magmatic host and magma system ([Sollas, 1894](#)), or antecrystic, i.e., recycled within the current magmatic system before inclusion in the host magma ([Charlier et al., 2005](#)). The second objective of this study is to comment on the origins of the crystal cargo of Taranaki lavas and the implications on our understanding of the magma storage region.

Volcanic eruptions produce a range of eruptive styles from Plinian eruptive columns and pyroclastic density currents to effusive eruptions characterised by lava flows and dome growth. The rates of magma ascent are thought to play a crucial role in the style of

eruption, and they are a function of the physical and chemical characteristics of the magma (density, viscosity, crystallinity, composition, pressure, and temperature), as well as the geometry of the conduit ([Lormand et al., 2020](#); [Mastin and Ghiorso, 2001](#); [Papale and Dobran, 1994](#); [Petrelli and Zellmer, 2020](#); [Pinkerton et al., 2002](#); [Rutherford, 2008](#); [Sparks et al., 2006](#); [Zellmer et al., 2016](#)). Slow ascent rates (cm/s to mm/s) are usually associated with effusive eruptions, while faster ascent rates result in explosive eruptions, typically attributed to gas exsolution from the magmas during syn-eruptive ascent in the conduit ([Rutherford, 2008](#)). Thus, constraining ascent rates provides critical insights into volcanic explosivity and helps inform hazard mitigation efforts. The third objective of this research is to attempt to constrain the timescales of magma ascent from storage to surface.

1.3. Aims

The research presented here addresses the processes that govern the nature of volcanism at Taranaki volcano, focussing on the episodes of extrusion that form part of the present-day edifice of Mt. Taranaki. Encompassing magma compositions of basalts to trachyandesites, the crystal cargoes of these lavas are studied in detail, to assess whether they have crystallised from the melt, entrained from older parts of the magmatic system or from the rocks that host the present-day plumbing system. An understanding of melt generation, the origin of the crystal cargo, and the effect of magma storage processes and ascent pathways on amphibole breakdown are the key aspects of the present thesis that will ultimately provide insights into the architecture of the magma plumbing system of this active back-arc volcano. To this end, three primary aims have been set:

Study 1 – Melt generation: Late-stage crystallization of mineral phases results in the formation of mineral rims that satisfy melt-mineral equilibria. Thermobarometric and

hygrometric calculations are used to determine melt characteristics and infer recent melt generation processes beneath Taranaki.

Study 2 – Crystal cargo: Chemical zoning patterns indicate the history of magmatic processes operating during the growth/destruction of the minerals. Therefore, studying mineral zonation of major, minor and trace elements in plagioclase, pyroxene and amphibole phases will offer key insights into the origin of the crystal cargo and their relationship with the variety of melts reaching Taranaki's storage region over its history.

Study 3 - Magma ascent times: Studying the wide range of breakdown textures of amphiboles hosted by Taranaki lavas enables further insights into the role of magmatic processes such as recharge and the shallow magma ascent pathways at Taranaki volcano.

Chapter 2.: Geological Background

2.1. North Island of New Zealand

New Zealand, along with four groups of Subantarctic islands (Antipodes, Auckland, Campbell and Chatham) and New Caledonia are the only emergent parts of the 4.9 million km² Zealandia continent ([Mortimer et al., 2017](#); [Timm et al., 2010](#)). The existence of the New Zealand land mass is attributed primarily to uplift associated with the Cenozoic plate convergence between the Indo-Australian and Pacific tectonic plates ([Reilly et al., 2015](#); [Wallace et al., 2007](#)).

The 1500 km section of the Pacific-Australian plate boundary through New Zealand, from the Hikurangi margin in the north to the Puysegur margin in the south ([King, 2000](#)), changes spatially from north to south and includes segments of subduction, back-arc rifting, fault transform systems, and continental collision ([Beavan and Haines, 2001](#); [Jiao et al., 2017](#); [Walcott, 1978](#)). This is accompanied by a general southward increase in the obliquity of relative plate motion and a rate of *c.* 40 mm/yr ([DeMets et al., 2010](#); [Nicol et al., 2017](#)).

In northern New Zealand, the Pacific Plate subducts westward beneath the Indo-Australian Plate at the Hikurangi Trough at rates of 40–48 mm/yr ([Barnes and Mercier De Lépinay, 1997](#); [Davey et al., 1986](#); [Wallace et al., 2004](#)). A transition to transpression in the northern South Island, accommodated by dextral slip along the Marlborough Fault System and continental collision at the Alpine Fault, has resulted in the formation of the Southern Alps ([Beavan et al., 1999](#); [Jiao et al., 2017](#); [Reilly et al., 2015](#)). Further south, at the Puysegur Trench, the Indo-Australian plate subducts eastward beneath the Pacific plate at 30–35 mm/yr with a sharp change in strike of the subduction zone and a steepening of the dip of

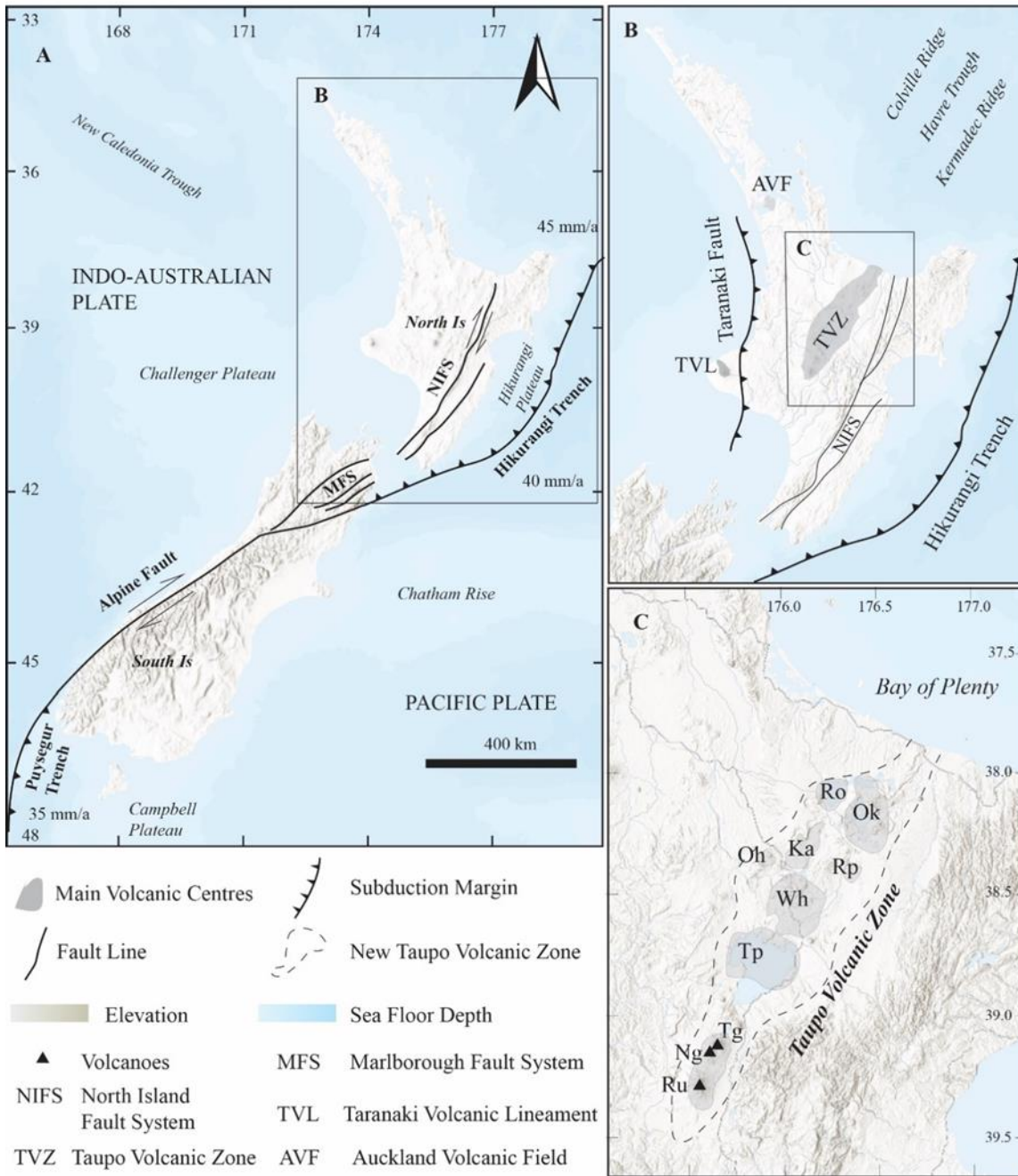


Figure 2.1: Tectonic framework of New Zealand and the principal volcanic centres in the North Island. shows the tectonics of New Zealand with subduction of the Pacific Plate off the North Island and the subduction of the Indo-Australian Plate in the South, connected by a transform boundary. (B) shows the North Island with the major volcanic centres marked (C) shows the Taupo Volcanic Zone comprising of several volcanic centres (Deering et al., 2011) including Rotorua (Ro), Okataina (Ok), Kapenga (Ka), Mangakino (Ma), Whakatane (Wh), Reporoa (Rp), Ohakuri (Oh), Taupo (Tp) and the Tongariro volcanic centre consisting of volcanoes Ruapehu (Ru), Ngauruhoe (Ng) and Tongariro (Tg). Modified from Cole et al. (2014).

the seismic zones (Eberhart-Phillips and Reyners, 2001; Lamarche and Lebrun, 2000; Reyners and Webb, 2002; Walcott, 1978, 1998).

2.1.1. Taupo Volcanic Zone (TVZ)

Active tectonism in the North Island, though dominated by subduction, is accompanied by strike-slip faulting in the eastern North Island Fault System (NIFS) and subduction-associated back arc rifting in the Taupo Volcanic Zone (TVZ) ([Cole and Lewis, 1981](#); [Davy and Wood, 1994](#); [Jiao et al., 2017](#); [Smith et al., 1989](#); [Wallace et al., 2004](#)). The TVZ is an area of frequently active Quaternary calc-alkaline volcanism, crustal magmatism and geothermal activity ([Stern et al., 2006](#); [Wilson et al., 1995](#)).

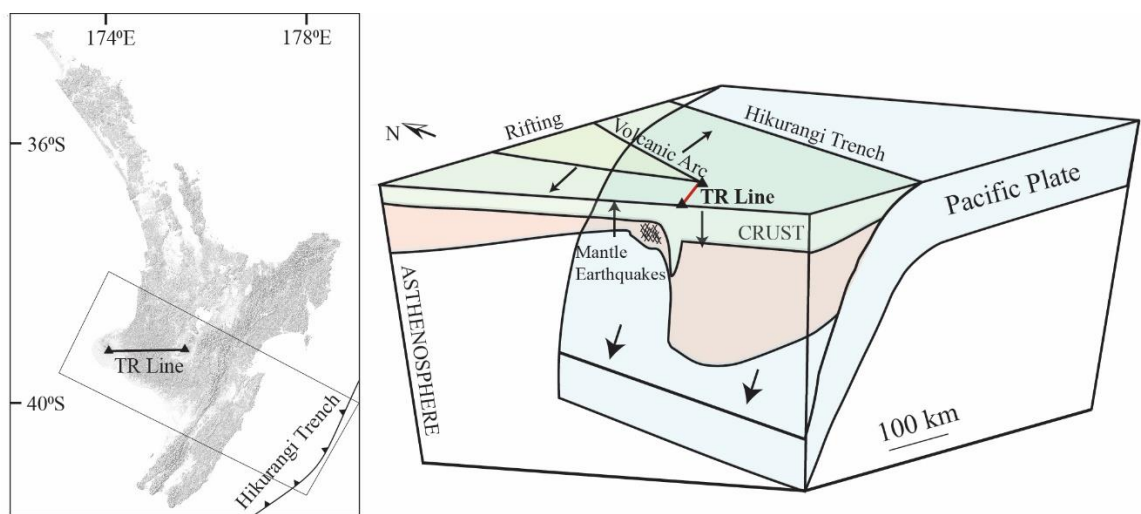


Figure 2.2: A subcrustal illustration of subduction beneath the North Island of New Zealand with the crust thickening below the Taranaki-Ruapehu Line (TR Line). Along the Hikurangi Trench, westward subduction of the Pacific Plate (including the Hikurangi Plateau) occurs beneath the North Island of New Zealand. Modified from [Dimech et al. \(2017\)](#)

Structurally, the TVZ represents the apparent continental continuation of the Kermadac Ridge (oceanic volcanic arc) - Havre Trough (oceanic back-arc) systems ([Karig, 1970](#); [Wilson et al., 2009](#); [Wright, 1992](#)) and is a part of the 2000 km long Lau-Havre-Taupo back-arc basin of the western Pacific ([Parson and Wright, 1996](#)). However, the TVZ axis of spreading is offset by 40–45 km to the east of the Havre Trough, linked tectonically by the development of *en échelon* faults ([Lewis and Pantin, 1984](#); [Wright, 1990](#)). The eastern end of the TVZ, the volcanic front, has been migrating towards the southeast since 4 Ma

([Calhaem, 1973](#)). The migration of the arc has been attributed to the rotation of the North Island in response to the change in tectonic boundary conditions along the Hikurangi Margin, resulting in the opening of the intra-arc ([Reyners et al., 2006](#); [Stern, 1987](#); [Stern et al., 2006](#); [Wallace et al., 2004](#)). Another model suggests the parallel SE migration of volcanism - based on coevality of volcanism in NNE–SSW trending belts - reflects the change from slab rollback along the Kermadec system to fixed hinge slab steepening under the central North Island ([Herzer, 1995](#); [Seebeck et al., 2014](#); [Wilson and Rowland, 2016](#)). Irrespective of models, intra-arc opening in the North Island took place from *c.* 23–15 Ma, seems to have stopped from *c.* 15–6 Ma and then began again from 5 to 1 Ma ([Mortimer et al., 2010](#)).

The back-arc also shows a change from extensional to compressional regimes from north to south and this transition appears to occur rapidly across the Taranaki-Ruapehu line, an ill-understood, likely fault zone, defined by a distinct zone of shallow seismicity ([Reyners, 1980, 1989](#)). This transition is supported by a strong gravity gradient, earthquakes with mixed focal mechanisms, and a steep jump in anelastic attenuation across the line ([Reyners, 1989](#); [Sherburn and White, 2005](#); [Smith et al., 1989](#); [Stern et al., 2006](#)).

The largest and most active andesitic volcanoes in the North Island are the Tongariro-Ruapehu massif at the southern tip of the TVZ, White Island in the north offshore of the TVZ, and the Taranaki Volcano in the west ([Price et al., 2005](#)). Mt. Taranaki, 130 km west of the volcanic front at Ruapehu, represents the westernmost expression of volcanism related to the Tonga-Kermadec subduction system ([Price et al., 1999](#); [Reyners et al., 2006](#)). The earliest volcanism in the TVZ involved construction of andesitic volcanoes at around 2 Ma and associated intrusion of andesitic magma into the crust, with later progressive development of more extensive rhyolitic systems

commencing at around 1.6 Ma ([Price et al., 2005](#); [Wilson et al., 1995](#)). Based on the chemistry of the volcanism, the TVZ has been divided into an andesitic arc and a rhyolite-dominated intra-arc, although this is not reflected in the temporal and spatial distribution of vents ([Cole et al., 1995](#); [Giggenbach, 1995](#); [Wilson and Rowland, 2016](#)). The TVZ is also divided into three segments based on the distribution of volcanism - Northern TVZ, Central TVZ and Southern TVZ ([Cole, 1979](#); [Wilson et al., 1995](#)) and based on the evolution of volcanism, the Old TVZ, the Young TVZ and the Modern TVZ have been defined ([Wilson et al., 1995](#)).

2.1.2. The Taranaki Basin

The Taranaki Basin is located mainly offshore west of the North Island of New Zealand but also includes the onshore Taranaki Peninsula west of the Taranaki fault. It is up to 60 km wide and extends for at least 350 km in the NNE direction from the south of the Taranaki Peninsula to the offshore west of Auckland ([Funnell et al., 1996](#); [King and Thrasher, 1996](#)). It contains late Cretaceous (*c.*84 Ma) and younger strata, up to a thickness of 8 km, and is the principal source of hydrocarbons in New Zealand ([Giba et al., 2010](#); [Knox, 1982](#)). The limestone, coal, silt and sandstone deposits overlie a calc-alkaline plutonic and metamorphic basement, a part of the Median Tectonic Zone ([Mortimer et al., 1997](#)). The Taranaki Basin has had a complex structural and geological history, right from its earliest initiation in the Late Cretaceous until the present day, and currently displays active tectonics, volcanism, and seismicity ([Anderson and Webb, 1994](#); [Giba et al., 2010](#); [Neall et al., 1986](#); [Sherburn and White, 2005](#); [Sherburn et al., 2006](#)).

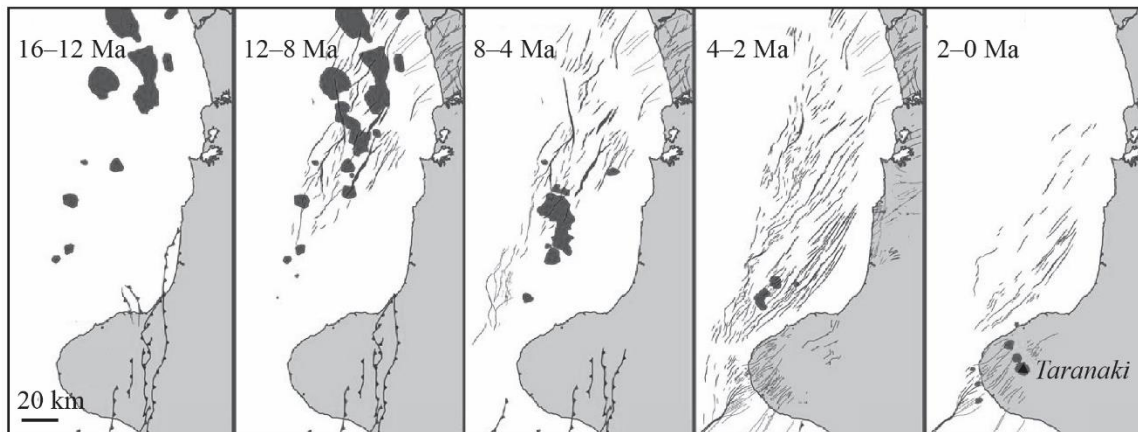


Figure 2.3 The evolution of the Taranaki basin and southward migration of Taranaki volcanism through time. Modified from [Giba et al. \(2010\)](#).

Three phases of deformation are recognized for the Taranaki Basin ([Giba et al., 2010](#)) – (i) Extension in the Late Cretaceous to Paleocene (c. 84–55 Ma) associated with the separation of New Zealand from Gondwana and the opening of the Tasman Sea ([King and Thrasher, 1996](#)). (ii) Crustal shortening and reverse faulting during Middle Eocene to Recent (c. 40–0 Ma) because of the onset of convergence between the Indo-Australian and Pacific plates ([Bache et al., 2012](#); [King, 2000](#); [Nicol and Wallace, 2007](#)). (iii) Extension of the basin and volcanism, which continues at Taranaki today, during the Late Miocene to Recent (c. 12–0 Ma), due to subduction system below New Zealand ([Holt and Stern, 1994](#); [Reilly et al., 2015](#); [Stagpoole and Nicol, 2008](#)). The Taranaki Basin transitions from regions of extension in the north to contraction in the south that marks the boundary between back-arc dominated processes, which extends up to the Havre Trough, and plate convergence in the north and south respectively ([Funnell et al., 1996](#); [Giba et al., 2010](#); [King and Thrasher, 1996](#); [Reilly et al., 2015](#)).

The extensive volcanism in the northern Taranaki Basin and the normal faults in this region, along with the volcanoes and sedimentary basins, are recognized to have migrated

southward during the last 20 Ma ([Ballance, 1976](#); [Herzer, 1995](#); [King and Thrasher, 1996](#); [Nicol et al., 2007](#); [Stern et al., 2006](#)), with volcanism preceding normal faulting in the north of the basin and faulting preceding volcanism at the southern end of the basin ([Giba et al., 2010](#)) (see Figure 2.3). Various models were proposed to explain this migration such as slab rollback ([Ballance, 1976](#)), movement of a Rayleigh-Taylor instability ([Stern et al., 2006](#)), erosion of continental crust by mantle corner flow ([Reyners et al., 2007](#)), propagation of the subducting plate ([Furlong and Kamp, 2009](#)), and a combination of slab rollback accompanied by the southward motion of the southern termination of the subduction system and the region of mantle flow ([Giba et al., 2010](#)).

2.1.3. Taranaki Volcanic Lineament

The Taranaki Volcanic Lineament (TVL) comprises four isolated Quaternary andesitic volcanoes (Figure 2.4) - the Sugar Loaf Islands and Paritutu (1.7 Ma), the Kaitake volcano (0.57 Ma), the Pouakai volcano (0.25 Ma) and Mt. Taranaki (0.25 Ma) ([Neall, 1979](#)). Paritutu and the seven Sugar Loaf Islands are eroded remnants of dykes, plugs, and volcanic necks composed of hornblende bearing andesites ([Neall, 1979](#)). Kaitake is a highly eroded 684 m high edifice of hornblende andesite and diorite dykes ([Gaylord et al., 2014](#); [Neall, 1979](#)). Pouakai is a 1222 m eroded remnant of predominantly amphibole- and pyroxene- bearing basaltic andesites and andesites ([Price et al., 2021](#)).

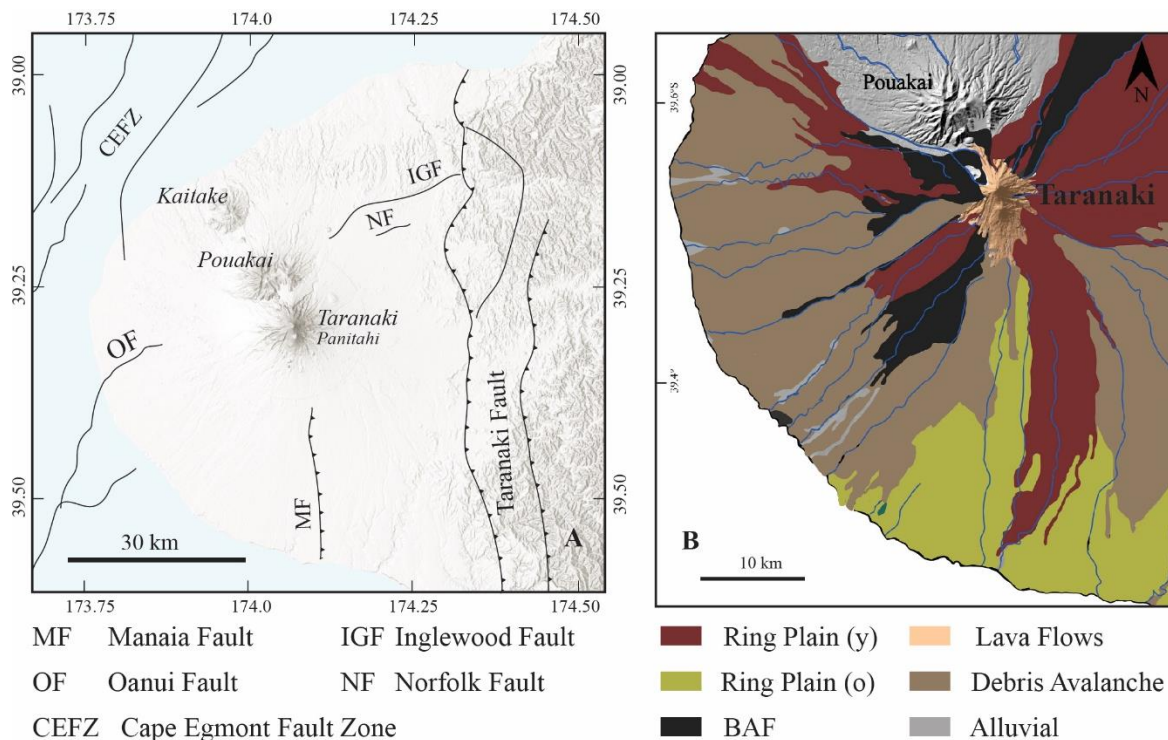


Figure 2.4 Tectonics and location of the Taranaki Volcanic Lineament in the western peninsula of the North Island of New Zealand. Modified from [Sherburn et al. \(2006\)](#), [Rajabi et al. \(2016\)](#) and [Giba et al. \(2010\)](#). (B) Volcanic products from Mt. Taranaki including lavas, debris avalanche deposits, ring plain deposits, young (y) and old (o), alluvial deposits and block and ash flows (BAF). Modified from [Zernack and Procter \(2021\)](#) and [Zemeny et al. \(2021\)](#).

This NW-SE trending lineament is in the back-arc region between the North and South Taranaki Basins, bounded by the NE trending Cook-Turi Lineament to the north and the Taranaki Fault to the south ([Price et al., 1999](#)). The TVL is approximately perpendicular to the principal axis of volcanism in the North Island, i.e., the Taupo Volcanic Zone (TVZ) and approximately parallel to the dip of the Wadati-Benioff zone ([Locke et al., 1994](#); [Neall et al., 1986](#); [Stewart et al., 1996](#)).

Seismic studies across the central and western North Island indicate that the crust-mantle boundary beneath the Taranaki Volcanic Lineament is at a depth of *c.* 35 km ([Sherburn and White, 2005](#); [Stern et al., 2006](#)). Seismic data suggests the TVL may be a high-level expression of the development of one of the segmenting fractures present in the subducting Pacific slab beneath the North Island, which is perpendicular to the Hikurangi

Trench ([Reyners and Cowan, 1993](#)). [Price et al. \(1992\)](#) suggested that a SE propagating fault/tear in the subducting slab focuses the fluid flow from the slab to produce a linear melting in the mantle wedge above. Another model suggests that the volcanism is due to the sinking of a delaminated lithosphere in to the asthenosphere, as the thickened crust became unstable ([Stern et al., 2006](#)); while an alternative explanation is the flow of the mantle around the edge of the slab causes such magmatism ([Jacoby, 1973](#)). Today, the only active volcano is Mt. Taranaki, the southernmost onshore volcano ([Downey et al., 1994](#); [Giba et al., 2010](#)).

2.2. Mount Taranaki

Mt. Taranaki (2518m) has been classified as a potentially active (Global Volcanism Program, 2013), a category that has been responsible for over two-thirds of volcanic fatalities since 1600 CE ([Auker et al., 2013](#)). Formerly known as Mt. Egmont, it is a near-symmetrical, andesitic stratovolcano in the western North Island of New Zealand ([Neall et al., 1986](#); [Turner et al., 2008b](#)). It lies *c.* 140 km west of the Taupo Volcanic Zone, *c.* 400 km west of the active Hikurangi Trench and *c.* 180 km above the Wadati-Benioff Zone ([Locke et al., 1994](#); [Stewart et al., 1996](#)). The volcano overlies *c.* 35 km thick continental crust characterised by a normal heat flow ([Price et al., 1999](#)) with infrequent seismic events occurring within a cluster of activity centred 600 km below Taranaki ([Boddington et al., 2004](#)).

Taranaki volcano is deeply incised by over 50 streams and rivers that flow radially away from the summits ([Davies and Lambert, 2015](#); [Grant-Taylor, 1964](#)). Fanthams Peak, or Panitahi, on the southern side of the main cone is a satellite vent rising to 1966 m, and interrupts the symmetry of the cone ([Downey et al., 1994](#)). The upper part of the volcano is a simple, near symmetrical cone, but the axis lies about a quarter of a mile southwest

of the centre of the lower base of the mountain. A somma ring is present, but slightly overlapped by the summit cone in the southwest ([Grant-Taylor, 1964](#)). Above 1000m altitude, eroded lava flows form steep bluffs, and the cone is deeply gullied with much scree ([McGlone et al., 1988](#)). Below, progressively gentler slopes, formed by detrital volcanoclastics, fan out onto the surrounding volcanic ring plain ([McGlone et al., 1988](#)). The extensive ring plain is constructed from debris avalanches, laharcic to fluvial deposits, pyroclastic flows and fall deposits, and alluvial volcanoclastic fans that reach up to 50 km from the summit ([Alloway et al., 1995](#); [Stewart et al., 1996](#); [Turner et al., 2018](#)).

Mt. Taranaki has been active for around 200 ky, and the current 12 km³ edifice, erupted over the last 10 ky, represents only a small percentage of the volume of material extruded from the volcano ([Alloway et al., 2005a](#); [Downey et al., 1994](#); [Procter et al., 2009](#); [Zernack et al., 2011](#)). Large-scale sub-Plinian eruptions from Taranaki occur on average every two to three centuries, with smaller, more frequent Merapian style eruptions typically producing lava domes, block-and-ash flows and small ash clouds. ([Alloway et al., 1995](#); [Green et al., 2013](#); [Platz et al., 2007](#); [Zernack et al., 2011](#)). During the last 600 years there have been several block-and-ash flow events ([Turner, 2008](#)) and one sub-Plinian eruption in 1655 CE ([Alloway et al., 2005a](#); [Neall et al., 1986](#); [Topping, 1972](#); [Wild et al., 2019](#)). The last eruption from Mt. Taranaki was *c.* 1790 CE ([Lerner et al., 2019b](#)). The long-term volcanic history of Mt. Taranaki comprises alternating cycles of edifice construction to a critical volume/height followed by catastrophic edifice collapse to generate widespread debris avalanche deposits that now surround the present cone ([Neall et al., 1986](#); [Palmer et al., 1991](#); [Zernack et al., 2011](#); [Zernack et al., 2009](#)).

Recent studies suggest that at least 13 edifice failures have occurred at Mt. Taranaki, every 10 ky on average, with five collapses being recognised over the last 30 ky ([Zernack et al., 2009](#)). These major sector collapses are triggered by an eruption, shallow-level

intrusions, cone instabilities, or regional earthquakes ([Zernack et al., 2009](#)). Edifice reconstruction follows with eruptions that range from explosive to effusive, generating volcanic products such as pyroclastic deposits, lava flows and dome extrusions ([Damaschke et al., 2017a](#); [Platz, 2007](#); [Platz et al., 2006](#); [Turner et al., 2009a](#); [Turner et al., 2008a](#); [Turner et al., 2011a](#)). Two periods of growth between 7000-2800 yrs and 700-400 yrs have been indicated through paleomagnetism ([Cronin et al., 2021](#)). Periods of quiescence are marked by sediment layers intercalated in the debris avalanche flows and extruded material ([Zernack et al., 2009](#)).

Previous work carried out at Mt. Taranaki includes mapping of general stratigraphic units (e.g. [Alloway et al., 1995](#); [Neall, 1972, 1979](#); [Zernack et al., 2011](#)), lava flows and lava domes (e.g. [Lerner et al., 2019b](#); [Platz et al., 2012](#); [Stewart et al., 1996](#)), debris avalanches, and lahars (e.g. [Alloway et al., 2005a](#); [Cronin et al., 2021](#); [Palmer et al., 1991](#); [Procter et al., 2009](#); [Ui et al., 1986](#); [Zemeny et al., 2021](#); [Zernack et al., 2011](#); [Zernack et al., 2009](#)); and tephra deposits and tephrostratigraphy (e.g. [Alloway et al., 1995](#); [Alloway, 1989](#); [Damaschke et al., 2017b](#); [Danišik et al., 2012](#); [Neall, 1972](#); [Shane, 2005](#)). Geophysical studies and structural data of the Taranaki region have offered insight into the isolated location of the Taranaki volcanoes and their relation to the main subduction zone (e.g. [Armstrong et al., 1998](#); [Boddington et al., 2004](#); [Funnell et al., 1996](#); [Locke and Cassidy, 1997](#); [Locke et al., 1993, 1994](#); [Mojtaba et al., 2016](#); [Nodder, 1994](#); [Reyners, 1980](#); [Sherburn and White, 2005](#); [Sherburn et al., 2006](#); [Stagpoole and Nicol, 2008](#); [Walcott, 1978, 1984](#); [Wallace et al., 2004](#)). Detailed geochemical studies of the lava flows emitted from the present day summit and satellite cone - Fanthams Peak (e.g. [Price et al., 2012](#); [Price et al., 1992](#); [Price et al., 2016](#); [Price et al., 1999](#); [Stewart, 2010](#); [Stewart et al., 1996](#); [Zernack et al., 2012](#)) and geochemical work on the xenoliths entrained in the lava flows and from debris avalanche deposits along the northern shore of the peninsula (e.g.

[Gruender et al., 2010](#); [Price et al., 2016](#)) have been the focus of previous studies at Mt. Taranaki. [Platz et al. \(2012\)](#) attempted to constrain the magma ascent rates for the Sisters dome by using hornblende crystals present in the block and ash flows.

Mt. Taranaki is located over a basement dominated by granitic and dioritic rocks of the Median Tectonic Zone (MTZ), which is defined as a zone of deformed or dismembered small crustal fragments and/or magmatic arc rocks ([Bradshaw, 1993](#); [Gruender et al., 2010](#); [Mortimer et al., 1997](#); [Price et al., 1999](#)). The Median Batholith is defined as a large volume composite intrusion comprising of many individual but contiguous plutonic and metaplutonic rocks and represents the result of the interaction of the Panthalassan oceanic plates with the South Gondwana continental plate during the Carboniferous to early-Cretaceous ([Kimbrough et al., 1994](#); [Mortimer et al., 1997](#); [Mortimer et al., 1999b](#)).

The ring plain deposits represent the episodes of cone collapse and were previously crudely placed into a stratigraphic order - 'Old Ring Plain' deposits (emplaced before 24 ka) and 'Young Ring Plain' deposits (emplaced between 24 and 8 ka) ([Price et al., 1999](#)).

However, detailed tephrostratigraphy and tephrochronological studies of debris avalanche deposits, and the sediments intercalated in them, have identified 13 edifice collapses and 12 periods of edifice regrowth (e.g. [Alloway et al., 2005a](#); [Alloway et al., 1995](#); [Damaschke et al., 2017a](#); [Neall, 1972](#); [Zernack et al., 2011](#)).

2.3. Stratigraphy and Age of Rocks of present Taranaki cone

A stratigraphy table for Taranaki eruptives over the last 10 ky is shown in Table 2.1. The oldest pyroclastic deposits at the present Taranaki cone are those of the Kahui block-and-ash flows and lahars (*c.* 13–8 ka), possibly representing a cycle of dome growth and collapse ([Neall, 1979](#); [Torres-Orozco et al., 2017a](#)). The oldest lavas are the Warwicks Castle lavas (8 ky BP), which collapsed (*c.* 7.5 ka) resulting in the Opuā debris

avalanche deposit ([Neall, 1979](#); [Stewart et al., 1996](#); [Zernack et al., 2011](#)). The Peters lavas (7–3.3 ka) were emplaced during a period of effusive activity, building the volcanic edifice ([Neall, 1979](#)). Fanthams Peak (*c.* 3.5–2.9 ka), the satellite cone, erupted explosively and then effusively ([Torres-Orozco et al., 2017b](#)) to emplace both tephra deposits and lava flows ([Stewart et al., 1996](#); [Zernack et al., 2011](#)). It is, however, believed to have been present from *c.* 7 ka based on cover bed stratigraphy ([Stewart et al., 1996](#)). Contemporaneously, the Skinner Hill, Beehives Dome and The Dome were emplaced as lava domes on the lower flanks of the edifice ([Grant-Taylor, 1964](#); [Neall, 1971](#); [Platz et al., 2012](#)). The Staircase and Skeet lavas (1.6–1.3 ka) erupted from the summit cone and partially filled the amphitheatre caused by the Opuia collapse ([Stewart et al., 1996](#)). The Summit lavas (0.8–0.4 ka) also fill up the amphitheatre and bifurcate around Fanthams Peak ([Downey et al., 1994](#); [Stewart et al., 1996](#)). Correlated block-and-ash flows and surge deposits (Newall, Waiweranui, Puniho), indicating dome-forming effusive and minor explosive activity, are believed to have been deposited between 1.1–1.6 ka ([Druce, 1966](#); [Neall et al., 1986](#)). This was followed by the pumice tephra of the Burrell eruption (*c.* 1655 CE) ([Druce, 1966](#)), the Tahurangi event (*c.* 1755 CE) ([Druce, 1966](#); [Neall, 1972](#)) and the extrusion of a lava dome and western sector collapse (*c.* 1800 CE) inside the summit crater ([Platz et al., 2012](#)). The lava dome marks the last eruption from Mt Taranaki at *c.* 1790 CE ([Lerner et al., 2019a](#); [Lerner et al., 2019b](#)).

Table 2.1: Summarised stratigraphy of the last 10 kyrs of Taranaki eruptions modified from previous studies ([Lerner et al., 2019b](#); [Platz, 2007](#); [Stewart et al., 1996](#); [Torres-Orozco et al., 2017a](#); [Zernack et al., 2011](#)). LD= Lahar Deposits; DAD= Debris Avalanche Deposits; BAF= Block and Ash Flows; A= Ash; B= Breccia; T= Tephra; PFD= Pyroclastic Flow Deposit; HFD= Hyperconcentrated Flow Deposits

Chr.	Period	Episode	Primary Volcanics			Volcaniclastics		Cal. age
			Lavas	Age(max.)	PF deposits	Tephras	LD	
Maero		Pyramid	Pyramid Dome	0.2	P. rock avalanche	Pyramid L		0.16 0.2
		Tahurangi	Fanthams 3	0.5–1.4	T. BAFs & surges	Tahurangi A Tahurangi B		0.2 0.3
		Mangahume Burrell	Burrell Coulee/ Dome	<1.4	B. pumice flows B. BAF & surges	Mangahume L Burrell L Burrell B		0.4
		Puniho			P. pumice flow P. BAF & surges	Puniho A Puniho B		0.4 0.4
		Waiweranui			W. BAF & surges	Waiweranui A Waiweranui B		0.5 0.5
		Newall			N. BAF & surges	Newall A Newall B		
			Minarapa Flows Skeet ridge Flows	<1.4 <1.4				
		Waingongoro				Waingongoro A		0.5
		Te Popo			TP BAF & surges	Te Popo A Te Popo B		0.8
		Hooker				Hooker L		
		Kaupokonui	Staircase Flows MacKays Flows Fanthams 2	3.3-1.4 3.3-1.4 3.3-1.4	BAFs, E-flank	Kaupokonui T		1.3 1.9
		Maketawa	Beehives, The Dome, Skinner Hill	c. 3.3		Maketawa T	Te Popo DFD	3.1–2.9 3.4–2.9
		Manganui	Fanthams 1	7–3.3		Manganui T		3.5–2.9
					At least 3 PFDs	Inglewood T	Ngatoro DFD	3.9–3.7 4–3.9
			Peters lavas	7–3.3		Korito T Mangatoki T Tariki T Waiopuku T	Warea 4 DF/HFDs DFD/HFD	7–3.3 4.6–4.4 5 5.4–5.3 6.1–5.7
OPUAN		Kahui	Warwick Castle	>7		Oakura T	pum. HFD	Opua 7.5 7.8

2.4. Petrology, mineralogy, and geochemistry

The volcanic deposits of Taranaki can be broadly classified as andesites ([Downey et al., 1994](#); [Gow, 1968](#)), with minor basalts ([Neall et al., 1986](#)) and dacites ([Stewart et al., 1996](#)). Fanthams Peak lavas were identified as basalts to basaltic andesites and the summit eruptives as basaltic andesites, andesites and dacites ([Stewart et al., 1996](#); [Torres-Orozco et al., 2017a](#)). Thin section textures range from holocrystalline to hypocrySTALLINE, some are seriate, but most are porphyritic ([Price et al., 1999](#); [Stewart et al., 1996](#)). Pilotaxitic or hyalopilitic textures are also typical of the Taranaki deposits ([Gow, 1968](#)).

2.4.1. Whole Rock Classification

The magmas of Taranaki are classified as high-K andesites in the [Gill \(1981\)](#) system ([Turner et al., 2008b](#)). [Gow \(1968\)](#) identified them as calc-alkalic aluminous andesites with some approaching dacitic composition. [Platz et al. \(2012\)](#) commented that the bulk rocks erupted over the past 10 ky at Taranaki are high-K, low-Si and high-Si andesites from the main summit cone, with minor high-K basalts from the satellite cone of Fanthams Peak. The general geochemical trend over the past 130 ky at this volcano shows that the rocks between eruptive periods become progressively more potassic and siliceous, but within any eruptive period, variations across the entire spectrum of compositions may occur ([Stewart et al., 2006](#)). According to the total alkali silica (TAS) classification scheme of ([Le Maitre, 1989](#)), 14% of the rocks were classed as basalts, 73% basaltic andesites, and 13% andesites ([Price et al., 2016](#)).

Further classification of the andesites, based on the dominant mineralogy, include hornblende andesite ([Hutton, 1889](#); [Neall et al., 1986](#)), augite andesite ([Clarke, 1912](#); [Hutton, 1889](#)), olivine andesite ([Hutton, 1889](#)), hornblende-augite andesite ([Clarke, 1912](#); [Marshall, 1908](#); [Morgan, 1927](#)). The eruptive products display a variety of textures

ranging from pumiceous dacites and andesites ([Stewart et al., 1996](#)) to holocrystalline andesites and scoria ([Gow, 1968](#)). In most of the rocks, porphyritic textures with phenocrysts of feldspar, hornblende and augite, often showing strongly developed flow structures, can be observed with the naked eye ([Gow, 1968](#)). [Downey et al. \(1994\)](#) stated that the flows and pyroclastics of Taranaki range in composition from red, scoriaceous, pyroxene-plagioclase-phyric basaltic andesites to glassy, black, plagioclase-pyroxene-phyric andesites.

2.4.2. Whole Rock Geochemistry

Ranges of the major oxides in wt% after [Price et al. \(2016\)](#) are shown in Figure 2.5 in a series of silica variation diagrams. TiO_2 , $\text{FeO}_{\text{total}}$, MgO , and CaO abundances decrease systematically and linearly with increasing SiO_2 abundances, whereas Na_2O and K_2O contents increase. Al_2O_3 variation is complex; the stratigraphic groups are, to some extent, distinguished in the Al_2O_3 vs. SiO_2 plots. A general observation is that within stratigraphic groups, SiO_2 abundance increases and between groups, K_2O increases. When compared to volcanism of the TVZ, the Taranaki primary basalts are relatively low in silica and enriched in LILE and HFSE, and are suggested to be generated by lower degrees of partial melting and / or by melting at pressures that were higher than for the primary basalts of the TVZ ([Price et al., 1992](#)).

The trace element abundance of the volcanism observed at Taranaki shows characteristics typical of subduction related igneous rocks or continental crust (Figure 2.6). These include relative enrichments in Rb and K and the light rare earth elements (LREE) relative to Zr, Y and the heavy rare earth elements (HREE); enrichment of Pb relative to Ce, and strong depletion of Nb relative to K and Th ([Price et al., 1992](#); [Price et al., 1999](#); [Zernack et al., 2012](#)). The arc or crustal signature is more pronounced in the basaltic andesites and andesites than in basalts ([Zernack et al., 2012](#)).

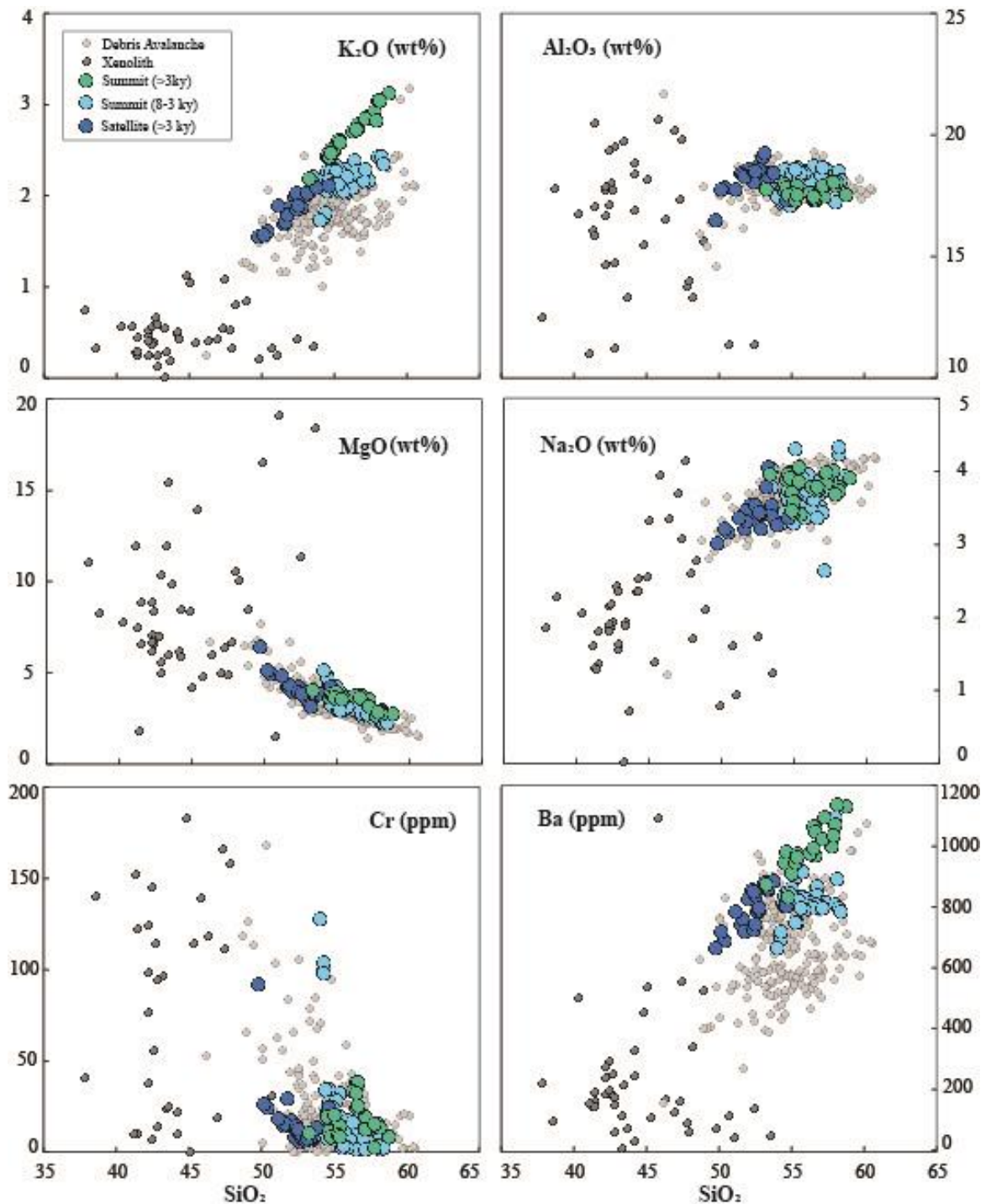


Figure 2.5: Major and minor element chemistry of the volcanic products of Taranaki over time. Data obtained from ([Price et al., 1992](#); [Price et al., 2016](#); [Price et al., 1999](#); [Stewart et al., 1996](#); [Zernack et al., 2012](#))

Trace element abundances of Rb, Ba and Zr, show systematic increase with increase in SiO_2 content and the variations in these elements are similar to that shown by K_2O . Sr shows much less coherent variation with SiO_2 and shows some distinctions between

different groups. Abundance variations for Ni, Cr, V, and Sc are similar to those shown by MgO and FeO, with systemic decrease with increase in SiO₂ ([Price et al., 1999](#)).

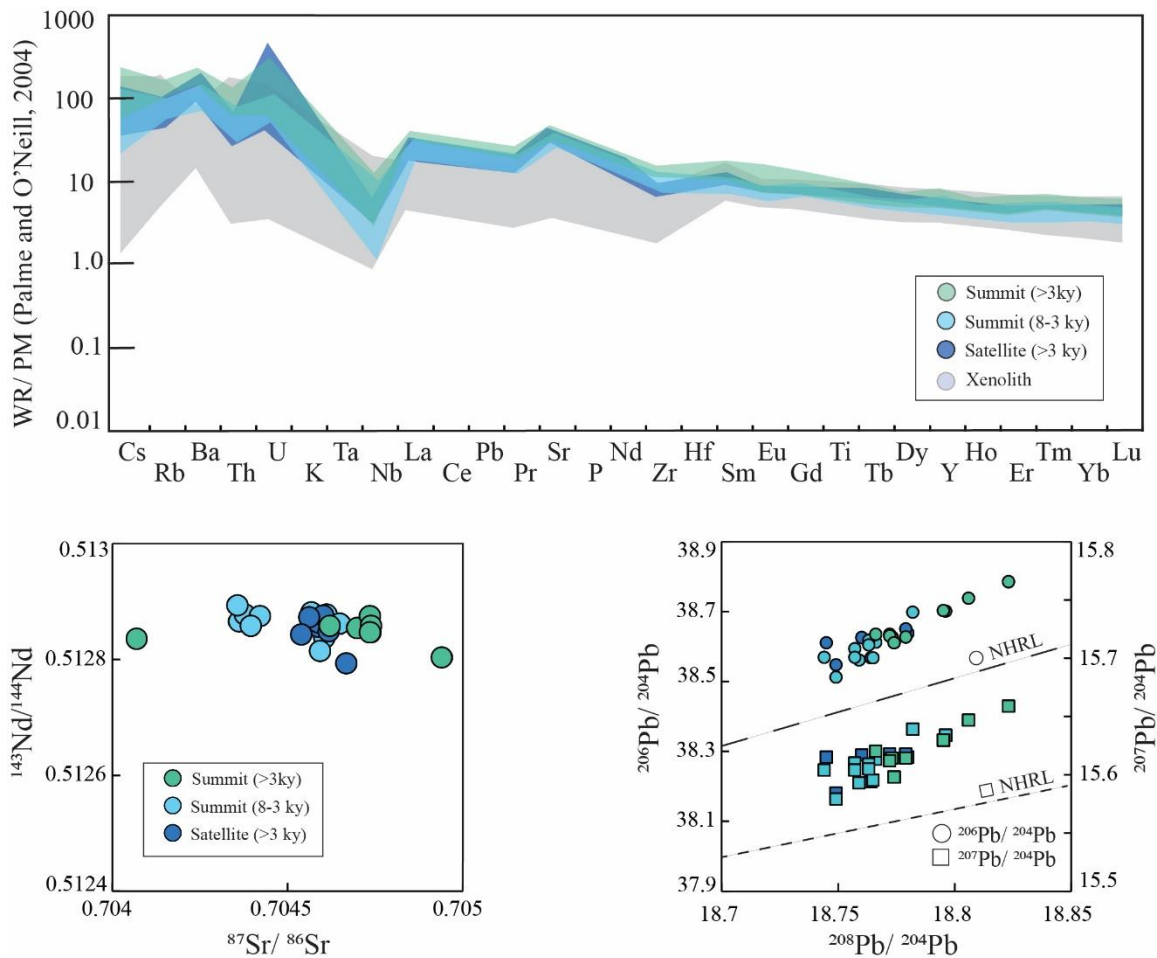


Figure 2.6: Trace element and isotopic data for Taranaki lavas with respect to age and vent. Data from ([Price et al., 1992](#); [Price et al., 1999](#); [Stewart et al., 1996](#))

Pb isotope diagrams of $^{207}\text{Pb}/^{206}\text{Pb}$ vs. $^{206}\text{Pb}/^{204}\text{Pb}$ and $^{208}\text{Pb}/^{204}\text{Pb}$ vs. $^{206}\text{Pb}/^{204}\text{Pb}$ show that the Taranaki samples plot above and parallel to the NHRL (Northern Hemisphere Reference Lines) of [Hart \(1984\)](#). The $^{143}\text{Nd}/^{144}\text{Nd}$ vs. $^{87}\text{Sr}/^{86}\text{Sr}$ isotopic ratios plot almost linearly above Bulk Earth (Figure 2.6). There is no apparent change in the $^{143}\text{Nd}/^{144}\text{Nd}$ isotopic ratio in relation to the stratigraphy. However, $^{87}\text{Sr}/^{86}\text{Sr}$ shows a progressive increase as the samples become younger.

2.4.3. Mineral Assemblages

Phenocryst assemblages in young Taranaki eruptives are dominated by plagioclase, hornblende and clinopyroxene ([Price et al., 1999](#); [Stewart et al., 1996](#)). Based on mineral geochemistry, [Stewart et al. \(1996\)](#) suggested that most of the apparent phenocrysts, including plagioclase cores, appear to be xenocrysts entrained from the lower crust or upper mantle. In glassy, highly vesiculated rocks, microlites of plagioclase and, to a lesser extent clinopyroxene, appear predominantly at the boundaries of phenocrysts ([Platz et al., 2007](#)).

Glomerocrysts are common and comprise clinopyroxene \pm titanomagnetite \pm plagioclase \pm olivine with rare orthopyroxene and amphibole. Groundmass includes glass, plagioclase, titanomagnetite, clinopyroxene, rare olivine, orthopyroxene, amphibole, and ilmenite. Apatite and zircon are accessory minerals, along with the presence of rare ilmenite in the groundmass ([Stewart et al., 1996](#)).

Plagioclase is the most common phase in the rocks (12–40%), and crystals commonly show complex zoning, resorption or sieve textures ([Higgins, 1996](#); [Neall et al., 1986](#); [Price et al., 1992](#)). The zoning is usually normal, but reverse and oscillatory zoning is also seen with cores displaying a range of An_{65-55} and rims of $An_{\leq 30}$ ([Higgins, 1996](#)). Inclusions were observed in the phenocrysts, closer to the cores ([Gow, 1968](#)). Microlites of plagioclase in the groundmass indicate compositions of andesine (*c.* An_{35}) with marked alignment of the microlites ([Gow, 1968](#)).

Clinopyroxene is the second most abundant mineral (2–26%), but is occasionally sub-equal to plagioclase ([Neall et al., 1986](#)). Identified as augite or diopside, the phenocrysts commonly show oscillatory or sector zoning with inclusions of magnetite ([Gow, 1968](#); [Higgins, 1996](#)). The clinopyroxenes are often associated with

titanomagnetite (1–6%), which is common in the groundmass and as microphenocrysts ([Gow, 1968](#); [Neall et al., 1986](#)). Orthopyroxene/hypersthene is less common, occurring as large crystals mantled by clinopyroxene with a core compositional range of En_{74-79} , while the groundmass, microphenocrysts and rare phenocrysts show varying compositions of En_{60-66} ([Stewart et al., 1996](#)).

Amphibole, occasionally present as large crystals (up to 4 mm), is commonly partially or completely resorbed with occasional very large phenocrysts. No inclusions are observed, but resorption rims of magnetite and pyroxene of varying thicknesses are seen ([Gow, 1968](#); [Price et al., 1992](#)). Olivine (< 5% of rock) is Mg-rich and occurs as xenocrysts, phenocrysts, microphenocrysts and rare constituents of glomerocrysts, with some crystals showing chromite as inclusions ([Higgins, 1996](#); [Stewart et al., 1996](#)). Some olivine xenocrysts show normal zoning with compositions of Fo_{84-87} in the cores to Fo_{71-77} at the rims ([Stewart et al., 1996](#)). Apatite and zircon, along with biotite, occur only in high-Si andesites ([Price et al., 1999](#); [Stewart et al., 1996](#)).

Xenoliths contained in the Taranaki deposits are dominated by gabbros and ultramafic rocks. Less common (< 10%) xenolith types include sedimentary rocks (sediments of the Taranaki Basin) entrained at shallow depths of < 6 km; gneiss, granite and granodiorite derived from the Permian-Cretaceous Median Batholith (6–12 km deep); and mafic hornfels, fine-grained gabbro and banded amphibolites from granulite facies metamorphic rocks ([Price et al., 2016](#)). Amphibolite and schist xenoliths are rare, while common xenoliths are other andesites, diorite, gabbro, rare pyroxenite and Tertiary sediments ([Stewart et al., 1996](#)). Glass inclusions in the xenoliths are rhyolitic, dacitic and trachytic, and their compositions appear to correlate with the depth of xenolith entrainment, with mid- to upper-crust xenoliths containing more silica rich glass ([Stewart, 2010](#)).

Geochemical and petrographical studies by [Price et al. \(1992\)](#) observed that the Fanthams Peak eruptives differ from the typical eruptives of Taranaki. They show smaller phenocrysts with magnetite and clinopyroxene as the dominant phases, although plagioclase exceeds their abundances in some samples. Olivines are common, and there are few amphiboles (partially or fully pseudomorphed by magnetite and clinopyroxene) and minor orthopyroxene.

2.5. Previous Petrological Model for Taranaki Eruptives

The petrogenesis and evolution of the high-K andesites have been studied by [Price et al. \(1992\)](#), [Stewart et al. \(1996\)](#), [Price et al. \(1999\)](#), [Price et al. \(2005\)](#), [Turner et al. \(2008b\)](#), and [Zernack et al. \(2012\)](#). The earliest eruptives of Taranaki, found in the ring plains, included low- and medium-K andesites, which have wider ranges of HFSE and LREE compositions and low K₂O and LILE contents. There are rare occurrences of unfractionated basalts with higher MgO, Cr and Ni ([Zernack et al., 2012](#)). Temporal evolution of magmatism is indicated by an increase in values of K₂O and progressively more radiogenic Sr isotope values in younger eruptives ([Stewart et al., 1996](#)). This has been explained by progressively more significant crustal involvement with time ([Graham and Hackett, 1987](#); [Stewart et al., 1996](#)) or variations in the source, such as declining degrees of partial melting, changes in fluid flux, and/or mantle source heterogeneity ([Price et al., 1999](#)). A multistage model for the origin of the volcanism was proposed by [Stewart et al. \(1996\)](#), and was modified by [Price et al. \(1999\)](#), [Price et al. \(2005\)](#) and [Zernack et al. \(2012\)](#).

The parental magma of Taranaki was taken to be a silica-undersaturated, relatively hydrous, oxidised, LILE-rich high-Mg basalt originating as low degree (< 20%) partial melts from a heterogeneous source in the mantle wedge above the subducting slab ([Price](#)

et al., 1999; Zernack et al., 2012). The heterogeneity of the mantle source is thought to have arisen from various degrees of metasomatism of a depleted (Iherzolite) mantle fluxed by slab-derived fluids, resulting in arc-like characteristics in terms of trace element composition (Stewart et al., 1996; Zernack et al., 2012).

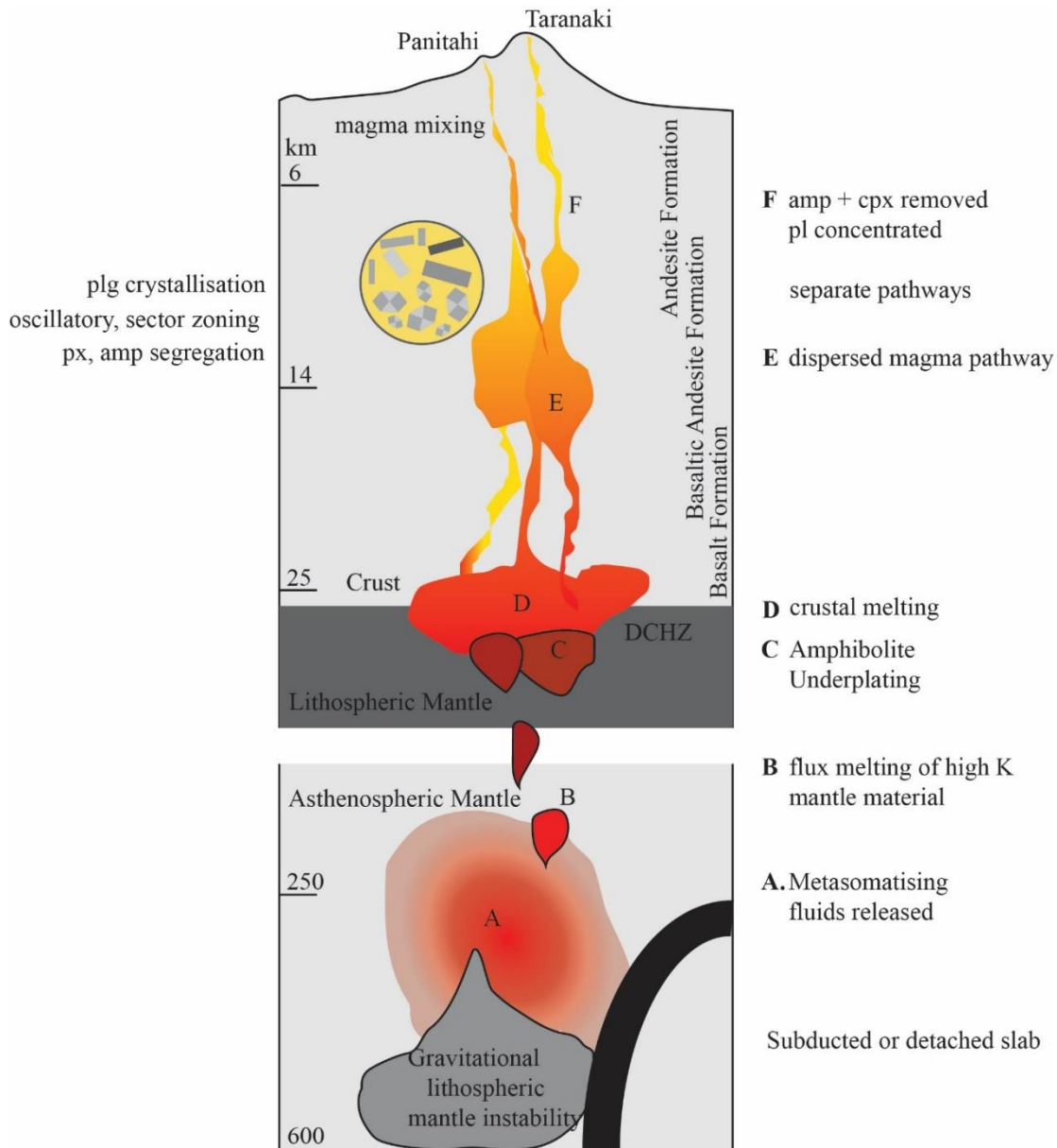


Figure 2.7: Illustration showing the petrological model for Taranaki volcano with metasomatized mantle releasing basaltic parental melts that partially melt an amphibolitic underplate. Subsequent assimilation and fractional crystallisation in a deep crustal hot zone (DCHZ) results in diverse melt compositions. Satellite vent and main summit have discrete conduits in the shallow crust. This is precluded by crystallisation in the storage zone. Modified from Cronin et al. (2021) and Price et al. (2021).

[Stewart et al. \(1996\)](#) proposed that the parental magmas ponded at the crust-mantle boundary and fractionation, involving olivine, chromite, clinopyroxene, spinel and titanomagnetite resulted in the generation of high-Al basalts ([Price et al., 1999](#); [Stewart et al., 1996](#)). Most of this magma solidified, and pressure and temperature conditions ([Foden and Green, 1992](#)) favoured fractionation of amphibole and complementary underplating of cumulates, including amphibolites and pyroxenites. Drier melts fractionated plagioclase and orthopyroxene, while hydrous melts reacted with cumulates and wall rock mafics to generate basaltic andesites. Rising magmas interacted with the crust and crustal melts, entraining wall rock xenoliths, which were melted to various degrees or resorbed.

With time, the thickness of the underplated and intruded lower crust increased along with the geothermal gradient. Reaction of high-Al basaltic magmas with crustal derived melts and lower crustal amphiboles is thought to have generated basaltic andesites with progressively higher K₂O contents. As the magmas rose into shallower chambers, magmas were segregated, and the more hydrous magma fractionated amphibole and biotite, which erupted as dacite and andesite. Those melts that did not fractionate amphibole instead fractionated plagioclase, olivine, pyroxene and magnetite and formed the andesitic lava flows and scoria deposits ([Stewart et al., 1996](#)).

[Zernack et al. \(2012\)](#) suggested that in its earliest stages, the magmas reached the surface rapidly and with little stalling and modification. As the magmatic system matured, repeated intrusions of the primitive high-Mg basalts into the lower crust led to the formation of a 'hot zone' ([Annen et al., 2006](#)) at the crust-mantle boundary. A complex of feeder dykes and sills ([Locke and Cassidy, 1997](#)) up to the mid- to shallow upper crust developed, resulting in a vertically differentiated plumbing and storage system ([Price et al., 2016](#)). The magma system under Taranaki is thought to contain several small magma

batches that have been in transient storage for various lengths of time ([Price et al., 2005](#)). Here, magma assembly, storage and modification, such as fractionation, magma mixing and mingling occurs, and primary magmas cannot reach the surface without being altered through these evolutionary pathways ([Price et al., 2012](#); [Zernack et al., 2012](#)).

This integrated model is supported by other observations of the Taranaki system. Geothermobarometry studies on the xenoliths by [Price et al. \(2016\)](#) shows that the physical conditions under which the xenoliths and their host lavas equilibrated are spread over a wide range of temperatures (750–1050°C) and pressures (80–800 MPa, equivalent to 3–30 km), indicating a polybaric magma storage and plumbing system dispersed through the crust. [Higgins \(1996\)](#) suggested that the rich variation among coexisting crystals suggests a dynamic environment of rapidly changing P–T–X conditions, such as expected in a sub-volcanic reservoir that is being refilled by new magma and drained by eruptions. Based on crystal size distribution analysis, [Higgins \(1996\)](#) suggested that the most recent eruptives from the Taranaki summit and Fanthams Peak have the shortest residence times of *c.* 30 years. No large scale magma reservoirs are evident in the upper crust for Mt. Taranaki ([Sherburn and White, 2005](#)), suggesting that the final magma storage level lies at a depth of about 10–11 km.

The youngest volcanics of Taranaki are magmas that ascended through 6 km of Tertiary sediments into the 2.5 km high edifice ([Platz et al., 2007](#)). They can be considered as dacitic melts (generated by complex processes including fractional crystallization, assimilation fractional crystallization, magma mixing and mingling), carrying a high percentage of crystal cargo and xenoliths, xenocrysts and glomerocrysts from melt zones in the lower crust that can affect the whole rock geochemistry ([Price et al., 2005](#); [Stewart et al., 1996](#)).

Chapter 3.: Methodology

3.1. Sample Site Selection and Mapping

Sample locations must be selected such that samples represent the stratigraphic and petrographic variety of eruptive products while considering access to these sites. This usually involves hours of fieldwork and sampling, as well as favorable weather conditions. To reduce time and effort required for sample site selection, we employed remote sensing techniques to digitally distinguish the eruptive products of Mt. Taranaki and then chose sites that showed most promise.

We used a Nikon D810 digital single-lens reflex camera, mounted on a Cessna 185 aircraft. The camera was mounted outside of the aircraft in a pod fixed on the wing strut. The camera was operated at ISO200 and 1/1600 exposure time with a ZEISS Milvus 2/35 mm lens. The camera was triggered remotely using an Aviatrix Cube system (AeroScientific, Australia). The flight height was maintained to be constant 3300 feet above ground (*c.* 1 km). This resulted in a maximum pixel size of 14 cm. The side and forward overlap between images were 60%. The survey took place on N–S oriented flight paths with a spacing of 410 m. In total, 40 lines were flown.

The images were saved in a raw format, adjusted for optimal lighting condition, and converted to JPEG images. The JPEG images were pre-processed with Pix4D, using the structure-from-motion approach ([James and Robson, 2012](#); [Westoby et al., 2012](#)). The initial image matching was performed using standard GPS metadata information from the images. This was followed by georectification using 3D ground control points from a high-resolution aerial photograph from Land Information New Zealand (<https://data.linz.govt.nz/>), and existing 25 m terrain models from Landcare Research

(<https://iris.scinfo.org.nz>). The resultant model represents a 50 cm top-of-the-canopy Digital Surface Model (DSM) with a spatial resolution of 0.3m, and a 50 cm orthophoto mosaic.

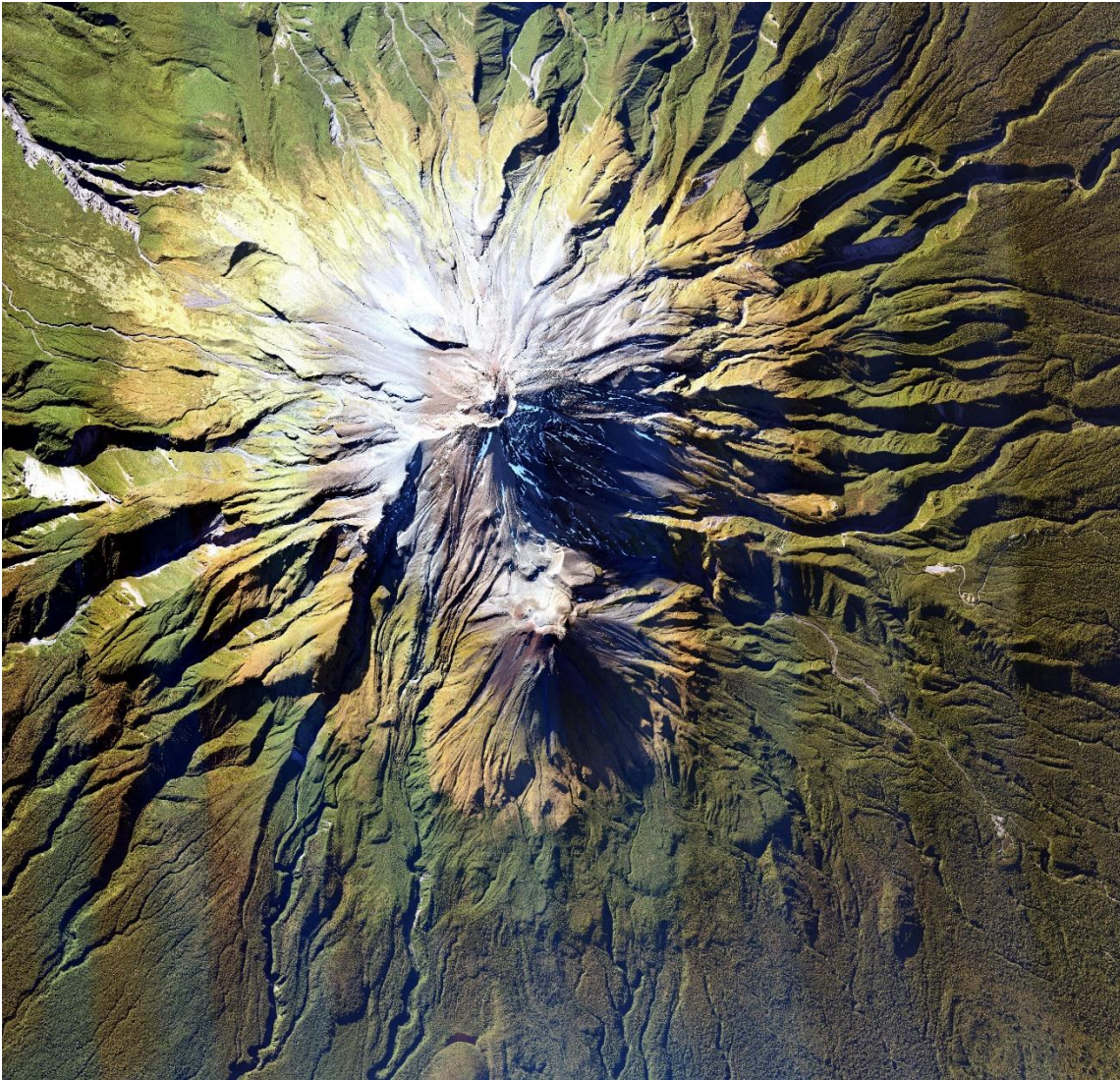


Figure 3.1: Mosaic image of Taranaki volcano with 60% overlap between flightpaths. This image was then imported into ArcGIS software to trace the lava flows.

These images were imported into the ArcGIS Pro software and it was possible to identify individual lava flows and lobes and trace their extent based on morphology. Each lava lobe was attributed with data obtained from other research, including age, composition

and stratigraphic group. The DSM was used to create a 3-D model of the Taranaki edifice using the structure from motion technique.

3.2. Field Work

Fieldwork was undertaken with the aid of the DSM map. Several fieldwork campaigns were required to explore the study area and distinguish the best locations in terms of accessibility and availability of samples. Geographical coordinates of potential sample sites were noted and selected from the map created.

Table 3.1: Table shows the samples of this study w.r.t. their location, stratigraphic unit, age, and lithology.

Sample	Flow Unit	Location		Age (kyr)	Lithology
		<i>latitude</i>	<i>longitude</i>		
ES3	Pyramid	39.2964	174.0637	<1.4	trachyandesite
ES5	Staircase	39.2968	174.0655	1.4-3.3	basalt
L18	MacKays	39.3127	174.0533	1.4-3.3	basaltic trachyandesite
L21	Skeet Ridge	39.3135	174.0561	<1.4	basaltic trachyandesite
CR	Warwicks	39.3043	174.0841	>7	basaltic trachyandesite
PYR	Warwicks	39.2879	174.0462	>7	basaltic trachyandesite
TUR	Warwicks	39.2940	174.0395	>7	basaltic trachyandesite
L16	Warwicks	39.3167	174.0743	0.5-1.4	trachybasalt
L5	Fanthams 3	39.3211	174.0650	1.4-3.3	basaltic trachyandesite
L2	Fanthams 2	39.3134	174.0793	3.3-7	basaltic trachyandesite
L9	Fanthams 1	39.3171	174.0739	3.3-7	basaltic trachyandesite
ES7	Fanthams	39.3097	174.0699	3.3-7	basalt

The first field traverse was across Fanthams Peak between 1400 and 1500m altitude, along the Upper Lake Dive Hut Trek. Samples of lavas from Fanthams Flows and samples from MacKays and Skeet Ridge Flows were also collected. The second traverse was at Fanthams Peak and along the flows from the Summit between 1900 and 2000 m altitude. The third traverse was to collect samples at a lower altitude of 900 m along the Lower Lake Dive Hut track and along Dawson Falls and the Egmont Visitor's Centre. Samples of eruptives from the summit were also collected along the trek at the Manganui Lodge. Samples from the Warwick Castle group were obtained from Prof. Robert Stewart, who collected them during previous fieldwork carried out at Mt. Taranaki. A summary of sample details is given in Table 3.1.

3.3. Laboratory Analyses

3.3.1. Petrographic glass mounted sections

Rock samples obtained were washed in an ultrasonic bath, cut and mounted onto glass slides. They were ground down to a thickness of approximately 100 μm , and then polished using 6 μm , 3 μm and finally 1 μm using a Buehler polishing machine. These thick sections were used for major and trace element analyses of the mineral phases (see below). Another set of glass mounted sections was prepared of *c.* 30 μm thickness and were used for petrographic observations and microphotography.

3.3.2. Back-scattered electron (BSE) imaging

Polished thick sections were coated using carbon sputter coaters. Back Scattered Electron (BSE) imaging was carried out using a FEI 200 Quanta Scanning Electron Microscope (SEM) at the Manawatu Microscopy Imaging Centre at Massey University, New Zealand. An accelerating voltage of 20 kV and a working distance of 10 mm was maintained. Spot analyses to identify mineral phases were conducted using Genesis EDAX software and the relative counts per second of Ca, Al, Mg, and Si. Images obtained were imported into ImageJ and adjusted for contrast and brightness. The colour threshold tool was used to determine the area percentage of vesicles for each sample.

3.3.3. X-ray fluorescence (XRF)

Unaltered samples of lava flows from Mt. Taranaki were cleaned in an ultrasonic bath and dried overnight in an oven set at 100°C. The samples were ground using a tungsten carbide ring mill to avoid Fe contamination and approximately 10 g of the sample was left in the oven for at least 2 hours. Loss in ignition (LOI) was calculated from the difference in weight of *c.* 2 g of sample before and after being kept in a Muffle furnace at 900°C for 3 hours. Fused glass discs were prepared by mixing 0.8 g (\pm 0.0010 g) of

sample with 8.0 g of lithium tetraborate:lithium metaborate (12:22) X-ray flux, followed by fusing and quenching in a platinum mould to form a glass disc using an XRFuse2 electrical fusion apparatus at Massey University. Oreas 24b and Oreas 24c Certified Reference Material were used as secondary standards. Glass discs were analysed for major element concentrations using a Bruker S8 Tiger Series II WD-XRF Spectrometer at Massey University. Interference-corrected spectra intensities were converted to oxide concentrations using calibration curves comprising natural standards. The results for Oreas 24b and Oreas 24c are consistent with the reference values within < 1% for elements used in this study, and replicate analyses indicate an analytical precision (1σ) of < 1.5%, and an accuracy of within 1–3% (except for Ti, where it is within 4%). See Appendix A for a list of analyses.

3.3.4. Electron microprobe analysis (EPMA)

Mineral major element compositional data were obtained using the JXA–8230 SuperProbe electron probe microanalyser at Victoria University of Wellington. Analysis was conducted with a focussed (1–5 μm) beam at 20 kV accelerating voltage and 12 nA beam current for mineral phases. For groundmass analysis, a defocussed 30 μm beam with a current of 8 nA was used to minimize Na-loss. Data was collected at 10–100 μm intervals along rim-to-rim or core-rim transects, depending on the size of the crystals. Amphibole breakdown regions with microlites larger than 2 μm were also analysed using EPMA to identify the reacted mineral phases. The instrument was calibrated using a variety of mineral, glass and oxide standards ([Jarosewich et al., 1980](#)) and the measurements were carried out with programme settings optimised for different mineral phases. Counting times were 30/15 s for peak/background for all elements except Na in glass, which was at 10/5 s. Instrumental drift was monitored by analysing standards of augite, hypersthene, and plagioclase multiple times as unknowns. We routinely achieved

an external precision of 0.5–1.5% on multiple replicates of standards run as unknowns, which are also within 5–10% of the certified values. Major elements are expressed as oxides and reported in weight percent (wt%). All analyses are listed in Appendix A

3.3.5. Laser ablation inductively coupled plasma mass spectrometry (LA-ICP-MS)

Rock powders previously fused in X-ray flux and quenched in a Pt mould to form glass discs were used for trace element analysis of the whole rock samples. Analyses of 35 trace and minor elements were conducted. Analyses were run as spots on the surface of the discs and pre-ablation to remove surface particles was carried out. Standards National Institute of Standards and Technology Standard Reference Material (NIST SRM) 612 and NIST SRM 610 were used as reference standards. Data are compiled in Appendix B.

Trace element compositions and zoning patterns of mineral crystals were investigated following the rastering technique ([Ubide et al., 2015](#)). Runs were carried out at the University of Queensland Centre for Geoanalytical Mass Spectrometry, Radiogenic Isotope Facility (UQRIF-lab). The instrument employed was an ASI RESolution 193 μm Eximer UV ArF laser ablation system with a dual volume Laurin Technic ablation cell and GeoStar Norris software, coupled with a Thermo iCap RQ quadrupole mass spectrometer operated by Qtegra software ([Ubide et al., 2019](#)). Ablation was performed in ultrapure He to which Ar make-up gas with trace amount of N_2 was added for efficient transport and to aid ionization. The mass spectrometer was tuned with scans on NIST SRM 612 glass reference material, maintaining low oxide production ($\text{ThO}/\text{Th} < 0.2\%$) and U/Th close to 1. Elemental maps were built using Iolite ([Paton et al., 2011](#)) ver. 2.5 in quantitative mode, using NIST 612 glass reference material as the calibration standard and Ca (cpx and amp) and Si (plg) concentrations obtained by EPMA as internal standards ($^{43}\text{Ca}_{amp} = 0.0856$; $^{43}\text{Ca}_{cpx} = 0.1510$; $^{29}\text{Si}_{pl} = 0.2583$). Secondary standards BCR, BHVO and BIR were used as unknowns, analysed regularly during the run to check for drift.

Precision was typically better than 1–5% for all measured elements and accuracy better than 1–5%, except for elements of low concentration where it was better than 5–10%. See list of results in Appendix B.

3.3.6. Electron back scatter diffraction (EBSD)

Determining the crystallographic orientation of the amphibole crystals in a 2-D rock surface was key to measuring the true thicknesses of reaction rims. Electron backscatter diffraction ([Prior et al., 1999](#)) data was collected at the University of Otago using an HKL INCA Premium Synergy Integrated EDS/EBSD system (Oxford Instruments) mounted on a Zeiss Sigma VP Field Emission Gun SEM. Glass slides were polished with 0.30 μm Al_2O_3 powder for optimal acquisition of EBSD patterns. Working conditions of 30 kV acceleration voltage, aperture of 120 μm , 70° sample tilt and high vacuum were maintained. For samples with few amphiboles, each crystal was analysed separately. For other samples, where amphiboles were hard to find or were too many, maps with colour coded orientations were obtained. *Channel 5* software (Oxford) was used for post-acquisition data processing to obtain stereoplots of the crystal faces.

3.4. Data Processing

3.4.1. Calculation of true thickness of reaction rims

BSE images were enhanced for brightness and contrast using Fiji ImageJ software. Crystal face Miller indices were determined by measuring the strike of the crystal face and tracing the corresponding pole position on the stereonet obtained by the hkl Channel 5 mambo software. Angle of dip of the face was then measured from the stereonet projection. Apparent rim thicknesses were measured from the BSE images. For each reacted amphibole, three measurements (maximum, minimum and random) were taken for each crystallographic face using the ImageJ measure tool. For larger grains, over 3

readings were recorded. The average of these measurements was used as the apparent thickness of the rim along a given crystal face. True thickness was calculated by using the formula:

$$T = A / (1 + |\tan(\theta + 90)|).$$

Where T = true thickness; A = apparent thickness; θ = angle of dip

Errors associated with this method are within 10% and include observational bias during stereoplot measurements, natural crystal imperfections and lack of clear crystal boundaries in some crystals, as well as number and site for apparent rim thickness measurements along crystal faces (rims are thicker at crystal faces).

3.4.2. Thermobarometry and Hygrometry

P-T conditions for Taranaki amphiboles were calculated using thermobarometers that use amphibole compositions only, as antecrysts are the predominant population. Calculations were done using the WinAmptb software ([Yavuz and Döner, 2017](#)) and employing the equations of [Ridolfi and Renzulli \(2012\)](#) and [Putirka \(2016\)](#). Temperatures of amphibole breakdown were calculated in rims where cpx and opx were present, employing the [Putirka \(2008\)](#) two-px thermometer. Clinopyroxene only compositions were used to determine the crystallization pressures for cpx using the barometer proposed by [Petrelli et al. \(2020\)](#). Equilibrium conditions between cpx rims and melt ([Mollo et al., 2017](#)) allowed for the use of the cpx-melt thermometer of ([Petrelli et al., 2020](#)) to determine the temperature of the host melt. Using these temperatures, we determined the water content of the melt using the plagioclase-melt hygrometer proposed by [Waters and Lange \(2015\)](#).

Table 3.2: Geothermometers, barometers and hygrometers employed in this study, along with equilibrium tests.

Model	Author	Error
Thermometer	Ridolfi and Renzulli (2012)	± 23.5 °C
Barometer	Ridolfi and Renzulli (2012)	$\pm 11.5\%$
Thermometer	Putirka (2016)	± 30 °C
Barometer	Putirka (2016)	± 4 kbar
Thermometer	Petrelli et al., (2020)	± 40 °C
Barometer	Petrelli et al., (2020)	± 3 kbar
Barometer	Neave and Putirka (2017)	± 1.4 kbar
Hygrometer	Waters and Lange (2015)	± 1.28 wt%
Hygrometer	Masotta and Mollo (2019)*	± 0.29 wt%
Hygrometer	Putirka (2008)	± 1.10 wt%

* Masotta and Mollo (2019) hygrometer for trachytes dataset too narrow with alkali content >10 wt%

Eq.	Author	Based on	Range
Plg-melt	Putirka (2008)	An-Ab exchange	0.1 ± 0.05 (T <1050°C)
Cpx-melt	Mollo et al. (2013)	DiHd and EnFs (Obs vs Cal)	$1:1 \pm 0.05$
Cpx-melt	Putirka (2008)	Kd Fe-Mg (liq-cpx)	0.28 ± 0.03

3.4.3. Major element mass balance calculations

Photographs of each sample were taken at 2.5× magnification using a Nikon camera attached to a Leica petrographic microscope. Heterogeneity in modal abundance of mineral phases due to large crystal sizes and their random distribution was minimised by considering 10 photographs per sample. The crystals were manually outlined, and colour coded, avoiding crystals smaller than 80 µm in length. Images were imported into Adobe Photoshop, stitched, and the sum area of each mineral/glass/vesicle was obtained using the measure tool. Mass of the individual mineral phases was calculated using the density, volume, and proportion of the respective phases. The oxide mass of the crystal cargo was then subtracted from the whole rock to obtain the oxide composition of the groundmass.

3.4.4. Calibration of EPMA major element maps

EPMA maps were obtained from Academia Sinica in Taipei, Taiwan. Maps were imported into ImageJ and colour adjusted for optimum colour variations for each element. A special Look Up Table (LUT) was created to calibrate images with the same colour scale as the LA-ICP-MS maps. X-ray intensity signals were converted into oxide wt% using the calibration tool. Oxide concentrations obtained from EPMA spot analyses were correlated to intensity values. The average intensity to oxide values of at least 20 spot analyses per element was used as a linear calibration from the origin to obtain images calibrated to display wt%, Mg# or anorthite (An) content.

Chapter 4.: Remobilization of cool mafic mushes by hot felsic melts: diverse primary melt compositions at Taranaki volcano, New Zealand

N. G. D'Mello¹, G. F. Zellmer¹, G. Kereszturi¹, J. N. Procter¹, T. Ubide², and R.B. Stewart¹

¹Massey University, Palmerston North, New Zealand

²The University of Queensland, Brisbane, Australia

Abstract

The prevalence of antecrysts carried in porphyritic lava domes extruded from arc volcanoes is widely accepted, but less is known about the origins of crystals in more fluid lava flows. The crystal cargo of Holocene lava flows from Taranaki volcano, New Zealand, is dominated by plagioclase, clinopyroxene, and amphibole, in chemical disequilibrium with the melt they are entrained in. Major element chemistry also reveals a compositional overlap of mineral data between phenocrysts and xenoliths from Taranaki. The suite of xenoliths includes ultramafic rocks, gabbros, and amphibolite. Further, the ratio of mafic crystals entrained in the lavas, ranging between 40 and 55 vol.%, exerts a strong control on the whole rock composition of the lavas, reducing magmatic silica contents by 5–11 wt%. Our data are inconsistent with commonly invoked processes of fractional crystallization and concomitant evolution to more felsic compositions. We propose that high-temperature, aphyric to sparsely phyric parental melt compositions (55–68 SiO₂ wt%) ascend through a colder, more mafic mush zone that contributes the crystal cargo. The data indicate that some of the back-arc primary melts from the Hikurangi mantle wedge are significantly more felsic than typical arc basalts

that are commonly invoked as parental magmas. Thermometric and hygrometric constraints also preclude a deep crustal hot zone model for the origin of these felsic melts.

4.1. Introduction

Arc magmas can contain a significant proportion of crystals that display disequilibrium textures, including reaction rims, multiple resorption zones, partial resorption zones, and changes in mineral chemistry (e.g. [Umino and Horio, 1998](#); [Zellmer et al., 2016](#)). The textures indicate variations in magmatic conditions, resulting in disequilibrium between crystals and melt ([Costa et al., 2008](#); [Martel et al., 2017](#); [Nixon, 1988](#); [Zellmer et al., 2016](#)). Furthermore, the origin of phenocrysts, here used as the original purely rock textural term, can be autocrystic (crystallized from the melt they are entrained in), xenocrystic (foreign to the magmatic host and magma system), and antecrystic (recycled within the current magmatic system before inclusion in the host magma), while microlites formed during ascent or eruption ([Zellmer, 2021](#)). Antecrysts and xenocrysts are critical, as they can significantly change whole-rock composition data and thus petrogenetic interpretations ([Larrea et al., 2013](#)).

Intermediate rocks (andesites and dacites, 57–68 wt% SiO₂) represent the bulk composition of the continental crust and constitute a significant proportion of arc volcanism ([Gill, 1981](#); [Reubi and Blundy, 2009](#); [Taylor and McLennan, 1985](#)). Constraining their petrogenesis is key to understanding the evolution of the crust, magmatic systems, as well as assessment of volcanic hazards. Intermediate magmas are conventionally viewed as originating from primary basaltic melts, released from the mantle into the overlying crust, where they remain in a polybaric (mid-to lower crustal) storage region. There they are thought to be subject to fractional crystallization, interactions with crustal rocks, crystal mush zones, and freshly injected melt batches, which may ultimately result in an array of melt compositions ([Annen et al., 2006](#); [Cashman and Blundy, 2000](#); [Hildreth and Moorbath, 1988](#)).

In contrast, it has more recently been proposed that differentiation of melts can occur in the mantle wedge through incorporating crustal (eroded forearc) and sedimentary components into the subduction channel through high-silica melanges; which upwell from the subducted plate, react with the mantle wedge peridotite forming low or high-silica pyroxenite ([Behn et al., 2011](#); [Gómez-Tuena et al., 2014](#); [Straub et al., 2011](#)). Partial melts of these lithologies are thought to be bimodal (basaltic to dacitic) in composition, and sub-crustal magma hybridization may therefore yield (high-Mg#) andesitic magmas ([Straub et al., 2011](#)). Further, direct melting of subduction melange diapirs may result in low-Mg# felsic melts ([Straub et al., 2020](#)).

In this study we investigate the porphyritic, high-K lava flows of Taranaki volcano, west of the Hikurangi margin off the coast of the North Island (New Zealand), to understand its magmatic plumbing system, as well as differentiation processes generating arc magmas more generally. The lava flows extruded over the last 10,000 years have compositions that range from basaltic to dacitic and hold a complex crystal cargo, providing an ideal setting to elucidate the origin of intermediate compositions in subduction zones.

4.2. Geological background

Volcanism in the North Island of New Zealand results from the subduction of the Pacific plate beneath the Australian plate along the Hikurangi margin ([Ballance, 1976](#)) (Figure 4.1). The westernmost expression of volcanism in the North Island is along the Taranaki Volcanic Lineament (Figure 4.1), which comprises three onshore volcanoes- Kaitake (0.57 Ma), Pouakai (0.25 Ma), and the youngest and the only active volcano, Taranaki ([Giba et al., 2010](#); [Neall, 1979](#)).

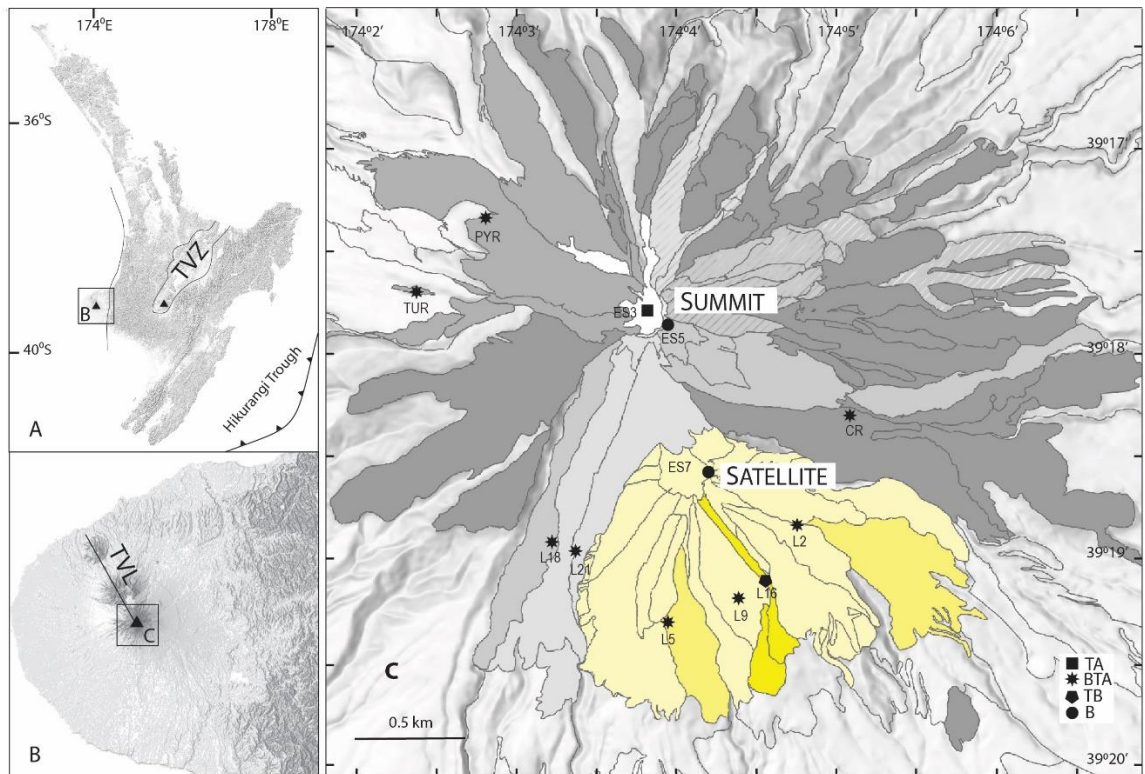


Figure 4.1 (A) Regional geology of the North Island of New Zealand showing the primary zone of subduction (Hikurangi Margin) and the location of the Taupo Volcanic Zone (TVZ). (B) shows the Taranaki Volcanic Lineament (TVL) comprising three onshore peaks: Kaitake, Pouakai and Taranaki. (C) shows lava flows of Taranaki from the summit (grey) and satellite (yellow). Sample locations marked with compositions TA- trachyandesite; BTA basaltic trachyandesite, TB trachybasalt and B basalt.

Mt. Taranaki lies 140 km west of the Taupo Volcanic Zone, *c.* 400 km west of the Hikurangi Trough, and *c.* 180 km above the Wadati-Benioff Zone ([Locke et al., 1994](#); [Stewart et al., 1996](#)). The basement of the volcano consists of sediments of the Taranaki basin, plutonic rocks of the Median Batholith, and metamorphic rocks of the deeper crust ([Mortimer et al., 1997](#); [Price et al., 2016](#)). The 2518 m stratocone was constructed over the last 10 kyr and represents only a small percentage of the volume of material extruded from the volcano, with earlier eruptions now forming the extensive ring plain deposits that surround the mountain ([Alloway et al., 2005b](#)). On the southern flank of the volcano is Fanthams Peak, or Panitahi, a satellite vent that breaks the near symmetry of the mountain.

The oldest lavas of Taranaki volcano are the Warwick Castle Lavas (8 kyr), which partially eroded through flank collapse (*c.* 7–5 ka). This was followed by the emplacement of the Peters lava (7–3.3 kyr), the Staircase, and McKays Flows. Contemporaneous activity at the summit vent and Fanthams Peak (*c.* 3.5–2.9 kyr) resulted in the eruption of tephra and lavas at Fanthams Peak (F1, F2, F3) ([Stewart et al., 1996](#); [Zernack et al., 2011](#)). This activity was followed by the eruption of the Skeet Ridge lavas from the summit (which bifurcated around the satellite cone) and the Minarapa Lavas (flowing towards the north) at 1.6–1.3 ka ([Stewart et al., 1996](#)). The last activity was the emplacement of a summit dome named Pyramid Dome ([Lerner et al., 2019b](#)).

4.3. Method

4.3.1. Sampling and sample preparation

Volcanic rocks were collected from several locations on Taranaki volcano representing different eruptive phases of the present-day cone and are shown in (Figure 4.1C). The rocks were cut to expose fresh surfaces and then used for thin section preparation and imaging with a Scanning Electron Microscope (SEM). The samples comprise trachyandesites, basaltic trachyandesites, trachybasalts, and basalts; and range from dense lavas to scoria samples. Figure 4.1 shows the lava flows sampled for this study and their locations and compositions. Eighty crystals from these lava flows were studied for major element chemistry. We here use the terms ‘microlite’ (< 30 μm), ‘microcryst’ ($\geq 30 \mu\text{m}$ to < 100 μm), ‘mesocryst’ ($\geq 100 \mu\text{m}$ to < 500 μm), and ‘macrocryst’ ($\geq 500 \mu\text{m}$) to categorise crystal size, with no implication on their genesis ([Zellmer, 2021](#)).

4.3.2. X-ray fluorescence (XRF) analysis

For each sample, approximately 10 g of unaltered material was cleaned in an ultrasonic bath and dried in an oven at 100°C overnight. The samples were ground using a tungsten

carbide mill and left in an oven for at least 2 hours. Loss on ignition (LOI) was calculated from the difference in weight of *c.* 2 g of the sample before and after being placed in a muffle furnace at *c.* 900°C for 3 hours. Fused glass discs were prepared by mixing 0.800 g (± 0.001 g) of sample powder with 8.000 g (± 0.001 g) of lithium tetraborate: lithium metaborate (12:22) X-ray flux, followed by fusion with a XRFuse2 electrical fusion apparatus at Massey University. Glass beads were then analysed for major element concentrations using a Bruker S8 Tiger Series II WD-XRF Spectrometer. Oreas 24b and Oreas 24c Certified Reference Materials were used as secondary standards. We report analytical precision (1σ) of $< 1.5\%$, and an accuracy of within 1–3% (except for TiO_2 , where it is within 4%).

4.3.3. Electron probe microanalysis (EPMA)

Major element concentrations were carried out at the Victoria University of Wellington using a JXA-8230 SuperProbe Microanalyser. Analysis was conducted using a focussed beam (1–5 μm) at 20 kV accelerating voltage and 12 nA beam current for mineral analysis and a defocused beam (30 μm) at 20 kV accelerating voltage and 8 nA beam current for groundmass analysis. Due to the abundance of microlites in the groundmass of Taranaki eruptives, the groundmass analysis includes microlites and glass, and the average of 35 spot analyses was used as the measured groundmass composition. Data were collected at 10–100 μm intervals along core to rim transects of minerals depending on the size of the crystal. The instrument was calibrated using a variety of mineral, glass, and oxide standards ([Jarosewich et al., 1980](#)) optimized for the minerals of interest. Counting times were 30/15 s for peak/background for all elements except Na in glass, which was at 10/5 s. A maximum relative precision of 1.5% and accuracy within 5% were obtained for all oxides in the sample suite.

4.3.4. Mass balance calculations for groundmass compositions

Groundmass compositions were also calculated from mass balance operations using whole rock and mineral major element compositions. For this, it was initially assumed that crystals < 100 µm are of autocrystic origin (i.e., crystallised from the melt that they are hosted by), and were thus included as part of the groundmass. Thin sections (30 µm thickness) were observed using a Leica petrographic microscope at Massey University, New Zealand. 10 regions of each thin section were photographed at 2.5× magnification using a Nikon camera mounted on to the microscope. Multiple images were obtained to reduce errors in estimation of modal abundances of mineral phases owing to heterogenous distribution of large crystals and abundance of crystal clots.

Crystals were manually outlined, and colour coded according to major mineral phases (pl- green; cpx- red, amp-blue, and ox-black). Images were imported into Adobe Photoshop, stitched, and the sum area of each mineral phase/groundmass/vesicles was obtained using the measure tool. The mass of individual mineral phases was calculated using the density, volume, and proportion of the respective phases. The major element oxide mass of the crystal cargo was then subtracted from the whole rock to obtain the major element oxide composition of the groundmass.

4.4. Results

4.4.1. Mineral chemistry

The eruptive products of Mt. Taranaki considered for this study range from dense lavas to scoria and display porphyritic textures. Variable proportions of mesocrysts and macrocrysts are hosted in a microlite rich groundmass (Figure 4.2). The crystal volume fraction in the samples varies from c. 40% (trachyandesite sample ES3) to 55% (basaltic trachyandesite sample TUR) as demonstrated in Figure 4.2.

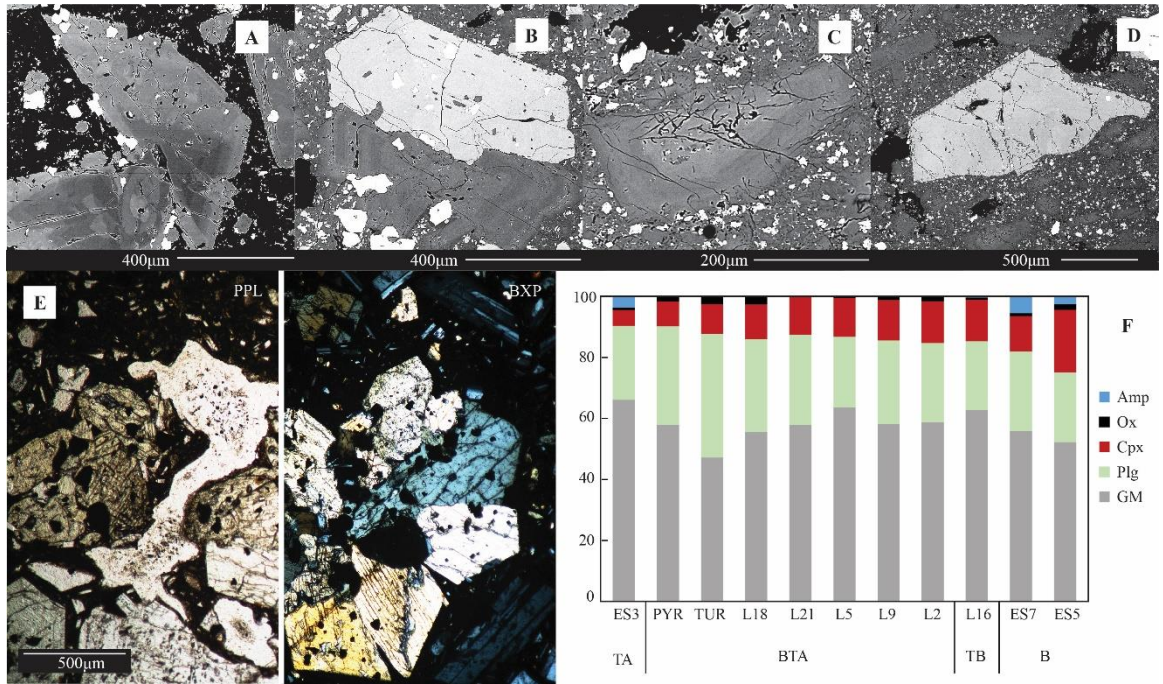


Figure 4.2 Panels showing glomerocrysts and fractured crystals and the relative proportions of phases. (A) presence of clinopyroxene glomerocrysts in sample TUR, (B) intergrown clinopyroxene and plagioclase from sample L2, (C) L18 fractured crystals of plagioclase and (D) clinopyroxene and (E) glomerocrysts in plane polarised light and between cross polars. (F) Histogram shows the relative abundance of phases in each sample with respect to composition (TA- trachyandesite; BTA basaltic trachyandesite, TB trachybasalt and B basalt).

Due to the large crystal sizes and the presence of glomerocrysts, the distributions of crystals vary between thin sections of the same samples. The crystals are dominantly feldspars, pale pink to green clinopyroxenes, brown amphiboles, and opaque minerals (Fe-Ti oxides), with rare olivine and orthopyroxene, and accessory biotite and apatite. The groundmass phases include plagioclase, pyroxene, and oxide microlites with interstitial glass. Glomerocrysts include intergrown clinopyroxene \pm plagioclase, clinopyroxene, and clinopyroxene and amphibole crystals. Fractured crystals are also commonly found in the studied samples (Figure 4.2 A, B).

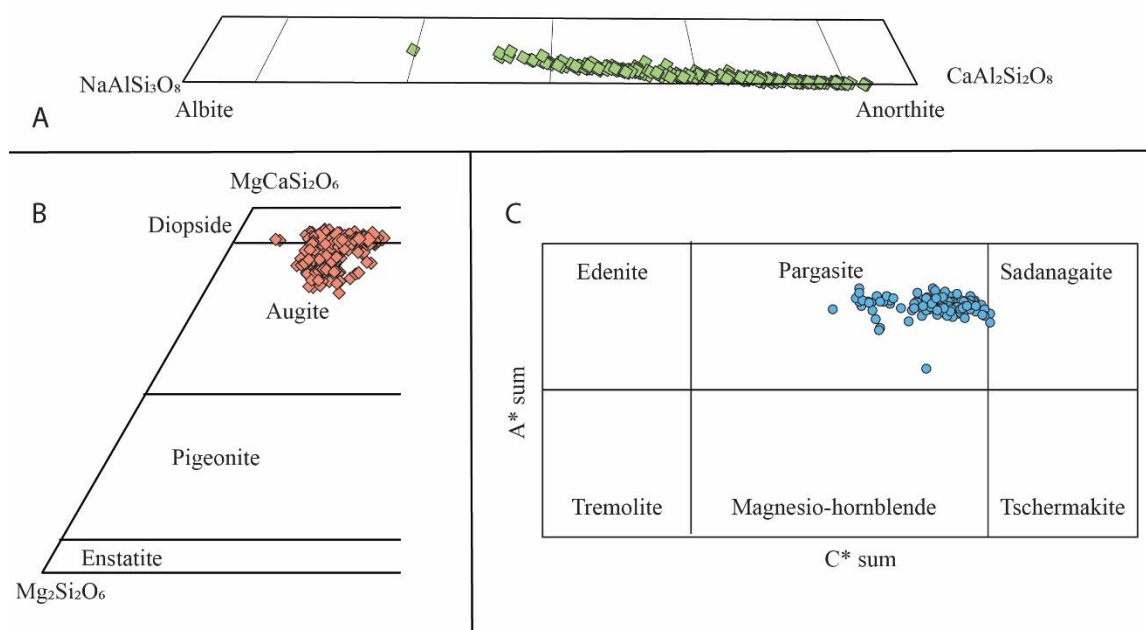


Figure 4.3 Chemical classification and nomenclature of dominant mineral phases (A) plagioclase ([Earnshaw and Greenwood, 1997](#)), (B) clinopyroxenes ([Morimoto, 1988](#)) and (C) amphiboles ([Hawthorne et al., 2012](#)); $A^* \text{ sum} = {}^A(\text{Li} + \text{Na} + \text{K} + 2\text{Ca} + 2\text{Pb})$; $C^* \text{ sum} = {}^C(\text{Al} + \text{Fe}^{3+} + \text{Mn}^{3+} + \text{Cr} + \text{V} + \text{Sc} + 2\text{Ti} + 2\text{Zr}) - {}^w\text{O} - {}^c\text{Li}$.

Plagioclase is the most abundant mineral phase in the Taranaki lavas ranging from 25 to 45 vol%, with compositions ranging from An₉₂ to An₄₀ ($\text{An} = 100 \times \text{molar Ca} / (\text{Ca} + \text{Na} + \text{K})$) (Figure 4.3A). Clinopyroxene is the second most abundant phase. Crystals are weakly pleochroic from green to pink in plane polarised light and form 12–20 vol% of the rocks. They have been identified as diopsides and augites (Figure 4.3B) and usually contain oxide inclusions. Clinopyroxenes have magnesium number ($\text{Mg}\# = 100 \times \text{molar MgO} / [\text{MgO} + \text{tot. FeO}]$) between 7 and 5, and high Ca content (*c.* 20 wt% CaO).

Amphibole, when present, makes up 1–3 vol% of the rock. Crystals are calcic amphiboles that classify as pargasites ([Hawthorne et al., 2012](#)) (Figure 4.3C). Heating and/or decompression of amphibole results in the breakdown of the mineral phase to form anhydrous plagioclase, orthopyroxene, clinopyroxene, and oxides ([D'Mello et al., 2021, Chapter 6](#)). Figure 4.4 shows a comparison of major element chemistry of plagioclase,

clinopyroxene, and amphibole mineral phases and whole rock chemistry on Harker diagrams.

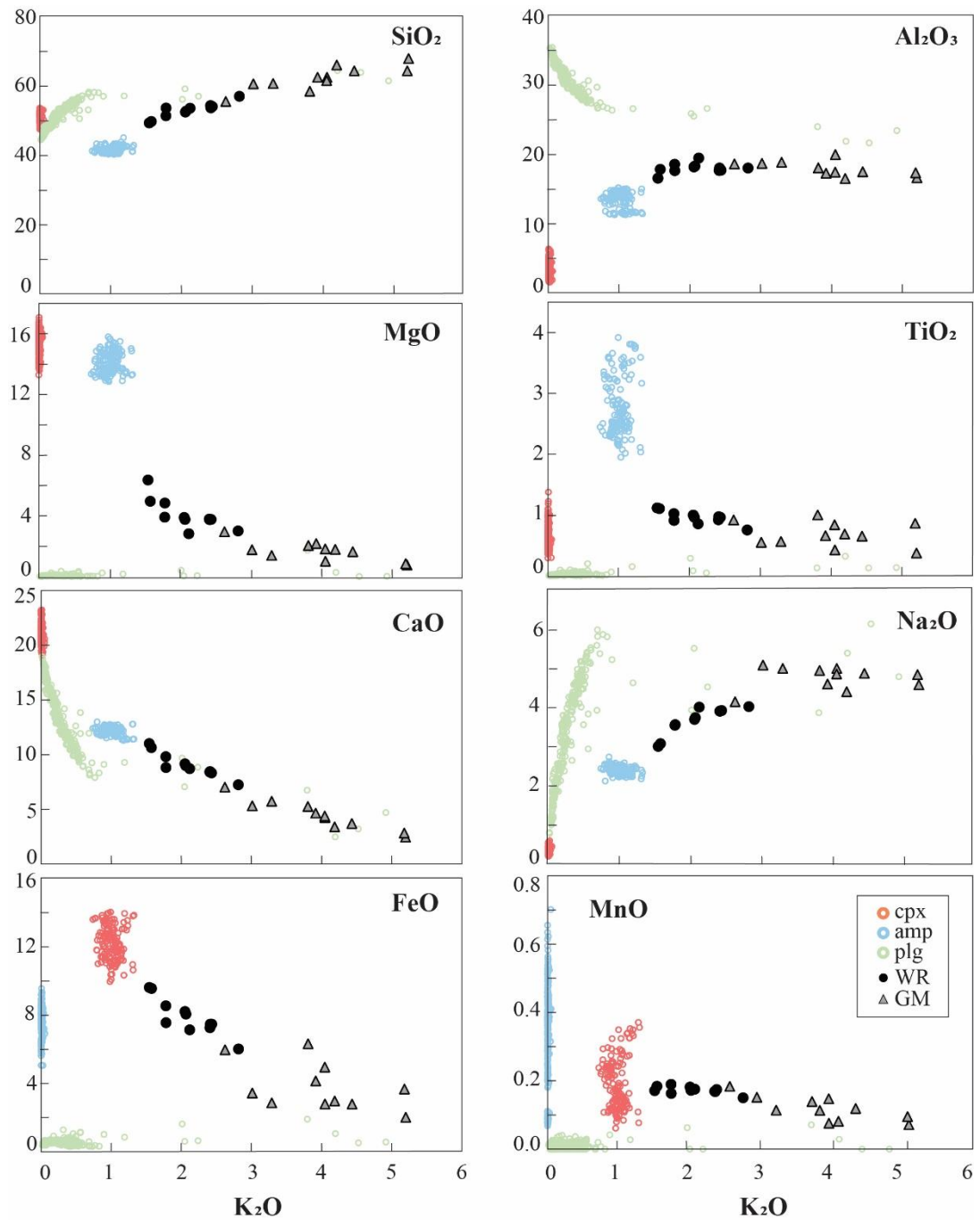


Figure 4.4 Major element variations between mineral phases in comparison to the whole rock compositions and measured groundmass compositions. The plots indicate simple mixing of mineral and groundmass to form whole rock compositions.

Oxides are mainly present as inclusions in clinopyroxene crystals or dispersed in the groundmass and contribute up to 3 vol%. They are identified as titanomagnetites and rare ilmenite, with inclusions of sulphide seen in some grains. Rare olivine crystals are found in basaltic samples from the Fanthams Peak cone, where amphibole is usually absent. Olivine crystals are anhedral and show thick reaction coronas. Few orthopyroxene grains are found in the groundmass, but orthopyroxene is a principal constituent of reaction rims on amphibole and olivine.

4.4.2. Whole Rock Chemistry

4.4.2.1. *Whole Rock Compositions*

Whole rock major and trace element concentrations that have been analysed are given in Table 4.1. The sampled lavas are potassic and range from basalts to trachyandesites based on the Total Alkali vs Silica (TAS) classification of [Le Maitre \(2002\)](#) and are dominated by basaltic trachyandesites (Figure 4.5). A general compositional difference is observed between summit and satellite sourced rocks, with the summit lavas being more felsic on average. However, basalts have also erupted from the summit (ES5), and there is large compositional overlap between summit and satellite vents within the basaltic trachyandesite field. The rocks have relatively low Mg# ranging from 40 to 55. Silica abundances for the studied sample suite range from 49 to 57 wt%, while K₂O ranges from 1.5 to 3 wt%. Based on the classification of [Gill \(1981\)](#), Taranaki lavas can be classified as high-K eruptives. Lavas from the summit and satellite show similar trends with decreasing TiO₂, Fe₂O₃, CaO with decreasing MgO, and increasing SiO₂, Al₂O₃, Na₂O, and K₂O with decreasing MgO.

Ni and Cr concentrations in Taranaki lavas are relatively low with concentrations rarely exceeding 20 and 50 ppm, respectively. Large ion lithophile elements (LILEs) as well as

Table 4.1: Whole rock chemistry of samples in this study (oxides in wt% and trace and minor elements in ppm).

Sample	ES3	L18	L21	PYR	TUR	CR	ES5	L5	L9	L2	L16	ES7
SiO ₂	56.94	53.85	53.99	54.62	53.91	54.43	49.6	54.13	53.17	53.41	51.44	50.3
Al ₂ O ₃	17.91	17.99	17.61	17.69	17.64	18.49	16.56	19.57	18.35	18.45	18.51	17.94
TiO ₂	0.75	0.97	0.96	0.92	0.91	0.93	1.12	0.86	1.01	0.97	1.02	1.12
MnO	0.15	0.17	0.17	0.17	0.16	0.18	0.172	0.18	0.18	0.17	0.19	0.19
FeO	6.68	8.33	8.29	8.11	8.43	8.43	10.74	8.01	9.25	9.07	9.50	10.73
MgO	3.01	3.77	3.76	3.81	4.87	3.29	6.393	2.85	3.95	3.82	3.92	5.01
CaO	7.23	8.46	8.31	8.46	8.85	8.59	11.06	8.80	9.27	9.09	9.81	10.74
Na ₂ O	4.02	3.93	3.93	3.94	3.59	3.70	3.032	4.06	3.75	3.80	3.56	3.12
K ₂ O	2.81	2.42	2.43	2.42	1.79	1.96	1.55	2.14	2.08	2.09	1.78	1.59
P ₂ O ₅	0.28	0.37	0.37	0.35	0.28	0.30	0.241	0.34	0.28	0.29	0.32	0.26
SO ₃	0.00	0.00	0.00	0.00	0.00	0.00	0.00	0.00	0.00	0.00	0.00	0
Tot.	99.79	100.26	99.82	100.49	100.45	100.30	100.5	100.94	101.30	101.16	100.05	101.00
Mg#	33.36	33.42	33.51	34.27	39.11	33.84	39.81	28.35	32.15	31.88	31.42	34.17
Sc	15.80	20.71	21.27	20.23	19.95	17.25	35.44	12.91	21.19	20.35	20.48	30.4
V	200.30	275.20	271.30	256.60	232.30	239.50	358.9	224.10	293.50	287.80	295.40	347.4
Co	59.42	54.38	44.55	31.77	45.56	39.16	70.76	44.08	40.96	62.94	54.56	83.33
Ni	13.64	14.30	15.34	16.83	66.00	14.95	35.9	9.91	12.67	13.57	19.25	21.14
Cu	66.95	109.60	108.10	116.80	95.50	48.22	98.7	49.88	111.10	85.80	69.87	122.6
Zn	82.20	97.80	93.90	90.70	90.10	95.60	88	103.10	98.80	97.50	100.30	101.7
Ga	18.81	20.64	20.16	19.08	18.59	19.71	18.65	20.83	20.34	20.26	20.07	19.16
Ge	6.52	2.68	2.13	1.26	1.58	1.54	2.95	1.74	1.76	2.75	2.31	1.68
Rb	70.69	55.59	56.76	54.05	38.48	41.57	30.71	44.45	44.67	47.08	35.37	30.40
Sr	603.20	707.10	695.40	682.60	631.20	610.00	544	716.80	639.70	640.60	647.50	616.40
Y	18.47	19.97	20.27	20.16	18.01	22.74	17.05	20.75	20.15	19.56	20.49	19.58
Zr	134.60	113.30	117.10	116.80	92.90	106.40	77.53	98.70	96.90	98.10	81.93	72.23
Nb	4.64	4.32	4.34	4.37	4.16	4.18	2.986	3.79	3.60	3.56	2.96	2.76
Mo	1.99	3.01	2.42	3.42	2.08	1.88	1.53	2.96	1.96	2.61	2.02	1.79
Cs	4.24	3.01	2.96	1.38	1.81	2.06	1.392	1.17	2.40	2.83	1.89	1.60
Ba	970.20	864.00	882.10	855.20	629.90	734.80	560.3	850.00	777.00	771.70	691.40	622.60
La	19.05	17.65	17.89	17.30	13.25	15.84	11.11	15.97	14.82	14.87	12.57	11.52
Ce	36.22	35.57	36.37	35.46	27.18	33.24	23.01	32.81	30.15	30.11	26.81	23.53
Pr	4.29	4.49	4.57	4.59	3.48	4.19	3.085	4.15	3.86	3.90	3.52	3.18
Nd	18.18	19.61	20.58	20.21	15.34	18.77	14.24	18.38	17.35	17.24	16.18	14.80
Sm	4.13	4.62	4.76	4.74	3.81	4.59	3.7	4.49	4.03	4.09	4.21	3.98
Eu	1.16	1.42	1.37	1.42	1.14	1.27	1.125	1.36	1.25	1.27	1.24	1.20
Gd	3.54	4.24	4.18	4.34	3.54	4.57	3.46	3.95	4.22	3.92	4.10	3.84
Tb	0.53	0.62	0.64	0.63	0.52	0.68	0.56	0.65	0.59	0.61	0.61	0.60
Dy	3.27	3.71	3.85	3.79	3.23	4.08	3.24	3.75	3.79	3.76	3.77	3.67
Ho	0.67	0.73	0.75	0.75	0.66	0.83	0.648	0.75	0.76	0.70	0.74	0.70
Er	1.92	2.09	2.08	2.07	1.85	2.33	1.802	2.15	2.10	2.11	2.18	2.01
Tm	0.29	0.29	0.30	0.29	0.27	0.33	0.252	0.31	0.30	0.29	0.30	0.31
Yb	1.79	1.92	1.93	1.87	1.78	2.21	1.54	2.14	1.95	1.93	1.96	1.95
Lu	0.30	0.28	0.28	0.29	0.26	0.32	0.237	0.32	0.29	0.24	0.30	0.28
Ta	2.33	2.17	1.10	0.88	0.99	0.89	1.706	1.76	1.15	2.19	1.27	2.68
Tl	0.13	0.01	0.03	0.08	0.03	0.10	0.027	0.15	0.03	0.05	0.04	0.05
Th	7.41	5.55	5.88	5.76	4.01	4.40	3.16	5.02	4.89	4.99	3.76	3.19
U	1.91	1.48	1.46	1.41	1.05	1.06	0.772	1.27	1.23	1.25	0.92	0.77
Pb	13.90	12.60	10.44	10.35	9.89	9.97	6.77	16.81	11.08	10.59	9.25	8.36

light rare earth elements (LREEs) are abundant, with Ba concentrations ranging from 550 to 1000 ppm and Sr concentrations from 550 to 750 ppm. Primitive mantle normalised trace element patterns are shown in Figure 4.5B, and they show features characteristic of subduction-related volcanic rocks (Kelemen et al., 2005). Cs, Ba, Rb (LILE) are enriched and the LREEs are enriched relative to the heavy REEs (HREEs), while Nb is depleted relative to K. Sr is enriched relative to La and Ce.

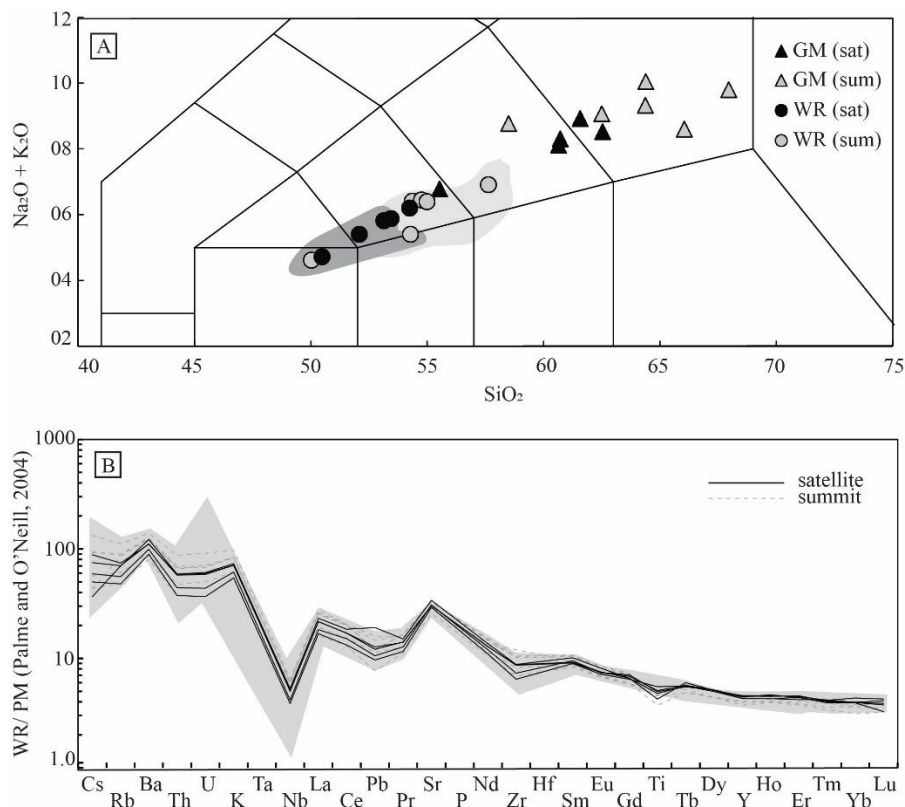


Figure 4.5 (A) Total Alkali vs Silica classification of the whole rock (WR) and groundmass (Le Maitre et al., 2002). (B) Trace element concentrations normalised to Primitive Mantle after [Palme and O'Neill \(2013\)](#). Grey shaded regions represent data from summit and satellite samples from literature ([Price et al., 1992](#); [Price et al., 1999](#); [Stewart et al., 1996](#)). Sat= satellite, sum= summit.

4.4.2.2. Groundmass Composition (Calculated and Measured)

Groundmass compositions are shown in Table 4.2 as measured (EPMA) groundmass and as calculated groundmass. Measured groundmass compositions range from basaltic trachyandesitic to trachytic in composition with silica concentrations of *c.* 55–70 wt.% SiO₂. Groundmass compositions constrained from mass balance calculations converge

towards basaltic trachyandesite to trachyandesitic compositions with SiO₂ of *c.* 52–60 wt.%. They are lower in silica content because of some of the mafic microcrysts that were assumed to be autocrystic in the calculation.

Table 4.2: Groundmass compositions determined through mass balance calculations and EPMA measurements.

Calculated	SiO₂	TiO₂	Al₂O₃	FeO	MnO	MgO	CaO	Na₂O	K₂O
ES3	60.50	0.85	16.05	6.74	0.17	2.47	4.92	4.22	4.07
ES5	52.85	1.42	15.13	12.40	0.25	5.42	4.94	4.74	2.85
L18	58.22	1.27	15.45	7.90	0.20	3.43	4.52	4.88	4.12
L21	56.23	1.53	15.00	11.11	0.21	3.12	4.01	4.73	4.06
PYR	57.25	1.22	14.45	9.00	0.22	4.09	5.74	4.39	3.65
TUR4	56.92	2.05	7.08	15.59	0.27	8.03	1.94	4.07	4.05
ES7A	52.68	1.39	13.70	15.00	0.26	4.26	5.21	4.36	2.68
L16	54.02	1.37	17.45	10.79	0.22	2.90	5.70	4.74	2.81
L05	55.84	1.12	18.05	10.06	0.20	1.59	4.25	5.15	3.22
L02	56.93	1.18	16.52	9.35	0.20	2.93	4.42	5.03	3.45
L09	56.06	1.42	15.63	10.51	0.24	3.22	4.51	4.95	3.48
Measured	SiO₂	TiO₂	Al₂O₃	FeO	MnO	MgO	CaO	Na₂O	K₂O
ES3	67.95	0.37	16.55	2.03	0.07	0.77	2.45	4.59	5.21
ES5	58.49	1.00	17.97	6.32	0.14	2.05	5.25	4.96	3.81
L18	64.39	0.86	17.27	3.67	0.10	0.85	2.82	4.85	5.19
L21	64.38	0.65	17.40	2.79	0.12	1.64	3.70	4.89	4.44
PYR	62.50	0.42	19.90	2.81	0.08	1.01	4.22	5.01	4.05
TUR4	66.05	0.69	16.43	2.97	0.08	1.79	3.38	4.42	4.19
ES7A	55.53	0.92	18.55	5.98	0.18	2.96	7.02	4.16	2.62
L16	60.72	0.56	18.78	2.87	0.11	1.40	5.72	5.01	3.29
L05	60.65	0.55	18.61	3.44	0.15	1.77	5.32	5.10	3.01
L02	62.53	0.66	17.20	4.15	0.11	2.18	4.64	4.61	3.92
L09	61.56	0.84	17.36	4.96	0.15	1.83	4.38	4.87	4.05

4.5. Discussion

4.5.1. The nature of the crystal cargo

Comparison of the crystal cargo to xenolith mineral chemistry (Figure 4.6) recorded by previous studies ([Gruender et al., 2010](#); [Price et al., 2016](#)) shows a virtually complete overlap of mineral compositions, suggesting that the crystal cargo of the lavas may be derived from the deeper regions of the crust that also sourced the xenoliths.

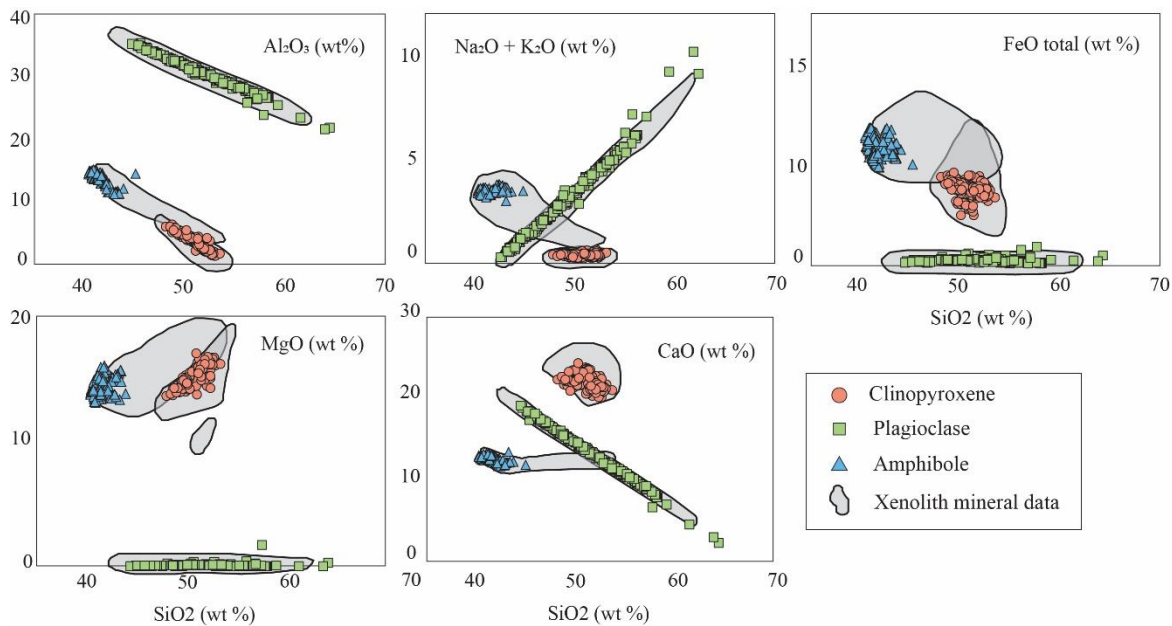


Figure 4.6 Major element chemistry of minerals from Taranaki lava flows (this work) in comparison with mineral data of xenoliths (cumulates, gabbros and diorites) entrained in Taranaki lavas ([Gruender et al., 2010](#); [Price et al., 2016](#)). This shows complete compositional overlap of crystals entrained in Taranaki lavas and crystals from xenoliths.

The xenoliths are dominated by gabbros and diorites and include ultramafic rocks, sediments from the Taranaki basin, metamorphic rocks from the deep crust, and plutonic rocks from the Median Batholith, which is a remnant of an old magmatic arc ([Gruender et al., 2010](#); [Mortimer et al., 1997](#); [Price et al., 2016](#)). [Price et al. \(2016\)](#) suggested that most xenoliths in the Taranaki suite are derived from a complex of basement lithologies, cognate cumulates and/or crystal mushes and restitic material derived from partial melting of amphibolitic crust and materials modified by metasomatic alteration associated with melts or fluids derived from both crustal and mantle sources.

[Zellmer et al. \(2016\)](#) demonstrated that the crystal cargo of the Trans-Mexican Volcanic Belt results from disintegration of glomerocrysts sometimes associated with the fragmentation of individual crystals. Fractured crystals are seen in Taranaki lavas as well, along with an abundance of crystal clots. These observations point to an antecrystic or xenocrystic origin for the macrocrysts and mesocrysts, which are picked up by rising

melts and are not crystallised from the melt they are entrained in, perhaps except for some crystal rims.

4.5.2. Thermobarometry and Hygrometry

Several thermobarometers based on mineral-melt equilibrium have been employed to determine the crystallization conditions in magmatic systems ([Putirka, 2008](#)). However, many of these thermobarometers require chemical equilibrium between the mineral phases and melt. With Taranaki, chemical disequilibrium between minerals and the whole rock was previously reported for Taranaki lavas (e.g. [Price et al., 1999](#); [Stewart, 2010](#); [Stewart et al., 1996](#)). Further evidence of disequilibrium between amphibole and melts is apparent in the formation of reaction rims ([D'Mello et al., 2021, Chapter 6](#)). While clinopyroxene shows chemical equilibrium with the melt based on the observed vs. predicted components demonstrated by [Mollo et al. \(2013b\)](#), disequilibrium is suggested by low K_D (Fe-Mg) of ([Putirka, 2008](#)) and reaction textures such as resorption surfaces. Frequent plagioclase disequilibrium is demonstrated through An_{plag} vs. An_{liq} diagram based on equilibrium experiments of [Waters and Lange \(2015\)](#), first employed by [Zellmer et al. \(2016\)](#). However, most plagioclase and clinopyroxene rims are generally euhedral and in equilibrium with an (H_2O saturated or slightly undersaturated) melt, as illustrated in Figure 4.7.

Nevertheless, given the antecrystic origin of the bulk of the crystal cargo, only thermobarometric calculations that are reliable in the absence of mineral-melt equilibrium were employed here. We used the amphibole-only thermobarometers of ([Ridolfi and Renzulli, 2012](#)) and [Putirka \(2016\)](#), and the clinopyroxene-only thermobarometer of [Petrelli et al. \(2020\)](#) to determine the P-T conditions of crystallisation through the recorded growth history of the crystal (precluding penultimate rim overgrowth). Then, to calculate the temperature of the melt, a clinopyroxene rim-melt thermobarometer was

used (Petrelli et al., 2020) as the equilibrium conditions (DiHd and EnFs components) were within 1SEE

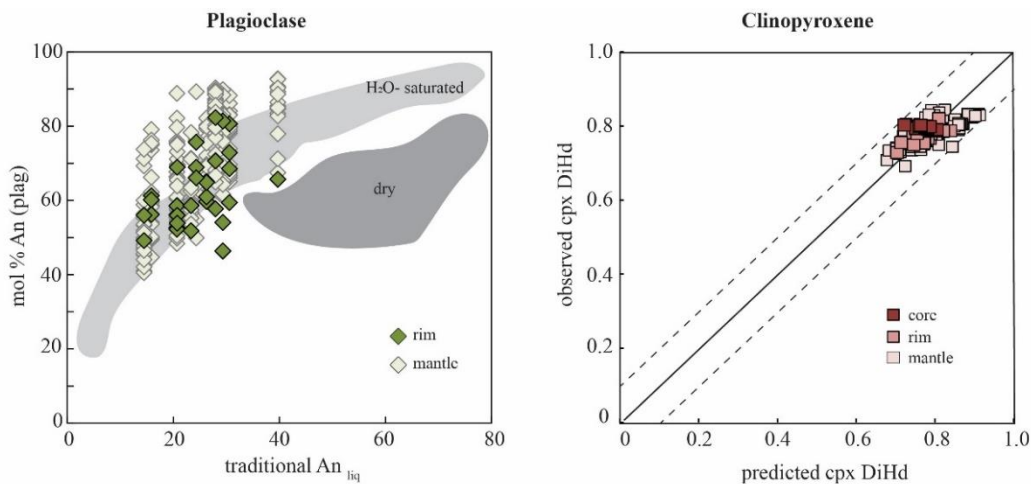


Figure 4.7 Equilibrium conditions between plagioclase and clinopyroxene minerals and melt. Many plagioclase mantles appear to be in equilibrium with a more mafic melt, while rims are in or near equilibrium with the host melt. Based on the equilibrium scheme of Zellmer et al. (2016). Although clinopyroxene appears in equilibrium, disequilibrium textures such as resorbed cores shows re-equilibration through long storage, cf. Chapter 5).

for clinopyroxene (Mollo et al., 2013b). Hygrometers of Waters and Lange (2015) as well as Masotta and Mollo (2019) were applied to plagioclase rim-melt compositions, and calibrated using temperatures obtained from the Petrelli et al. (2020) thermometer, to get melt water contents. Water contents obtained were compared with results from the Masotta and Mollo (2019) and (Putirka, 2008) hygrometers.

Amphibole-only thermobarometry (Figure 4.8A) yields temperatures between 940–1010 (± 24) $^{\circ}$ C and pressures between 300–600 (± 400) MPa. Clinopyroxene barometry returns pressures that range from 200–600 (± 400) MPa for the cores and mantles; while the cpx rim-melt thermobarometer returns temperatures from 970–1100 (± 40) $^{\circ}$ C and pressures from 200–400 (± 200) MPa (Petrelli et al., 2020). The amphibole thermometer is independent of melt composition and serves as a good indicator of the mush zone temperature beneath Taranaki, while the cpx-melt thermometer indicates the temperature

of the cpx rim that formed in equilibrium with the ascending melt and can therefore be used as an indicator of melt temperatures, at the time of interaction with the mush zone.

The hygrometers of [Waters and Lange \(2015\)](#) and [Masotta and Mollo \(2019\)](#) on plagioclase rims, combined with the groundmass compositions, were calibrated to the temperatures

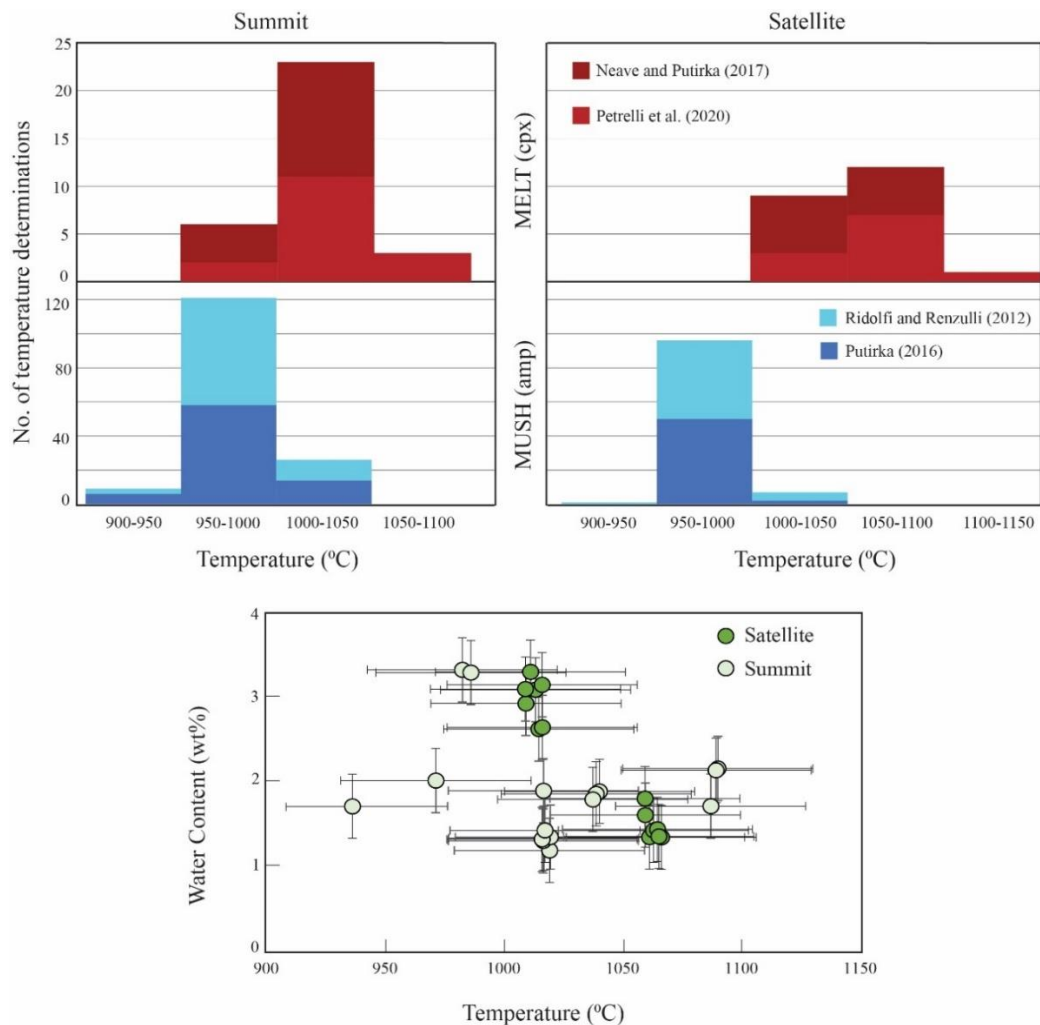


Figure 4.8 (A) Thermobarometry of amphibole and clinopyroxene ([Neave and Putirka, 2017](#); [Petrelli et al., 2020](#); [Putirka, 2016](#); [Ridolfi and Renzulli, 2012](#)) indicating cooler mush zone (amp) and hotter intruding melts (cpx-melt). (B) Hygrometry for summit and satellite lavas ([Waters and Lange, 2015](#)) calibrated with temperatures obtained from cpx-melt thermometer ([Petrelli et al., 2020](#)).

obtained from cpx compositions (Figure 4.8B). The [Waters and Lange \(2015\)](#) and [Putirka \(2008\)](#) parameterizations yield H₂O contents of Taranaki lavas that range from 1–3

(± 0.35) wt% H₂O for measured groundmass compositions, while the [Masotta and Mollo \(2019\)](#) hygrometer for trachytic magmas yields higher water contents of 2.5–5.75 (± 0.29) wt% H₂O. However, the [Masotta and Mollo \(2019\)](#) hygrometer uses a narrow sample set of 16 samples with alkalis > 10 wt%, which is higher than the alkali contents of Taranaki lavas. Although the [Waters and Lange \(2015\)](#) hygrometer is calibrated with a dataset with alkalis < 7 wt%, which is lower than that of Taranaki lavas, the results overlap with [Putirka, 2008](#)) hygrometer outputs that are based on a much larger and diverse dataset.

4.5.3. Origin of microcrysts of Taranaki

Calculated groundmass compositions are significantly lower in SiO₂ than the measured groundmass (Table 4.2) and show a narrower range. The calculated groundmass includes microcryst populations as a component of the groundmass, while the measured groundmass includes microcryst populations as a component of the crystal cargo of the lavas. Therefore, the difference in compositions could be attributed to the microcryst populations.

To determine melt compositions of Taranaki lavas (excluding antecrystic cargo), calculated and measured groundmass liquidus temperatures were obtained using the Rhyolite MELTS software ([Gualda et al., 2012](#)). The parameters used were pressure at 400 MPa and f_{O_2} unconstrained. Pressure was taken as the average pressure obtained from cpx barometry using [Petrelli et al. \(2020\)](#) which ranges from 300–700 MPa. Liquidus temperatures would indicate the original temperature of the crystal free melt, and values ranging from *c.* 1000 to 1200°C (measured) and *c.* 1200–1500°C (calculated) were acquired. The upper end of the latter is unrealistic. This indicates that if ascending melts beneath Taranaki were initially free of crystals, most of the microcrysts attributed to the groundmass in this calculation cannot be autocrystic but would in fact also be of antecrystic origin. Alternatively, they may have crystallized from the primary melt during

its ascent, before or during uptake of pre-existing mesocrysts and macrocrysts. Either way, all crystals > 100 µm are antecrysts, and some or all crystals > 30 µm may also be of antecrystic origin. Thus, it can be inferred that an initially aphyric or sparsely phytic melt picked up most or all of the crystals from the crustal mush zone while ascending to the surface.

4.5.4. Influence of antecrysts on the whole rock compositions

The influence of antecrysts on whole-rock compositions has been highlighted in porphyritic rocks from a range of settings (e.g. [Larrea et al., 2013](#); [Ubide et al., 2014](#)). Taranaki magmas carry variable volume fractions of antecrysts ranging from *c.* 35 to 60 vol% (Figure 4.2). Mixing models using the PETROMODELER ([Ersoy and Helvacı, 2010](#)) between the groundmass and bulk mineral compositions (considering the relative proportions of mineral phases) indicate that the whole rock compositions can be reproduced solely by mixing of felsic melt with the lower silica crystals mushes, and do not require any traditional form of crystal fractionation (Figure 4.9). A simple mixing model can be expressed as:

$$C_{WR} = X C_{MIN} + (1-X) C_{MELT}$$

Where C_{WR} is whole rock composition; C_{MIN} is the average mineral composition; C_{MELT} is melt composition and X is mineral proportion.

Based on this equation, we predict whole rock compositions and compare them with the measured compositions (Figure 4.9). It is observed that the predicted compositions are almost 1:1 for the major oxides Al_2O_3 , CaO , Na_2O and K_2O , while a lower measured SiO_2 and higher measured TiO_2 , FeO and MgO are observed. Petrographic observations show that plagioclase is a dominant phase in macrocryst, mesocryst and microlite crystal populations. Microcryst populations, however, have significant populations of the more

mafic mineral phases, such as titanomagnetite, pyroxene and olivine. Thus, the difference in measured and predicted values can be attributed to microcrysts of titanomagnetite, pyroxene and olivine in the samples, which are not accounted for in either measured groundmass or mineral phase analyses.

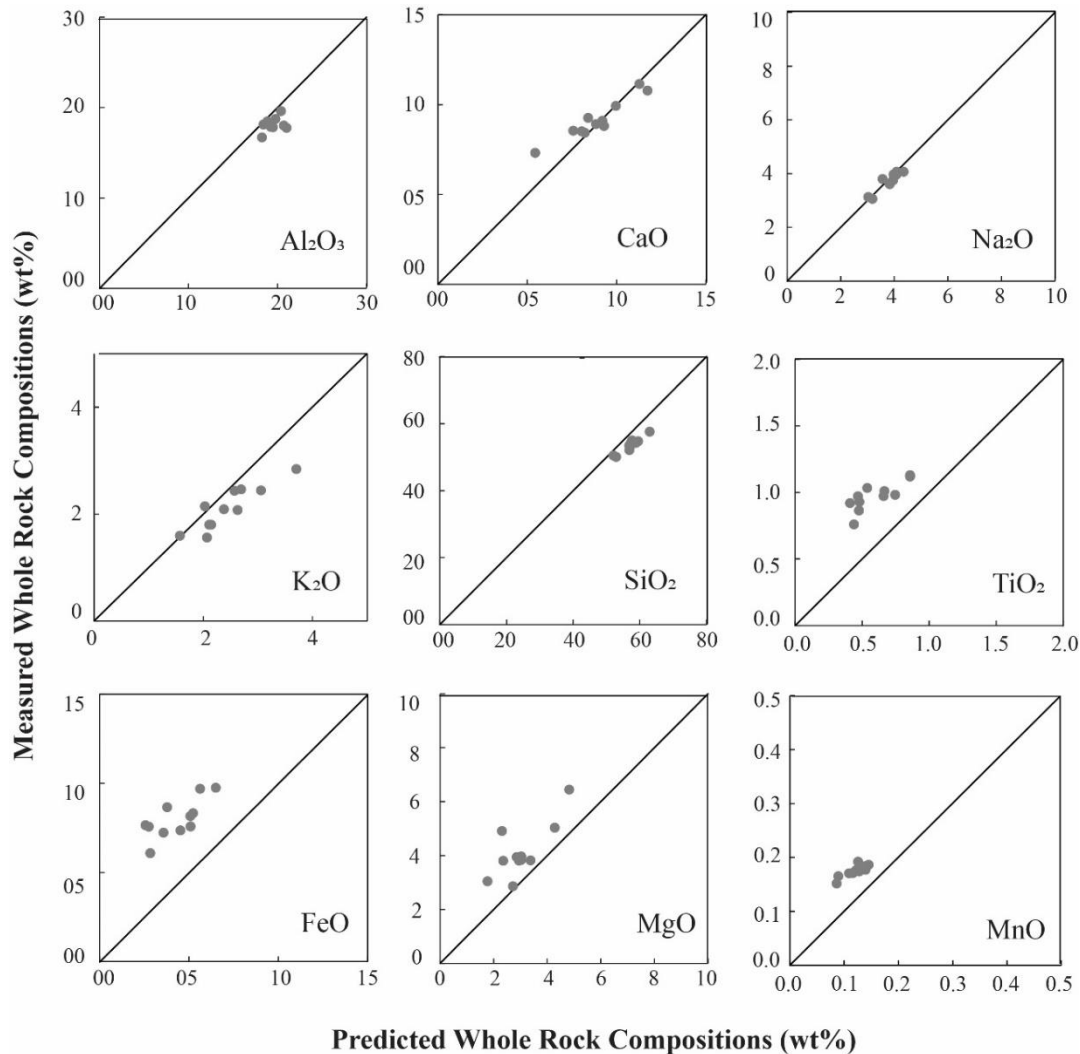


Figure 4.9 Mixing model for crystals and groundmass to produce whole rock compositions based on PETROMODELLER (Ersoy and Helvacı, 2010), indicating that crystal fractionation is not a dominant process in generating compositional diversity. Predicted whole rock compositions deviations can be attributed to microcrysts of olivine, orthopyroxene and breakdown products that were not included in the mixing model.

The trachyandesitic sample (ES3) has the lowest crystal content and the basaltic sample (ES5) has a significantly higher crystal content (Fig. 4.2). However, a direct correlation between crystal proportion and SiO_2 content is not seen in the more intermediate

compositions and the basaltic trachyandesite sample (TUR) has the highest crystal proportion of all samples studied here. Consequently, the mineral proportion is not the sole influence on the whole rock chemistry; the melt composition also plays a significant role. Therefore, hot (1000+ °C) aphyric to sparsely pyric melts, ranging in composition from 55–68 SiO₂ wt%, interact with and remobilise mafic crystals from the cooler (940–1010°C based on amphibole geothermometry) crystal mush, decreasing the SiO₂ content of the resulting bulk rock by 5–11 wt% relative to the more felsic melts. This interaction would have reduced the temperature of the melt (970–1100 °C based on cpx rim–melt equilibrium) and triggered the crystallization of crystal rims.

4.5.5. Generation of felsic, aphyric to sparsely pyric parental melts at Mt. Taranaki

The range of melt compositions commonly found in arc magmas are typically attributed to the differentiation of basaltic magmas to form more silica rich magmas in a deep crustal hot zone (DCHZ) where assimilation of basement rocks occurs ([Annen et al., 2006](#)). [Melekhova et al. \(2013\)](#) conducted crystallization experiments at pressures of 1.3, 1.0 and 0.7 GPa, with three different initial H₂O contents of 0.6, 2.3 and 4.5 wt%. (Figure 4.10). shows a comparison of temperature and SiO₂ content of a typical DCHZ melt suite, together with melt thermometric constraints from Taranaki lavas. The experimental upper limit is defined by a dry magma suite of ([Villiger et al., 2004](#)), while the lower limit is defined by the wet magmas of [Nandedkar et al. \(2014\)](#). Taranaki melt temperatures, determined from cpx-melt temperatures, are significantly higher than those of magmas from a DCHZ, and are less hydrous. DCHZ melts are so wet that they would reach H₂O saturation during ascent. The high temperatures and moderate H₂O contents of Taranaki melts suggest that they cannot have formed in a DCHZ, and therefore likely originate from greater depths, i.e. the mantle.

The generation of variable magma compositions at Taranaki was previously attributed to fractional crystallization of parental basalts and assimilation of continental crust in a deep crustal hot zone and MASH (mixing, assimilation, storage, and hybridization) processes

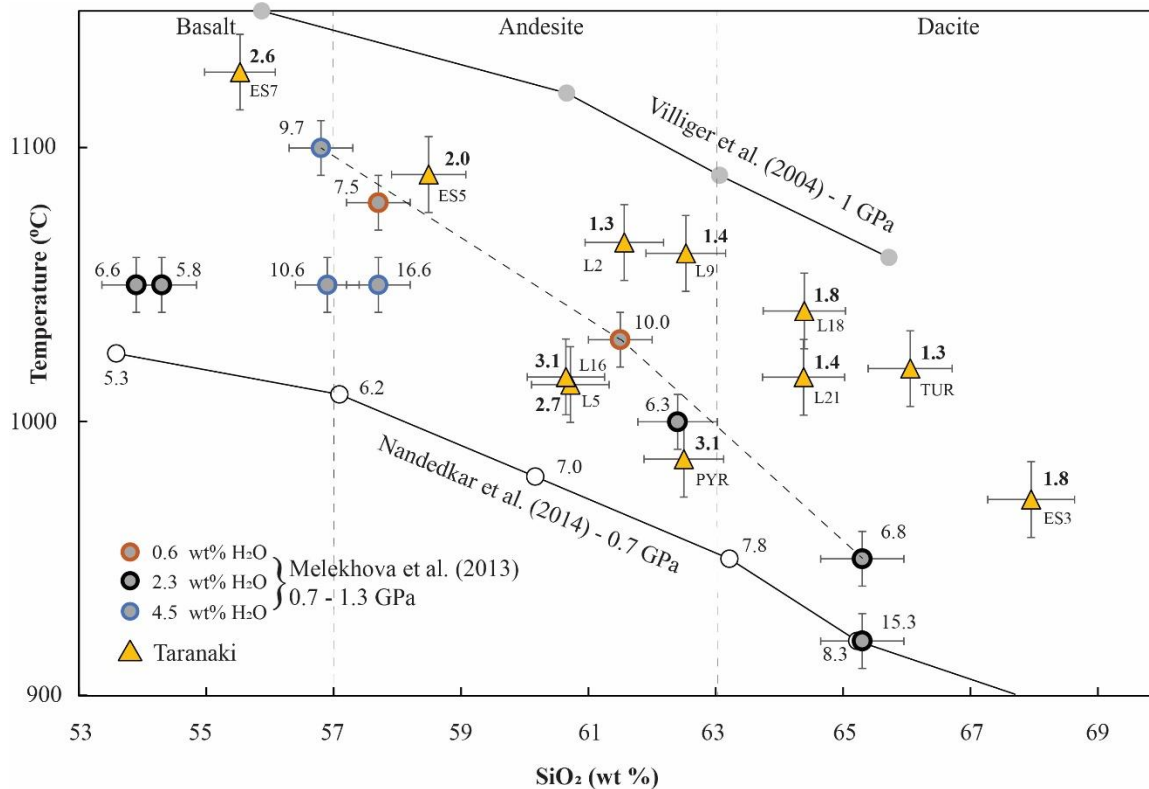


Figure 4.10 Silica-temperature relation of Taranaki lavas and wet (Nandedkar et al., 2014), dry (Villiger et al., 2004) and experimental hydrous magmas simulating a deep crustal hot zone (Melèkhova et al., 2013) with starting water contents of 0.6, 2.3 and 4.5 wt%. Numbers along the circles show the high water contents of experimental run products (in wt%). Most Taranaki lavas plot much higher temperatures than expected for a typical hydrous magma in a DCHZ, thus indicating that the compositionally diverse melts observed in Taranaki are likely sourced from below the crust, i.e. the mantle.

(Price et al., 2016; Price et al., 1999; Stewart et al., 1996; Zernack et al., 2012). We propose an alternate model whereby primary aphyric to sparsely phyric, felsic melts are generated in the mantle beneath Mt. Taranaki. Behn et al. (2011) suggested that crustal derived material subducted along with altered oceanic crust can form a subduction melange that may rise as diapirs into the mantle. A subduction melange is defined as a combination of mantle, altered oceanic crust, and eroded debris from the forearc (Parolari et al., 2021). Further, with the infiltration of slab components, discrete segregations of

silica-deficient and silica-excess reaction pyroxenites may develop in an originally peridotitic mantle [Straub et al. \(2011\)](#).

Our data suggest that the subducted Hikurangi plate, SE of Taranaki, releases subduction melange diapirs into the peridotitic mantle wedge (Figure 4.11). The various components of the subduction melange (sediment, AOC, forearc crust) mix in different proportions. Partial melting of these melanges result in the formation of silica-excess regions in the mantle that generate felsic melts, or silica-depleted regions which produce mafic melts. The composition of the melt is determined by the proportion of melange components melted. Subcrustal mixing of mafic and felsic melts results in a range of intermediate compositions with high temperatures typical of the wedge core (up to *c.* 1300°C) ([England and Katz, 2010](#)). These melts then rise from the mantle into the crust, initially forming few if any crystals. As these melt batches ascend, they encounter the cold, mafic mush zone and interact with pre-existing crystals heterogeneously. Most magmas (melt + mush crystals) likely fail to escape the mush zone. Those that rise through the mush zone and breach the surface carry crystals from the mush zone with new rims formed in equilibrium with the felsic host melt, with exception of amphiboles, most of which show breakdown textures ([D'Mello et al., 2021, Chapter 6](#)).

4.6. Conclusions

1. Mineral-melt chemical disequilibrium, the common occurrence of glomerocrysts and fractured crystals, as well as the compositional overlap with xenocryst mineral data, indicate that antecrysts and xenocrysts are the prevalent components of the crystal cargo in Taranaki lavas.

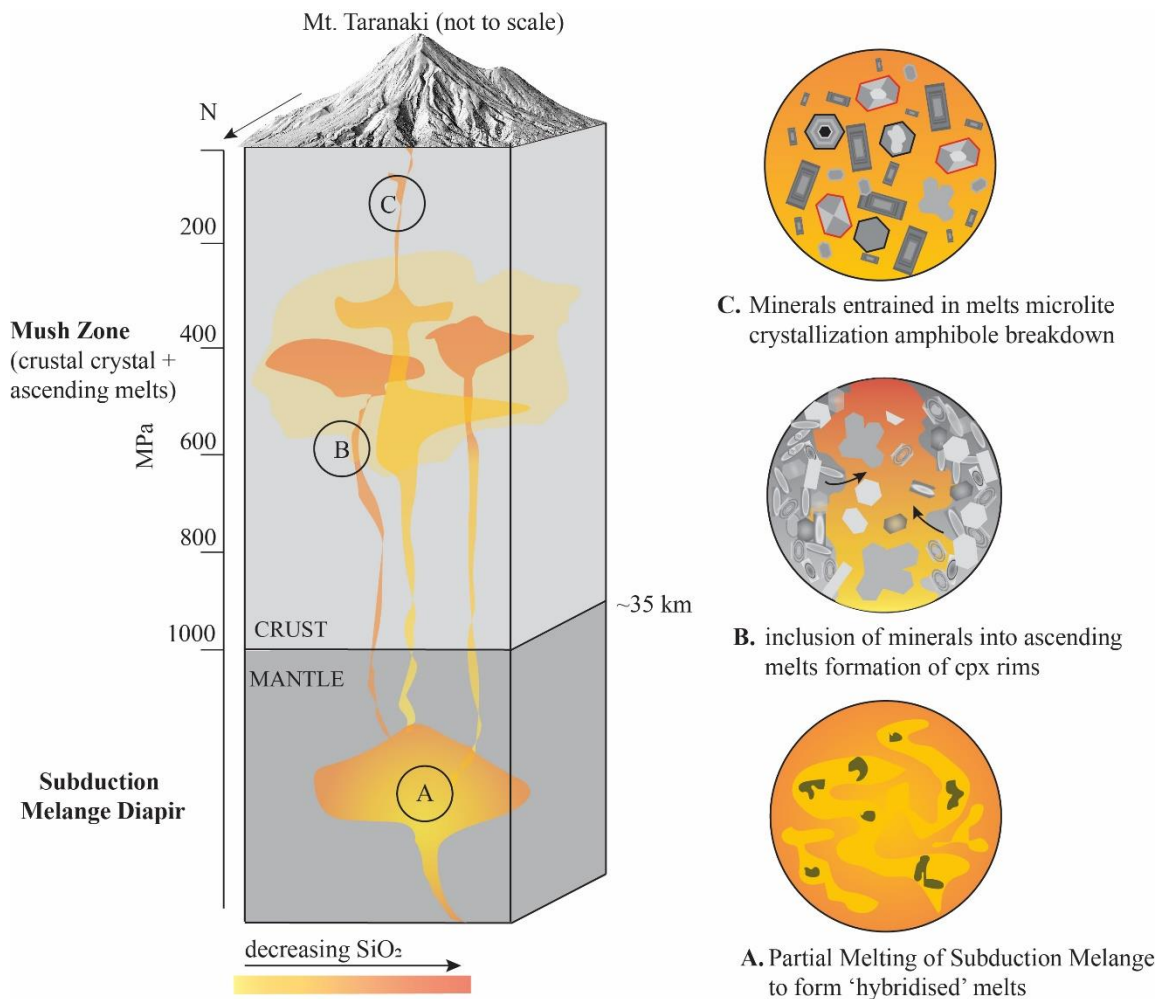


Figure 4.11 Schematic diagram showing melt generation in Taranaki. Subduction melange diapirs rising from the Hikurangi Plate and interacting with the mantle wedge beneath Taranaki to form small-volume, silica-deficit melts and high-volume, silica-excess melts. In addition, diapir melts may enter the crust without reacting with the ultramafic mantle lithologies. These diverse melts then rise through the crust and interact with the crystals, remobilizing them through the mush zone. Ascent of the melts through the shallow crust and through the edifice results microlite crystallisation, formation of rims on plg and cpx in equilibrium with the melt and breakdown of hydrous amphibole.

2. Thermobarometry of the mineral phases suggests that hot, more felsic melts intrude into a colder, more mafic mush zone, remobilizing and entraining crystals. These melts are hydrous and contain few crystals, if any, prior to entering the mush zone.

3. The presence and proportion of antecrysts strongly influence the range of whole-rock compositions observed at Mt. Taranaki. However, there are also indicators of melt heterogeneity, implying an interplay of melt composition and mineral proportion in the erupted whole rock.

4. The observation of more felsic parental melts differentiating to more mafic bulk compositions through uptake of a mafic crystal cargo contrasts with common models of the differentiation of mafic mantle melts towards more felsic compositions in the crust. The origin of hot, aphyric to sparsely phyric and occasionally H₂O-undersaturated intermediate composition parental melts casts doubt on magmatic differentiation in crystal-rich MASH reservoirs or a deep crustal hot zone. Instead, the results presented here support the notion that the sub-arc mantle may be the origin of primary melts that are more felsic than typical primary arc basalts.

Chapter 5.: The crystal cargo of Taranaki lavas: exploring intrusive processes through the crystal cargo of volcanic rocks

N. G. D’Mello¹, G. F. Zellmer¹, T. Ubide², J. Caulfield³, M. Usuki⁴, Y. Iizuka⁴, G. Kereszturi¹, J. N. Procter¹, and R.B. Stewart¹

¹Massey University, Palmerston North, New Zealand

²The University of Queensland, Brisbane, Australia

³Queensland University of Technology, Brisbane, Australia

⁴Institute of Earth Sciences, Academia Sinica, Taipei, Taiwan

Abstract

Mt. Taranaki is a stratovolcano located in the western peninsula of the North Island of New Zealand. The current edifice has developed over the last 10 kyrs. Effusive eruptions ranged from basaltic to trachyandesitic composition and carry a mineral assemblage including plagioclase, clinopyroxene, amphibole and oxides, with rare olivine and orthopyroxene. The dominant mineral phases display a complex and varied history through their zoning patterns of various major, minor, and trace elements. These types of crystals are not exclusive to lavas of any stratigraphic unit and can be found within the same sample over very short length scales (within a single petrographic thin section). The zoning patterns and elemental concentrations in the crystal types reveal mineral-melt interactions, which result in repeated resorption and recrystallisation in varied environments. Convection within the storage region results in low degrees of undercooling evidenced by plagioclase crystals developing low amplitude oscillatory zoning and clinopyroxenes displaying strong sector zoning. The common occurrence of resorbed cores within the crystals and the prevalence of glomerocrysts indicate an antecrystic/ xenocrystic origin of the crystals. We hypothesise that the repeated intrusion of melts into the 120 Myr old Median Batholith, which forms part of the crustal basement

of Taranaki volcano, has resulted in the formation of a crystal mush system that interacts heterogeneously with intruding melts from the mantle. These interactions result in disaggregation of crystal clots from the Batholith and remobilization of the crystals through various sub-environments of the mush zone. Eruption-triggering injections of melt then pick up these crystals with varied histories to be extruded with a rim that has crystallised in equilibrium with the melt.

Key words: mush zone, antecrysts, elemental mapping

5.1. Introduction

Magma is stored in reservoirs, defined as regions of partially or wholly molten rock with varying proportions of melt, crystals and exsolved volatiles ([Bachmann and Bergantz, 2008](#)), or as the domains of the magmatic system that contain melt (\pm exsolved fluids) and are above solidus ([Sparks et al., 2019](#)). The magma reservoir is heterogeneous and can have regions that have high enough crystal contents to form a semi-rigid framework, termed a mush ([Wager et al., 1960](#)). During storage, the crystal mush interact with injected melts that alter the intrinsic parameters of the region.

These changes in melt compositions and temperature ([Bachmann and Dungan, 2002](#); [Ginibre et al., 2007](#); [Humphreys et al., 2006](#)) as well as other open system processes such as mixing ([de Maisonneuve et al., 2016](#); [Degruyter et al., 2016](#); [Ganne et al., 2018](#)) result in chemical zoning of crystals. These changes are reflected in the distribution of major, minor or trace element chemistry, as well as their isotopes, in the mineral (e.g. [Ginibre et al., 2007](#); [Kahl et al., 2011](#); [Kahl et al., 2017](#); [Mollo et al., 2020](#); [Streck, 2008](#); [Ubide et al., 2019](#)). Thus, variations in crystal chemistry provide an extremely sensitive record of change over the lifetime of a crystal, from nucleation to final quenching ([Holness et al., 2007a](#); [Lange et al., 2013](#); [Nielsen et al., 2020](#)). However, not all changes promote crystal growth and therefore textural studies such as sieve texture, breakdown and resorption surfaces are also key to understanding magmatic processes.

The characteristic behaviour of certain chemical elements is key to interpreting magmatic processes and transportation paths from the zonation of minerals. Petrological tools, such as thermobarometry and hygrometry, can be employed to reconstruct the conditions and processes that these crystals and the magma in which they are contained experience in the subsurface (e.g., [Mollo et al., 2010](#); [Neave et al., 2019a](#); [Putirka et al., 1996](#)). The crystal

cargo is sensitive to variations in conditions such as pressure, temperature, f_{O_2} , composition of the host melt and volatile content ([Costa et al., 2013](#); [Humphreys et al., 2006](#); [Nakamura, 1995b](#); [Streck, 2008](#); [Zellmer et al., 2003](#)).

Quantitative analysis of major and minor elements in combination with imaging methods has been employed, such as EPMA and LA-ICPMS mapping for major and minor and for trace elements, respectively. In this chapter, we use elemental maps and textural features of the crystal cargo of recent Taranaki lavas to gain insight into the long-term intrusive magmatic processes and conditions beneath the Taranaki volcano.

5.2. Geological background and petrology

Mt. Taranaki is a near symmetrical stratovolcano on the western peninsula of the North Island of New Zealand. It is the youngest and only active of three onshore volcanoes that form the Taranaki Volcanic Lineament (TVL). Seismic studies indicate that the crust-mantle boundary beneath the TVL is at a depth of *c.* 35km. Insight into the rocks that form the crustal basement has been obtained from studies that focussed on the xenoliths entrained in the eruptive products of the TVL ([Gruender et al., 2010](#); [Price et al., 2021](#); [Price et al., 2016](#)). [Mortimer et al. \(1997\)](#) correlated xenolith and drill-core data to the Median Tectonic Zone in the South Island, suggesting that the Median Batholith underlies the present-day edifices of Kaitake, Pouakai and Taranaki (Figure 5.1). Other xenoliths include the sedimentary rocks of the Taranaki Basin and volcanic rocks.

Mt. Taranaki has been active for at least 13 ky, and the current 12 km³ edifice, erupted over the last 10 ky, represents only a small percentage of the volume of material extruded from the volcano ([Alloway et al., 2005a](#); [Procter et al., 2009](#); [Zernack et al., 2011](#)). The long-term volcanic history includes at least 13 cycles of cone growth and collapse, with each collapse phase generating debris avalanche flows that form the extensive ring plain

surrounding the volcano (Neall et al., 1986; Palmer and Neall, 1991; Zernack et al., 2011; Zernack and Procter, 2021; Zernack et al., 2009). Edifice reconstruction then follows through eruptions that range from explosive to effusive, generating volcanic products such as pyroclastic deposits, lava flows and dome extrusions (Damaschke et al., 2017a; Lerner et al., 2019a; Platz, 2007; Platz et al., 2006; Turner et al., 2009a; Turner et al., 2011a; Turner et al., 2008c).

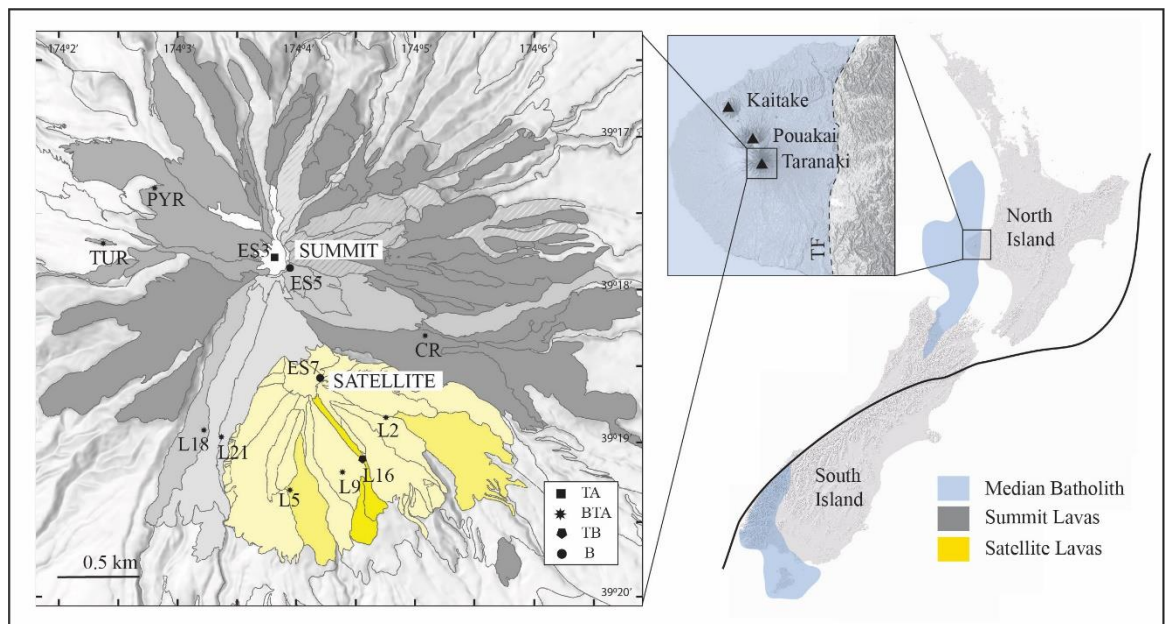


Figure 5.1 Geological Map of New Zealand showing the extent of the Median Batholith, a suite of plutonic and metaplutonic rocks formed as magmatic products of the interaction of the Panthalassan oceanic plates with the South Gondwana continental plate. Inset shows the Taranaki Volcanic Lineament of the Quaternary volcanoes Kaitake, Pouakai and Taranaki. The map shows the lava flows that form the current edifice of Mt. Taranaki and sample locations for this study.

The eruptive products of Mt. Taranaki considered for this study range from dense lavas to scoria and display porphyritic textures. Basaltic trachyandesites are the predominant lithology, along with basalts and trachyandesites (Figure 5.2). Variable proportions of crystals (40–55 vol%) are hosted in microcryst- and microlite-rich groundmasses. The larger macrocrysts are up to 4 mm in size and are dominated by plagioclase, clinopyroxenes, amphiboles, and opaque minerals (Fe-Ti oxides), with rare olivine and orthopyroxene, and accessory biotite and apatite. Glomerocrysts are common and

comprise intergrown clinopyroxene \pm plagioclase and amphibole crystals. The groundmass phases include plagioclase, pyroxene, and oxide microlites with interstitial glass. The trace element pattern for whole rock data remains uniform throughout the stratigraphy due to a chemically relatively invariable slab signature from the subducting Hikurangi plate entering the mantle wedge in the backarc.

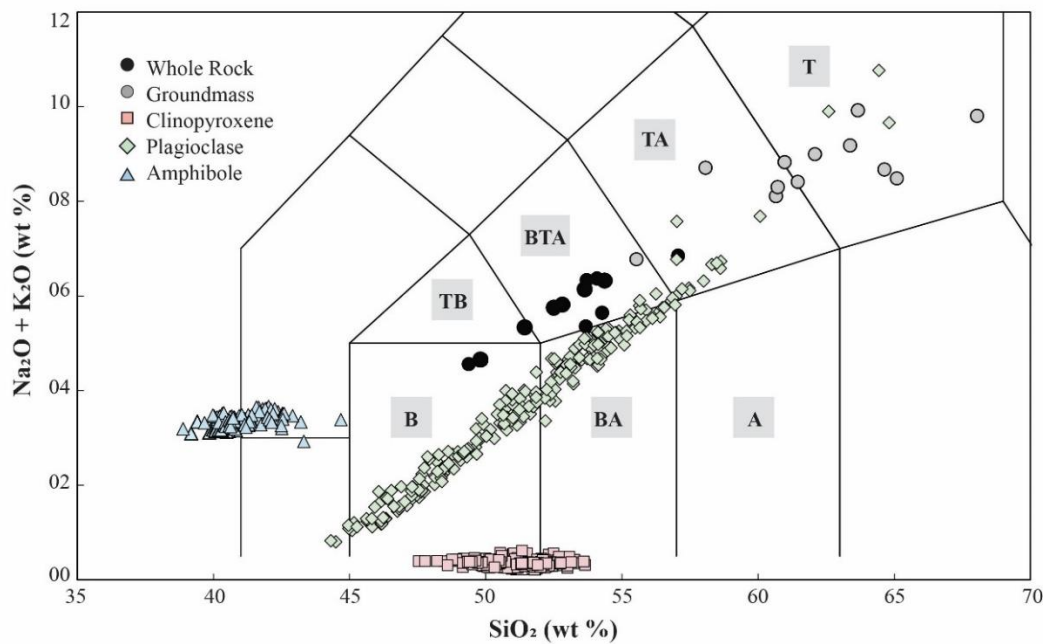


Figure 5.2 Total Alkali vs Silica diagram for samples from this study with major mineral phase data superimposed. Groundmass compositions are also illustrated in the figure. The field markings refer to rock compositions (B= basalt, BA basaltic andesite, A= andesite, TB= trachybasalt, BTA= basaltic trachyandesite; TA= trachyandesite, T= trachyte).

5.3. Methodology

Samples were selected from lava flows representing different stratigraphic units and whole rock compositions ranging from basalts to trachyandesites (Figure 5.1). Major crystal phases of plagioclase (n= 36), clinopyroxene (n= 31), and amphibole (n= 16) (if present in the sample) were classified by size as microcrysts (<100–30 μm), mesocrysts (100–500 μm) and macrocrysts (500 μm –<10 mm) (Zellmer, 2021). Based on genesis, they are identified as autocrysts (crystallising from the host melt), antecrysts (not

crystallising from the host melt, but at an earlier time from the same magma system) and xenocrysts (foreign from the magmatic system) ([Zellmer, 2021](#)).

Crystals were analysed using Electron Probe Micro Analysis (EPMA) at Victoria University of Wellington, New Zealand, and at Academia Sinica, Taiwan. Laser Ablation Induced Couple Plasma Mass Spectrometry (LA-ICP-MS) was also used to measure concentrations of minor and trace elements at the University of Queensland in Brisbane, Australia. LA-ICP-MS for whole rock compositions was conducted at the University of Waikato in Hamilton, New Zealand. EPMA spot analyses show an external precision of 0.5–1.5% with an accuracy of within 5%. LA-ICP-MS precision and accuracy were typically better than 1–5%. For details, refer to Chapter # for each of these techniques.

X-ray intensity maps for major elements obtained from Academia Sinica, Taiwan, were calibrated to EPMA spot analyses to obtain maps for major element concentrations in wt% as well as Mg# (clinopyroxene and amphibole) and An content (plagioclase) using Fiji ImageJ software. Elemental concentrations for ‘regions of interest’ in EPMA and LA-ICP-MS maps were obtained using Fiji ImageJ and Iolite, respectively.

5.4. Results

The crystal cargo of Taranaki lavas show disequilibrium textures such as sieve texture and resorption surfaces, as well as normal, reversed and oscillatory zoning. These zoning patterns are better observed in BSE images due to the higher resolution than LA-ICP-MS.

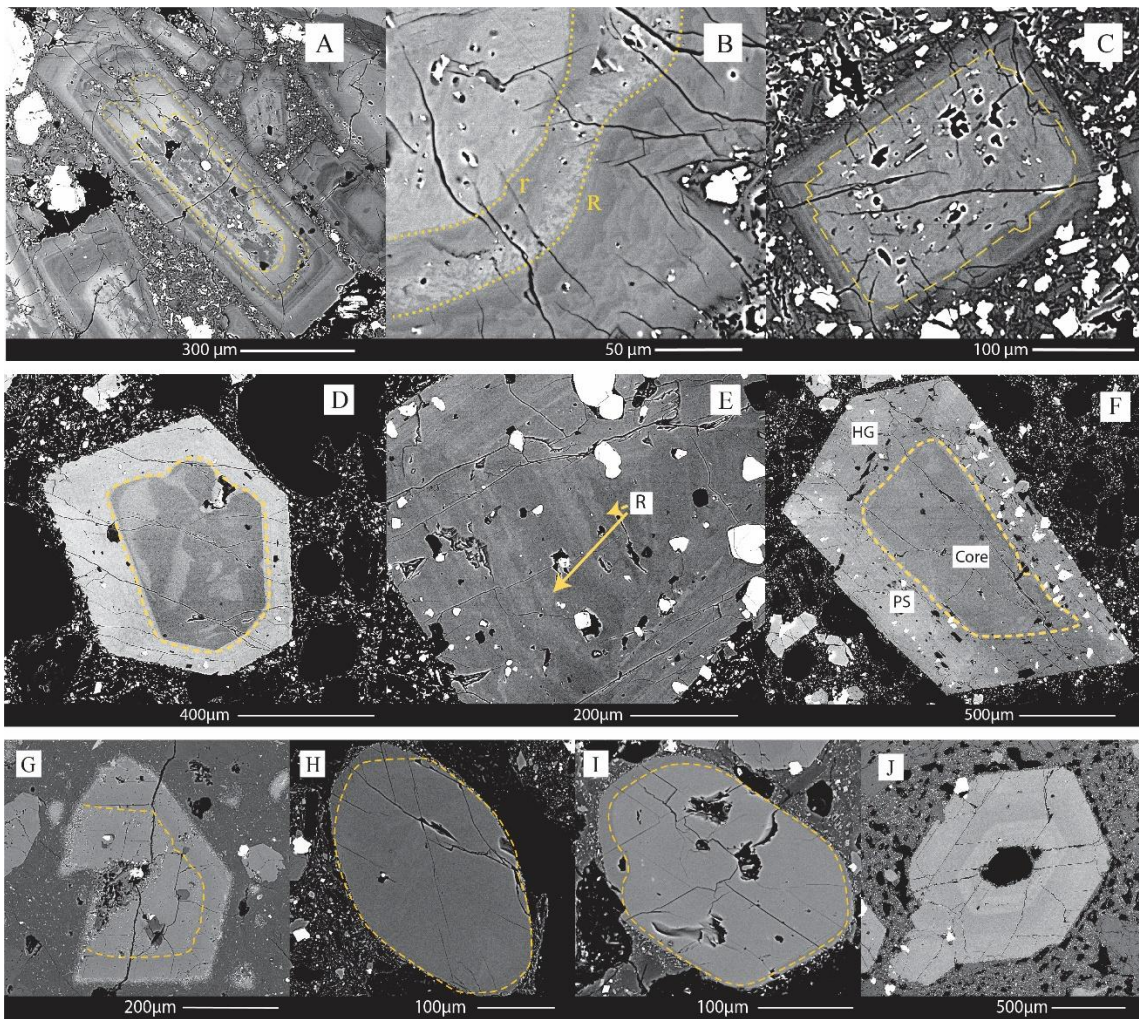


Figure 5.3: Panel 1 show the different types of textures of crystal phases plagioclase: (A) patchy core, (B) minor (r) and major (R) resorption surface and wavy oscillatory zoning; (C) cellular and sieve texture. Panel 2 shows textures in clinopyroxene: (D) patchy zoned core and oscillatory zoned mantle; (E) wavy oscillations in the hourglass sector and straight oscillations in the prism sector with resorption surface (R); and (F) distinct patchy zoned core and sector zoned mantle showing hour glass (HG) and prism (PS) sectors. Panel 3 shows textures in amphibole: (G) euhedral core with mantle and reaction rim, (H) rounded patchy core and thin rounded rim, (I) unzoned large core and mantle, and (J) oscillatory zoned crystal with completely resorbed core.

5.4.1. Plagioclase

Plagioclase is the most abundant mineral phase in the Taranaki lavas ranging from 25–45 vol% and is found as macrocrysts (500 μm–10 mm; [Le Maitre, 2002](#)), mesocrysts (100- 500 μm), and microcrysts (< 100 μm) ([Welsch et al., 2009](#)). Texturally, the microcrysts are generally euhedral, while the larger crystals are often subhedral to

subrounded with sieve textures. Plagioclase compositions range from labradorite (An₄₀) to anorthite (An₉₂), where An = 100 × molar Ca/(Ca + Na + K). (Figure 5.4)

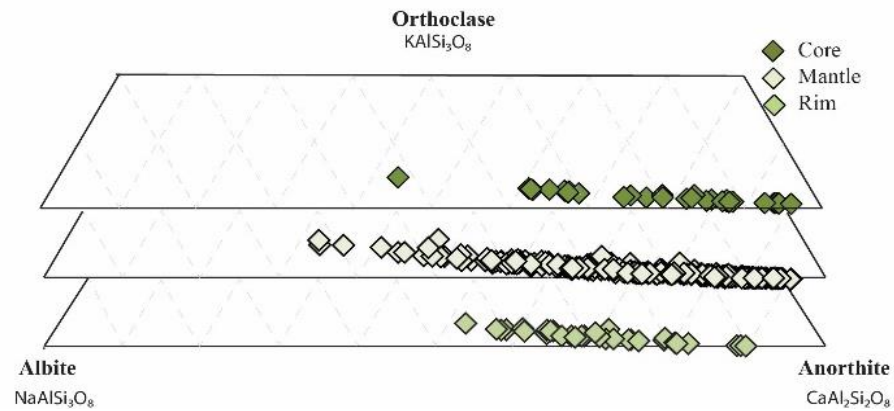


Figure 5.4 Chemical classification of plagioclase crystals based on the scheme of (Earnshaw and Greenwood, 1997) for cores, mantles and rims.

Despite the textural variation observed, the classification of plagioclases can be based on the presence and composition of a distinct core (Figure 5.5) shown by most crystals (n=32), enveloped by a mantle and rim. The An content of these cores in relation to the mantle and rim, further classifies them as (i) normal zoned with a high An core and an oscillatory mantle and rim with progressive decrease in An (n= 22), (ii) reverse zoned crystal with a low An core that is usually rounded and a high An mantle that is often associated with sieve texture (n=4), (iii) a patchy zoned core with an oscillatory zoned mantle and rim (n=6), (iv) a normally zoned crystal without the presence of a distinct core but a gradual decrease in An from its centre to the rim (n=4). The microlites are normally zoned with no evidence of disequilibrium textures. Commonly, the outermost rim of the larger crystals corresponds to the An content of the microlites in the EPMA maps.

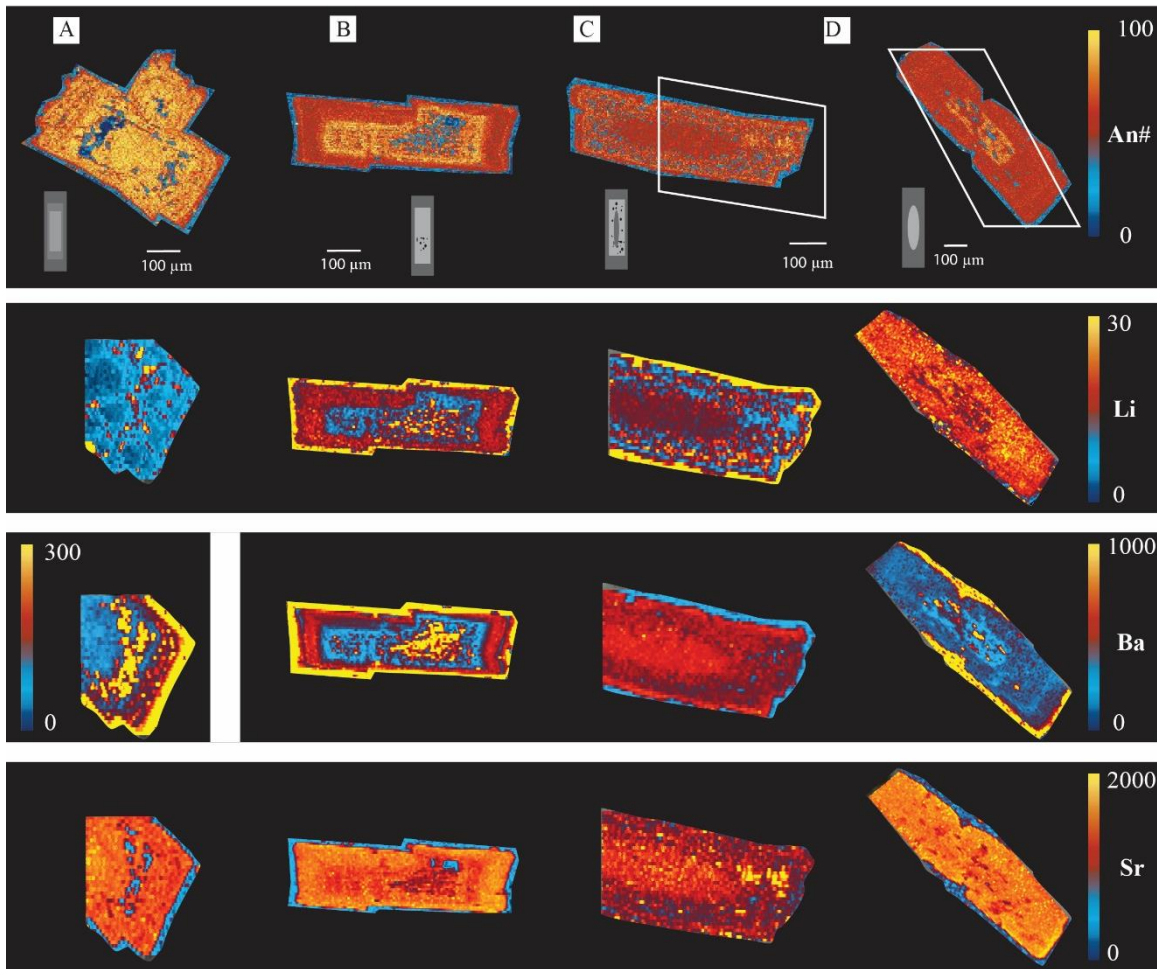


Figure 5.5 Types of zoning seen in plagioclases of Taranaki lavas. (A) An-rich, distinct core with sieved interior and oscillatory zoned mantle from ES3; (B) normally zoned crystal with a sieved mantle and oscillatory zoning from L16; (C) reverse zoned crystal with an An-poor core and sieved mantle from PYR; (D) normally zoned crystal with patchy core and oscillatory zoned mantle. Graphs show profile values for elements Li, Ba and Sr from core to rim (in ppm).

Along with patchy zoned cores, some cores show high An with box like patches of low An, that have been described as cellular ([Van Gerve et al., 2020](#)) and vary from boxy to rounded or irregular. The oscillatory zoned mantles contain numerous low amplitude cycles and are associated with resorption features that appear convoluted in BSE images (Figure 5.3). Sieve texture bands in the core and mantle are associated with lighter BSE image tones, indicating higher An content. The mantles are usually euhedral and are overgrown by a euhedral, thin rim.

Based on this preliminary classification, Taranaki plagioclase crystals are also distinguished based on zoning of elements Si, Fe, Ba, Sr and Li. Step zoning is commonly observed in most crystals, where the change in composition is abrupt, demarcating a core. Ba zonation typically compliments that of An zonation, thereby demarcating cores, oscillatory zoned mantles and rims. Sr zonation shows a positive and negative correlation to the An content, but also displays flat profiles in some crystals. The zoning patterns observed for Li concentrations in the plagioclase crystals can be flat (low/ high), high in the cores or high in the rims/mantles with respect to the An content.

5.4.2. Pyroxene

Major element compositional data for all clinopyroxenes from Taranaki indicate they are diopsides and augites based on the classification scheme of ([Morimoto, 1988](#)) (Figure 5.6). Cpx is commonly present as zoned, euhedral macrocrysts; as large crystal clots; and as normally zoned microlites in the groundmass. Clinopyroxenes have a narrow range for magnesium number ($Mg\# = 100 \times \text{molar MgO} / [\text{MgO} + \text{tot. FeO}]$) between 73–85, and high Ca content (*c.* 20 wt.% CaO). The clinopyroxenes of Taranaki contain low concentrations of Cr, reflected in the low Cr content of the whole rock compositions.

The most common type of zoning is oscillatory zoning, characterised by multiple, concentric growth layers in the mantles. Zones along the prism face (110,100,010) are generally thicker and show more pronounced resorption, which crosscuts multiple layers as compared to the hourglass sector that shows scarcely resorbed, parallel oscillatory zoning. Crystal rims are narrow and show euhedral outlines, while mantles that develop in glomerocrysts share similar growth patterns.

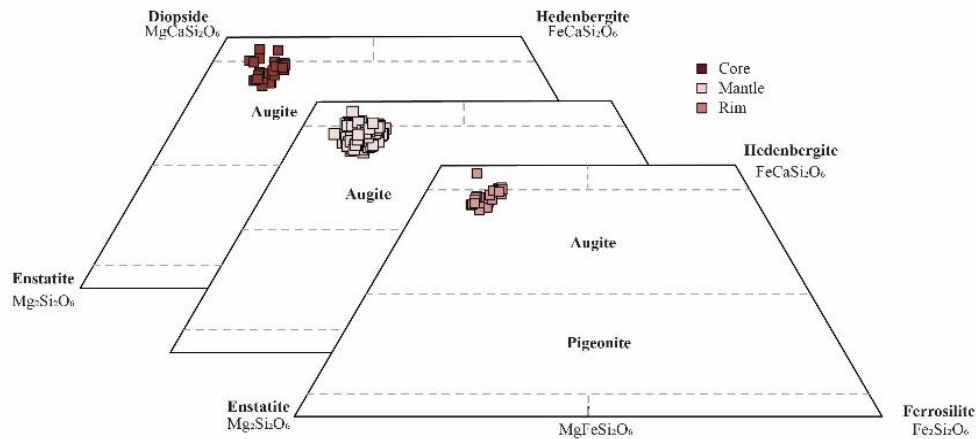


Figure 5.6 Classification of clinopyroxenes based on the scheme of [Morimoto \(1988\)](#). All cores, mantles and rims plot in the augite-diopside field.

Clinopyroxenes were categorised based on the presence of chemically distinct cores, which appear anhedral and resorbed with a sharp interface with the mantle. Figure 5.7 illustrates the following three types: (i) no distinct core observed for the intersect ($n=15$), (ii) a distinct core present and identified for all elements ($n=6$), and (iii) large patchy zoned core with thin rim and mantle ($n=3$). Most cpx crystals ($n=21$) show sector zoning of the mantles chemically dividing the crystal into prism and hourglass sections.

These sectors are characterised by oscillatory zoning to form euhedral crystal outlines. Sector zoning shows preferred uptake of Si and Mg in the hourglass sector of the crystal and preferred uptake of Ti, Al, and REE (Zr) in the prism sector, while most transition elements do not show sector zoning. Partitioning of elements in four sector zoned crystals of different lava flows is represented in Figure 5.8. It is observed that the difference in major oxide (SiO_2 , MgO and Al_2O_3 in wt%) and trace element (Ti and Zr in ppm) is comparable between samples although they are in ‘equilibrium’ with melts of varying compositions.

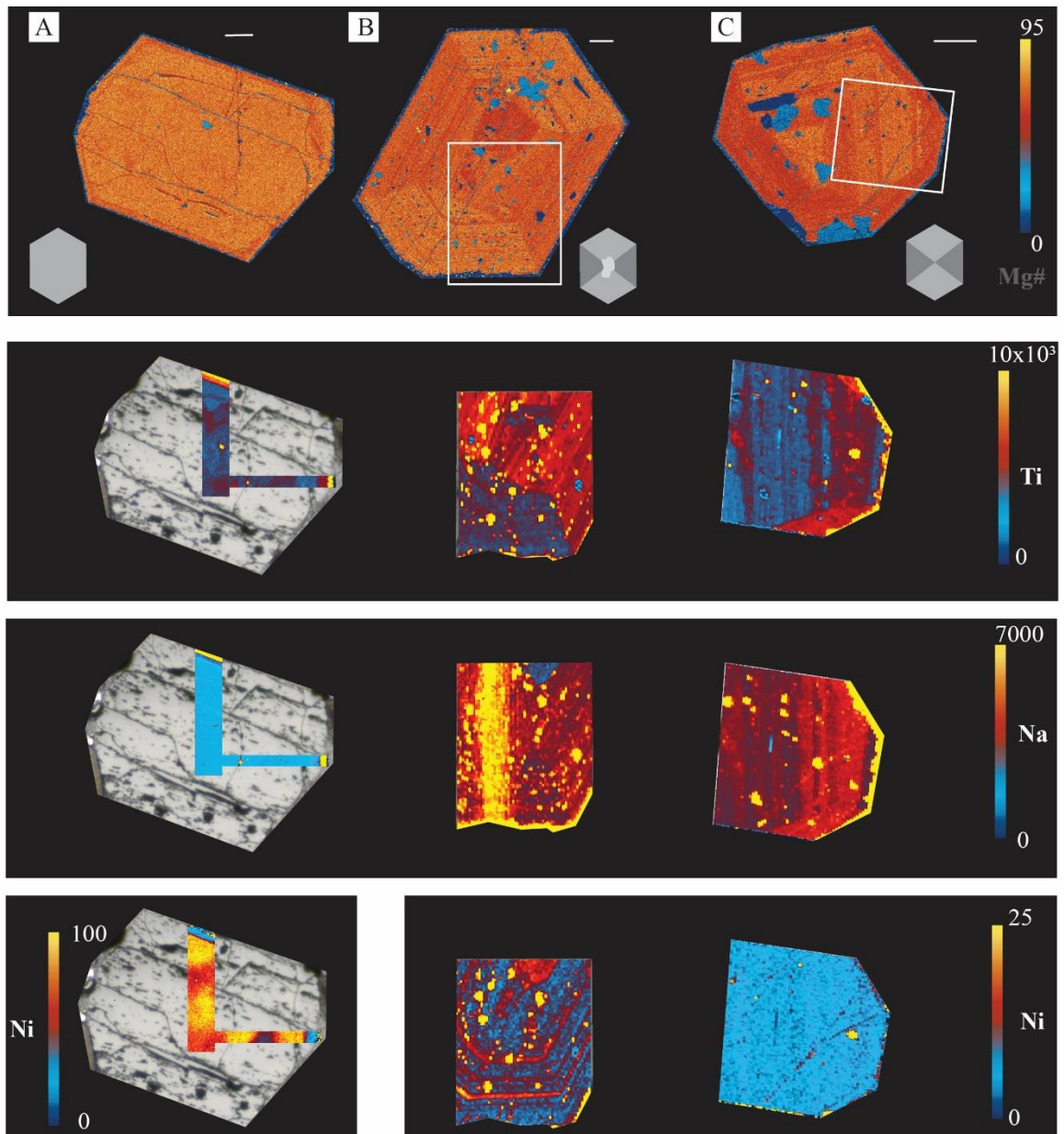


Figure 5.7 Types of zoning seen in clinopyroxenes of Taranaki lavas. (A) patchy zoned core with low Mg# mantle and high Mg# rim from ES5; (B) sector zoned crystal showing Mg-Si rich hourglass sectors and Al-Ti rich prism sectors, also present is a resorbed core from L9; (C) sector zoned crystal cut oblique to the c-axis without distinct core, from sample L5. Panels show relative concentration of elements Na, Ti, Ni and Zr (in ppm) from core to rim.

Furthermore, the clinopyroxenes have been distinguished based on the zoning patterns of key elements such as Na, Mg (reported as Mg#); transition elements (Cr, Ni and Sc) and rare earth elements (Zr, La). Na displays weak sector zoning and when present, the cores either show lower or higher Na concentration as compared to the mantle and rim. The same is observed for Ti and Mg#, although the mantles show strong sector zoning. REE

distribution is represented by La and Zr that behave like elements Ti and Al and are enriched in the prism sectors of the crystal. Cr concentrations are relatively low and enriched zones are rare, however when present crystals show either an enriched core, multiple/single enrichment zones in the mantle or an enriched rim. Sc and Ni zonation are more common, and zones/cores defined by transition elements are rarely reflected by the major elements. However, the transition metal V displays sector zoning.

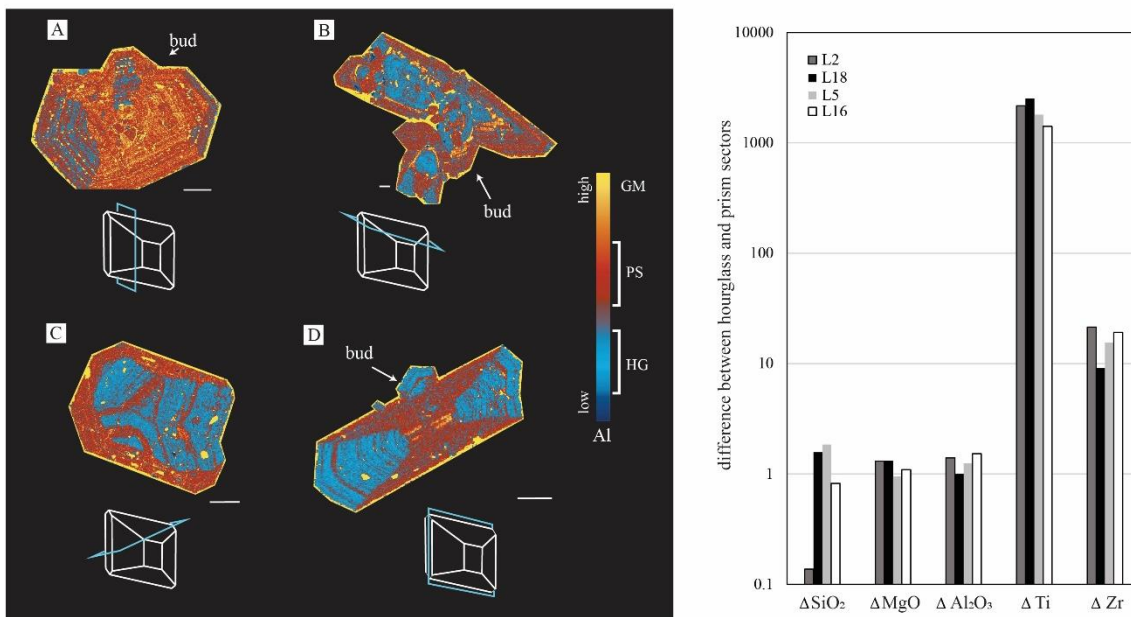


Figure 5.8 Sector zoned clinopyroxenes from samples (A) L2; (B) L18; (C) L5 and (D) L16. The white bar represents 200 μm . Crystal outlines show the intersect of the crystals which results in the sector patterns observed. The graph illustrates the comparable partitioning difference of oxides and elements between the hourglass (HG) and prism (PS) sectors. Hourglass sectors are enriched in SiO_2 and MgO , while the prism sectors are enriched in Al_2O_3 , Ti and Zr. SiO_2 , MgO and Al_2O_3 are in wt%, while Ti and Zr are in ppm. Groundmass SiO_2 for the host lavas are L2= 62.59; L18= 64.39; L5= 60.64; L16= 60.71 in wt%.

5.4.3. Amphibole

Amphiboles found in Taranaki lavas are calcium-rich and are classified as pargasites (Hawthorne et al., 2012) shown Figure 5.9.

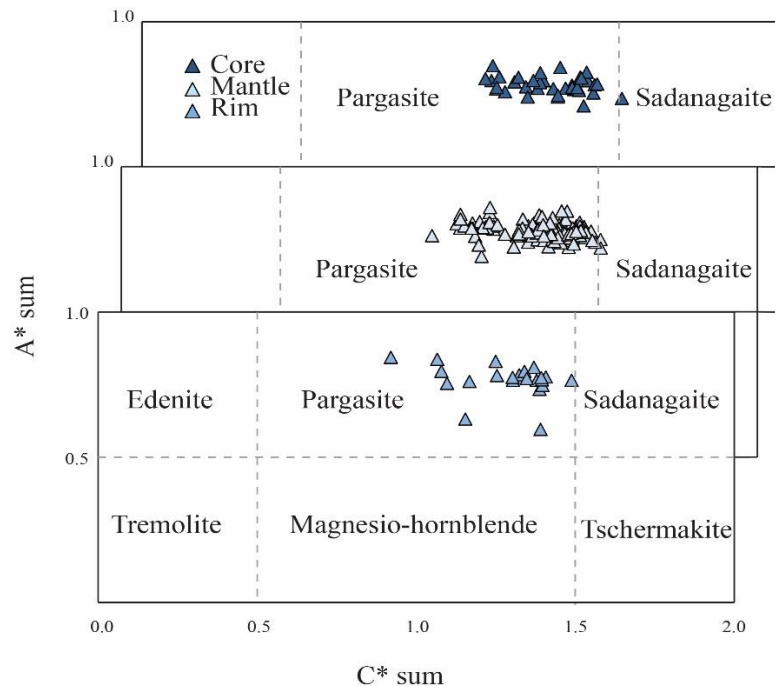


Figure 5.9 Amphibole classification based on the scheme of Hawthorne et al., (2012). All cores, mantles and rims fall in the pargasite field. $A^* \text{ sum} = {}^A(\text{Li} + \text{Na} + \text{K} + 2\text{Ca} + 2\text{Pb})$; $C^* \text{ sum} = {}^C(\text{Al} + \text{Fe}^{3+} + \text{Mn}^{3+} + \text{Cr} + \text{V} + \text{Sc} + 2\text{Ti} + 2\text{Zr}) - {}^w\text{O} - {}^c\text{Li}$.

Amphiboles are not present in all the samples and their abundances vary between samples of the same lava flow. Reaction rims and regions of decomposition are characterised by the replacement of amphibole with anhydrous phases of plagioclase, orthopyroxene, clinopyroxene, and oxides (D'Mello et al., 2021, Chapter 6). Based on BSE images and Mg# of the crystals, the amphiboles were categorised as (i) unzoned (n= 5), (ii) normal zoned with a high Mg# distinct core and a lower Mg# oscillatory zoned mantle (n= 3), and (iii) oscillatory zoned (n= 9) (Figure 5.10).

Oscillatory zoning is characterised by cyclic changes in greyscale with no abrupt interface, but rather a diffuse contact between zones. Major element zonation is weak, except for Al.

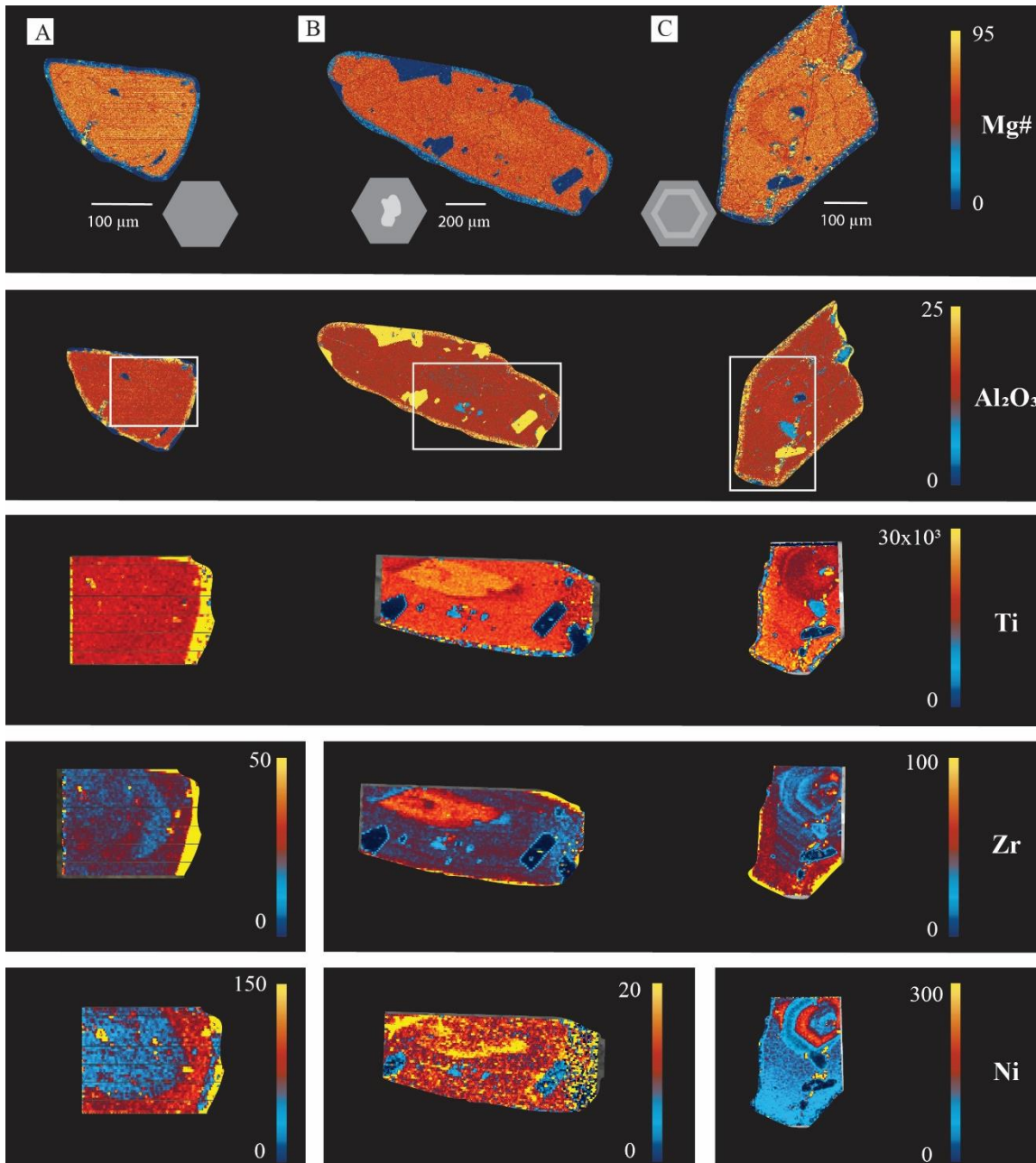


Figure 5.10 Types of zoning seen in amphiboles of Taranaki lavas. (A) unzoned crystal from ES3; (B) high Mg# core and low Mg# mantle from L5; (D) high Mg# crystal with low Mg# but high Cr mantle resorption interface from L16. Panels show relative concentration of elements Al, Ti, Ni and Zr (in ppm).

However, minor and trace elements show stronger variations in the crystal from core to rim. Amphibole zoning has been further distinguished using Ni and V, and REEs La and

Ce, Cr, Ni and V show similar enrichment patterns, although Cr concentrations are often too low to quantify.

5.5. Discussion

5.5.1. Mineral- melt equilibrium

Evaluation of mineral-melt equilibrium or disequilibrium is key to understanding the origin of the crystal cargo and whether crystals are autocrystic, i.e. crystallising from the melt they are entrained in ([Miller et al., 2007](#)). However, most arc volcanic rocks have a significant proportion of crystals that are not in equilibrium, especially in intermediate composition rocks, which typically show between 60–80% of disequilibrium crystals in a given population ([Ganne et al., 2018](#)). Several tests have been designed to determine melt-mineral equilibrium conditions, which are essential to conduct mineral-melt thermobarometry and hygrometry.

A model for plagioclase-melt equilibrium was proposed by ([Namur et al., 2012](#)), using the ratio of predicted vs. measured An content, where a 1:1 ratio was taken to define equilibrium. As shown in Figure 5.11A, the mantles and cores of plagioclase are not in equilibrium with the melt, apart from the rims, which show a close match between predicted and measured An content. However, these equilibrium models do not consider the effect of water content on the relationship between plagioclase An content and liquid An# in equilibrium. Figure 5.11B shows a comparison of H₂O-saturated (light grey field) and dry experiments (black field) data from [Waters and Lange \(2015\)](#). Following the methodology of [Zellmer et al. \(2016\)](#), Taranaki plagioclase data are superimposed on these, showing that the plagioclases are not in equilibrium with the melt they are entrained in. Taranaki plagioclases appear to have been in equilibrium with a dry to water-saturated

mafic melts at the time of crystallisation, yielding high An contents, but they have been entrained in a relatively felsic (low An) melt.

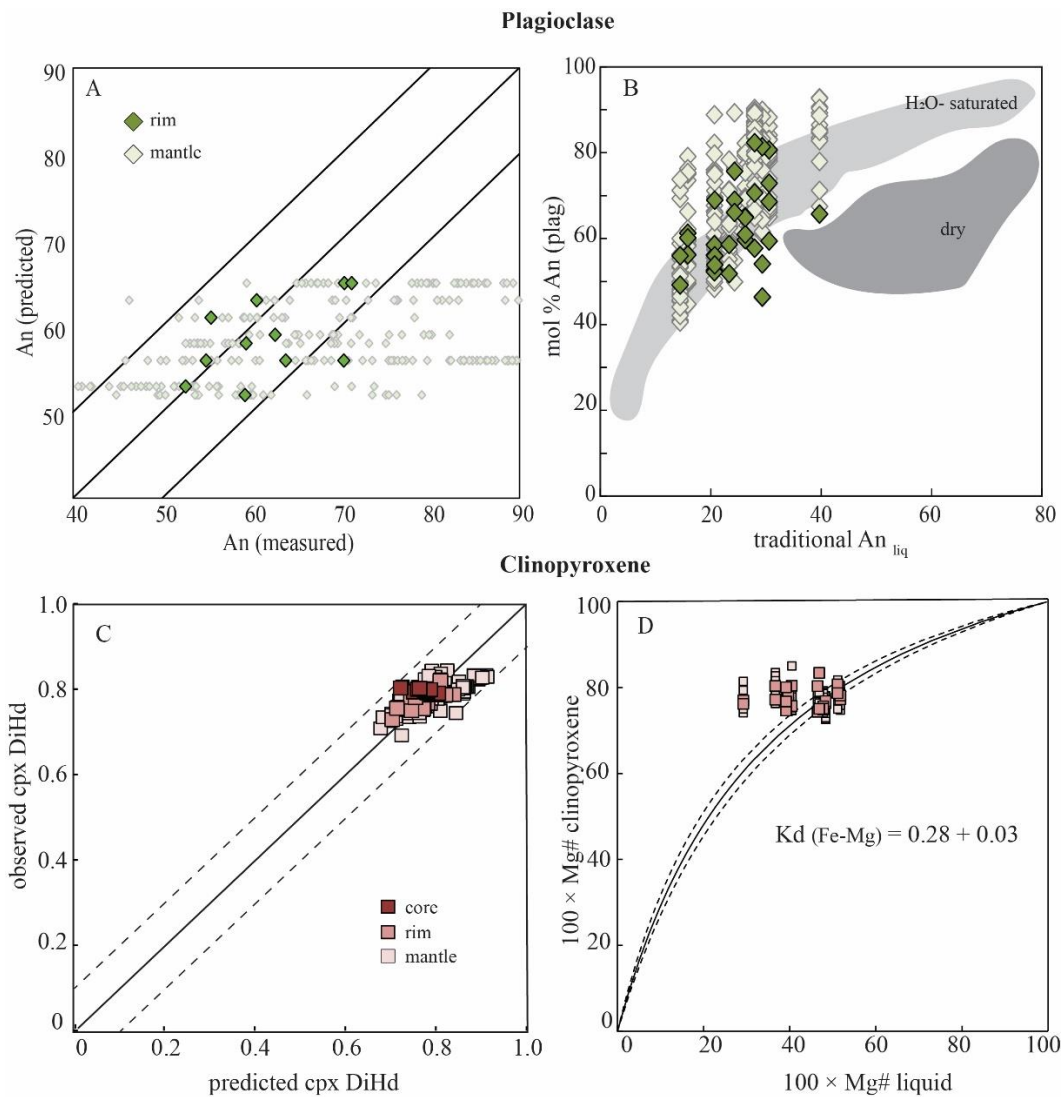


Figure 5.11 Equilibrium conditions for plagioclase and clinopyroxene. (A) plagioclase equilibrium after [\(Namur et al., 2012\)](#) showing rim-melt equilibrium (B) plagioclase after [Zellmer et al. \(2016\)](#) showing high An crystals in equilibrium with more mafic melts (C) clinopyroxene after [Mollo et al. \(2013b\)](#) and [\(Putirka, 2008\)](#) (D). Clinopyroxenes are within 1 SEE of the equilibrium, however, pronounced disequilibrium textures indicate re-equilibration of crystals over long residence timescales.

Clinopyroxene equilibrium is calculated from the Fe-Mg exchange coefficient between cpx and melt, where $K_D (\text{Fe-Mg}) = 0.27 \pm 0.03$ ([Mollo et al., 2010](#); [Putirka, 2008](#)). Another test is comparing predicted and measured cpx components DiHd (diopside-hedenbergite) as suggested by [Mollo et al. \(2013b\)](#). As illustrated in Fig. Figure

5.11B, the cpx population of Taranaki is in near equilibrium crystallization conditions, which are achieved when the clinopyroxene compositions plot within 10% of the one-to-one equilibrium line corresponding to values of $\Delta\text{DiHd} \leq 0.1$ ([Jeffery et al., 2013](#)). However, this does not necessarily indicate for the formation of autocrystic clinopyroxenes in equilibrium but may instead point to a prolonged storage period during which Fe-Mg re-equilibration of the clinopyroxene mantles, as well as antecrystic cores that show clear disequilibrium textures such as resorbed surfaces, has occurred.

5.5.2. Interpretation of zoning textures

Sieve texture: Sieve texture is common in the plagioclase of volcanic rocks and mantle xenoliths, and it can develop as a result of changes in temperature, pressure or melt compositions ([Humphreys et al., 2006](#); [Nelson and Montana, 1992](#); [O'Brien et al., 1988](#); [Pan et al., 2018](#); [Stewart and Pearce, 2004](#); [Tomiya and Takahashi, 2005](#)). In Taranaki samples, sieve texture in plagioclase is associated with higher An contents indicative of interaction of the crystal with hotter, more mafic magma compositions. This interaction resulted in the partial dissolution of the crystal and recrystallization of plagioclase in equilibrium with the new environment.

[Neave and MacLennan \(2020\)](#) show that sieved cores in clinopyroxenes can be indicative of rapid ascent dissolution of clinopyroxene. High Al content in the clinopyroxene is indicative of high-pressure crystallisation and during rapid ascent, decompression-driven dissolution of high Al_2O_3 cores is coupled with low Al_2O_3 in the rim. However, the sieved cores of Taranaki clinopyroxenes have similar Mg# range and low Al_2O_3 relative to the mantles and rims and are thus unlikely to have formed by rapid decompression. Instead, the sieved cores may be attributed to the partial dissolution of early formed low Al_2O_3 cores by the groundmass melt at late stage.

Patchy cores: Patchy texture is interpreted as the result of partial dissolution of high-An plagioclase that was then overgrown by plagioclase with lower An contents, filling the voids present in the core. Therefore, to observe this texture, resorption of high An plagioclase followed by growth of low An plagioclase is required.

Resorption of plagioclase occurs either upon a change in magma chemistry ([Nakamura and Shimakita, 1998](#); [Tsuchiyama, 1985](#)), an increase in temperature ([Johannes et al., 1994](#)), a decrease in pressure ([Nelson and Montana, 1992](#); [Vance, 1962](#)) or a combination of changes in the system. However, temperature increase and decompression-associated exsolution of water from the melt would both result in crystallization of a An rich plagioclase ([Grove et al., 1992](#); [Namur et al., 2012](#)). A regular supply of evolved magma infiltrating a mafic crystal mush, or the transport of the crystals into a region where the pre-existing melt was in equilibrium with lower-anorthite plagioclase, can result in patchy zoned crystals ([Van Gerve et al., 2020](#)). Diverse primary melts reported for Taranaki (Chapter 4) can supply low An melts as well as remobilize the crystal cargo into Ca-poor regions of the crystal mush with consecutive injections. Infiltration of interstitial melts in crystal mushes could lead to reactive dissolution of minerals ([Coogan et al., 2000](#); [Lissenberg and MacLeod, 2016](#)).

The patchy zoning of clinopyroxenes also indicates intense dissolution of early crystallized clinopyroxene by fresh magma, as evidenced by the presence of abundant melt inclusions in the high-Mg#, dark domains of the patchy zones. However, the contact of patches of different Mg# appear diffuse, indicating prolonged residence at elevated temperature may have resulted in Fe-Mg interdiffusion.

Cellular texture in cores: Cellular textures are different from patchy cores and are attributed to the skeletal growth of disequilibrium, low An plagioclase followed by infilling and overgrowth by higher An plagioclase ([Bennett et al., 2019](#); [Nakamura and](#)

[Shimakita, 1998](#); [Tsuchiyama, 1985](#)). The low An area in the cellular textural zones are remnants of the partially dissolved plagioclase, and higher-anorthite cells represent channel sections along which dissolution–reprecipitation of high An plagioclase occurred.

Resorption surfaces: The macrocrysts in this study shows clear major and minor wavy surfaces, which erode previous growth layers and are indicative of resorption. In plagioclase, this is characterised by gradual decrease of An content and a sharp increase across the next resorption surface. Temperature and magma composition have the greatest effects on plagioclase stability and composition, and small fluctuations can induce such resorption events ([Almeev et al., 2012](#); [Grove et al., 1992](#); [Namur et al., 2012](#); [Tsuchiyama, 1985](#)).

Clinopyroxenes also show overgrowth of a single layer with a sharp resorption surface, which is attributed to a change of melt composition during crystallization of a crystal ([Ginibre et al., 2002a](#); [Ginibre et al., 2002b](#)). These resorption surfaces are categorised as major resorption surfaces (high amplitude oscillation), while minor resorption surfaces (low-amplitude oscillation) are attributed to local mixing of magmas with less contrasting compositions ([Elardo and Shearer, 2014](#); [Ginibre et al., 2007](#)). Therefore, the resorption surfaces in clinopyroxene are the result of variable degrees of magma mixing. The major and minor resorption surfaces are sometimes associated with either high Mg# and high Cr or low Mg# and low Cr oscillations, indicating multiple recharging events involving primary or evolved magmas during the growth of a crystal.

Oscillatory zoning: There are two possible causes for the formation of oscillations of chemistry during crystal growth: (1) extrinsic causes such as changes in pressure (P), temperature (T) or magma composition (X); or (2) intrinsic causes such as fluctuations between diffusive and advective supply of cations in a melt boundary layer immediately

adjacent to the growing crystal ([Alloway et al., 2005b](#); [Schoneveld et al., 2020](#); [Shore and Fowler, 1996](#); [Streck, 2008](#)). Short-wavelength (1–10 μm) oscillations are common in clinopyroxene and plagioclase and are attributed to growth kinetics, magma recharge events and convection processes ([Ginibre et al., 2002a](#); [Ginibre et al., 2002b](#); [Humphreys et al., 2006](#); [Tsune and Toramaru, 2007](#)). Kinetic models and detailed microanalytical observations [Zellmer et al. \(2016\)](#) indicate that high crystal growth rates with moderate degrees of undercooling result in the formation of a boundary layer, in which elements become depleted when mineral growth rates exceed the diffusive supply of elements from the melt. Repeated, small volume injections of melt of different compositions can also form oscillatory zoning.

Sector zoning: Clear Si and Mg rich hourglass sectors, and Al, Ti and REE rich prism sectors are observed in Taranaki clinopyroxenes. This type of zonation is common in natural terrestrial ([Downes, 1974](#); [Hollister and Gancarz, 1971](#); [Leung, 1974](#); [Ubide et al., 2019](#); [Welsch et al., 2016](#)), lunar ([Hollister and Gancarz, 1971](#)) and experimental pyroxene ([Lofgren et al., 2006](#); [Schwandt and McKay, 2006](#)).

These sector zones represent differences in chemistry of a crystal due to kinetic effects at the growth surface, whereby elements are incorporated into the structure at different rates along different crystallographic surfaces, rather than changes in chemistry or conditions of the surrounding magma ([Hollister and Gancarz, 1971](#)). There are at least four controlling factors for the creation of sector zones, as explained by ([Hollister and Gancarz, 1971](#)); (1) size and composition of ionic complexes added to the crystal as it grows, (2) rate of addition of material, (3) rate of equilibration of the new material with the matrix at the surfaces of growth steps, and (4) rate of re-equilibration of surface layers with the matrix by exchange of ions perpendicular to the crystal faces.

Sector zoning is formed at low degrees of undercooling, which in turn could be a result of regular degassing of the chamber or due to frequent crystal movement between the hot interior and cold margin caused by magma convection ([Ubide et al., 2019](#)). High degrees of undercooling, on the other hand, can also produce sector-zoned crystals where rapid skeletal growth is followed by a spongy space filled with matrix ([Masotta et al., 2020](#)). However, no distinct skeletal or dendritic zoning with regular fine layers is observed in Taranaki crystals, indicating a near equilibrium crystallisation environment with low degrees of undercooling. The differences in SiO₂, MgO, Al₂O₃, Ti and Zr between the hourglass and prism sectors are comparable to each other, despite being hosted in melts of differing compositions (Figure 5.8). This suggests that the crystals formed in similar environments with the similar degrees of undercooling.

5.5.3. Crystallization environments

5.5.3.1. *Inferences based on An contents of plagioclase:*

Changes in melt composition, temperature, and pressure are recorded in the compositional zonation of plagioclase crystals ([Bowen, 1913](#); [Drake, 1976](#); [Longhi et al., 1993](#); [Putirka, 2008](#); [Waters and Lange, 2015](#)). If zones of similar composition exist among different crystals, it is reasonable to assume that they crystallized in similar magmatic environments at comparable pressure, temperature and compositions conditions (e.g. [Kahl et al., 2011](#); [Mollo et al., 2015](#); [Viccaro et al., 2016](#)).

In Taranaki samples, we identify plagioclase zones with 55–70 and 75–80% An ranges, which distinguish the low An and high An environments of crystallisation (Figure 5.12). The various types of plagioclase crystals observed can be explained by crystallisation in one environment, followed by the introduction of the crystal into a new environment and the subsequent resorption, dissolution and recrystallisation.

Figure 5.12 illustrates the effect of the crystallising environment on the zoning patterns of the plagioclase crystals. Formation of a crystal in a felsic environment result in a low An core that is then introduced into an environment of high An content. This results in the dissolution and resorption of the crystal forming sieve textures or rounding of the core (A). If resorption is complete, only a sieve portion of the core is left, and the core of the crystal appears An rich (B). In this new An-rich environment, An-rich cores of new crystals form in equilibrium and then these crystals are introduced into a new An-poor environment, indicated by a sharp boundary where they may reside for short (D) or long (C) periods.

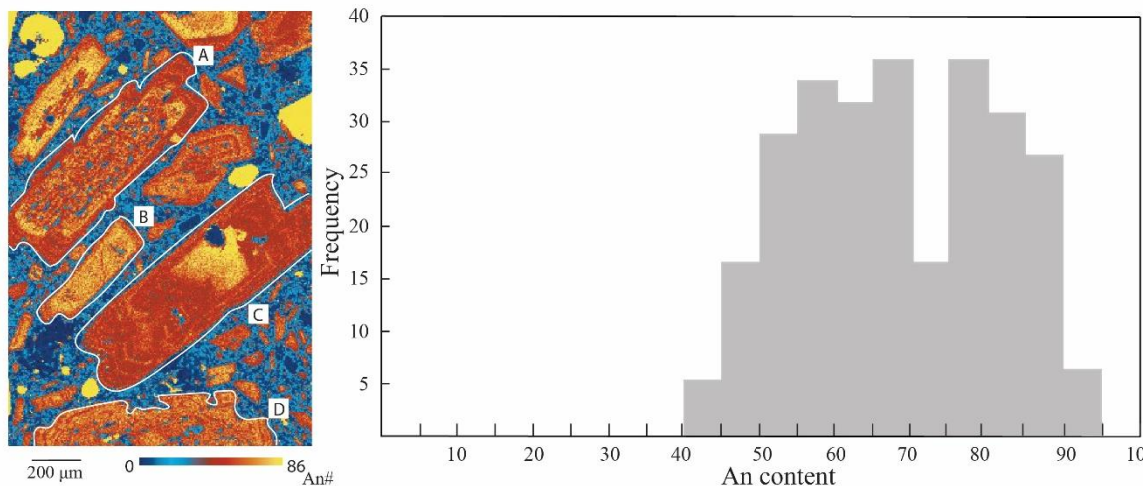


Figure 5.12 Histogram showing at least 2 populations of plagioclase with distinct An contents for all Taranaki crystals. Plagioclases from sample TUR showing (A) patchy, sieved low An core with high An interface mantled by low An plagioclase in equilibrium with the melt; (B) high An core overgrown by low An mantle in equilibrium; (C) high An core with oscillatory zoned thick mantle; and (D) patchy zoned core with no mantle and narrow rim. All crystal types occur within a short length scale.

These sub-environments within the mush system can be attributed to (i) repeated, small volume, injections of diverse melts into a crystal-rich mush zone, (ii) transportation of crystals between different sub-environments. A combination of these processes results in a plagioclase population with varied histories and zoning types over short length scales that would not have been possible if the crystals had grown *in situ*.

5.5.3.2. *Inferences based on Sr and Ba contents of plagioclase:*

Concentrations of Ba and Sr in the plagioclase crystal lattice are a result of Ca substitution and is strongly dependent on An content, with subordinate influence of crystal structure, melt composition, and temperature ([Bindeman et al., 1998](#); [Blundy and Wood, 1991](#); [Giletti and Casserly, 1994](#)). If major-element zoning patterns are preserved, the equilibrium concentration of Sr and Ba obtained after diffusion in the crystal are inversely correlated with An content ([Zellmer et al., 1999](#)). The variable Ba and Sr concentration at high An content in Taranaki lavas reflects the influence of different initial magmas combined with long storage in a cool environment to preclude diffusive equilibration of these trace elements.

5.5.3.3. *Inferences based on Li contents of plagioclase:*

Lithium is a moderately incompatible element in plagioclase ($K_D \sim 0.15\text{--}0.7$), as determined by experimental data covering a range of temperatures (1153–1299°C) and anorthite contents ($An_{39\text{--}77}$) ([Giletti and Shanahan, 1997](#)). Li is extremely mobile and prefers the exsolved fluid phase relative to melt at low pressures, and the rapid diffusion rate of Li allows constraining of timescales of minutes to seconds to be recorded in the crystals ([Genareau and Clarke, 2010](#); [Genareau et al., 2015](#)). Experimental results of [Coogan \(2011\)](#) show that the Li is far more compatible in sodic plagioclase than calcic plagioclase within the compositional range of $An_{60\text{--}90}$, while crystals that are in equilibrium with the melt should show flat profiles from core to rim ([Bindeman and Davis, 2000](#); [Bindeman et al., 1998](#)).

In Taranaki lavas, Li is seen either as enriched cores, enriched rims or flat profiles which often correlate inversely to the An content. However, in some crystals, Li is positively correlated to An content, while in normally zoned crystals the Li profile is flat, despite An

zoning It can be inferred from Li zoning in plagioclase, that most of the crystals reside in the mush zone long enough for Li to equilibrate within the crystal. Decreasing concentrations of Li towards the rim of the crystal are seen in eruptive products of Mount St Helens ([Kent et al., 2007](#)) and Monserrat ([Genareau and Clarke, 2010](#); [Genareau et al., 2009](#)). This implies significant diffusive disequilibrium between Li and An during the final growth stages caused by either the loss of Li from the melt due to volatile exsolution or the intrusion into a low Li melt just prior to eruption ([Giuffrida et al., 2018](#)). Li enriched rims were reported from the Oruanui eruption in Taupo, New Zealand, and was attributed to changing Li partitioning behaviour due to preferential exsolution of chlorine from the system during decompression ([Charlier et al., 2012](#)). Another hypothesis is the storage of volatiles (and Li-rich gases) in the shallower parts of the volcano, which ascended from deeper regions. The rising melts with entrained low Li plagioclases interact with these gases, resulting in the formation of a high-Li rim ([Berlo et al., 2004](#); [Blundy et al., 2008](#); [Kent et al., 2007](#)). Thus, in Taranaki lavas, plagioclase crystals with short storage times (Li zoning independent of An zoning) and longer storage times (Li anticorrelated to An) are seen within the same thin section indicating different storage environments and remobilization prior to eruption.

5.5.3.4. Inferences based on Cr zoning in clinopyroxene:

Cr is highly compatible with clinopyroxene and Cr enrichment indicates recharge with mafic magmas. However, the magmas of Taranaki are generally poor in Cr, indicating felsic parental melts, and therefore Cr zoning in clinopyroxene alone cannot be evidence of magma recharge episodes. When present, Cr zoning shows either no enrichment at all, single or multiple enrichment zones in the mantle, an enriched core, or an enriched mantle (Figure 5.13). These types of zoning patterns are indicative of an heterogeneous interaction of the mush system with injected Cr rich melt, as suggested by [Bergantz et al. \(2017\)](#). It

is possible that, during an intrusive event, some crystals never encounter the intruding melt and just experience a thermal spike, while others have repeated interactions resulting in multiple zones of enrichment. The growth stage during which interaction occurs determines whether the enrichment is observed in the core, mantle or the rim of the crystal. Another key observation is the differences in the concentration of Cr enrichment, varying from 300 – 5200 ppm, which indicates different recharge episodes with variable concentrations of Cr.

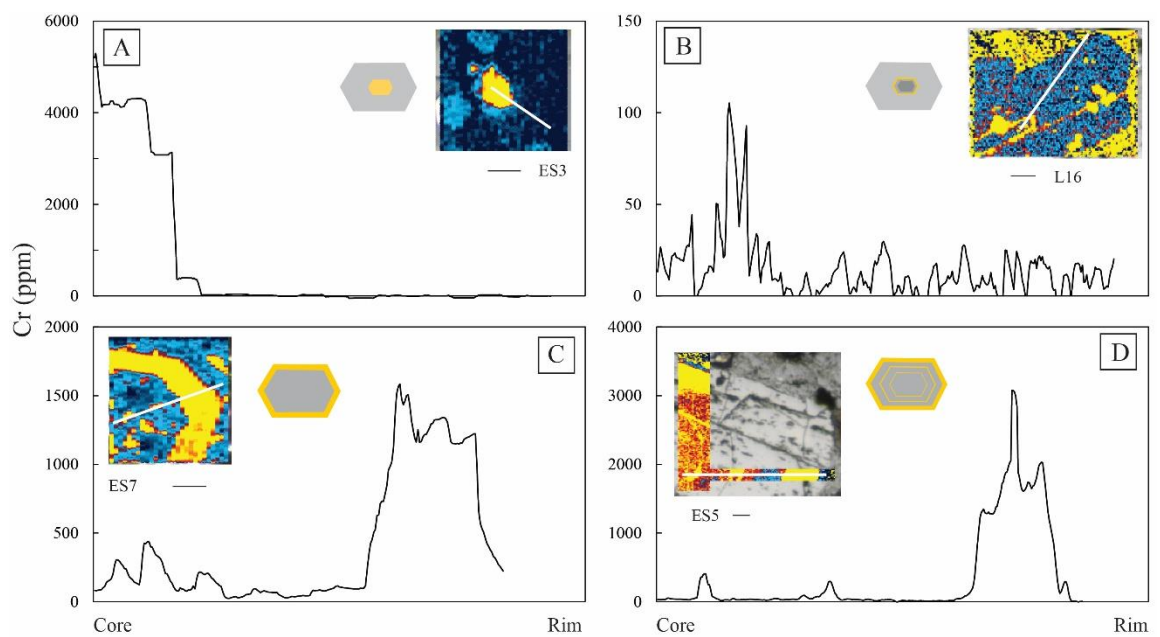


Figure 5.13 Cr zonation patterns in clinopyroxene showing (A) Cr enriched core in ES3; (B) Cr enrichment marking resorption of the core in L16; (C) Cr enriched rim in ES7; (D) multiple Cr enrichment episodes with high Cr enrichment in the rim in ES5

5.5.3.5. Inferences based on Na contents of clinopyroxene:

Na zoning in clinopyroxene shows weak sector zoning but is positively correlated with Si and Mg and negatively correlated with Al, Ti and the REEs. Jadeite melting is highly sensitive to pressure changes and higher Na in the cores as a result of compaction of crystals is indicative of higher pressure ([Bédard, 2014](#); [Blundy et al., 1995](#); [Nimis, 1995](#)).

Experimental data suggest that changes in Na are primarily controlled by pressure, assuming the melt compositions are uniform.

In Taranaki clinopyroxenes, we see cores that have low Na content, mantled by oscillatory zones, which would indicate movement of crystals from a region of low pressure to high pressure. The history of the Taranaki volcano identifies phases of cone growth and collapse ([Palmer and Neall, 1991](#); [Procter et al., 2009](#); [Zernack and Procter, 2021](#)) and could contribute to the changes in pressure indicated by Na concentrations. However, given the diversity of melt compositions, it is more likely that the melt from which the core crystallised is different in composition from the melt in which the mantles crystallised. This is complimented by differences in concentrations of other elements between core and mantle.

5.5.3.6. *Inferences based on Al contents of amphibole:*

The composition of amphibole is affected by the P, T, f_{O_2} and pH_2O ([Scaillet and Evans, 1999](#)). Temperature increase causes an increase in Al, Na and Ti of amphibole. If the heating event is small enough, zones with increasing Al are formed, and if heating is extreme, magma temperatures beyond amphibole stability are attained, resulting in the formation of augite or the volumetric decomposition of amphibole ([D'Mello et al., 2021, Chapter 6](#)). The zoning of Al is preserved in amphibole macrocrysts and is rarely associated with an enrichment in Cr, indicating a recharge event with a hotter magma.

5.5.3.7. *Inferences based on Mg# of amphibole:*

The Mg# of amphibole is strongly increased with the increase in f_{O_2} of the system due to the decrease of Fe^{2+} activity in the melt ([Czamanske and Wones, 1973](#); [Humphreys et al., 2006](#); [Scaillet and Evans, 1999](#)). Taranaki samples show the formation of Mg- and Si-rich rims, which are accompanied by a decrease in Ti, consistent with gradual cooling

during crystallisation of the core ([Bachmann and Dungan, 2002](#)). Recharge events are also indicated with the sharp contacts between Mg-poor cores and Mg-rich rims.

5.5.4. The source of crystals and the Median Batholith

The Median Tectonic Zone is defined as a zone of deformed or dismembered small crustal fragments and/or magmatic arc rocks ([Bradshaw, 1993](#); [Frost and Coombs, 1989](#); [Kimbrough et al., 1994](#)). It includes terranes, formations, plutons, igneous complexes, gneisses and faults ([Mortimer et al., 1999b](#)). This zone also forms the basement for the Taranaki Peninsula overlain by the sediments of the Taranaki Basin ([Mortimer et al., 1997](#)). The MTZ plutons are of Carboniferous to early Cretaceous age and are mainly of calc-alkaline I-type petrological character ([Kimbrough et al., 1994](#)). The Median Batholith is defined as a large volume composite intrusion comprising of many individual but contiguous plutonic and metaplutonic rocks ([Mortimer et al., 1999a](#)). It represents the main locus of magmatism in the New Zealand sector of Gondwana and probably developed *in situ* as a result of the interaction of the Panthalassan oceanic plates with the South Gondwana continental plate ([Mortimer et al., 1999b](#)).

It is hypothesised that at the Taranaki Volcanic Lineament, repeated intrusions of mantle derived melts over a long period of time have developed an extensive mush system in the crust. The bulk of the crystal populations in this mush system are crystal clots and disengaged crystals that have interacted with the injected interstitial melt of varying compositions and volumes. This includes large clots of amphibole, clinopyroxene, and plagioclase, which inherit the magmatic signatures of the Median Batholith. Consequent evolution of the mush system and continued intrusion of subduction derived melts from the current east New Zealand system feeds the present edifice of Mt. Taranaki. The longevity of this system and the complexities of tectonics and melt generation have yielded a crystal cargo that reflects these complex magmatic processes and heterogeneity

of the mush system and its precursory plutonic rocks that formed > 100 Million years ago.

5.5.5. Model for Taranaki

Lavas erupted from Taranaki show varying compositions and mineral assemblages ranging from basalts to dacites. Whole rock compositions can be interpreted as the sum product of diverse melt compositions and uptake of crystals in varying proportions from the mush zone (Median Batholith?), which have then reacted with the melt to varying degrees during storage.

The magnitude of recharge events can be assessed from ubiquitous textures such as sieved plagioclase macrocrysts and reacted amphiboles. These large events affect a large proportion of the mush zone and are recorded in the chemistry of the crystals growing at the time. On the other hand, comparatively small volume events do not significantly change the bulk properties of the mush zone and are reflected in the limited proportions of crystals that reflect these changes in conditions. Small volume events facilitate the contemporaneous growth of different zoning types in different parts of the chamber. For macrocrysts with different zoning patterns and similar rims to erupt in the same sample, melt homogenization and mixing must cease only shortly before eruption.

The presence of glomerocrysts with intergrown clinopyroxene, clinopyroxene + plagioclase, and amphibole show that crystallisation occurred in a crystal rich environment with crystal faces impeding on the growth of other crystals ([Holness et al., 2019](#); [Holness et al., 2007b](#)). These cumulate textures are common in xenoliths found in Taranaki lavas and debris avalanche deposits. The grains that crystallized may have accumulated together, forming glomerocrysts that show similar zoning patterns.

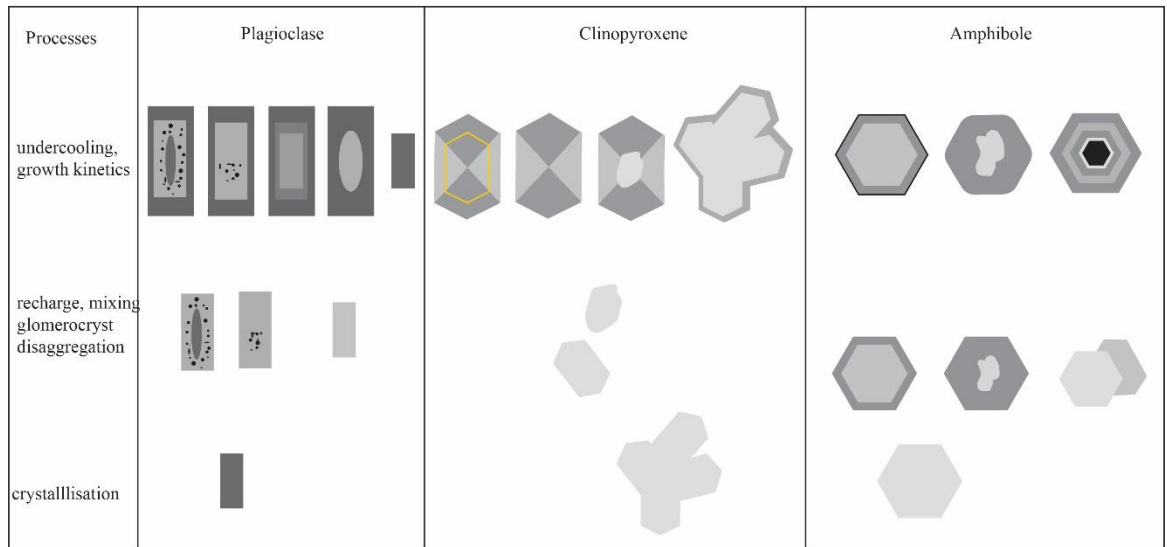


Figure 5.14 Panels illustrating the various zoning patterns seen in plagioclase, clinopyroxene and amphibole. Variations in greyscale indicate crystallisation in different environments resulting in chemical zoning. Clinopyroxene crystal clots are also represented.

Subsequent magma intrusions may disaggregate the crystal-rich mush. Transport of crystals and recrystallization in a mush zone results in a euhedral outline of the clinopyroxene macrocrysts (Figure 5.14). The oscillatory rims of glomerocrysts are continuous, encompass all constituent grains and are not found along the internal grain boundaries. This suggests that they formed in a liquid-dominated environment after separation of crystal clusters from the mush in which they previously grew. Further disaggregation results in free crystals that grow in the mush, experiencing different sequences of processes, which include mixing, ascent and remobilization. The texture and composition of these crystals respond not only to thermodynamic conditions, but also to kinetic effects during crystal growth; for example, high degrees of undercooling or rapid decompression ([Lofgren et al., 2006](#); [Masotta et al., 2020](#); [Mollo et al., 2013a](#); [Mollo et al., 2010](#); [Neave et al., 2019a](#); [Pontesilli et al., 2019](#)).

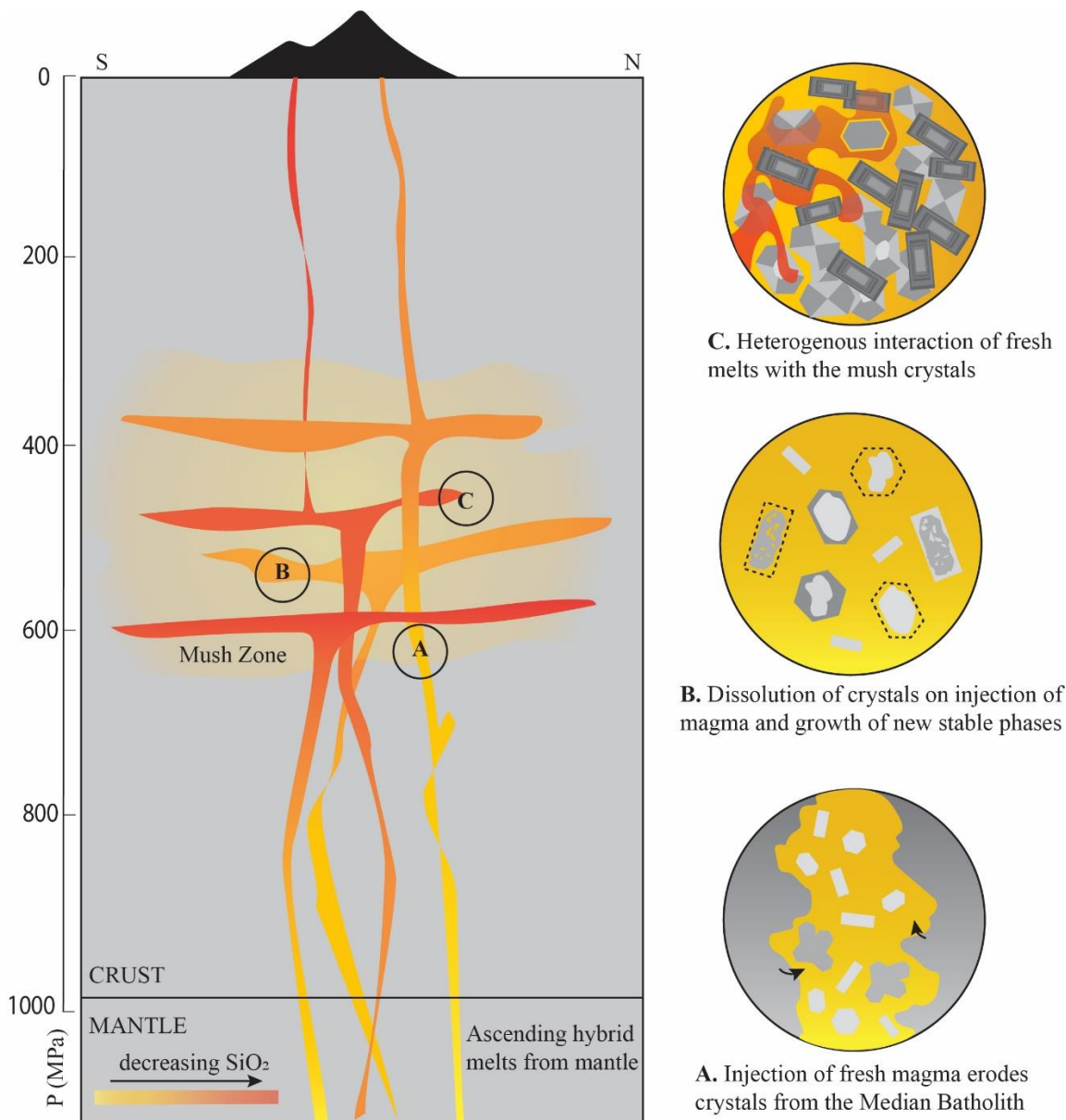


Figure 5.15 Model for Taranaki eruptives. (A) Hybridised melts from the mantle pick up crystals and crystal clots from the country rock (Median Batholith) resulting in a population of xenocrystic crystals within an otherwise aphyric to sparsely phyrlic melt. (B) during storage within the mush zone (300-700 kbar) these xenocrystic/antecrystic cores are then resorbed or dissolved, followed by euhedral overgrowth of new material on remnant crystal cores. (C) Influxes of fresh melts of varying compositions interact heterogeneously with the mush zone, affecting crystal compositions and zoning patterns provided the crystal is in contact with the melt.

The disparities in zoning patterns found in crystals of the same lava flow indicate that these crystals must have grown far apart, before mixing and melt homogenization were complete as reflected by crystals with similar rims and rims with comparable compositions to groundmass microlites. This is accomplished through a final recharge

episode, which picks up crystals with varying histories, and the mush-melt mixture ultimately ascends through the plumbing system to breach the surface (Figure 5.15).

5.6. Conclusions

1. The lava flows of Taranaki have a rich crystal cargo with diverse zoning patterns and textures suggesting varied sequences of magmatic processes recorded in the crystal. These processes include magma recharge, magma mixing with mafic as well as felsic melts, and remobilization of crystal cargo.
2. The crystal rich mush system in Taranaki may be a product of repeated injections of melts from the subduction system into the Median Batholith basement. These melt intrusions disengage crystal clots and trigger overgrowth crystallisation.
3. The mush zone is heterogenous, and the extent of influence of the intrusion is largely dependent on its volume. This results in different sub-environments created in the mush zone with unique compositions and intrinsic parameters.
4. The final magmatic intrusion that ultimately results in an eruption remobilises crystals from different environments, triggering crystallization of microlites and rims on the crystals prior to extrusion.

Chapter 6.: Deciphering magma storage and ascent processes of Taranaki, New Zealand, from the complexity of amphibole breakdown textures

Nessa G. D’Mello^{a*}, Georg F. Zellmer^a, Marianne Negrini^b, Gabor Kereszturi^a, Jonathan Procter^a, Robert Stewart^a, David Prior^b, Masako Usuki^c, Yoshiyuki Iizuka^c

^a Volcanic Risk Solutions, Massey University, Tennent Drive, Palmerston North 4442, New Zealand

^b Department of Geology, University of Otago, 362 Leith Street, Dunedin 9016, New Zealand

^c Institute of Earth Sciences, Academia Sinica, 128 Academia Road Sec. 2, Nankang, Taipei 11529, Taiwan

*Corresponding author: N.D’Mello@massey.ac.nz

Abstract

Lava flows that constitute the current edifice of Taranaki volcano, New Zealand, contain a complex crystal cargo including plagioclase, pyroxene, amphibole, oxides, and rarely olivine. Amphibole textures and mineral chemistry indicate that crystals are peritectic antecrysts entrained at various depths by ascending magmas. The crystals record a complex growth history within a range of temperature and pressure conditions (*c.* 950–1010°C at mid- to deep crustal levels). Most amphiboles show the development of distinct reaction rims where the mineral is in contact with the ambient melt. Texturally, the rims are identified as detached, symplectic, granular or coarse. True rim thicknesses vary little ($\pm 20\%$, 1σ , on average) within individual thin sections but show a large variation between samples from different lava flows, from < 5 to > 450 μm . Reaction rim formation on Taranaki amphiboles is attributed to degassing during magma ascent as well as small increases in temperature. Associated with the formation of rims, the amphiboles also show two types of volumetric decomposition, identified as irregular and aligned. The

former is indicative of slow reaction of amphibole with melt entrapped in fractures and cleavages during decompression-induced degassing, while the other is indicative of heating-induced breakdown of the amphibole triggered by their uptake into hot magmas prior to the onset of eruption. The combined evidence indicates that despite the complex and variable growth history of the remobilized crystal cargo, such crystals may be useful in constraining volcanic pre- and syn-eruptive processes and, when appropriate experimental data become available, their rates, which may be of the order of days to weeks.

Keywords: amphibole; reaction rim; pargasite; ascent time; arc magmatism

6.1. Introduction

Volcanic eruptions produce a range of eruptive styles from Plinian eruptive columns and pyroclastic density currents to effusive eruptions characterised by lava flows and dome growth. The rates of magma ascent play a crucial role in the style of eruption, and they are a function of the physical and chemical characteristics of the magma (density, viscosity, crystallinity, composition, pressure, and temperature), as well as the geometry of the conduit ([Lormand et al., 2020](#); [Mastin and Ghiorso, 2001](#); [Papale and Dobran, 1994](#); [Petrelli and Zellmer, 2020](#); [Pinkerton et al., 2002](#); [Rutherford, 2008](#); [Sparks et al., 2006](#); [Zellmer et al., 2016](#)). Slow ascent rates (cm/s to mm/s) are usually associated with effusive eruptions, while faster ascent rates result in explosive eruptions, typically attributed to gas exsolution from the magmas during syn-eruptive ascent in the conduit ([Rutherford, 2008](#)). Thus, constraining ascent rates provides critical insights into volcanic explosivity and helps inform hazard mitigation efforts.

Crystal textures and chemistry offer insight into magmatic processes and also reflect the stability conditions and in which minerals have crystallized, with deviation from these conditions resulting in mineral breakdown. Decompression driven dehydration, heating, oxidation, or fluxing of melt with CO₂-rich fluids may cause the breakdown of hydrous mineral phases like amphiboles ([De Angelis et al., 2015](#); [Rutherford and Hill, 1993](#)), and these textures can elucidate magmatic processes ([Browne and Gardner, 2006](#); [De Angelis et al., 2015](#); [Devine et al., 1998](#); [Garcia and Jacobson, 1979](#); [Plechov et al., 2008](#); [Rutherford and Devine, 2003](#); [Rutherford and Hill, 1993](#)). However, previous studies have been based on experimental data sets using specific melt and amphibole conditions; for example, dacite and hornblende from Mount St. Helens ([Rutherford and Hill, 1993](#)), and andesite and hornblende from Soufrière Hills, Montserrat ([Rutherford and Devine, 2003](#)).

The principal factors affecting amphibole stability are temperature, pressure, water content, and oxygen fugacity. Experiments involving natural samples form the basis to interpret the type of breakdown associated with changes in these parameters. Amphibole breakdown in calc-alkaline melts is usually attributed to heating ([Browne, 2005](#); [De Angelis et al., 2015](#); [Rutherford and Devine, 2003](#)), or isothermal decompression ([Browne and Gardner, 2006](#); [Buckley et al., 2006](#); [Nicholis and Rutherford, 2004](#); [Rutherford and Devine, 2003](#); [Rutherford and Hill, 1993](#)). Breakdown rims due to heating and decompression can have overlapping properties such as similar thicknesses of rims and sizes of microlitic breakdown products; however, the key differences are the type and abundance of pyroxene in the rims ([De Angelis et al., 2015](#); [Rutherford and Devine, 2003](#)). Experiments also indicate that the magnitude of instability (increase in temperature or rate of decompression) and melt properties play an important role in the development of breakdown products ([De Angelis et al., 2013](#); [De Angelis et al., 2015](#); [Nicholis and Rutherford, 2004](#)).

A range of amphibole breakdown classification schemes have been used in the literature, and the textures are summarized in Supplementary Figure S1. [Garcia and Jacobson \(1979\)](#) distinguished two types of reaction rims: (1) A black type in which amphibole is completely or partially replaced by fine-grained aggregates of Fe oxides and pyroxene, suggest syn- or post-eruption oxidation, and (2) a ‘gabbroic’ type in which amphibole is partially or completely replaced by fine- to medium-grained aggregates of orthopyroxene, clinopyroxene, plagioclase, and magnetite that develop in response to dehydration of the melt. [Murphy et al. \(2000\)](#) distinguished three types of reaction rims: (1) fine grained (5–30 µm), (2) coarse grained (30–200 µm), and (3) opaque replacing aggregates. [Rutherford and Devine \(2003\)](#) identified three populations of rim types in samples from the Soufrière Hills Volcano, Montserrat. Based on isothermal decompression experiments, (1) thin rims

were identified as being decompression-induced (1–20 μm); (2) thicker rims heat-induced (200–500 μm) and (3) aggregates of opaque minerals formed as a product of oxidation. [Plechov et al. \(2008\)](#) identified three kinds of breakdown textures: (1) volumetric decomposition was the term used for regions within the amphibole crystal where it was replaced by anhydrous mineral aggregates of plagioclase, clinopyroxene, and oxides owing to isobaric heating; (2) symplectic rims, which appear as intergrown streams of submicron mineral aggregates, as a result of late stage oxidation; and (3) granular rims of plagioclase, pyroxene and oxides in zones of varying proportions, which form because of a bi-metasomatic reaction between amphibole and melt. The variety of textural types and their interpretations indicate several processes may operate during amphibole breakdown, and that detailed study is required for each volcanic system to gain a better understanding of the particular processes involved in forming these breakdown products.

Amphibole crystals entrained in the effusive eruptions of Taranaki volcano, New Zealand, over the last 10,000 years have a range of compositions and breakdown textures. Here, we use these features to constrain magma storage and subvolcanic magma ascent processes. Textural and chemical features of the Taranaki amphiboles, together with their reaction products, inform the temporal development of shallow magma storage and source-to surface transport of magmas. It provides a conceptual model of late-stage magmatic processes, which may be applied to other composite andesite volcanoes. Challenges in constraining ascent timescales include determining the depth from where the ascent began, variations in ascent rates, and changes in the various parameters that affect amphibole stability.

6.2. Geological and petrological background

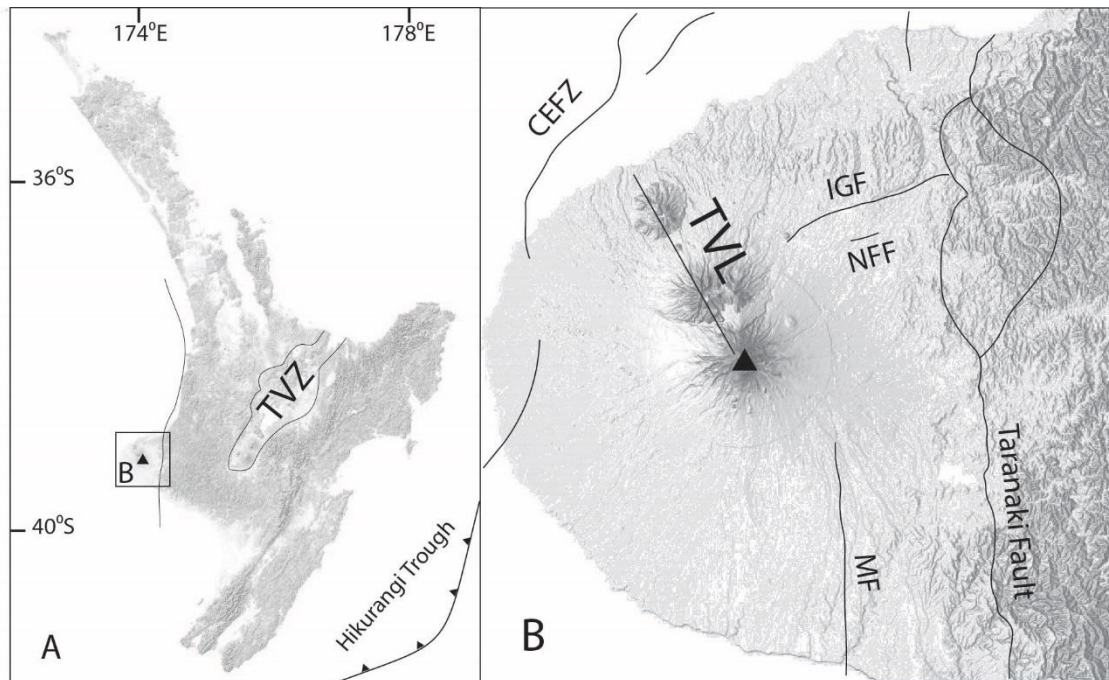


Figure 6.1 Location of Mt. Taranaki and the Taranaki Volcanic Lineament with respect to the North Island of New Zealand (inset) and the western peninsula, along with the Taupo Volcanic Zone (TVZ) and the Alexandria Lineament (AL). Triangles represent the three onshore volcanoes as well as Taranaki's satellite vent, Fathams Peak. Also identified are the major structural features of the Taranaki Peninsula CEFZ: Cape Egmont Fault Zone; IGF: Inglewood Fault; NFF: Norfolk Fault; MF: Manaia Fault (modified from [King and Thrasher, 1996](#); [Torres-Orozco et al., 2017a](#)).

The subduction of the Pacific Plate under the Australian Plate along the Hikurangi Margin dominates the tectonics of the North Island of New Zealand (Figure 6.1). The Taupo Volcanic Zone (TVZ) is the principal region of arc volcanism. Behind the arc, on the western peninsula of the North Island of New Zealand, four Quaternary volcanoes ranging in age from 1.75 Ma to present, collectively form the SSW trending Taranaki Volcanic Lineament (Fig. 1). These are the Sugar Loaf Islands and Paritutu (1.7 Ma), Kaitake volcano (90.57 Ma), Pouakai volcano (0.25 Ma), and Taranaki volcano (*c.* 200 ka–present) ([Neall, 1979](#); [Neall et al., 1986](#)). The near-symmetrical shape of the Taranaki volcano is interrupted by the satellite vent of Fathams Peak on its southern flank, also known as Panitahi.

Taranaki volcano, formerly known as Mt. Egmont, is located 400 km west of the Hikurangi Margin and 140 km west of the TVZ. Over the last 200k years of activity, Taranaki volcano has experienced at least 13 episodes of cone collapse and regrowth, with each collapse phase contributing to the large volume of debris avalanche deposits that form the surrounding ring plain ([Alloway et al., 2005a](#); [Procter et al., 2010](#); [Zernack et al., 2011](#)). Eruption products obtained from the present edifice ([Platz et al., 2006](#); [Stewart et al., 1996](#); [Torres-Orozco et al., 2017a](#); [Torres-Orozco et al., 2017b](#)) as well as studies of the ring plain deposits ([Damaschke et al., 2017b](#); [Platz, 2007](#); [Platz et al., 2006](#); [Turner et al., 2009a](#); [Turner et al., 2008a](#); [Turner et al., 2011b](#); [Zernack et al., 2011](#)) have revealed eruptions that ranged from explosive to effusive, generating volcanic products such as pyroclastic deposits, lava flows, and dome extrusions. Periods of quiescence are indicated by sediment and soil layers intercalated with the debris avalanche flows and extruded material ([Zernack et al., 2009](#)).

The volcanic products of Mt. Taranaki include tephras and lava flows. This study focuses on the recent (Holocene) lava flows of Taranaki as they best reflect the processes operating within the present-day subvolcanic plumbing system. The stratigraphic succession of the lava flow deposits is shown in Table 6.1 and Figure 6.2 ([modified from Stewart et al., 1996](#); [Zernack et al., 2012](#)) and is briefly summarised here. The first dated deposits at the present Taranaki cone are those of the Kahui block-and-ash flows and lahars (*c.* 13–8 ka), possibly representing a dome formation/collapse cycle ([Neall et al., 1986](#); [Torres-Orozco et al., 2017a](#)). The oldest lavas are the Warwicks Castle lavas (*c.* 8 kyr), the collapse of which (*c.* 7.5 ka) resulted in the Opuā debris avalanche deposit ([Neall, 1979](#); [Stewart et al., 1996](#); [Zernack et al., 2011](#)). The Peters lavas (7–3.3 ka)

Table 6.1: Stratigraphy of the Taranaki volcano modified from [Stewart et al. \(1996\)](#), [Platz et al. \(2012\)](#), and [Zernack et al. \(2012\)](#).

Chr.	Period	Episode	Primary Volcanics			Volcaniclastics		Cal. age	
			Lavas	Age(max.)	PF deposits	Tephras	LD		DAD
Maero		Pyramid	Pyramid Dome	0.2	P. rock avalanche	Pyramid L		0.16 0.2	
		Tahurangi	Fanthams 3	0.5–1.4	T. BAFs & surges	Tahurangi A Tahurangi B		0.2 0.3	
		Mangahume Burrell	Burrell Coulee/ Dome	<1.4	B. pumice flows B. BAF & surges	Mangahume L Burrell L Burrell B		0.4	
		Puniho			P. pumice flow P. BAF & surges	Puniho A Puniho B		0.4 0.4	
		Waiweranui			W. BAF & surges	Waiweranui A Waiweranui B		0.5 0.5	
		Newall			N. BAF & surges	Newall A Newall B			
			Minarapa Flows Skeet ridge Flows	<1.4 <1.4					
		Waingongoro				Waingongoro A		0.5	
		Te Popo			TP BAF & surges	Te Popo A Te Popo B		0.8	
		Hooker				Hooker L			
		Kaupokonui	Staircase Flows MacKays Flows Fanthams 2	3.3-1.4 3.3-1.4 3.3-1.4	BAFs, E-flank	Kaupokonui T		1.3 1.9	
		Maketawa	Beehives, The Dome, Skinner Hill	c. 3.3		Maketawa T	Te Popo DFD	3.1–2.9 3.4–2.9	
		Manganui	Fanthams 1	7–3.3		Manganui T		3.5–2.9	
					At least 3 PFDs	Inglewood T	Ngatoro DFD	3.9–3.7 4–3.9	
			Peters lavas	7–3.3		Korito T Mangatoki T Tariki T Waiopuku T	Warea 4 DF/HFDs DFD/HFD	7–3.3 4.6–4.4 5 5.4–5.3 6.1–5.7	
OPUAN		Kahui	Warwick Castle	>7	Oakura T	pum. HFD	Opuā 7.5 7.8		

were emplaced during a period of effusive activity, building the volcanic edifice ([Neall, 1979](#)). Fanthams Peak (*c.* 3.5–2.9 ka), erupted explosively and then effusively ([Torres-Orozco et al., 2017b](#)) emplacing both tephra deposits and lava flows ([Stewart et al., 1996](#); [Zernack et al., 2011](#)). It is believed to have been present from *c.* 7 ka based on the stratigraphy of overlying sediments (Stewart et al., 1996). Contemporaneously, the Skinner Hill, Beehives Dome, and The Dome were emplaced as lava domes on the lower flanks of the edifice ([Grant-Taylor, 1964](#); [Neall, 1971](#); [Platz et al., 2012](#)). The Staircase and Skeet lavas (1.6–1.3ka) erupted from the summit cone and partially filled the amphitheatre caused by the Opuā collapse bifurcate around Fanthams Peak ([Downey et al., 1994](#); [Stewart et al., 1996](#)). Correlated block-and-ash flows and surge deposits (Newall, Waiweranui, Puniho) indicating dome-forming effusive and minor explosive activity are believed to have been deposited between 1.6 and 1.1 ka ([Druce, 1966](#); [Neall et al., 1986](#)). This was followed by the pumice tephra of the Burrell eruption (*c.* AD 1655; [Druce, 1966](#)), the Taurangi event (*c.* AD 1755; [Druce, 1966](#); [Neall, 1972](#)), and the extrusion of the Burrell dome (*c.* AD 1800) inside the summit crater ([Platz et al., 2012](#)).

Geochemically, Taranaki eruptive products have been classified as andesites ([Downey et al., 1994](#); [Gow, 1968](#)), with minor basalts ([Neall et al., 1986](#)) and dacites ([Stewart et al., 1996](#)). A petrographic distinction is seen between the products of the main and satellite vent, with satellite vent eruptives being more mafic, evidenced by a greater amount of modal olivine and pyroxene. The crystal assemblage in Taranaki lavas is dominated by plagioclase, clinopyroxene, oxides, and hornblende, with rare orthopyroxene and olivine. [Stewart et al. \(1996\)](#) suggested that most phenocrysts are of antecrystic origin, i.e., picked up by the host melt from other regions of the same magmatic system. This was based on mineral geochemistry and disequilibrium between minerals and melt. Glomerocrysts are common and contain clinopyroxene, titanomagnetite, and plagioclase, with rare

orthopyroxene, hornblende, and olivine (Stewart, 2010). The groundmass of lava samples is rich in microlites, which are predominantly plagioclase displaying normal zoning. Also present are clinopyroxene microlites, Fe-Ti oxide microlites, interstitial glass, with rare orthopyroxene, olivine, and amphibole, whereas apatite and zircon are accessories (Stewart, 2010; Stewart et al., 1996).

6.3. Materials and methods

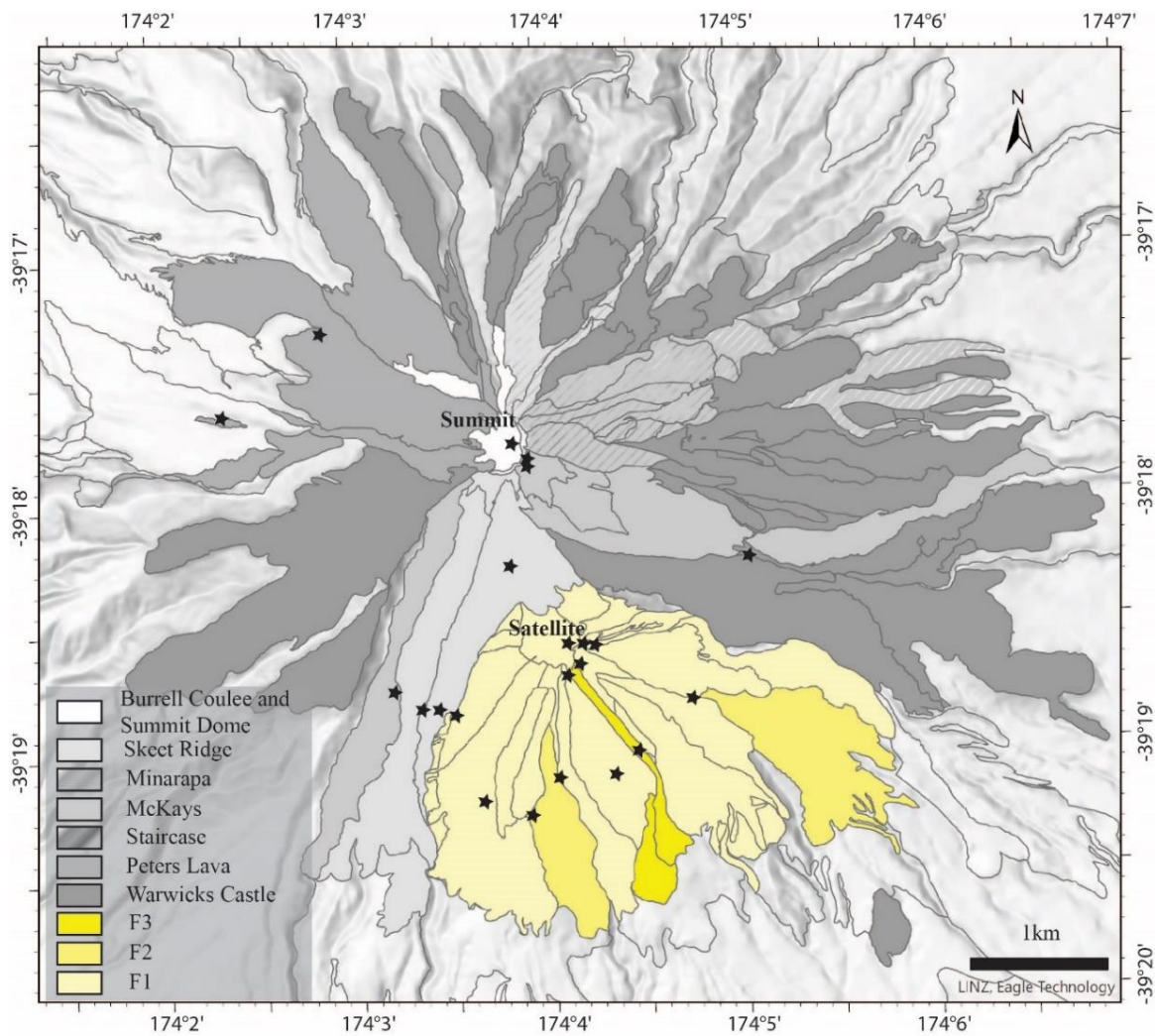


Figure 6.2 Map showing the Holocene lava flows that form the current day edifice of Taranaki. The yellow shades represent the satellite vent eruptives and the grey shades represent the summit eruptives. Star symbols represent sample locations for this study.

This study used multiple samples from different eruptive phases of the present cone. Representative samples from the Warwicks Castle Group, MacKays Lavas, Skeet Ridge Flows, Burell Coulee, and Dome from the summit vent and the three lava flows from Fanthams Peak (F1, F2, and F3) were selected. Also represented are samples from another vent under the Rangitoto Flat that appear to be older than Fanthams eruptives and the mafic lavas of Turehu Hill (Figure 6.2). We have studied 270 amphibole crystals in 24 samples representing variations in composition, vesicularity, source vent, and age (supplementary material). The samples range from dense lavas to scoria samples.

6.3.1. X-ray fluorescence

Unaltered samples of lava flows from Mt. Taranaki were cleaned in an ultrasonic bath and dried in an oven at 100°C overnight. The samples were ground using a tungsten carbide mill and approximately 10 g were left in an oven for 2 hours. Loss on ignition (LOI) was calculated from the difference in weight of *c.* 2 g of the sample before and after being placed in a muffle furnace at *c.* 900°C for 3 h. Fused glass discs were prepared by mixing 0.8 g (± 0.0010 g) of sample powder with 8.000 g (± 0.0010 g) of lithium tetraborate: lithium metaborate (12:22) X-ray flux, followed by fusing with an XRFuse2 electrical fusion apparatus at Massey University. Glass discs were then analysed for major element concentrations using a Bruker S8 Tiger Series II WD-XRF Spectrometer at Massey University. Oreas 24b and Oreas 24c Certified Reference Materials (CRM) were used as secondary standards. Interference-corrected spectra intensities were converted to oxide concentrations using calibration curves comprising natural standards, closely approximating the mafic matrix of our samples. The long-term reproducibility of Oreas standard reference materials is better than $\pm 1\%$ relative (1σ) for all oxides except MnO (*c.* $\pm 1.5\%$ relative, 1σ).

6.3.2. Backscatter imaging

Backscatter electron images were collected using an FEI Quanta 200 scanning electron microscope at Massey University. Images were acquired using a 20 keV accelerating voltage and a 10 mm working distance. Pyroxenes and amphiboles were distinguished using the Genesis EDAX software and the relative counts per second (cps) of Ca, Al, and Mg. Images were then imported into ImageJ and adjusted for contrast and brightness, and the colour threshold tool was used to determine the area percentage of vesicles. BSE greyscale images were used to identify mineral phases of submicron microlites of the breakdown products.

6.3.3. Electron probe microanalysis

Amphibole major-element compositional data were obtained using a JXA-8230 SuperProbe electron probe microanalyser at Victoria University of Wellington. Analysis was conducted with a focused (1–5 μm) beam, at 20kV accelerating voltage and 10 nA beam current. Data were collected at 10–100 μm intervals along rim-to-rim or core-to-rim transects, depending on the size of the phenocryst. Amphibole breakdown regions with microlites larger than 5 μm were selected using BSE imaging and were spot analysed using EPMA to identify the mineral phases. The small size of individual microlites of the reaction rims (< 3 μm) made a dependable quantitative determination of major oxides impossible. Defocussed beams of 30 μm diameter were used to analyse the average opacite reaction rims (when rims were thick enough) and the groundmass compositions for some samples. Calibration standards used were silicate mineral phases and oxides from [Jarosewich et al. \(1980\)](#).

EPMA maps were created at the Institute of Earth Sciences, Academia Sinica in Taipei, Taiwan using a JEOL JXA-8900R electron probe microanalyser with four wave-length

dispersive spectrometers (WDS). An acceleration voltage of 15kV and a beam current of 50 nA was applied. The beam diameter was 2 μm with a pixel size of 5 μm square. The dwell time was 20 ms. These maps were used to determine the mineral phases of coarse reaction rims (Appendix C). We encountered difficulties with mass balance calculations for amphibole and reaction rim compositions. Mass balance requires compositional data for both the host amphibole and all reaction rim microlite phases present.

6.3.4. Electron backscatter diffraction analyses

To measure the true thicknesses of the reaction rims and to correct for intersectional artefacts, electron back scatter diffraction was employed to determine the orientation of the crystal grains. Electron backscatter diffraction (EBSD) data were collected at the University of Otago using an HKL INCA Premium Synergy Integrated EDS/EBSD system (Oxford Instruments) mounted on a Zeiss Sigma VP Field Emission Gun-SEM ([Prior et al., 1999](#)). Thin-sections were polished to 0.3 μm using aluminium oxide powder before the acquisition of EBSD data. Working conditions were an acceleration voltage of 30 kV, an aperture of 120 μm , 70° sample tilt, and high vacuum mode. The step size dependent on the size of the crystal (3 μm to 10 μm). The *Channel 5* software was used for post-acquisition data processing. Reaction rims were also analysed using EBSD, but high-resolution orientation data could not be obtained owing to the small microlite size.

6.3.5. Calculation of true thickness of reaction rims

The BSE images were enhanced for brightness and contrast using Fiji ImageJ software. Crystal face Miller indices were determined by measuring the strike of the crystal face and tracing the corresponding pole position on the stereonet plotted by the *hkl Channel 5 mambo* software. The angle of dip (θ) of the face was then measured from the stereonet projection. Apparent rim thicknesses were measured from the BSE images. For each

reacted amphibole, three measurements (maximum, minimum, and random) were taken for each crystallographic face using the ImageJ measure tool. The average apparent thickness (A) of the rim along a given crystal face was used to calculate the true thickness (T) using the formula $T = A / (1 + |\tan(\theta + 90^\circ)|)$. Errors associated with this method include observational bias during stereoplot measurements, natural crystal imperfections, and lack of clear crystal boundaries in some crystals, as well as number and sites for apparent rim thickness measurements along crystal faces (rims are thicker at crystal edges). We estimate typical uncertainties in rim thickness of *c.* $\pm 10\%$ relative.

6.3.6. P-T conditions

Stability fields of Taranaki amphiboles were calculated by employing thermobarometers that use amphibole compositions only. Calculations were done using the WinAmptb software ([Yavuz and Döner, 2017](#)), and the thermobarometers of [Ridolfi and Renzulli \(2012\)](#) and [Putirka \(2016\)](#) were employed. Volumetric decomposition temperatures were constrained using the two-pyroxene thermometer of [Putirka \(2008\)](#). The orthopyroxene and clinopyroxene were selected from the same decomposed amphibole crystal of sample L18, where the pyroxenes were big enough to determine their composition dependably.

6.4. Results

6.4.1. Whole rock and melt chemistry

Whole-rock compositions of the 24 Taranaki eruptives studied here range from basalts to trachyandesites based on the total alkali vs. silica (TAS) classification of ([Le Maitre, 2002](#)), rather than andesites *sensu stricto* (Figure 6.3). Groundmass compositions, determined on every second sample, are significantly enriched in silica and alkalis ($\text{Na}_2\text{O} + \text{K}_2\text{O}$) and range from basaltic trachyandesites to trachytes. Among the samples

analysed, basaltic lavas are found from both the summit and satellite vents, but trachyandesitic samples dominate the summit lavas.

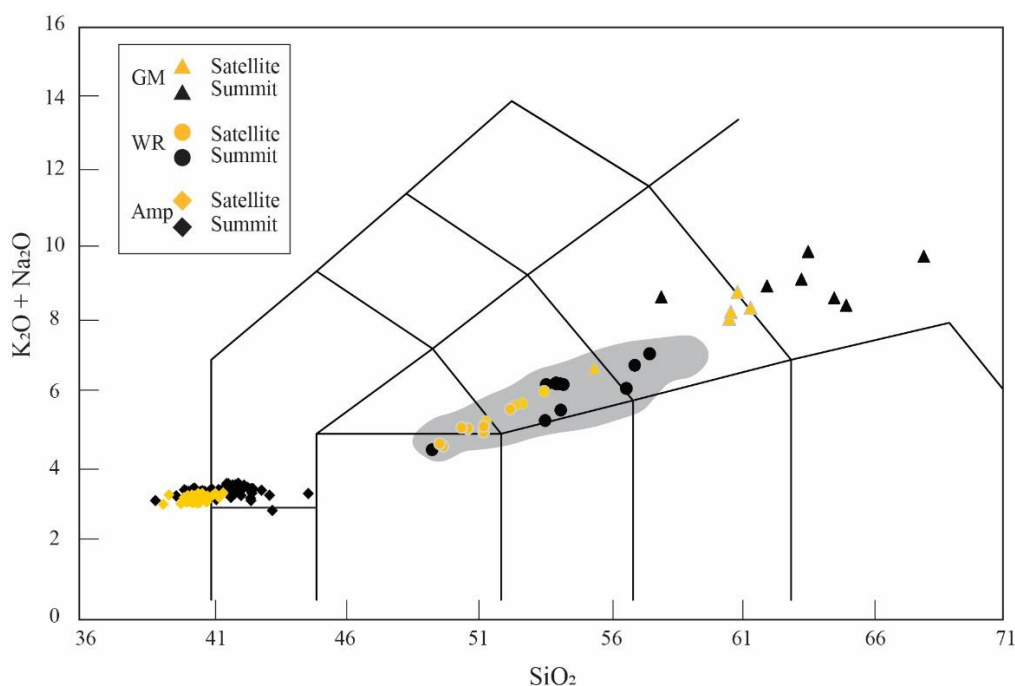


Figure 6.3 Geochemical classification according to [Le Maitre \(2002\)](#) of whole rocks, groundmasses, and amphiboles of Taranaki. The shaded region encompasses the whole rock composition of Taranaki lavas from literature ([Stewart et al., 1996](#); [Zernack et al., 2012](#)).

6.4.2. Petrographic observations and mineral chemistry

Taranaki lavas are crystal-rich rocks, containing ‘phenocrysts’, microphenocrysts, and numerous microlites in the groundmass. The term ‘phenocryst’ is used here purely in a grain size sense for crystals exceeding 300 μm , ‘microphenocrysts’ for crystals ranging from 300 down to 30 μm and microlites for those < 30 μm in size. The relative abundances of the mineral phases were calculated using the area percentage of each phase in photomicrographs taken at $\times 2.5$ magnification. The principal mineral phases are (in order of abundance) plagioclase, clinopyroxene, and oxides. Amphibole abundance varies between samples of different lava flows and is rarely seen in association with olivine. Orthopyroxene and apatite are rare phases. Amphibole and olivine abundance are

inversely correlated. The groundmass is microlite-rich and dominated by plagioclase, clinopyroxene, and oxides with rare orthopyroxene and amphibole.

Feldspar (Figure 6.4a) is the most common phase (30–45%), dominated by plagioclase (An_{92} – An_9) with rare anorthoclase of up to Or_{30} forming crystal rims. At least two distinct plagioclase populations are reported: larger crystals displaying patchy cores and sieve texture, and smaller pristine, euhedral crystals. Most plagioclases have An-rich cores and An-poor rims, with the rim chemistry of phenocrysts corresponding to the composition of smaller crystal populations. Plagioclase microlites are also normally zoned. Clinopyroxene (Fig. 4b) is the second most abundant phase (12–20%), and the phenocrysts are present as euhedral, zoned crystals. Most crystals are identified as diopside with rare augite.

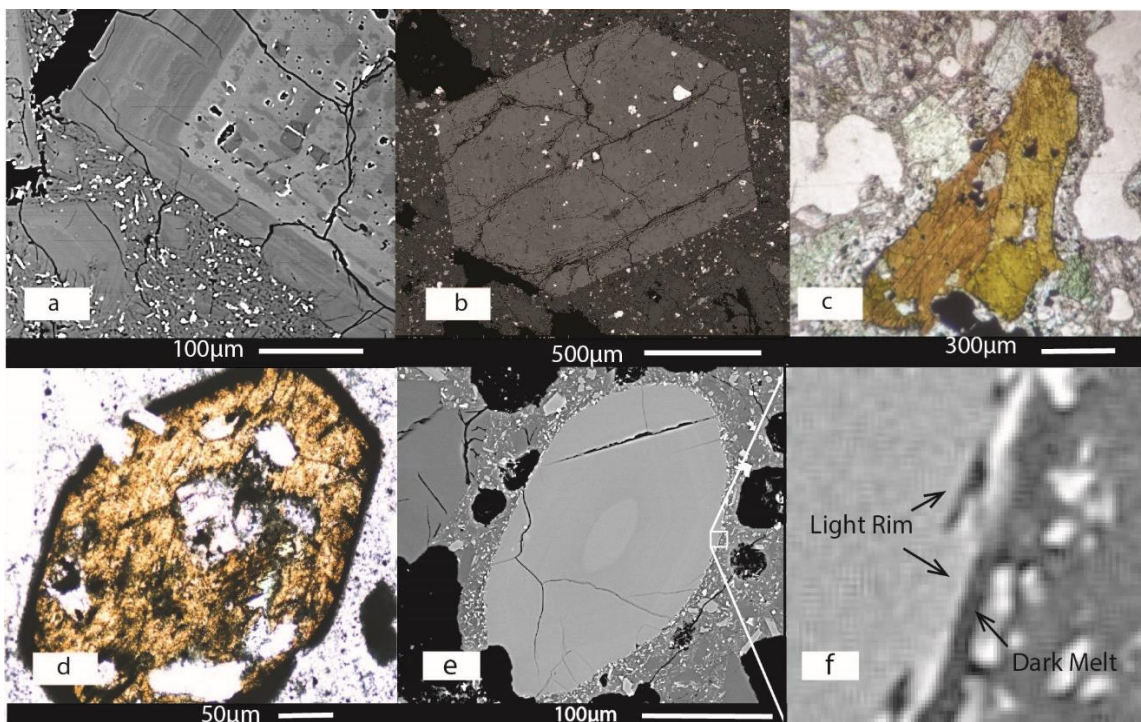


Figure 6.4 Petrographic images of Taranaki crystal assemblage (a) SEM image of plagioclase showing zoning and sieve texture. (b) SEM image of euhedral clinopyroxene with oxide inclusions. (c, d) Amphiboles showing reaction rims in plane polarised light images; (e) rounded amphiboles showing internal zoning; (f) zoomed-in image of the amphibole rim showing greyscale zoning as a result of reaction between crystal and melt.

Oxides (Figure 6.4b) in Taranaki samples makeup 2–5% and are present in the groundmass or as inclusions in pyroxene and amphibole phases. They are mostly titanomagnetites with rare ilmenite. Rare inclusions of chalcopyrite are seen. Feldspars, clinopyroxene, and opaques are abundant in the groundmass and as breakdown products of amphibole. Amphibole phenocryst abundances vary between samples and are discussed in the following section. Orthopyroxene and olivine are not common and when present, olivine crystals are anhedral with thick corona rims. Orthopyroxene is present as a dominant mineral in coarse reaction rims of amphiboles.

Table 6.2: Normalised major element oxide concentrations for the amphibole samples in this study.

Sample	SiO ₂	Al ₂ O ₃	TiO ₂	MgO	FeO	MnO	CaO	Na ₂ O	K ₂ O	Cr ₂ O ₃
ES3.1	42.07	13.38	2.55	14.66	11.52	0.17	12.20	2.30	1.12	0.01
ES3.2	41.93	13.16	2.72	14.44	12.09	0.18	12.05	2.30	1.12	0.00
ES3.3	42.11	13.49	2.58	14.05	12.04	0.17	12.20	2.28	1.06	0.01
ES5.1	40.79	14.62	2.88	14.26	11.61	0.13	12.26	2.42	1.02	0.01
ES5.2	41.04	14.08	2.76	13.71	12.63	0.16	12.19	2.42	1.00	0.00
L16.1	41.12	13.66	2.44	13.26	13.56	0.23	12.44	2.39	0.88	0.01
L16.2	40.89	14.19	2.57	14.16	12.30	0.15	12.38	2.37	0.98	0.01
L18.1	41.25	13.35	2.66	13.56	13.23	0.25	12.20	2.47	1.00	0.01
L18.2	42.49	11.64	3.54	13.66	13.21	0.32	11.47	2.43	1.22	0.01
L21.1	42.35	12.53	3.14	15.07	11.13	0.21	12.11	2.41	1.06	0.00
L21.2	41.99	12.41	3.41	14.76	11.67	0.22	12.01	2.45	1.07	0.00
L21.3	41.96	12.98	2.70	14.62	11.79	0.14	12.41	2.32	1.07	0.01
L21.4	42.60	11.89	3.29	14.81	11.77	0.25	11.91	2.40	1.09	0.01
ES7.1	41.55	14.39	2.18	15.48	10.38	0.09	12.61	2.30	0.99	0.02
ES7.2	41.67	13.53	3.08	14.30	11.88	0.21	11.94	2.51	0.85	0.02
L5.1	41.78	13.19	3.23	13.91	12.25	0.22	12.04	2.51	0.85	0.01
PYR1	43.00	11.39	3.49	14.72	11.95	0.29	11.68	2.55	0.91	0.01
L7.1	41.68	14.38	2.43	14.51	11.06	0.12	12.54	2.35	0.93	0.00
L7.2	41.63	14.30	2.31	14.84	11.00	0.11	12.50	2.45	0.81	0.04
FPD1	41.11	14.73	2.04	14.95	10.94	0.10	12.72	2.24	1.16	0.01

6.4.3. Amphibole

Amphiboles are the third most abundant silicate phase in Taranaki rocks and vary in abundance from 0% to 7%. Variations are seen within the same lava flow units, with some

samples showing numerous amphiboles while others show few to no crystals. The crystals are usually subhedral with rounded crystal edges, and crystal sizes range from $< 30 \mu\text{m}$ to $> 2 \text{mm}$.

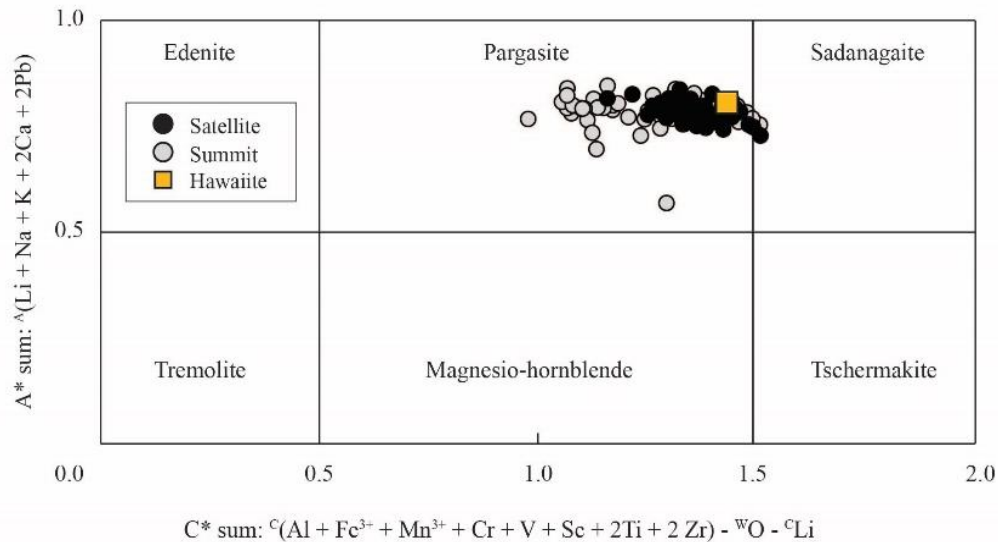


Figure 6.5 Mineral chemistry of amphiboles of Taranaki according to the [Hawthorne et al. \(2012\)](#) classification, from the summit and satellite. Comparison of amphibole sample from hawaiiite rocks from the Crater Flat volcanic zone near Yucca Mountain, Nevada ([Nicholis and Rutherford, 2004](#)).

In transmitted light, they are pleochroic in shades of brown. They usually contain inclusions of plagioclase and oxides. Occasionally, pseudomorphs of replacement anhydrous minerals (cpx, opx, pl, ox) are seen. Most of the amphiboles in Taranaki samples possess rims that either appear black in plane polarised light (Figure 6.4c) or thicker, crystalline rims (Figure 6.4d), although rimless amphiboles dominate other samples (Figure 6.4e).

Amphibole chemistry (Table 2) reveals that the amphiboles are rich in CaO (11–13%) and are almost exclusively pargasites (Figure 6.5) ([Hawthorne et al., 2012](#); [Locock, 2014](#)). A positive correlation is seen between Al_2O_3 and CaO with inverse correlations between Al_2O_3 and SiO_2 , MnO, and TiO_2 as shown in Figure 6.6. This variation in compositions is observed between crystals of different lava flows as well as within the

individual crystals from the same sample. Complex zoning in BSE images is attributed to compositional variation in major elements including SiO_2 , Al_2O_3 , FeO , and MgO (see Figure 6.4e). Darker regions correspond to Mg and Si enrichment, while the brighter regions correspond to Al, Fe, Ti, Na, and K enrichment.

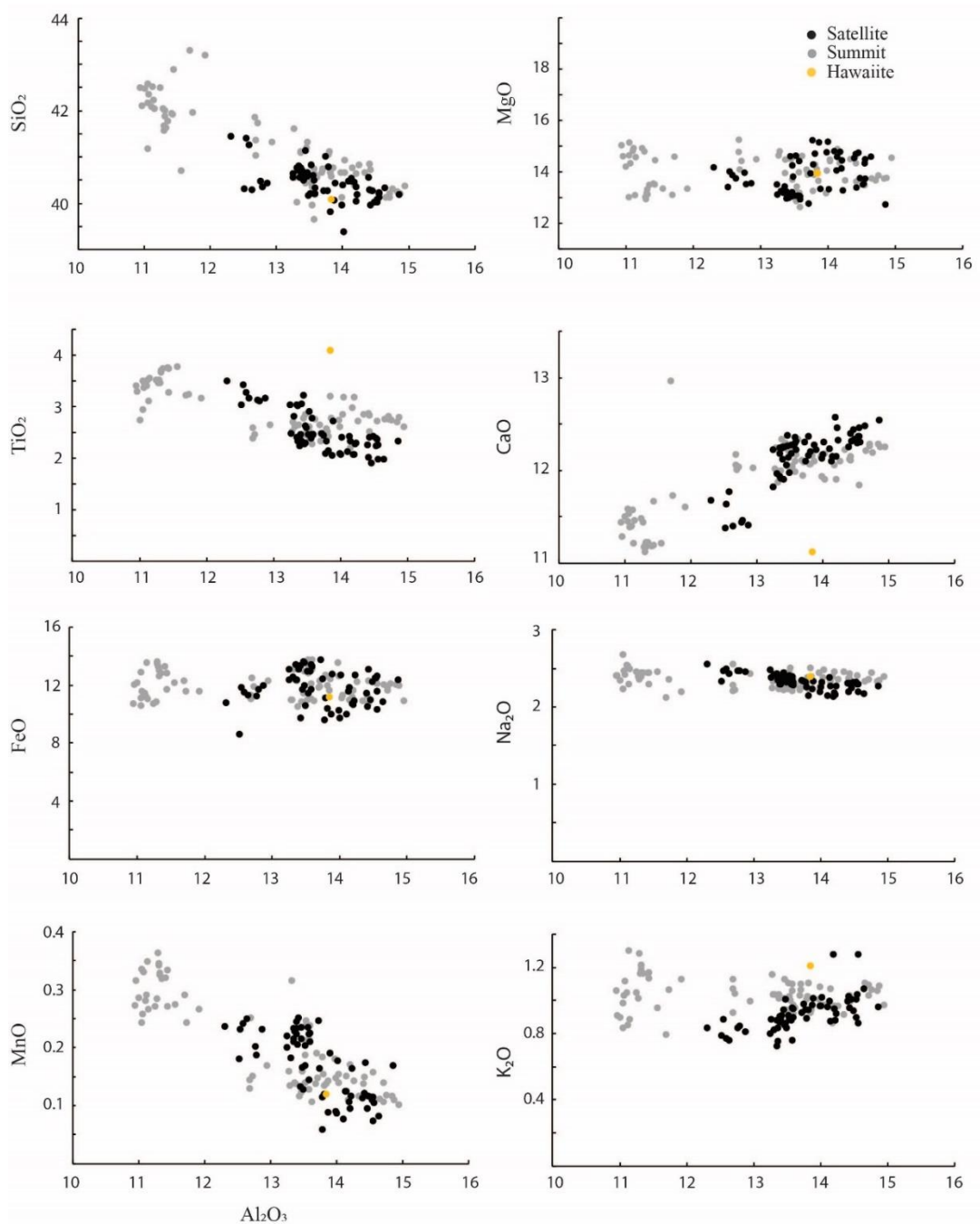


Figure 6.6 Binary plots of oxide compositions of Taranaki amphiboles in comparison to the natural composition of amphibole from the Crater Flat volcanic zone near Yucca Mountain, Nevada (Nicholis and Rutherford, 2004).

6.4.4. Breakdown textures

The predominant feature of most of the amphiboles from Taranaki lavas is the presence of breakdown textures, forming reaction rims or volumetric breakdown. Textural details of these features are provided below and summarized in Figure 6.7, and breakdown in each sample is illustrated in Figure 6.9.

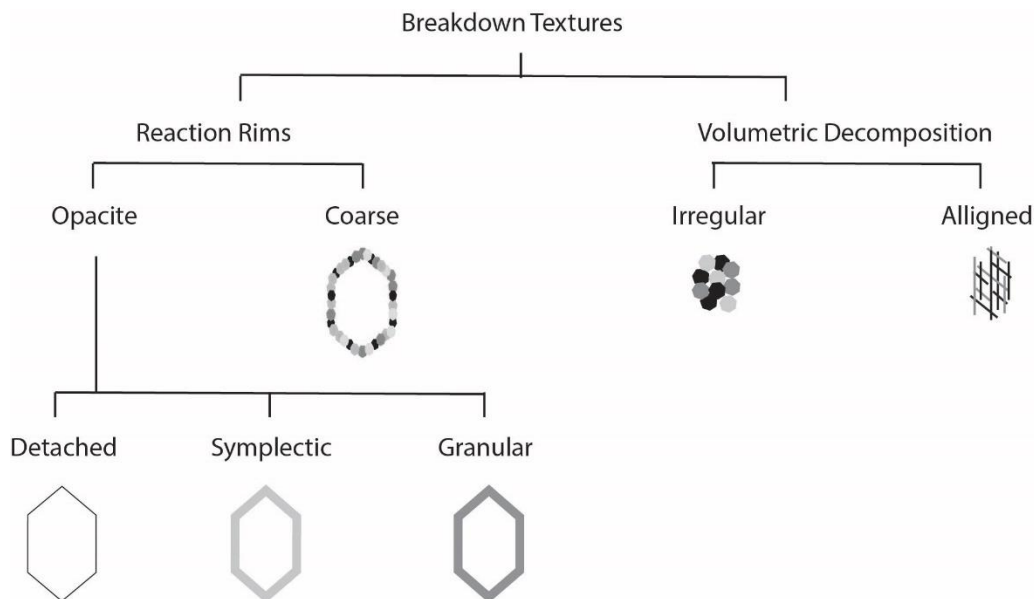


Figure 6.7 Summary diagram of the types and appearance of the breakdown products seen in Taranaki

6.4.4.1. *Reaction rims*

The most common reaction rims observed in Taranaki amphiboles are ‘opacite’ rims (Plechov et al., 2008). They appear black in plane polarised light, and when present, they usually are present in all cross-sections of the crystals. An exception is seen in sample L18, where the reaction rim forms on select faces/portions of faces. Based on the classification of Plechov et al. (2008), the opacite rims were divided into ‘granular’ and ‘symplectic’ and further classified based on oxide content as ‘oxide-poor’ and ‘oxide-rich’.

Pyroxene detached rims and coarse-grained reaction rims are seen along with these rims.

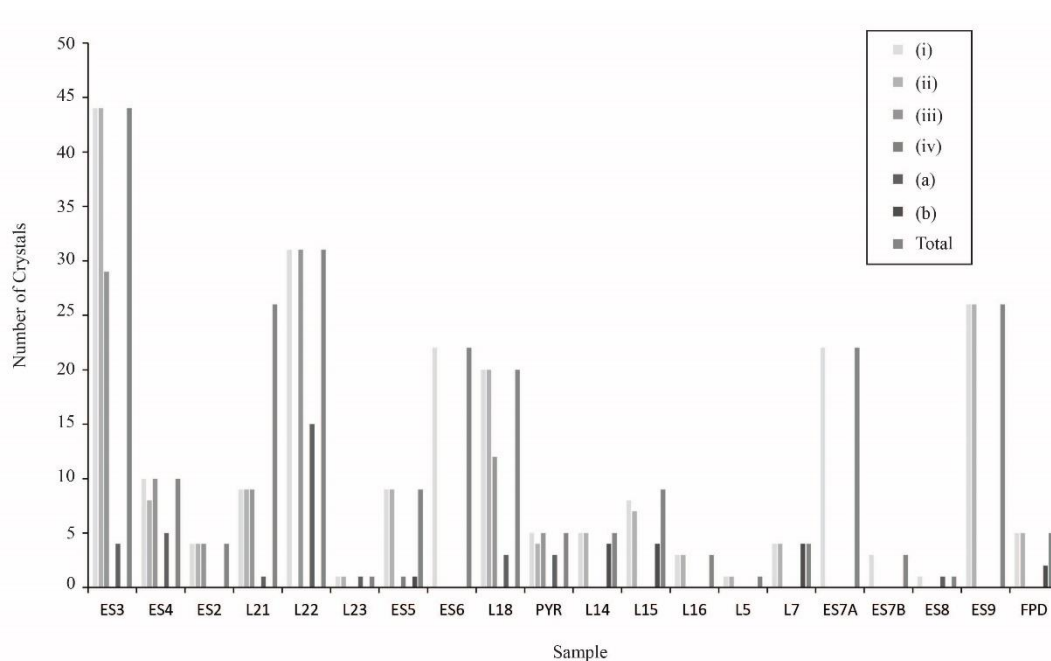


Figure 6.8: Graphical representation of the types of rims and their abundance for each sample considered for this study.

The reaction rim types observed in Taranaki amphiboles are:

- (i) Detached Rims: pyroxene grains (typically *c.* 1 μm , rarely $>$ 3 μm) that appear to be floating in the melt and are usually oriented parallel to sub-parallel to the crystal faces of the original amphibole (Figure 6.9 a,b). These rims are approximately 1–10 μm thick and are the outermost reaction rim.
- (ii) Symplectic rims: interlaced streams of plg + px + ox that ‘flow’ perpendicular to the crystal face and are most common (Figure 6.9 b,c). The submicron size of the microlites makes it difficult to identify the silicate phases using EPMA data. These rims usually occur closest to the amphibole mineral phase, between the amphibole and melt; and are absent when the crystal is not in contact with the melt. Symplectic rims are thicker at crystal edges when compared to along the face (Figure 6.9c).

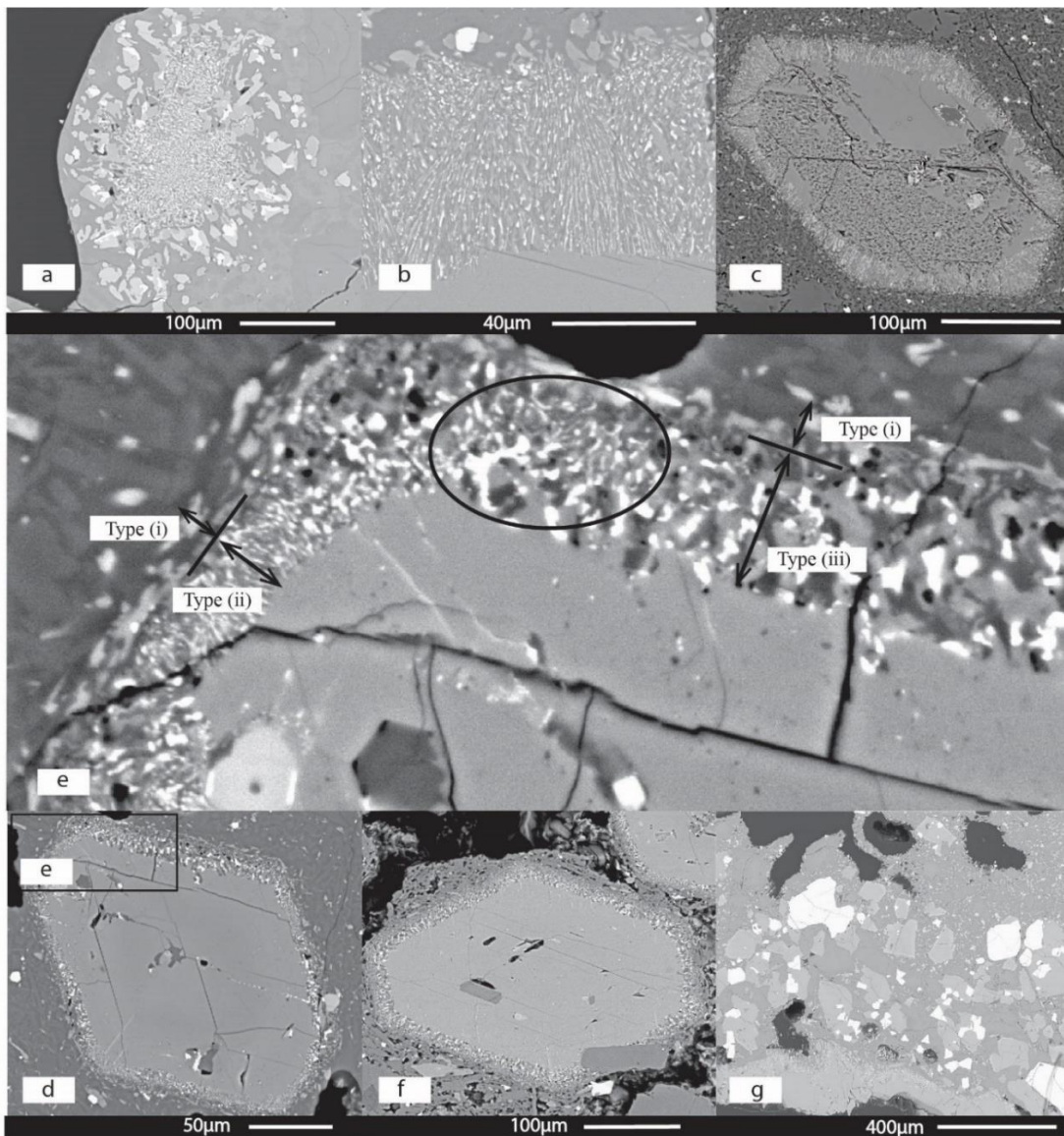


Figure 6.9 Variation in amphibole reaction rim types seen in Taranaki eruptives : (a) L23 thick detached rims and breakdown with no amphibole core; (b) L16 symplectic rim showing elongated mineral phases interlaced perpendicular to the crystal phase; (c) L21 amphibole showing thicker rims at crystal edges; (d) ES3 euhedral amphibole with a zoomed view of the reaction rim; (e) different type of rims and their relation to each other, yielding co-existence of symplectic and granular rims on the same crystal as well as intergrowth of different types of rims indicated by the ellipse ; (f) L22 showing the absence of reaction rims when the amphibole is in contact with another mineral phase and not the melt; (g) coarse reaction rims seen in ES5 with large grains of pl, opx, cpx and oxides

Based on oxide abundance and grain size, they are further classified as (a) oxide-poor, and (b) oxide-rich. The proximity of the oxide-rich zone to the crystal face changes between samples, while in other cases the oxides are homogeneously

distributed. The symplectic rims show lower concentrations of SiO₂ and higher Na₂O and K₂O as compared to the amphibole (Table 6.3).

Table 6.3: Comparison of amphibole (A), reaction rim (RR) and melt compositions (M)

Sample	SiO ₂	Al ₂ O ₃	TiO ₂	MgO	FeO	MnO	CaO	Na ₂ O	K ₂ O	Cr ₂ O ₃	Total
L21 A	42.31	12.50	3.13	14.99	11.27	0.20	12.11	2.41	1.06	0.00	100
L21 RR	42.62	11.59	3.03	11.24	18.44	0.49	10.94	1.46	0.18	0.01	100
L21 M	64.37	17.40	0.65	1.64	2.79	0.12	3.70	4.89	4.44	0.01	100
L18 A	42.43	11.90	3.00	13.80	12.99	0.30	12.18	2.34	1.06	0.01	100
L18 RR	41.31	12.00	3.00	13.59	18.07	0.45	10.00	1.40	0.18	0.01	100
L18 M	64.39	17.27	0.86	0.85	3.67	0.10	2.82	4.85	5.19	0.01	100
L16 A	41.01	13.93	2.50	13.71	12.93	0.19	12.41	2.38	0.93	0.01	100
L16 RR	40.21	13.34	2.65	13.12	17.01	0.37	11.69	1.45	0.16	0.01	100
L16 M	61.65	19.07	0.57	1.42	2.92	0.12	5.81	5.09	3.34	0.01	100
ES5 A	41.14	14.21	2.80	14.24	11.90	0.15	12.21	2.37	0.98	0.01	100
ES5 RR	39.74	12.55	2.83	14.55	17.97	0.33	10.25	1.61	0.16	0.01	100
E5 M	58.48	17.97	1.00	2.05	6.32	0.14	5.25	4.96	3.81	0.01	100
ES3 A	42.17	13.26	2.56	14.11	11.85	0.18	12.63	2.22	1.02	0.01	100
ES3 RR	43.18	12.64	2.90	10.62	17.37	0.47	11.02	1.60	0.20	0.00	100
ES3 M	67.95	16.55	0.37	0.77	2.03	0.07	2.45	4.59	5.20	0.01	100

- (iii) Granular rims: Observed in only two samples, granular rims have anhedral aggregates of pl + px ± ox (> 1 μm) (Figure 6.9d–f). When present, these rims have an (a) oxide-poor outer zone and (b) oxide-rich inner zone. In rare cases, these rims also form along the cleavage planes and fractures of the amphibole crystals. In cases where both granular and symplectic rims coexist, the granular rims replace portions of the symplectic rims along crystal faces, prefer certain crystal faces, or occur along cleavage planes/fractures (Figure 6.9e). Rims are absent when the amphibole is in contact with another mineral phase and not the melt (Figure 6.9f).
- (iv) Coarse rims: thick reaction rims (> 300 μm) that comprise pl+ px + ox (> 50 μm). These rims are only observed in 3 crystals of one sample (ES 5) (Figure 6.9g).

6.4.4.2. Volumetric decomposition

Another common breakdown feature seen in Taranaki amphiboles is regions of volumetric decomposition ([Plechov et al., 2008](#)), where amphibole is replaced by aggregates of pl, px, and ox within the crystal (Figure 6.10). These regions can touch or transect the reaction rim or be contained within the crystal grain, with no apparent contact with the groundmass. Based on the mineral phases present and their orientation, we divided the volumetric decomposition into two types: irregular and aligned, which do not co-exist.

- A. Irregular: Subhedral to anhedral grains of pl + px + ox occupying regions within the amphibole crystal. They may or may not touch the reaction rims and vary in area within samples (Figure 6.10a).
- B. Aligned: Euhedral, elongated grains in areas bounded by cleavage and fracture planes with crystals of pl + px (rare oxide) (Figure 6.10b). In some samples, a complete replacement of the amphibole is observed, with an outer opacite rim around fully decomposed amphibole (Figure 6.10c). These decomposition regions can also form zones between the opacite rims and the amphibole remnant (Figure 6.10d). These aligned crystals retain the crystallographic orientation of the original amphibole, as demonstrated by EBSD analysis seen in Figure 6.10e, f. This orientation is seen preserved in the clinopyroxenes (monoclinic system).

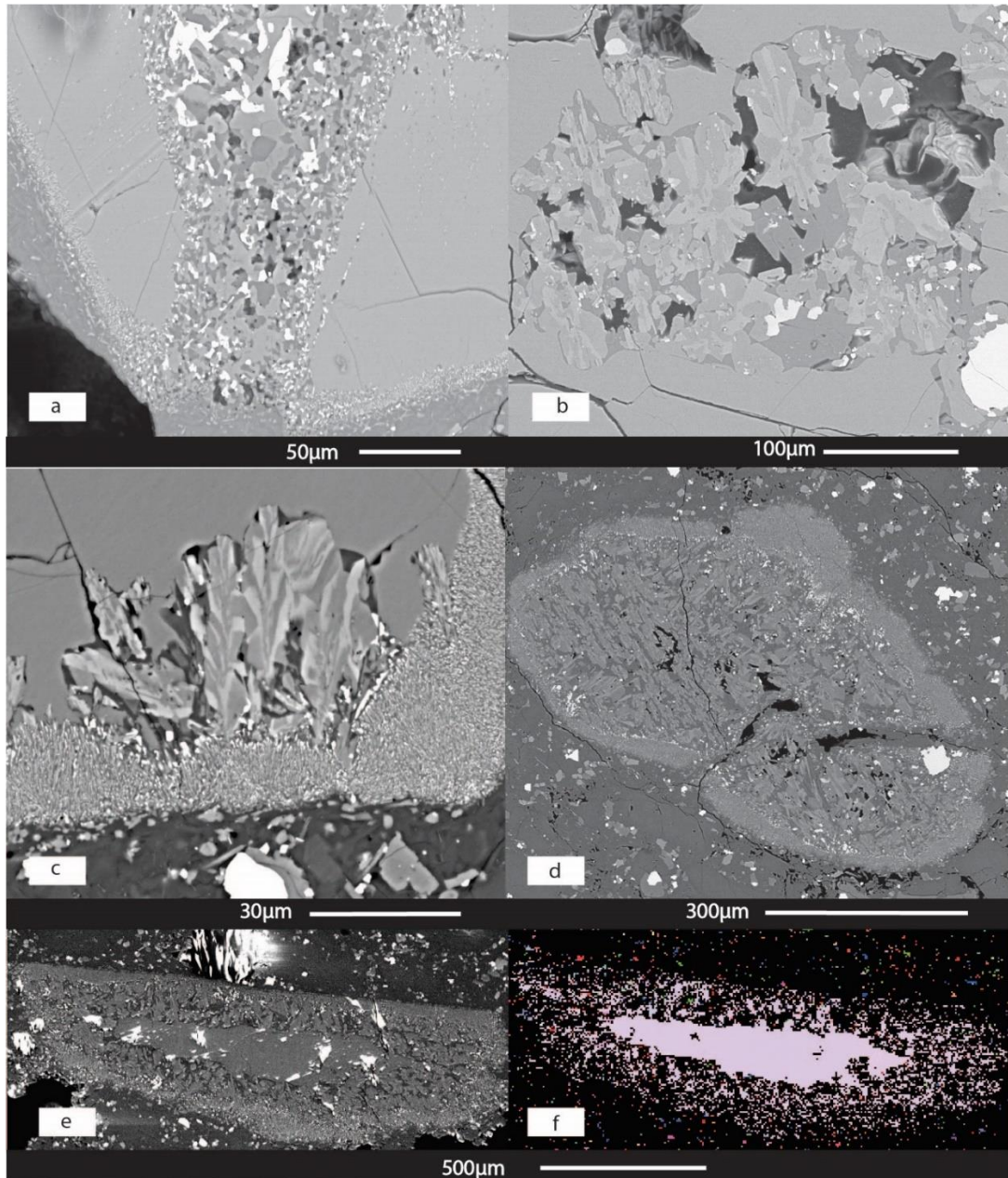


Figure 6.10 Volumetric decomposition as a result of amphibole breakdown. (a) ES3 regions of irregular volumetric decomposition occupying a fracture in amphibole crystals; (b) L26 oxide poor, aligned cpx and pl in amphibole decomposition; (c) L15 reaction rims associated with complete volumetric breakdown of the crystal; (d) L7 aligned volumetric decomposition crosscutting symplectic rims; (e) L7 original amphibole mantled by aligned volumetric decomposition and symplectic rims, and (f) corresponding EBSD imaging showing retained alignment of replacement minerals.

6.4.4.3. *Rimless amphiboles*

Rounded amphibole crystals that are devoid of inclusions and evidence of volumetric decomposition are the exclusive amphibole population in some samples (ES7A/B, ES6).

Their internal oscillatory zonation is euhedral, as seen in the high contrast images Figure 6.4e. They are typically surrounded by what appear to be detached rims in association with oxides (Figure 6.4f).

Table 6.4: Reaction rim thicknesses of amphiboles sampled. (i) = detached; (ii) = symplectic (iii) g= granular; (iv) = coarse reaction rims; (a) irregular; (b) = aligned volumetric decomposition. # = number of amphiboles in the sample

	Flow	Sample	Lithology	#	Breakdown Type and Thickness					
					(i)	(ii)	(iii)	(iv)	(a)	(b)
Summit	Tholoid	ES3	Trachyandesite	44	4.32	7.84	11.6		x	
	Tholoid	ES4	Trachyandesite	10	4.18	14.47	10.9			x
	Skeet Ridge	ES2	Basaltictrachyandesite	4	5.86	31.14				
	Skeet Ridge	L21	Basaltictrachyandesite	26	4.71	18.89				
	Skeet Ridge	L22	Trachyandesite	31	1.42	18.29				x
	Skeet Ridge	L23	Trachybasalt	1						
	McKays Flows	ES5	Basalt	9	2.69	7.14		421.8		x
	McKays Flows	ES6	Basaltictrachyandesite	22	2.35					
	McKays Lavas	L18	Basaltictrachyandesite	20	10.16	12.11				
	Peters Lava	PYR	Basaltictrachyandesite	5	5.12	43.17				
	Warwicks	TUR	Basaltictrachyandesite	0						
	Satellite	Fanthams 3	L14	Trachybasalt	5	9.86	74.21			
Fanthams 3		L15	Trachybasalt	9	8.33	55.47				
Fanthams 3		L16	Trachybasalt	3	9.51	61.68				x
Fanthams 2		L5	Basaltictrachyandesite	1	2.8	6.78				
Fanthams 1		L2	Basaltictrachyandesite	0						
Fanthams 1		L7	Basaltictrachyandesite	4	4.89	45.57				x
Fanthams 1		L9	Basaltictrachyandesite	0						
Fanthams 1		ES7A	Basalt	22	4.12					
Fanthams 1		ES7B	Basalt	3	3.84					
Fanthams 1		ES9	Basalt	26	1.06	7.42				x
Fanthams 1		ES8	Basalt	1					x	
Xenolith		FPD	Trachybasalt	5	5.42	43.49				
Xenolith		T89/20	Cumulate	20	0	0				

6.4.5. Rim thicknesses

An important observation of Taranaki samples is the large range in reaction rim thicknesses between samples (< 5 μm to > 50 μm) together with the similarity of rim thicknesses ($\pm 20\%$, 1s) of amphiboles within the same thin section (Table 6.4). Sample ES 5, L21, and ES 9 are the exceptions, where two amphibole populations are seen with distinct reaction rim thicknesses. In samples where reaction rims and groundmass compositions were analysed, no direct correlation between the melt composition and

reaction rim thickness could be established (Table 6.4). Further, we did not note any increase in microlite size with an increase in rim thicknesses.

6.5. Discussion

6.5.1. Amphibole stability field for Taranaki

Constraining conditions under which amphiboles are stable is crucial for understanding the implications of the breakdown features. Many experimental studies have shown that amphibole compositions can quantify pre-eruptive conditions including temperature, pressure, oxygen fugacity, and water content. Many amphibole thermometers require compositions of plagioclase that are in equilibrium with the amphibole phase ([Blundy and Holland, 1990](#); [Holland and Blundy, 1994](#); [Molina et al., 2015](#)). [Otten \(1984\)](#) and [Féménias et al. \(2006\)](#) used Ti composition in amphibole to determine crystallization temperature. An amphibole-plagioclase thermometer was developed by [Blundy and Holland \(1990\)](#) and later revised by [Holland and Blundy \(1994\)](#). Amphibole-only compositions were used by [Ridolfi et al. \(2010\)](#) to develop a model that calculated temperature, pressure, oxygen fugacity, and water content of crystallization. This was later revised by [Ridolfi and Renzulli \(2012\)](#) for higher temperature and pressure conditions. [Molina et al. \(2015\)](#) proposed liquid-only and amphibole-liquid thermometers and an amphibole-plagioclase barometer, while [Putirka \(2016\)](#) proposed liquid-only, amphibole-only, and amphibole-liquid thermometers; as well as an amphibole-liquid barometer. Further, an Al-in-hornblende barometer ([Hammarstrom and Zen, 1986](#)) has been calibrated for various calc-alkaline igneous rocks (e.g., [Anderson and Smith, 1995](#); [Ernst, 1998](#); [Hollister et al., 1987](#); [Johnson and Rutherford, 1989](#); [Krawczynski et al., 2012](#); [Mutch et al., 2016](#); [Putirka, 2016](#); [Schmidt, 1992](#)). A useful Excel-based software, WinAmpTB, was developed by [Yavuz and Döner \(2017\)](#) that estimates calcic-amphibole

only, amphibole-plagioclase and amphibole-liquid thermometers and barometers for igneous systems based on standard cation normalizations (e.g., [Krawczynski et al., 2012](#); [Mutch et al., 2016](#); [Putirka, 2016](#); [Ridolfi and Renzulli, 2012](#); [Ridolfi et al., 2010](#)).

In Taranaki lavas, the variation in the major element geochemistry of the amphiboles (Table 6.2) within the same sample reveals the amphiboles found in the same eruptive unit have different growth histories. Crystals with similar histories can also be found in different units irrespective of lithology and source vent. This, along with chemical disequilibrium conditions between melt and crystals as well as fractured/broken crystals, indicates that the crystals entrained in Taranaki lavas are antecrysts that have been picked up by ascending magmas. Therefore, thermobarometers using amphibole-liquid or amphibole-plagioclase compositions are not useful for Taranaki samples.

The thermobarometers suitable for Taranaki lavas are restricted to equations that only use amphibole chemistry to calculate temperature and pressure. Some of the [Ridolfi et al. \(2010\)](#) temperature estimates exceed the maximum stability limit of amphiboles in primitive magmas. This suggests that this earlier thermobarometric calibration may be less reliable. Evaluations carried out by [Erdmann et al. \(2014\)](#) also show that the [Ridolfi et al. \(2010\)](#) thermometer overestimates temperatures for high-Al (> 13 wt%) amphiboles and may therefore not be ideal for the Taranaki amphiboles (11.53–14.40 wt% Al₂O₃). The low Mg# (calculated as Mg/[Mg+Fe] in mol%) of Taranaki amphiboles (65–75, rarely > 80) also means that the [Krawczynski et al. \(2012\)](#) single amphibole thermobarometer does not apply to Taranaki. Further, the [Mutch et al. \(2016\)](#) thermobarometer is calibrated for granitic compositions and is therefore not ideal for Taranaki. This leaves the thermobarometers of [Ridolfi and Renzulli \(2012\)](#) and [Putirka \(2016\)](#) are suitable calibrations for Taranaki rocks.

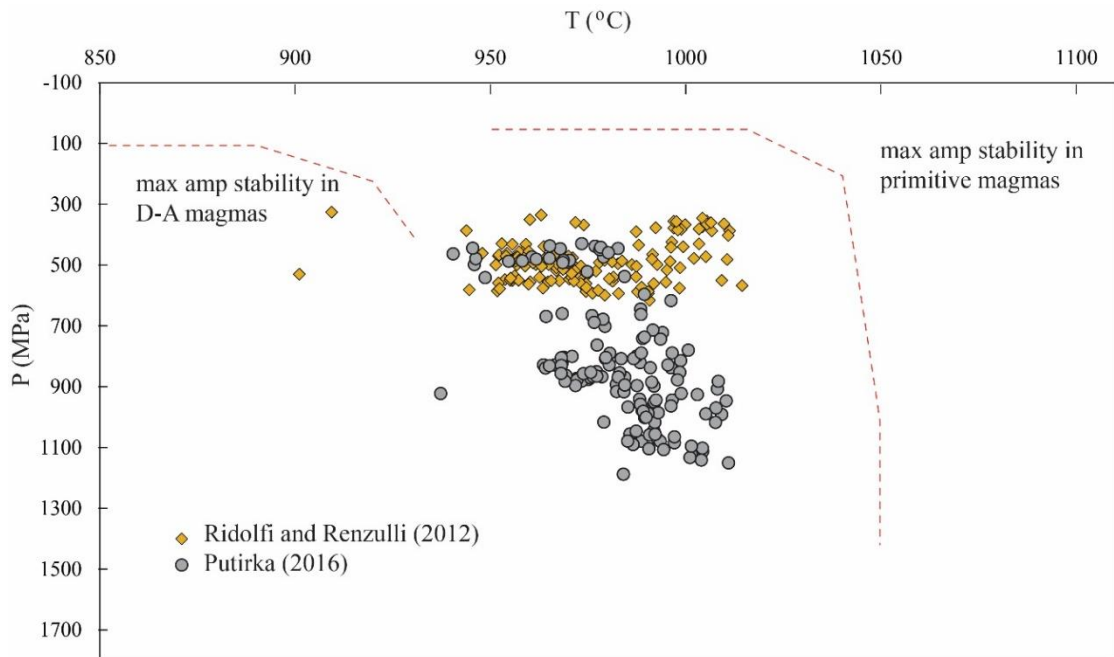


Figure 6.11 P-T stability field for Taranaki amphiboles using various thermobarometers. Maximum stability of amphiboles taken from [Kiss et al. \(2014\)](#) for D-A (dacitic- andesitic magmas) and primitive magmas (basalt, basaltic andesite and high-Mg andesite).

We have used appropriate thermobarometric equations ([Putirka, 2016](#); [Ridolfi and Renzulli, 2012](#)) and compared the results in Figure 6.11. The data reveal a relatively well-defined temperature range of *c.* 950–1010°C. The compositions of hawaiite amphiboles from the Crater Flat volcanic zone, Nevada, studied by [Nicholis and Rutherford \(2004\)](#) are comparable to those of Taranaki (Figure 6.6 and Figure 6.7). Pre-eruptive conditions were determined to be *c.* 970–1005 °C, for both the Little Cone and Lathrop Wells samples. There is a systematic offset of barometric results between the [Ridolfi and Renzulli \(2012\)](#) and [Putirka \(2016\)](#) calibrations, with the former yielding lower pressures (*c.* 300–600 MPa) than the latter (dominantly 700–1100 MPa). This range in pressure estimates illustrate the high level of uncertainty associated with using amphibole barometry, and we conclude that pressure estimates cannot be deemed reliable, other than indicating that these crystals were stored at mid-to-lower crustal levels, from where

ascending melts picked them up as they primed the system for eruption. The estimated temperatures of 950–1010°C are consistent with mid-to-lower crustal storage.

6.5.2. Magmatic processes and breakdown textures

In natural systems like Taranaki volcano, it is difficult to attribute amphibole breakdown to a single process like heating or decompression that were observed in the experimental studies of [De Angelis et al. \(2015\)](#) and [Rutherford and Hill \(1993\)](#); breakdown may rather result from a complex interplay of many mineral and melt characteristics such as composition, viscosity, water content, temperature and pressure ([Browne and Gardner, 2006](#)). To constrain the contributions of these factors, we interpret the breakdown textures recorded and assign them to the primary magmatic processes that result in their formation.

6.5.2.1. Detached rims: Type (i)

The detached rims of Taranaki are similar to those reported by [Plechov et al. \(2008\)](#) in the 1956 eruption products of Bezymianny volcano and the experimental samples of ([De Angelis et al., 2015](#)). Similar rims were also identified in Monserrat samples by ([Rutherford and Devine, 2003](#)) and were attributed to a small but significant increase in temperature within the stability field of the amphibole. [Zellmer et al. \(2016\)](#) studied the initiation of the peritectic reaction between olivine and melt to form orthopyroxene, in natural tephras from central North Island, New Zealand. They showed that when unstable, the olivine crystals begin to dissolve, resulting in a Fe-rich olivine rim and an Mg-rich melt boundary layer that favours the growth of orthopyroxene. They concluded that the reaction between melt and olivine to form orthopyroxene is a two-step process of olivine dissolution followed by orthopyroxene overgrowth. In the Taranaki examples, a similar formation of lighter (Fe rich) amphibole rims and a darker melt boundary layer (Mg- and Si-rich) is observed in samples that show the formation of detached rims only (Figure

6.4e, f). We suggest that there may be a similar two-step process of amphibole dissolution followed by clinopyroxene microlite growth in the melt boundary later. The formation of detached rims is seen in all samples, irrespective of the presence of symplectic or granular rims. We postulate that the dissolution of amphibole and crystallization of pyroxene marks the initiation of amphibole breakdown when the crystals are entrained in ascending, hot, low-viscosity melt.

6.5.2.2. *Symplectic and granular opacite rims: Type (ii) and (iii)*

Opaque rims were previously considered to be late-stage (syn- or post-eruption) oxidation-dehydrogenation reactions of the amphiboles ([Murphy et al., 2000](#); [Plechov et al., 2008](#); [Rutherford et al., 1998](#)). In these previous studies, it was seen that the opacite rims are found in every section of the crystal and in addition occupied cracks and fractures. The opacite rims of Taranaki samples differ in that melt-amphibole reactions are apparent, because there is no rim formation when the amphibole crystal is not in direct contact with melt (Figure 6.10f). ([Turner et al., 2008b](#)) also reported similar rims on amphibole crystals in the pumice and scoria samples of the Curtis Ridge pyroclastic deposits. This suggests that the symplectic and granular rims of Taranaki amphiboles are a magmatic reaction of an unstable amphibole with its host melt rather than a product of late-stage post-eruptive oxidation.

[Plechov et al. \(2008\)](#) proposed a reaction for the formation of granular rims, based on observations of Bezymianny samples. The sequence of zones observed was px + pl + Ti-mt in contact with the amphibole, followed by a px + pl zone and a px zone in contact with the melt (see Figure 6.10e). The outermost zone of this sequence is represented by the thin px rim floating in the melt around the amphibole grains, which are identified here as detached rims.

The opaque appearance of opacite rims is attributed to the sub-micron scale of mineral phases of the reaction rim with numerous interlaced oxides. These small crystal sizes and high crystal number density indicate nucleation-dominated reactions in which the system is forced far from equilibrium over short timescales ([McCanta et al., 2007](#)). This is explained by kinetic studies of crystallization, which show that nucleation rates are higher at high degrees of undercooling and growth rates are highest at low degrees of undercooling ([Browne and Gardner, 2006](#); [Brugger and Hammer, 2010](#); [Hammer and Rutherford, 2002](#); [Hammer et al., 2002](#)). We also observe an intergrowth between symplectic and granular rims, where the granular rim microlites are larger and equant (sample ES3). An explanation is the formation of melt pockets around the crystal, resulting in local regions of lower undercooling favouring the growth of larger crystals in the rims. Another explanation has been proposed by [Plechov et al. \(2008\)](#), where the crystallography determines the nature of the rims. They reported that sections perpendicular to the elongation of the grains showed both symplectic and granular rims, while parallel sections showed only symplectic rims. This is not seen in Taranaki samples. Only in sample L22, we recorded granular rims and detached rims with no symplectic rim formation (Figure 6.9f). The presence of a highly crystalline, trachytic groundmass in this sample further suggests that the lower temperatures of the melt resulted in lower degrees of undercooling, which favoured coarser rim formation.

The similar thicknesses of reaction rims within the same thin section indicate that despite their different initial growth histories (crystallization at moderately variable temperatures and highly variable pressures), these crystals share the same late-stage process, likely decompression induced breakdown during ascent and/or heating due to an insurgent magma batch. The observation of within-sample constancy of rim thickness differs from what has been observed at Augustine volcano ([De Angelis et al., 2013](#)) and Mount St.

Helens ([Rutherford and Hill, 1993](#)), where at least two populations with unique reaction rim thicknesses are found. Such heterogeneous populations indicate multiple different processes at different spatial and temporal conditions, including multiple storage levels and mixing of magmas ascending at different rates and being extruded together by the final eruptive melt ([McCanta et al., 2007](#)). The observation of within-sample constancy of rim thickness in most samples suggests that at Taranaki, (i) amphibole breakdown occurs during magma ascent rather than within subvolcanic mid to lower crustal mush zones that are the source of the crystal cargo, and (ii) ascent of magmas beyond the stability of amphiboles almost always results in an eruption, as poly-modal reaction rim thicknesses would be more common otherwise.

6.5.2.3. Coarse rims: Type (iv)

Experiments conducted by [De Angelis et al. \(2015\)](#) and [Buckley et al. \(2006\)](#) reveal that the distinguishing feature between heating and decompression-induced rims is the type of pyroxene present and its abundance. While decompression rim assemblages contain opx + pl + Fe-Ti oxides, the heating rim assemblages comprise opx + cpx + pl + Fe-Ti oxides. Furthermore, [De Angelis et al. \(2015\)](#) showed that with an increase in the duration of the heating experiment, opx abundance increases with a decrease in cpx (without an increase in microlite size). The only sample in Taranaki eruptives with rim microlites large enough to analyse using EDAX is the coarse type (iv) rims of sample ES5 (Figure 6.9f). These rims show significant opx as a component of the reaction rims with few microlites of cpx. The presence of opx is consistent with the coarse rims corresponding to the decompression induced breakdown reported by [Rutherford and Hill \(1993\)](#); however, they may indicate heating over long periods ([De Angelis et al., 2015](#)), or simply that the melts generated prefer the crystallization of opx over cpx. [Murphy et al. \(2000\)](#) suggested that thick and coarse rims greater than 200 μm , such as those seen in ES5, could

result from long periods of residence in the conduit, i.e., years to decades at depths shallower than amphibole stability.

6.5.2.4. *Unrimmed Amphibole*

The observations of thin or no amphibole rim formation are markedly different from those reported in Augustine amphiboles by [De Angelis et al. \(2013\)](#). At Augustine, the rim-free amphiboles were found in high silica andesites that showed little or no evidence of storage region disequilibrium, indicating low temperature melts with high viscosity, and that short ascent durations resulted in little to no reaction. However, the amphiboles from Taranaki without significant rim formation are the sole population in more mafic samples with high vesicularity (scoria) and low viscosity.

These crystals show euhedral internal zoning and rounded crystal faces (Figure 6.4e). [Nicholis and Rutherford \(2004\)](#) observed similar crystals in experimental and natural amphibole-bearing hawaiite tephras from Little Cone, Crater Flat, in Nevada. They suggested that for the formation of such crystals, the dissolution rate of amphibole is lower than the transport rate of material away from the rim. The result is amphibole dissolution and growth of new anhydrous phases away from the amphibole-melt boundary. For Taranaki, we propose that a moderately low dissolution coupled with higher transport rate results in the formation of well-rounded crystals with an extremely thin rim of px and oxides that do not have enough time to develop into a reaction rim.

6.5.2.5. *Volumetric decomposition (A and B)*

Regions of volumetric decomposition (B) can be described to form by the open system reaction proposed by [Buckley et al. \(2006\)](#) for Monserrat samples: $hbl \rightarrow cpx + opx + pl + il + mt$ (or Ti-mt). At Taranaki, the amphibole decomposition products are dominated by pyroxene and plagioclase, and oxides occur in minimal amounts. Using the

two-pyroxene thermometer ([Putirka, 2008](#)) on opx and cpx within the same amphibole crystal that shows type A volumetric decomposition, we obtain a temperature of 1020°C ($\pm 50^\circ\text{C}$), which is not significantly higher than the average temperature estimates from the pargasites of Taranaki ($980^\circ\text{C} \pm 30^\circ\text{C}$) (Figure 6.11). This shows that despite the presence of cpx, regions of volumetric decomposition (type A) are likely not caused by heating but because of the slow reaction of interstitial melts entrapped in cracks and cleavages with the amphibole during decompression-induced degassing. In contrast, regions of volumetric decomposition (type B) appear similar to the breakdown documented by [De Angelis et al. \(2015\)](#), where oriented mineral replacements are seen to form when the amphibole is heated beyond its stability limit. The extent of volumetric decomposition is time-dependent and [De Angelis et al. \(2015\)](#) noted that after 48 hours of heating, amphiboles are completely replaced by pseudomorphs. This was also observed in St. Helens and Soufriere Hills samples by [Rutherford and Hill \(1993\)](#) and [Rutherford and Devine \(2003\)](#), and these breakdown textures were attributed to an increase in temperatures beyond the amphibole stability limit, possibly due to magma mixing. Evidence of heating episodes is also seen in the sieve textures of plagioclase phenocrysts within the same samples.

6.5.3. Stability Conditions

Variation in the stability conditions is evidenced in crystals like ES3Amp4 and ES3Amp1, where the internal zoning is seen separated by a breakdown interface (see Figure 6.12a,b). This implies mixing between at least two regions of stability. [Putirka \(2016\)](#) observed a strong correlation between SiO₂ content and temperature of

amphiboles. Using this relation, we propose some amphiboles are mobilized within the subvolcanic crystal mush zones and moved between regions of stability.

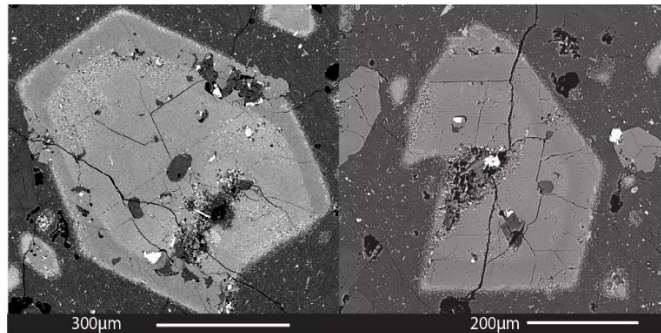


Figure 6.12 (a) Amphibole zonation with evidence of reaction at zone boundary (ES Amp4); (b) BSE image of a lighter reacted core and reverse zoned mantle (ES3 Amp1)

In the case of ES3Amp1, the hotter crystal core was brought into a cooler storage region and the amphibole overgrew under the new conditions (Figure 6.13). As progressive injection of hot magma continued, a gradual increase in temperature resulted in reverse zoning in the mantle of the amphibole. This suggests that crystal residence times in the subvolcanic mush zone are long enough to allow resorption and overgrowth of amphiboles under changing conditions. A similarly complex amphibole growth history was described by [Kiss et al. \(2014\)](#) in the composite zoned amphiboles of Ciomadul volcano.

In summary, based on these observations, we postulate that at Taranaki, detached rims (type i) and volumetric decomposition (B) are attributed to heating, and symplectic rims, granular rims, coarse rims, and volumetric decomposition (A) are due to decompression-induced degassing.

6.5.4. Progression of amphibole breakdown

To understand the chronological order of reaction rim formations, we consider the 6 textures observed: reaction rim types (i)–(iv) and volumetric decomposition (A) and (B).

It has been determined that the rims form due to a reaction between the amphibole and melt. The reaction begins at the initial interface between the crystal and melt and then proceeds towards the centre of the crystal. Therefore, the outermost rim is the first to form, and the innermost rim the last reaction front prior to quenching.

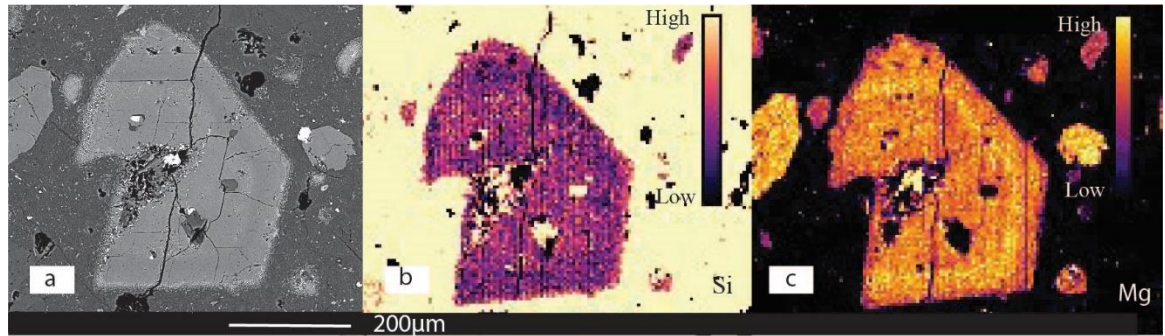


Figure 6.13 Amphibole zonation seen in sample ES3. Points mark locations of EPMA analysis from core to rim. Graphs show the variation in major oxides with approximate distances in μm .

The formation of the detached rim can be considered as the primary reaction zone as it is the outermost rim, where amphibole is brought into contact with the hot melt that remobilizes the crystals from their mush zone. As the melt and entrained crystals ascend the reaction progresses inwards, forming symplectic and granular reaction rims with microlite sizes that are governed by melt composition, the viscosity of the adjacent melt, and the rate of crystallization of reaction products. In sample ES3, we observe the coexistence of symplectic and granular rims along the same crystal faces (Figure 6.9e), with granular rims replacing portions of the symplectic rims with comparable thicknesses, indicating simultaneous growth. When in association with coarse rims, the detached rim is not the outermost rim. In sample ES5 we have an outer coarse rim, inner detached and symplectic rim, and volumetric decomposition (B) (Figure 6.9g). This can be explained by a two-step ascent pathway, with the first uptake resulting in coarse rims (slow ascent / long residence in shallow regions) and the second uptake by a hot melt forming detached and symplectic rims, and volumetric decomposition (B).

Where reaction rims and regions of volumetric decomposition are found together, the regions of decomposition (A) and (B) appear to overprint the symplectic rims, and sometimes, thick reaction rims are seen around amphiboles that have been completely decomposed (Figure 6.9c). As rim formation does not occur without the presence of amphibole and melt, we can state with certainty that the rims formed earlier due to melt-amphibole reaction, which was later followed by the volumetric decomposition of the amphibole.

6.5.5. Extent of amphibole breakdown

The extent of amphibole breakdown is inferred from the width of the reaction rims and the area of volumetric decomposition. This can be affected by four primary factors:

- (i) Composition and natural zonation of the amphibole grain ([e.g., Kiss et al., 2014](#))
- (ii) Characteristics of the melt (including composition and viscosity) ([e.g., De Angelis et al., 2013](#); [De Angelis et al., 2015](#); [McCanta et al., 2007](#); [Nicholis and Rutherford, 2004](#); [Rutherford and Devine, 2003](#));
- (iii) Magnitude of instability (differences in P-T of stable amphiboles and new environments) ([e.g., De Angelis et al., 2015](#); [Rutherford and Devine, 2003](#));
- (iv) Duration of instability ([e.g., De Angelis et al., 2015](#); [Murphy et al., 2000](#); [Rutherford and Hill, 1993](#)).

Amphiboles within the same sample show varied histories but similar reaction rim thicknesses, and we can thus argue that mineral chemistry does not significantly affect the extent of rim formation (though it may have influenced the abundance of oxides found in the reaction rims). A correlation cannot be established; however, mafic melts generally have rounded amphibole grains with no significant rim thickness, thick rims with decomposed cores, or no modal amphibole.

[De Angelis et al. \(2015\)](#) found that prolonged heating at low temperatures formed thin rims. However, at higher temperatures and for longer durations, complete pseudomorphs were observed once a critical threshold was passed, implying a catastrophic breakdown of amphiboles. In some samples from Fanthams Peak, thick rims associated with a complete internal breakdown of the amphibole are observed, which suggests that after the initial reaction, the breakdown of amphibole entrained in hot melts was ‘catastrophic’.

6.5.6. Magma ascent times from reaction rim thicknesses

The duration of instability is the primary criterion used in extracting timescales from amphibole breakdown. The rate of formation and thickening of reaction rims on amphiboles were determined experimentally by [Rutherford and Hill \(1993\)](#), [Rutherford and Devine \(2003\)](#), and [Nicholis and Rutherford \(2004\)](#). These experiments used hornblendes obtained from natural samples entrained in melts of different compositions and decompressed at different rates.

[Rutherford and Hill \(1993\)](#) used the starting material of dacitic pumice (63–64 wt.% SiO₂) from the 1980 Mount St. Helens eruption. Constant rate decompressions between 900° and 830°C showed that from a depth of 8 km, no reaction rims were observed for ascent durations of less than 5 days. Progressively thicker rims were formed in longer durations (25µm in 15 days, 32µm in 20 days). Shallower magmas stored at 3.5 km depth also showed progressive widening of rims in relation to the ascent rate with 50 µm rims in 11 days at 900°C (Figure 6.14).

[Rutherford and Devine \(2003\)](#) estimated magma ascent rates for hornblende-bearing siliceous andesites (57–61 wt.% SiO₂) from the Soufriere Hills volcano on Montserrat from a depth of 5–6 km (130 MPa) at 830, 845 and 860°C. These three isothermal-decompression runs show various thicknesses of amphibole rims formed at

different rates. Amphibole stability was determined to be between 825 and 855°C, and the constant rate decompression experiment at 845°C was considered appropriate to simulate and calibrate the rim growth of amphiboles at the Soufriere Hills.

[Nicholis and Rutherford \(2004\)](#) used hawaiite as a starting material for their experiments with a SiO₂ content of 49.2 wt.%. An isothermal (970°C) constant rate decompression path from an initial pressure of 180 MPa down to 15 MPa was simulated through several decompression experiments. It was observed that no reaction rims were experimentally produced; however, rounded crystals and a decrease in modal amphiboles strongly suggested the dissolution of amphiboles in the less viscous melt.

Figure 6.14 summarizes the observations of rim thicknesses developed over time from the experimental literature, and the associated ascent timescales estimated for natural systems. We find that reacted amphiboles from Taranaki volcano display a range of rim thicknesses (from unrimmed to > 420 µm) encompassing observations from previous studies of hornblende breakdown. The pargasitic amphiboles of Taranaki yield (and are stable to) higher temperatures than the hornblende crystals in dacites and andesites ([Rutherford and Devine, 2003](#); [Rutherford and Hill, 1993](#)) and may also have a different limit of H₂O-pressure stability during decompression-induced degassing of the magma.

Although Taranaki pargasites comparable to those in hawaiites ([Nicholis and Rutherford, 2004](#)), most Taranaki magmas have higher alkali contents than the magmas investigated experimentally. These higher alkali contents can significantly affect reaction rates, as demonstrated by [First et al. \(2021\)](#) using trachydacitic samples from the Quizapu volcano. For a quantitatively reliable determination of ascent timescales at Taranaki volcano, decompression experiments on pargasites in trachytic melts at a higher temperature will be required. Given the range of observed reaction rim thicknesses, it is evident that ascent times at Taranaki are highly variable and would lend themselves to quantification if

experimental data were available. Further, Taranaki satellite vents eruptives are more mafic, but there are no consistent differences between satellite and main vents in terms of their reaction textures or, by inference, ascent times.

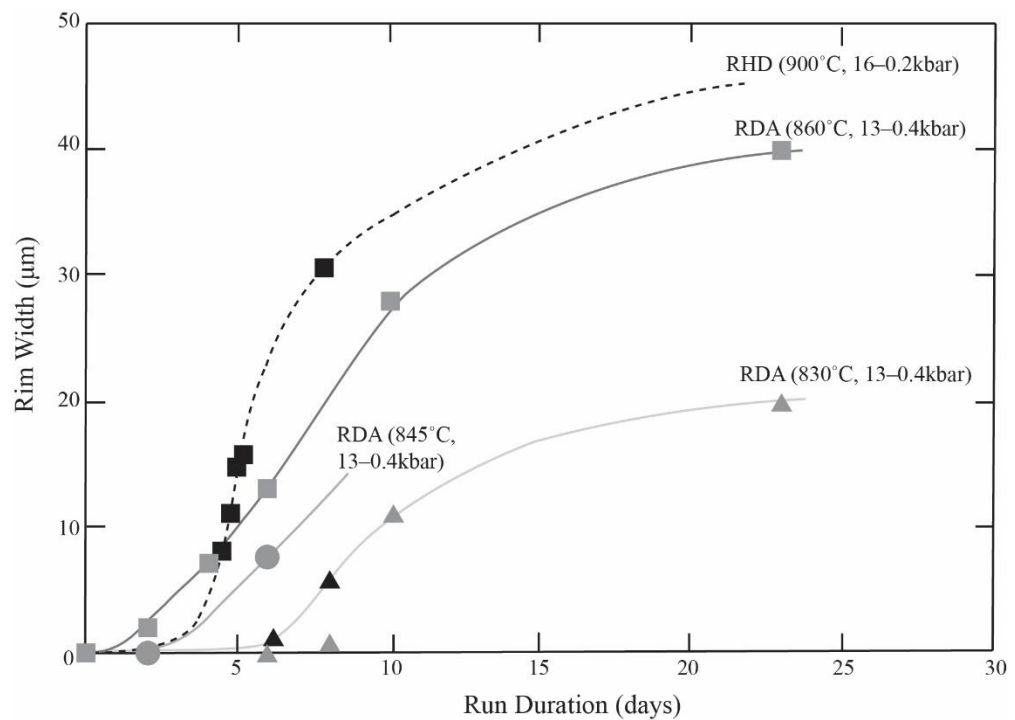


Figure 6.14 Magma ascent times based on the experimental runs of [Rutherford and Hill \(1993\)](#) using dacites (RHD); and [Rutherford and Devine \(2003\)](#) using andesite melts (RDA). Grey symbols denote experimental data, black symbols denote rim thicknesses for Taranaki samples. Amphiboles with reaction rims larger than 50 µm have not been plotted.

While experimental decompression studies to assess the effect of melt alkali content and amphibole composition on rim thickness will be required to derive reliable ascent times for Taranaki eruptives, the similarity in rim thickness ranges between Taranaki pargasites and previously studied hornblende crystals may suggest similar orders of magnitude in ascent times (i.e., days to weeks for thinner rims, decades to years for thick rims). Short ascent times of days would be useful for volcanic hazard mitigation efforts and are in line with ascent times calculated from amphibole breakdown of other volcanoes such as Soufrière Hills (2 to > 20 days), Mount St. Helens (< 4 to 16 days), Redoubt Volcano (1 to 13 days), Black Butte (6 to > 20 days), Bezymianny (4 to 7 days), Santiaguito

(6 to 18 days), and Ciomadul (6 to 22 days) ([Browne and Gardner, 2006](#); [Kiss et al., 2014](#); [McCanta et al., 2007](#); [Plechov et al., 2008](#); [Rutherford and Devine, 2003](#); [Rutherford and Hill, 1993](#); [Scott et al., 2012](#)) and ascent times at other active volcanoes in New Zealand estimated through different methods ([Cooper et al., 2017](#); [Kilgour and Mader, 2014](#); [Liu et al., 2007](#); [Lormand et al., 2020](#); [Matthews et al., 2012](#); [Myers et al., 2018](#)).

6.5.7. A model for magma ascent at Taranaki

The stability field of Taranaki amphiboles extends over a range of P-T conditions. Injection of hot new magmas into the crustal magmatic plumbing system results in the remobilization of amphiboles. Amphiboles may remain in the mush zone under different conditions, resulting in zoned crystals, or they are picked up by the ascending melts and transported out of their field of stability. These changes in temperature and pressure result in the reaction of hydrous amphiboles with hot and increasingly volatile-deficient melts as they are carried upwards.

Reaction with the melt begins with the formation of detached rims, and in viscous melts these rims progress to form either symplectic or granular rims, depending on degrees of undercooling. As the duration of the instability continues, the rims thicken. A large increase in temperature beyond a critical threshold result in the complete breakdown of the amphibole, leaving behind rims with decomposed centres. Further instability may lead to complete dissolution of the amphibole, resulting in amphibole-free lavas. In low viscosity melts, however, dissolution of amphiboles leads to the formation of rounded crystals with the development of dissolution rims (px + oxide).

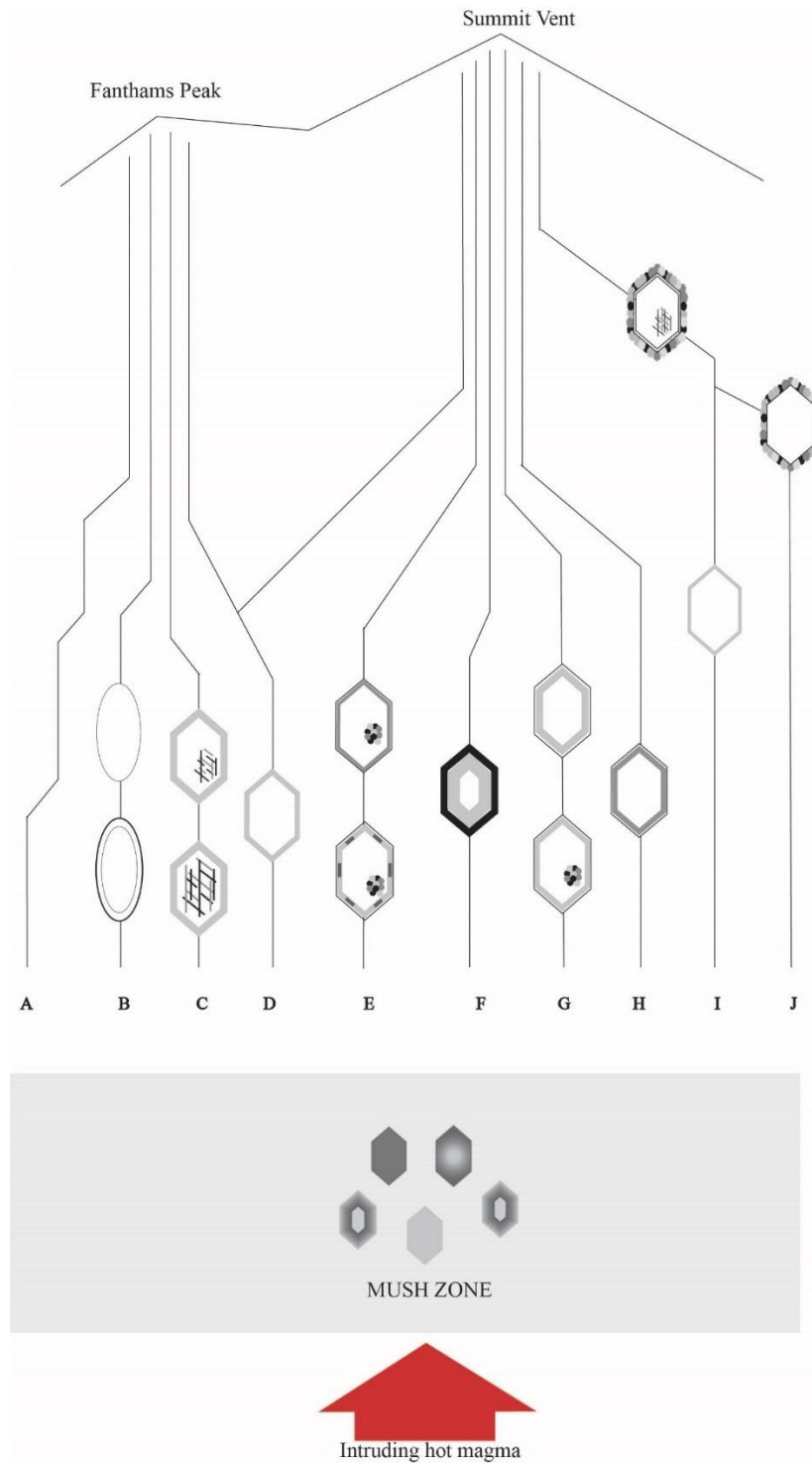


Figure 6.15 Model of magma storage and ascent of magmas at Taranaki. Black outlines represent type (i)/detached reaction rim, light grey represents type (ii)/ symplectic rims, dark grey outlines represent type (iii)/ granular rims, cobbled borders represent type (iv)/ coarse rims. Volumetric decomposition type (a) is represented by round clusters, type (b) by line clusters. Thickness of the rims indicated by thickness of outlines.

A model of these interactions is shown in Figure 6.15. Eruptive products from the satellite vent include amphibole-free melts (A) that may be the result of extensive breakdown and resorption of the crystals ([Nicholis and Rutherford, 2004](#)). Unreacted amphiboles or amphiboles with thin reaction rims (B) indicate hot, low viscosity melts, forming rounded mineral grains that are typical of satellite vent eruptives. Formation of granular, symplectic, or both reaction rims are seen in summit and satellite vent eruptives and result from decompression during ascent. The thickness of these rims and the extent of volumetric decomposition are determined by the ascent times of the magmas (C–I). A bimodal population of amphiboles is seen in sample ES5 (I, J). The coarse-rimmed amphiboles may stem from crystals intruded to a shallow depth where these thick, coarse rims formed. At a later stage, these reacted crystals were picked up by a hotter melt that contained amphiboles with thinner rims. This melt then reacted with the older, coarse-rimmed amphibole to form regions of volumetric decomposition and a granular rim. All these crystals were then extruded together, resulting in diverse crystal populations, as seen in ES5. More evidence of mixing and uptake is seen in ES9 and L21, where bimodal populations of symplectic rim thicknesses are seen.

6.6. Conclusions

This study highlights the range in amphibole compositions and breakdown textures, which reflects complex magmatic processes operating beneath the Taranaki volcano. The combined data demonstrate that:

- (i) Taranaki amphiboles are pargasitic in composition, originate from mid-to-lower crustal depths, and record temperatures of *c.* 960–1010°C.
- (ii) Taranaki eruptions are usually preceded by the injection of fresh magma into its subvolcanic crystal mush zones. The fresh melt picks up its crystal cargo

and reacts with the amphibole mineral phases as it ascends towards the surface. The extent of this breakdown reaction is a function of the time the amphibole resides out of its stability field and, for Taranaki samples, is attributed mainly to decompression-induced degassing and heating of amphiboles.

- (iii) Amphibole breakdown textures attributed to ascent-driven decompression include the formation of reaction rims, while heating associated with intruding melts results in aligned volumetric decomposition and dissolution of amphibole crystals.
- (iv) Reaction rim thicknesses vary little ($\pm 20\%$, 1σ , on average) within individual thin sections but show a large variation between samples from different lava flows, from $< 5 \mu\text{m}$ to $> 400 \mu\text{m}$. The pargasites of Taranaki would therefore lend themselves to timescale estimation between magma injection into the subvolcanic crystal mush and eruption at the surface, which may range from days to years.
- (v) Appropriate experimental data on pargasite breakdown in alkali-rich melts and the effects of amphibole and melt composition on the development of reaction rims and their widths will be required to provide fully quantitative constraints on magma ascent times. Quantifying the role of amphibole and melt composition in the formation of reaction rims under isobaric/isothermal conditions will be an important avenue for future research and ultimately will be useful for hazard mitigation in the Taranaki region.

Chapter 7.: Synthesis

7.1. Introduction

In this chapter, a coherent result of the three research objectives and their implications on our understanding of Taranaki volcano are presented. In Chapter 4, whole rock, crystal, and groundmass geochemistry was studied to build a model for magma generation and gain insight into the source regions of intermediate magmas and crystal cargo. A focussed study on textures and zoning patterns of the principal mineral phases of plagioclase, clinopyroxene and amphibole in Chapter 5 revealed a complex mush system which interacts heterogeneously with diverse intruding melts from the mantle. Final ascent of the magmas (melt + crystals) through various pathways and varying rates are recorded in the breakdown features of amphiboles and are discussed in Chapter 6. Together, these studies construct an almost complete model for the magmatic plumbing system feeding recent volcanic eruptions at Taranaki.

7.2. Role of mafic antecrysts in Taranaki lavas

With the knowledge that the presence of antecrysts in magmatic systems is common, it was important to separate the main components of the whole rocks into the crystal and melt fractions and study each constituent individually. In doing so, misinterpretations of whole rock chemistry are minimised. What emerges is a complex evolution for each component, which results in the evolution of the whole rock. This study challenges the conventional understanding of the generation of intermediate composition magmas. It has been traditionally accepted that primary mafic melts, generated from an ultramafic mantle wedge metasomatized by subduction fluids, rises into the crust, where they fractionate and assimilate crustal rocks to form higher silica, evolved magmas ([Elliott et al., 1997](#); [Kelemen et al., 2005](#); [Stern, 2002](#); [Tatsumi and Eggins, 1995](#)). Through such AFC

processes, diverse magmas with a mafic crystal cargo and a relatively felsic groundmass component are thought to be formed. However, the contrary is proposed here: mineral-melt disequilibrium indicates that most of the crystal populations are antecrystic/xenocrystic in origin. Thermobarometry of the mesocryst population indicate that they reside in a ‘mush zone’ at mid-crustal pressures, with temperatures between 940-1050 °C. The groundmass (microlites + glass) compositions indicate that the melts are relatively felsic and span compositions from basaltic trachyandesite to trachyte (55–70 wt% SiO₂), with little or no crystallisation occurring. These diverse melts entrain crystals from the mush zone, which reduce the silica content by 5–11 wt% SiO₂. [Beier et al. \(2017\)](#) also suggested a similar model for Pukeonake lavas from the TVZ, where intrusion of silicic melts into a crustal-level reservoir of mafic crystals results in intermediate composition lavas. However, Taranaki lavas show negligible fractionation or assimilation in the crust and can be interpreted as a simple mixing system of crystals and melt.

7.3. The case for ‘Subduction Melanges’

It was earlier suggested that the evolution of primary basaltic melts to hybridised basalts–dacites in Taranaki was achieved through AFC in a deep crustal hot zone and subsequent FC ([Annen et al., 2006](#)), while the *c.* 35 km of crust contributes complex ascent pathways that further facilitate AFC processes ([Price et al., 1999](#); [Stewart et al., 1996](#); [Zernack et al., 2012](#)). Yet, in this study, it is argued that the melt component of Taranaki lavas is diverse, silica-rich, and hot, and occasionally water-undersaturated, indicating that they cannot be obtained through deep crustal hot zone or shallower AFC processes, but instead are generated in the mantle. This model has two challenges: (i) trace element ratios show evidence of crustal contamination such as high La/Yb and La/Sm signatures, and (ii) the basaltic lavas of Taranaki have Mg# <0.3, Ni usually <25 ppm and Cr <30ppm, indicating that the basalts are not primary. The origin of crustal

signature typical of arc magmas can be difficult to interpret as similar geochemical signatures can be obtained by contamination of mantle melts by subduction and melting of sediments ([Ishizuka et al., 2003](#)), and contamination of mantle-derived magmas by assimilation of lithospheric mantle or crustal rocks during ascent and emplacement ([Sobolev et al., 2007](#)). These concerns, however, can be addressed using the model of subduction melanges.

Subduction melanges are solid state mixtures of altered oceanic crust (AOC), forearc debris, and hydrous ultramafic matrix that can originate from the mantle wedge or the incoming oceanic lithosphere ([Marschall and Schumacher, 2012](#); [Parolari et al., 2021](#)). Melanges have a lower solidus and density than the surrounding mantle and can rise spontaneously into the core of the wedge where melting occurs ([Behn et al., 2011](#); [Gerya and Yuen, 2003](#)). It is proposed that the mixing of melange components occurs initially in the forearc and then in the mantle, and the partial melting of these components serves as the source of the diverse melts for Taranaki, with little to no contribution of the mantle.

Figure 7.1 shows a comparison of Taranaki lavas to the Mariana arc system and shows that the isotopic composition of the lavas is a result of sediment mixing with the mantle/AOC is the initial process, followed by melting. To produce the observed isotope ratios from mantle and sediment mixing melanges, a larger proportion of mantle material would be required. However, mixing of AOC and forearc crust followed by partial melting are more likely to produce the ratio of Nd/Sr and Sr isotopes observed in Taranaki. Simple mixing of eroded forearc material and AOC with sediments to form the melange melt source is also demonstrated in similar studies of the Trans Mexican Volcanic Zone ([Parolari et al., 2021](#)). The subduction melange model can account for diverse felsic melts at mantle depths with crustal assimilation-like chemistry of high K₂O, SiO₂, La/Sm and La/Yb. The mantle contribution, albeit less, results in very small volume

melts with significantly higher Ni and Cr, expressions of which are seen in the crystal zoning patterns (Chapter 5). Thus, even in the case of a back arc volcano, subduction

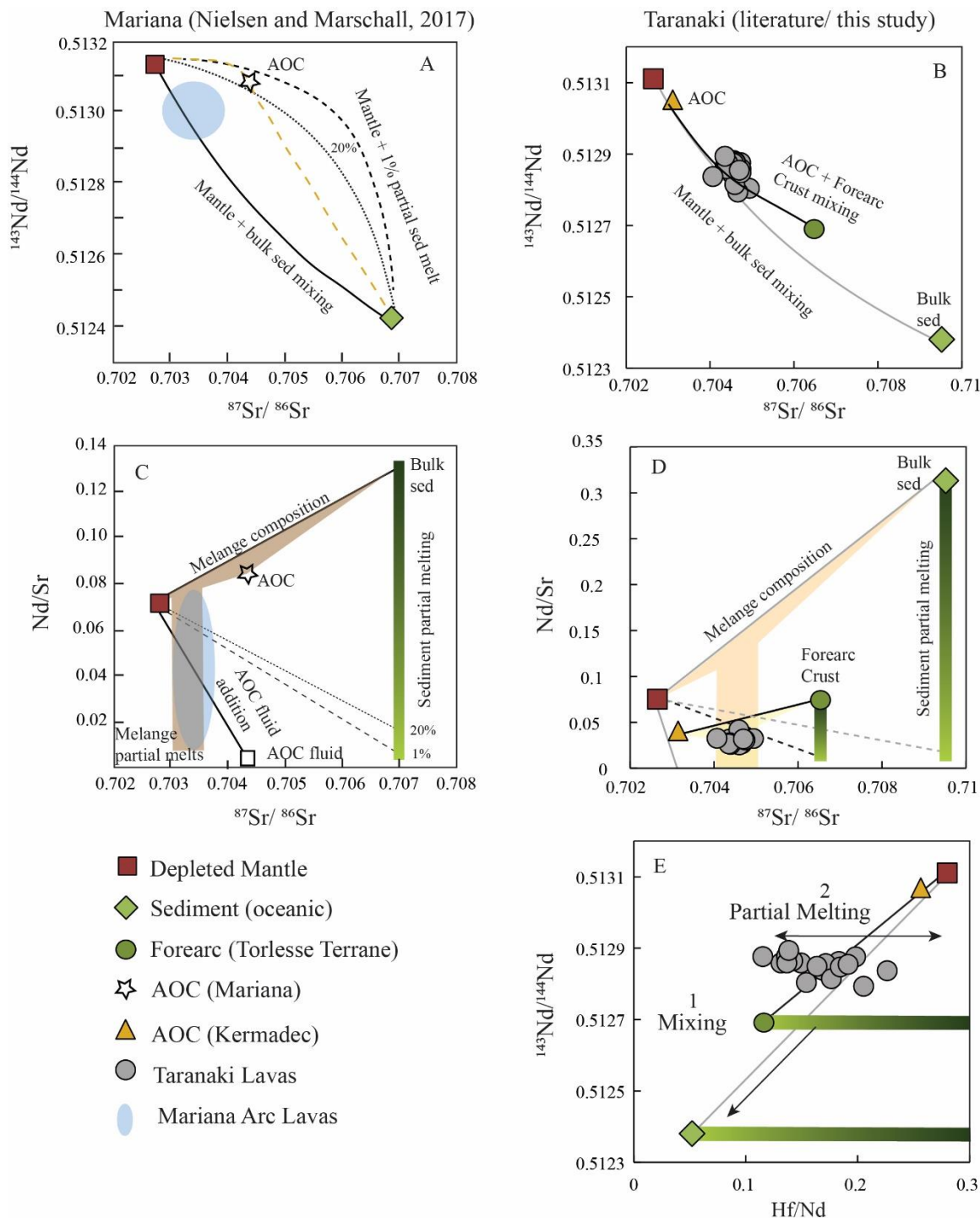


Figure 7.1: Comparison of Taranaki subduction components with the Mariana Arc illustrating the predominance of mixing processes over partial melting. (A-D) Plots of Sr isotopes against Nd isotopes and the Nd/Sr ratio for lavas from the Mariana arc and Taranaki. Mariana arc data and model was obtained from [Nielsen et al. \(2020\)](#), while Taranaki model uses Pacific sediments ([Plank, 2013](#)), subducting slab for NZ AOC ([Castillo et al., 2009](#); [Turner et al., 2009b](#)), isotopic data for Taranaki lavas ([Price et al., 1992](#)) and crustal forearc (Torlesse and Waipapa Terrane averages) ([Price et al., 2015](#)). (Appendix D).

dynamics conserves and recycles crustal material from eroded forearcs with negligible mantle contribution (cf. [Gómez-Tuena et al., 2018](#); [Parolari et al., 2021](#); [Straub et al., 2020](#)).

7.4. Summit and Satellite vents

The symmetry of Taranaki volcano is interrupted by the presence of a satellite vent on the southern flank, Fanthams Peak (Panitahi), which developed over the last 3.5 kyr ([Neall et al., 1986](#); [Stewart et al., 1996](#)). Flank eruptions are common in many stratovolcanoes, often associated with lateral draining of magma from the central conduit ([Rubin and Pollard, 1987](#)). However, a few flank eruptions are triggered by intrusions that are not fed through the summit conduit and are termed peripheral, or eccentric eruptions, as for example the Mt Etna flank eruptions in 1974 and 2001 ([Acocella and Neri, 2009](#)), and Eyjafjallajökull ([Moune et al., 2012](#); [Villiger et al., 2007](#)). The eruptions at Fanthams Peak are independent of the Summit system with both vents being active at approximately the same time, evidenced by light grey tephra beds intercalated between dark grey tephra between 3 and 1.5 kyr BP ([Torres-Orozco et al., 2017a](#); [Torres-Orozco et al., 2017b](#)). The question arises as to whether the satellite vent taps into a different source, entrains a larger crystal cargo, or ascends through a less complex plumbing system, thereby decreasing assimilation.

Fanthams has erupted volcanic products that are generally lower in major elements SiO₂ and K₂O and show no differences in trace element abundances or ratios Figure 7.2. Differences are also observed in (i) groundmass compositions (Chapter 4) and liquidus temperature estimates (Chapter 5), (ii) mineral chemistry, (iii) mineral abundances (satellite crystal cargo contains higher modal olivine and lower amphibole than the summit eruptives) as well as (iv) zoning patterns and textures. There is a complete overlap

between mineral compositions, but satellite eruptives have a smaller range of compositions in SiO₂ for plagioclase, amphibole and pyroxene; Al₂O₃ concentrations in cpx and Na₂O concentrations in amphiboles.

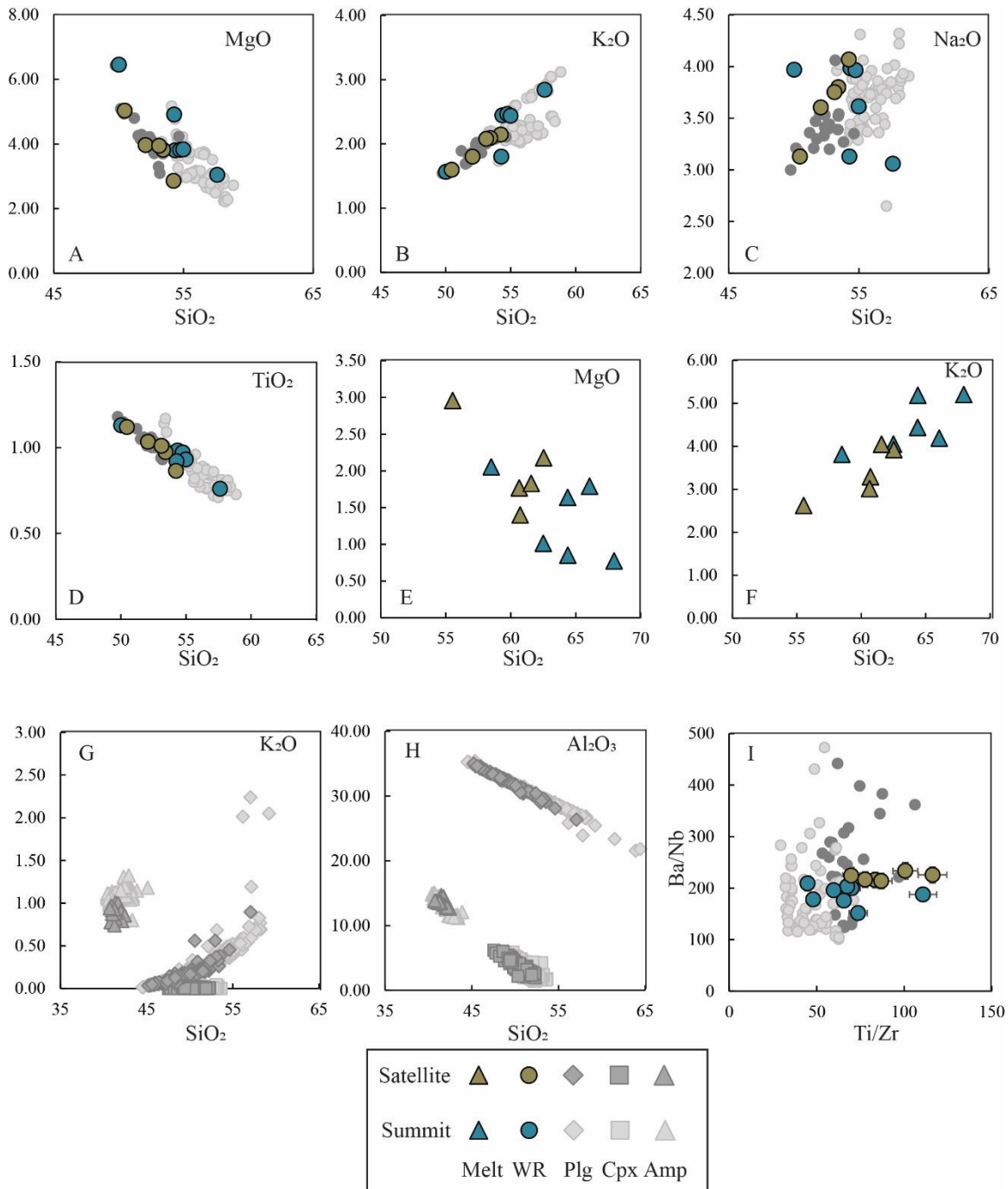


Figure 7.2: Comparison of summit and satellite eruptives based on whole rock chemistry (A-D), groundmass compositions (E,F), mineral compositions (G,H) and trace element ratios (I) Whole rock oxide and element data for Taranaki lavas obtained from ([Price et al., 1992](#); [Price et al., 1999](#); [Stewart et al., 1996](#); [Zernack et al., 2012](#)).

The extent of melting in a subduction melange is modulated by the proportion of crustal vs. mafic lithologies in the diapir, which then results in a range of primitive melts ([Parolari et al., 2021](#)). It is possible to explain the difference in the melt compositions between the satellite and main summit vent as a result of the satellite cone consistently tapping different regions of the melting melange with different proportions of components, especially the AOC (Chapter 4). On rising through the mantle, tectonic controls of the region may result in the satellite melts rising through different conduits than the summit melts (Chapter 2, tectonics of the Taranaki Basin). The crystal mush system beneath Taranaki does not interact with rising melts homogeneously ([Perugini et al., 2006](#)) and interactions with intruding melts results in changes in their chemistry. The mush region tapped by the satellite vent conduit is relatively pristine and contains higher modal olivine, with repeated mafic injections of hotter melts resulting in the breakdown of amphibole phases. The central mush region, on the other hand, has negligible modal olivine due to the repeated injection of high alkali and silica melts into the system (Chapter 5). On interaction with the melts, amphiboles from the satellite conduit begin to break down or dissolve in the hotter melts rising up through the satellite vent and are often completely resorbed; while the main summit melts react with the amphiboles to mainly form reaction rims of thicknesses determined by the ascent duration (Chapter 6). Therefore, the differences in summit and satellite lavas may be a combined outcome of melange melting heterogeneity, conduit geometry and regional tectonics, and melt-mush interaction.

7.5. A simple three (?) member mixing system

We identify three potential end members that can account for the range of lava compositions observed in Taranaki: AOC, crustal forearc, and crystal mush (\pm mantle wedge). The first mixing is likely to take place during subduction erosion inboard from

the Hikurangi trench, where the AOC and crustal forearc (along with some sediments) are physically ground and mixed to form melanges, which are released into the mantle as diapirs. Melting of cold melange components in the mantle to high temperatures (>1000 °C) results in the subcrustal formation of felsic melts. These may partially mix with the depleted mantle, but only to a limited extent.

The second phase of mixing occurs when these diverse melts encounter the crystal mush system (Figure 7.3). This mid-crustal region was initially a part of the Median Batholith, which forms the current basement of Taranaki and represents a 120 Ma magmatic system. Repeated intrusion of diverse melts results in the resorption and recrystallisation of mineral phases. Due to the longer-lived main summit cone, the mafic mineral chemistry has been overwritten with the increase in K₂O and SiO₂ concentrations, while mafic minerals continue to be dominant in the satellite cone. The movement of intrusive melts within the

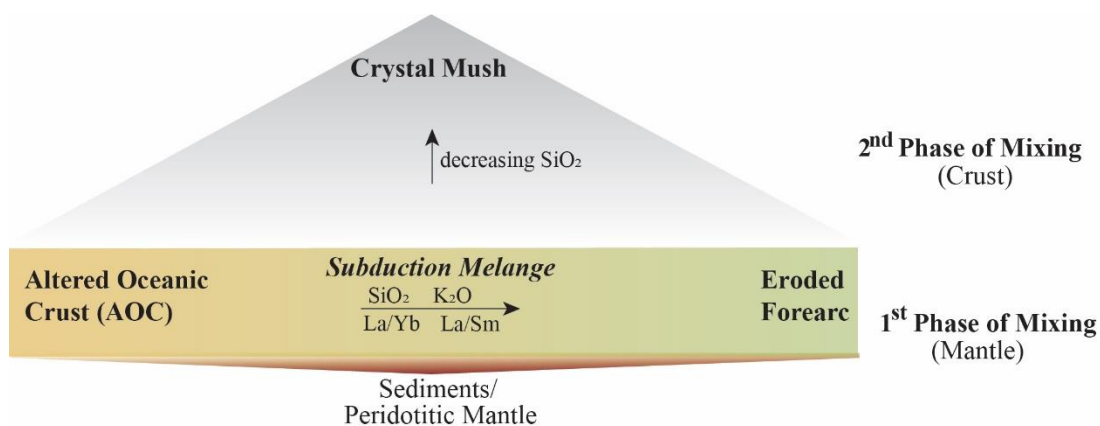


Figure 7.3: A schematic illustration of the three key mixing endmembers that contribute in forming the lava flows seen in Taranaki. The initial mixing of AOC and Forearc material that forms the melange and then partially melt in different proportions resulting in a range of primary melt compositions. Sediment and mantle contribution to melt compositions is minimal. They then rise into the crust and encounter the crystal mush, which decreases the SiO₂ content through the uptake of mafic minerals by the melts.

mush system is heterogenous and results in the remobilisation of crystals through various regions of the conduit, with different sub-environments of variable temperature, pressure,

melt composition and oxygen fugacity. An eruption triggering intrusion picks up crystals from different regions of the conduit, resulting in a varied crystal cargo over short length scales.

7.6. Testing and applying the subduction melange model

Subduction associated volcanism is characterised by LILE enriched and HFSE depleted trace elements and as well as isotopic signatures which are indicative of a strong crustal component in arc magmas (Stern, 2020). It has been the focus of recent research whether the crustal input is during assimilation of the overriding crust during storage or as melting of the subduction melange in the mantle with the forearc crust as a major component. The subduction melange model for the generation of diverse melts at Taranaki volcano attributes the crustal isotopic / trace element signature to the eroded forearc. To test this model, future studies using trace element data of potential melange components will have to be conducted and plotted against Taranaki lava data. This includes Sr, Nd, Hf, K, Be, and Mo isotopes of the AOC, forearc, and crustal xenoliths. Resistant minerals such as zircons can be compared to forearc material for compositional similarities.

The Hikurangi trench system is the southward extension of the Tonga-Kermadec arc as the Pacific plate subducts beneath the Indo-Australian Plate. [Timm et al. \(2014\)](#) investigated the Kermadec arc volcanism and demonstrated the effect of the subducting Hikurangi Plateau on the processes in the mantle and the crust beneath the southern Kermadec arc, just north of New Zealand. They propose that increased tectonic erosions in the forearc creates a thick, H₂O rich melange layer which contains fragments of the overriding forearc crust and the subducting Hikurangi Plateau in a metasedimentary matrix. This melange is subducted and rises buoyantly as cold diapirs to underplate the arc front.

Diapir formation depends on the temperature, viscosity, and thickness of the buoyant layer ([Behn et al., 2011](#)). It is likely that the bulk of the melange material is dragged to greater depths, where the melange zone lowers the slab surface temperature and stabilises hydrous mineral phases to greater depths ([Grove et al., 2009](#); [Marschall and Schumacher, 2012](#); [Nielsen et al., 2020](#); [Schmidt and Poli, 1998](#)). It is observed that Taranaki lavas are more hydrous than recent Ruapehu products which show water contents of *c.* <1 wt% ([Arpa et al., 2017](#); [Kilgour et al., 2013](#); [Lormand et al., 2020](#)). Thus, the melange melting model can also explain the hydrous, potassium rich, back-arc magmas of Taranaki in relation to its location to the TVZ.

Taranaki is a unique volcano because of (i) its location away from the principal zone of volcanism in the North Island, and (ii) repeated cycles of cone collapse and regrowth throughout its history ([Cronin et al., 2021](#); [Zernack and Procter, 2021](#)). However, the melange melting model proposed for Taranaki can be applied to other back-arc systems, where the diversity in ‘source’ components (as seen through trace element abundances and ratios) can be interpreted as mixing of melange components in varying proportions. This includes the AOC, eroded forearc crust, sediments (pelagic and volcanoclastic), and mantle (e.g. [Behn et al., 2011](#); [Codillo et al., 2018](#); [Marschall and Schumacher, 2012](#); [Nielsen and Marschall, 2017](#); [Parolari et al., 2021](#); [Straub et al., 2020](#); [Timm et al., 2014](#); [Wu et al., 2020](#)). The subduction melange model has been applied to the Trans-Mexican Volcanic Belt (e.g. [Straub, 2020](#); [Parolari et al., 2021](#); [Gomez-Tuena et al., 2018](#)) and the role of eroded forearc in magma generation at the Andean arc has been documented (e.g., [Cliff et al., 2009](#); [Straub et al., 2020](#); [Stern, 2020](#)). The model invoked in this study for Taranaki can be tested at similar volcanoes in other arc settings including, but not limited to, the Taupo Volcanic Zone, New Zealand; Merapi in the Java-Sunda arc, Indonesia; Rishiri, Kurile Arc, Japan; and the Andean arc, where the continental crust is thick.

Chapter 8.: Conclusions

8.1. From melt generation to extrusion

This study has interrogated whole rock and mineral chemistry of the <10 kyr Taranaki lava flows with samples spanning the diverse lava compositions, stratigraphic age as well as source vent in order to gain insight into the processes of magma generation, storage and ascent at this back-arc volcano. Lavas ranging from basalts to trachyandesites, dense lavas to scoria, and with crystal cargo ranging from 40 to 55 vol% reveal a complex history for this long-lived stratovolcano. The following conclusions are derived from this research:

1. Mesocrysts (100–500 μm) and macrocrysts (> 500 μm) hosted in Taranaki lavas show chemical disequilibrium with the melt they are entrained in and display disequilibrium textures and zoning patterns. Major element chemistry of the crystals hosted in the lavas also show a complete overlap with the chemistry of xenolith hosted crystals. This, along with the high proportion of fractured crystals and glomerocrysts with similar zoning patterns, suggest that the crystal cargo has antecrystic/ xenocrystic origins. Further investigation revealed that microcrysts (30–100 μm) are also possibly antecrystic and that the melts feeding Taranaki eruptions are aphyric to sparsely phyrlic.
2. Groundmass compositions show a range of melt compositions and yield temperatures that are too hot (>1000 °C) and carry too little water (1–3 wt% H₂O) to be developed in a deep crustal hot zone. These melts are likely of subcrustal origin. It is proposed that the source of these felsic melts is from the partial melting of subduction melange diapirs in the mantle wedge. Heterogeneous melting of different components (AOC, forearc crust \pm sediments) of the melange, with

negligible mantle input, results in an array of felsic melts that rise through into the crust.

3. Thermobarometric estimates, using mineral chemistry, indicate a mid-crustal mush zone, ranging in temperature between *c.* 940°C and *c.* 1010°C. Heterogeneous propagation of diverse melts through the mush zone creates sub-environments with different temperatures, pressures, oxygen fugacities and melt compositions. Repeated injections of varying melt compositions as well as transportation of crystals through various regions of the mush zone result in a complex, and individually diverse zoning of the crystals.
4. The mush zone coincides with the 120 Ma Taranaki basement- the Median Batholith. It is probable that the Median Batholith is the crustal source of these crystals, which are overgrown through crystallisation from Taranaki melts.
5. Using mass balance calculations, it was determined that the range of whole rock compositions can be obtained through simple mixing of crystals and melt in various proportions. Eruption triggering injections of melt remobilize crystals and carries them towards the surface, resulting in crystals with diverse histories observed over short length scales (i.e., within centimetres from each other).
6. Entrainment of crystals by ascending melts results in rims that are common for all crystal populations, despite their complex histories. These include plagioclase and clinopyroxene rims in equilibrium with the host melt as well as amphibole reaction rims.
7. Ascent pathways through the crust are dependent on regional faulting and existing conduits, as well as the viscosity of the magmas, which in turn is dependent on the melt composition, crystal proportions and volatile content. Breakdown of amphiboles due to decompression induced degassing during ascent suggests that

timescale of magma ascent from the mush zone to the surface ranges from days to years.

8.2. Outlook

Through this research a few gaps in knowledge were identified, the findings of which would improve on the results of this study and contribute to our understanding of not only Taranaki volcano and the New Zealand subduction system, but also other, similar volcanoes around the world.

1. In this study, the diverse melts generated beneath Taranaki are attributed to the partial melting of a subduction melange. However, the key components of the subduction melange proposed are the AOC, and the eroded forearc. The Torlesse Terrane has been assumed to be the forearc component for this study, but it would be beneficial to have a complete data set of the subducting forearc complex, which would include forearc sediments, forearc melange rocks and associated volcanoclastics. Such data should include isotopic compositions ($^{86}\text{Sr}/^{87}\text{Sr}$, $^{143}\text{Nd}/^{144}\text{Nd}$, $^{206}\text{Pb}/^{208}\text{Pb}$, and $^{176}\text{Hf}/^{177}\text{Hf}$) of the various potential components as well as the Hikurangi Plateau. Insights may also be gained through the U-Pb, O and Hf isotopic compositions of zircon, which are present as accessory phases in Taranaki lavas.
2. The crystal cargo has been determined to be antecrystic or xenocrystic for Taranaki lavas, however trace element mineral analyses may shed light on whether the Median Batholith is the source of the crystals, or if its crystals served as crystallising nuclei that were eventually completely overgrown with minerals derived from the ascending melts of Taranaki. The Median Batholith is a remnant arc system, and therefore separating the influence of Taranaki melts through major

elements alone is insufficient. If trace element data of the Median Batholith crystals overlap with those of mineral data in this current study, then the crystal cargo would truly be xenocrystic, challenging the widely accepted models for the evolution of Taranaki volcano. Thus, obtaining trace element (and isotopic) data of crystals from the Median Batholith would be useful.

3. Thermobarometry and hygrometry have been key components of this study and its interpretations. However, thermobarometers and hygrometers are less reliable in the absence of mineral-melt equilibrium in the case of prevalent antecryst/xenocryst populations. New single-phase thermobarometers employ machine learning calibration techniques with large data sets and lower errors than earlier models (e.g., [Higgins et al., 2021](#)). Although melt-mineral equilibrium tests were satisfied for plagioclase hygrometry, the current data set calibrations do not cover the alkali content of Taranaki lavas, which lie between the hygrometers of [Waters and Lange \(2015\)](#) and [Masotta and Mollo \(2019\)](#). Hence, obtaining more applicable experimental data would be useful.
4. A similar issue is faced when determining ascent rates from the thickness of amphibole reaction rims. The pargasitic composition of Taranaki amphiboles is similar to those from Crater Flat, Nevada ([Nicholis and Rutherford, 2004](#)). However, Taranaki pargasites contain lower TiO_2 and higher CaO and are entrained in a more alkali and silica rich melt. Thus, although ascent timescales can be approximated, experimental decompression runs using amphiboles and melts of more suitable compositions is required to obtain better constraints on magma ascent rates at the onset of eruption.
5. Timescales of magmatic processes may be estimated from the complex zoning patterns that are observed in the Taranaki crystals through diffusion modelling, as

well as other chronometers such as textural analysis of bubbles/ mineral phases and decay of radiogenic isotopes ([see Costa et al., 2020](#)). Elemental zoning such as Sr, Li, and Ba in plagioclase; Fe-Mg in clinopyroxene and Li in quartz. Future work on this topic may elucidate the timescale history of the crystal cargo.

6. The disparities seen between the summit and satellite eruptions may be attributed to the local faulting and tectonics of their sources are chemically similar. Future high resolution geophysical studies of Taranaki volcano may offer an important understanding of conduit geometry and also shed light on the potential influence of faulting on mush zone heterogeneity.

References

- Acocella, V., Neri, M., 2009. Dike propagation in volcanic edifices: overview and possible developments. *Tectonophysics* 471, 67-77.
- Alloway, B., Mc Comb, P., Neall, V., Vucetich, C., Gibb, J., Sherburn, S., Stirling, M., 2005a. Stratigraphy, age, and correlation of voluminous debris-avalanche events from an ancestral Egmont Volcano: Implications for coastal plain construction and regional hazard assessment. *Journal of the Royal Society of New Zealand* 35, 229-267.
- Alloway, B., Neall, V.E., Vucetich, C.G., 1995. Late Quaternary (post 28,000 year B.P.) tephrostratigraphy of northeast and central taranaki, New Zealand. *Journal of the Royal Society of New Zealand* 25, 385-458.
- Alloway, B.V., 1989. Late Quaternary cover-bed stratigraphy and tephrochronology of north-eastern and central Taranaki Region, New Zealand. Late Quaternary cover-bed stratigraphy and tephrochronology of north-eastern and central Taranaki.
- Alloway, B.V., Pillans, B.J., Carter, L., Naish, T.R., Westgate, J.A., 2005b. Onshore-offshore correlation of Pleistocene rhyolitic eruptions from New Zealand: Implications for TVZ eruptive history and paleoenvironmental construction. *Quaternary Science Reviews* 24, 1601-1622.
- Almeev, R.R., Holtz, F., Koepke, J., Parat, F., 2012. Experimental calibration of the effect of H₂O on plagioclase crystallization in basaltic melt at 200 MPa. *American Mineralogist* 97, 1234-1240.
- Anderson, H., Webb, T., 1994. New Zealand seismicity: Patterns revealed by the upgraded National Seismograph Network. *New Zealand Journal of Geology and Geophysics* 37, 477-493.
- Anderson, J.L., Smith, D.R., 1995. The effects of temperature and fO₂ on the Al-in-hornblende barometer. *American Mineralogist* 80, 549-559.
- Annen, C., Blundy, J.D., Sparks, R.S.J., 2006. The genesis of intermediate and silicic magmas in deep crustal hot zones. *Journal of Petrology* 47, 505-539.
- Annen, C., Sparks, R.S.J., 2002. Effects of repetitive emplacement of basaltic intrusions on thermal evolution and melt generation in the crust. *Earth and Planetary Science Letters* 203, 937-955.
- Armstrong, P.A., Allis, R.G., Funnell, R.H., Chapman, D.S., 1998. Late Neogene exhumation patterns in Taranaki Basin (New Zealand): Evidence from offset porosity-depth trends. *Journal of Geophysical Research: Solid Earth* 103, 30269-30282.
- Arpa, M.C., Zellmer, G.F., Christenson, B., Lube, G., Shellnutt, G., 2017. Variable magma reservoir depths for Tongariro Volcanic Complex eruptive deposits from 10,000 years to present. *Bulletin of Volcanology* 79, 56.
- Auker, M.R., Sparks, R.S.J., Siebert, L., Crosweller, H.S., Ewert, J., 2013. A statistical analysis of the global historical volcanic fatalities record. *Journal of Applied Volcanology* 2, 2.
- Bache, F., Sutherland, R., Stagpoole, V., Herzer, R., Collot, J., Rouillard, P., 2012. Stratigraphy of the southern Norfolk Ridge and the Reinga Basin: A record of initiation of Tonga–Kermadec–Northland subduction in the southwest Pacific. *Earth and Planetary Science Letters* 321-322, 41-53.
- Bachmann, O., Bergantz, G.W., 2008. Rhyolites and their source mushes across tectonic settings. *Journal of Petrology* 49, 2277-2285.

- Bachmann, O., Dungan, M.A., 2002. Temperature-induced Al-zoning in hornblendes of the Fish Canyon magma, Colorado. *American Mineralogist* 87, 1062-1076.
- Ballance, P.F., 1976. Evolution of the Upper Cenozoic Magmatic Arc and plate boundary in northern New Zealand. *Earth and Planetary Science Letters* 28, 356-370.
- Barclay, J., Herd, R.A., Edwards, B.R., Christopher, T., Kiddle, E.J., Plail, M., Donovan, A., 2010. Caught in the act: Implications for the increasing abundance of mafic enclaves during the recent eruptive episodes of the Soufrière Hills Volcano, Montserrat. *Geophysical Research Letters* 37.
- Barnes, P.M., Mercier De Lépinay, B., 1997. Rates and mechanics of rapid frontal accretion along the very obliquely convergent southern Hikurangi margin, New Zealand. *Journal of Geophysical Research B: Solid Earth* 102, 24931-24952.
- Beavan, J., Haines, J., 2001. Contemporary horizontal velocity and strain rate fields of the Pacific-Australian plate boundary zone through New Zealand. *Journal of Geophysical Research: Solid Earth* (1978–2012) 106, 741-770.
- Beavan, J., Moore, M., Pearson, C., Henderson, M., Parsons, B., Bourne, S., England, P., Walcott, D., Blick, G., Darby, D., Hodgkinson, K., 1999. Crustal deformation during 1994–1998 due to oblique continental collision in the central Southern Alps, New Zealand, and implications for seismic potential of the Alpine fault. *Journal of Geophysical Research: Solid Earth* (1978–2012) 104, 25233-25255.
- Bédard, J.H., 2014. Parameterizations of calcic clinopyroxene - Melt trace element partition coefficients. *Geochemistry, Geophysics, Geosystems* 15, 303-336.
- Behn, M.D., Kelemen, P.B., Hirth, G., Hacker, B.R., Massonne, H.-J., 2011. Diapirs as the source of the sediment signature in arc lavas. *Nature Geoscience* 4, 641-646.
- Beier, C., Haase, K.M., Brandl, P.A., Krumm, S.H., 2017. Primitive andesites from the Taupo Volcanic Zone formed by magma mixing. *Contributions to Mineralogy and Petrology* 172, 33.
- Bennett, E.N., Lissenberg, C.J., Cashman, K.V., 2019. The significance of plagioclase textures in mid-ocean ridge basalt (Gakkel Ridge, Arctic Ocean). *Contributions to Mineralogy and Petrology* 174.
- Bergantz, G.W., Schleicher, J.M., Burgisser, A., 2017. On the kinematics and dynamics of crystal-rich systems. *Journal of Geophysical Research: Solid Earth* 122, 6131-6159.
- Berlo, K., Turner, S., Blundy, J., Hawkesworth, C., 2004. The extent of U-series disequilibria produced during partial melting of the lower crust with implications for the formation of the Mount St. Helens dacites. *Contributions to Mineralogy and Petrology* 148, 122-130.
- Bindeman, I.N., Davis, A.M., 2000. Trace element partitioning between plagioclase and melt: investigation of dopant influence on partition behavior. *Geochimica et Cosmochimica Acta* 64, 2863-2878.
- Bindeman, I.N., Davis, A.M., Drake, M.J., 1998. Ion Microprobe Study of Plagioclase-Basalt Partition Experiments at Natural Concentration Levels of Trace Elements. *Geochimica et Cosmochimica Acta* 62, 1175-1193.
- Blatter, D.L., Carmichael, I.S.E., 2001. Hydrous phase equilibria of a Mexican high-silica andesite: A candidate for a mantle origin? *Geochimica et Cosmochimica Acta* 65, 4043-4065.
- Blundy, J., Cashman, K.V., Berlo, K., 2008. Evolving magma storage conditions beneath Mount St. Helens inferred from chemical variations in melt inclusions from the 1980-1986 and current (2004-2006) eruptions. *US Geological Survey Professional Paper*, 755-790.

- Blundy, J.D., Falloon, T.J., Wood, B.J., Dalton, J.A., 1995. Sodium partitioning between clinopyroxene and silicate melts. *Journal of Geophysical Research* 100, 15,501-515,515.
- Blundy, J.D., Holland, T.J.B., 1990. Calcic amphibole equilibria and a new amphibole-plagioclase geothermometer. *Contributions to Mineralogy and Petrology* 104, 208-224.
- Blundy, J.D., Wood, B.J., 1991. Crystal-chemical controls on the partitioning of Sr and Ba between plagioclase feldspar, silicate melts, and hydrothermal solutions. *Geochimica et Cosmochimica Acta* 55, 193-209.
- Boddington, T., Parkin, C.J., Gubbins, D., 2004. Isolated deep earthquakes beneath the North Island of New Zealand. *Geophysical Journal International* 158, 972-982.
- Bowen, N.L., 1913. The melting phenomena of the plagioclase feldspars. *American Journal of Science* 35, 577-599.
- Bradshaw, J., 1993. A review of the Median Tectonic Zone: terrane boundaries and terrane amalgamation near the Median Tectonic Line. *New Zealand Journal of Geology and Geophysics* 36, 117-125.
- Browne, B.L., 2005. Petrologic and experimental constraints on magma mingling and ascent: examples from Japan and Alaska. *Petrologic and experimental constraints on magma mingling and ascent; examples from Japan and Alaska*.
- Browne, B.L., Gardner, J.E., 2006. The influence of magma ascent path on the texture, mineralogy, and formation of hornblende reaction rims. *Earth and Planetary Science Letters* 246, 161-176.
- Brugger, C.R., Hammer, J.E., 2010. Crystallization kinetics in continuous decompression experiments: Implications for interpreting natural magma ascent processes. *Journal of Petrology* 51, 1941-1965.
- Buckley, V.J.E., Sparks, R.S.J., Wood, B.J., 2006. Hornblende dehydration reactions during magma ascent at Soufrière Hills Volcano, Montserrat. *Contributions to Mineralogy and Petrology* 151, 121-140.
- Calhaem, I.M., 1973. Asymmetric spreading from a volcanic arc to an active continental margin.
- Carmichael, I.S.E., 2002. The andesite aqueduct: Perspectives on the evolution of intermediate magmatism in west-central (105-99°W) Mexico. *Contributions to Mineralogy and Petrology* 143, 641-663.
- Carmichael, I.S.E., 2004. The activity of silica, water, and the equilibration of intermediate and silicic magmas. *American Mineralogist* 89, 1438-1446.
- Cashman, K., Blundy, J., 2000. Degassing and crystallization of ascending andesite and dacite. *Philosophical Transactions of the Royal Society A: Mathematical, Physical and Engineering Sciences* 358, 1487-1513.
- Cashman, K.V., Sparks, R.S.J., Blundy, J.D., 2017. Vertically extensive and unstable crystals mushes: a unifying view of igneous processes associated with volcanoes. *Science* 355.
- Castillo, P.R., Lonsdale, P.F., Moran, C.L., Hawkins, J.W., 2009. Geochemistry of mid-Cretaceous Pacific crust being subducted along the Tonga–Kermadec Trench: Implications for the generation of arc lavas. *Lithos* 112, 87-102.
- Castro, A., Gerya, T., García-Casco, A., Fernández, C., Díaz-Alvarado, J., Moreno-Ventas, I., Löw, I., 2010. Melting Relations of MORB–Sediment Mélanges in Underplated Mantle Wedge Plumes; Implications for the Origin of Cordilleran-type Batholiths. *Journal of Petrology* 51, 1267-1295.
- Charlier, B., Morgan, D., Wilson, C., Wooden, J., Allan, A., Baker, J., 2012. Lithium concentration gradients in feldspar and quartz record the final minutes of magma

- ascent in an explosive supereruption. *Earth and Planetary Science Letters* 319, 218-227.
- Charlier, B.L.A., Wilson, C.J.N., Lowenstern, J.B., Blake, S., van Calsteren, P.W., Davidson, J.P., 2005. Magma generation at a large, hyperactive silicic volcano (Taupo, New Zealand) revealed by U-Th and U-Pb systematics in zircons. *Journal of Petrology* 46, 3-32.
- Clarke, E.d.C., 1912. The geology of the New Plymouth subdivision, Taranaki. *New Zealand Geological Survey Bulletin* 14.
- Codillo, E.A., Le Roux, V., Marschall, H.R., 2018. Arc-like magmas generated by mélange-peridotite interaction in the mantle wedge. *Nature Communications* 9.
- Cole, J.W., 1979. Structure, petrology, and genesis of Cenozoic volcanism, Taupo Volcanic Zone, New Zealand—a review. *New Zealand Journal of Geology and Geophysics* 22, 631-657.
- Cole, J.W., Darby, D.J., Stern, T.A., 1995. Taupo Volcanic Zone and Central Volcanic region: Backarc structures of North Island, New Zealand. *Backarc Basins: Tectonics and Magmatism*, 1-28.
- Cole, J.W., Deering, C.D., Burt, R.M., Sewell, S., Shane, P.A.R., Matthews, N.E., 2014. Okataina Volcanic Centre, Taupo Volcanic Zone, New Zealand: A review of volcanism and synchronous pluton development in an active, dominantly silicic caldera system. *Earth-Science Reviews* 128, 1-17.
- Cole, J.W., Lewis, K.B., 1981. Evolution of the Taupo-Hikurangi subduction system. *Tectonophysics* 72, 1-21.
- Coogan, L.A., 2011. Preliminary experimental determination of the partitioning of lithium between plagioclase crystals of different anorthite contents. *Lithos* 125, 711-715.
- Coogan, L.A., Saunders, A.D., Kempton, P.D., Norry, M.J., 2000. Evidence from oceanic gabbros for porous melt migration within a crystal mush beneath the Mid-Atlantic Ridge. *Geochemistry, Geophysics, Geosystems* 1.
- Coombs, M.L., Sisson, T.W., Bleick, H.A., Henton, S.M., Nye, C.J., Payne, A.L., Cameron, C.E., Larsen, J.F., Wallace, K.L., Bull, K.F., 2013. Andesites of the 2009 eruption of Redoubt Volcano, Alaska. *Journal of Volcanology and Geothermal Research* 259, 349-372.
- Cooper, G.F., Morgan, D.J., Wilson, C.J., 2017. Rapid assembly and rejuvenation of a large silicic magmatic system: Insights from mineral diffusive profiles in the Kidnappers and Rocky Hill deposits, New Zealand. *Earth and Planetary Science Letters* 473, 1-13.
- Cooper, K.M., Kent, A.J.R., 2014. Rapid remobilization of magmatic crystals kept in cold storage. *Nature* 506, 480-483.
- Costa, F., Andreastuti, S., Bouvet de Maisonneuve, C., Pallister, J.S., 2013. Petrological insights into the storage conditions, and magmatic processes that yielded the centennial 2010 Merapi explosive eruption. *Journal of Volcanology and Geothermal Research* 261, 209-235.
- Costa, F., Dohmen, R., Chakraborty, S., 2008. Time scales of magmatic processes from modeling the zoning patterns of crystals, *Reviews in Mineralogy and Geochemistry*, pp. 545-594.
- Costa, F., Shea, T., Ubide, T., 2020. Diffusion chronometry and the timescales of magmatic processes. *Nature Reviews Earth and Environment* 1, 201-214.
- Crisp, J.A., 1984. Rates of magma emplacement and volcanic output. *Journal of Volcanology and Geothermal Research* 20, 177-211.

- Cronin, S.J., Zernack, A.V., Ukstins, I.A., Turner, M.B., Torres-Orozco, R., Stewart, R.B., Smith, I.E., Procter, J.N., Price, R., Platz, T., 2021. The geological history and hazards of a long-lived stratovolcano, Mt. Taranaki, New Zealand. *New Zealand Journal of Geology and Geophysics*, 1-23.
- Czamanske, G.K., Wones, D.R., 1973. Oxidation during magmatic differentiation, Finnmarka complex, Oslo Area, Norway: Part 2, the mafic silicates. *Journal of Petrology* 14, 349-380.
- D'Mello, N.G., Zellmer, G.F., Negrini, M., Kereszturi, G., Procter, J., Stewart, R., Prior, D., Usuki, M., Iizuka, Y., 2021. Deciphering magma storage and ascent processes of Taranaki, New Zealand, from the complexity of amphibole breakdown textures. *Lithos*, 106264.
- Damaschke, M., Cronin, S.J., Holt, K.A., Bebbington, M.S., Hogg, A.G., 2017a. A 30,000 yr high-precision eruption history for the andesitic Mt. Taranaki, North Island, New Zealand. *Quaternary Research (United States)* 87, 1-23.
- Damaschke, M., Cronin, S.J., Torres-Orozco, R., Wallace, R.C., 2017b. Unifying tephrostratigraphic approaches to redefine major Holocene marker tephras, Mt. Taranaki, New Zealand. *Journal of Volcanology and Geothermal Research* 337, 29-43.
- Danišik, M., Shane, P., Schmitt, A.K., Hogg, A., Santos, G.M., Storm, S., Evans, N.J., Keith Fifield, L., Lindsay, J.M., 2012. Re-anchoring the late Pleistocene tephrochronology of New Zealand based on concordant radiocarbon ages and combined $^{238}\text{U}/^{230}\text{Th}$ disequilibrium and (U-Th)/He zircon ages. *Earth and Planetary Science Letters* 349-350, 240-250.
- Davey, F.J., Hampton, M., Childs, J., Fisher, M.A., Lewis, K., Pettinga, J.R., 1986. Structure of a growing accretionary prism, Hikurangi margin, New Zealand. *Geology* 14, 663-666.
- Davies, R.B., Lambert, R.E., 2015. Under the Mountain- how a volcanic peak has influenced the culture, ecology and landscape history of Taranaki, New Zealand., *International Federation of landscape Architects Asia Pacific Congress (Ed.)*, Lombok, Indonesia, pp. 107-117.
- Davy, B., Wood, R., 1994. Gravity and magnetic modelling of the Hikurangi Plateau. *Marine Geology* 118, 139-151.
- De Angelis, S.H., Larsen, J., Coombs, M., 2013. Pre-eruptive magmatic conditions at Augustine volcano, Alaska, 2006: evidence from amphibole geochemistry and texture. *J Petrol* 0, 1-23.
- De Angelis, S.H., Larsen, J., Coombs, M., Dunn, A., Hayden, L., 2015. Amphibole reaction rims as a record of pre-eruptive magmatic heating: An experimental approach. *Earth and Planetary Science Letters* 426, 235-245.
- de Maisonneuve, C.B., Costa, F., Huber, C., Vonlanthen, P., Bachmann, O., Dungan, M.A., 2016. How do olivines record magmatic events? Insights from major and trace element zoning. *Contributions to Mineralogy and Petrology* 171.
- Deering, C.D., Bachmann, O., Dufek, J., Gravley, D.M., 2011. Rift-related transition from andesite to rhyolite volcanism in the Taupo volcanic zone (New Zealand) controlled by crystal-melt dynamics in mush zones with variable mineral assemblages. *Journal of Petrology* 52, 2243-2263.
- Degruyter, W., Huber, C., Bachmann, O., Cooper, K.M., Kent, A.J.R., 2016. Magma reservoir response to transient recharge events: The case of Santorini volcano (Greece). *Geology* 44, 23-26.
- DeMets, C., Gordon, R.G., Argus, D.F., 2010. Geologically current plate motions. *Geophysical Journal International* 181, 1-80.

- Devine, J.D., Rutherford, M.J., Gardner, J.E., 1998. Petrologic determination of ascent rates for the 1995–1997 Soufriere Hills Volcano andesitic magma. *Geophysical Research Letters* 25, 3673-3676.
- Dimech, J., Stern, T., Lamb, S., 2017. Mantle earthquakes, crustal structure, and gravitational instability beneath western North Island, New Zealand. *Geology* 45, 155-158.
- Downes, M.J., 1974. Sector and oscillatory zoning in calcic augites from M. Etna, Sicily. *Contributions to Mineralogy and Petrology* 47, 187-196.
- Downey, W.S., Kellett, R.J., Smith, I.E.M., Price, R.C., Stewart, R.B., 1994. New palaeomagnetic evidence for the recent eruptive activity of Mt. Taranaki, New Zealand. *Journal of Volcanology and Geothermal Research* 60, 15-27.
- Drake, M.J., 1976. Plagioclase-melt equilibria. *Geochimica et Cosmochimica Acta* 40, 457-465.
- Druce, A.P., 1966. Tree-ring dating of recent volcanic ash and Lapilli, Mt Egmont. *New Zealand Journal of Botany* 4, 3-41.
- Druitt, T.H., Bacon, C.R., 1989. Petrology of the zoned calcalkaline magma chamber of Mount Mazama, Crater Lake, Oregon. *Contributions to Mineralogy and Petrology* 101, 245-259.
- Earnshaw, A., Greenwood, N.N., 1997. *Chemistry of the Elements*. Butterworth-Heinemann Oxford.
- Eberhart-Phillips, D., Reyners, M., 2001. A complex, young subduction zone imaged by three-dimensional seismic velocity, Fiordland, New Zealand. *Geophysical Journal International* 146, 731-746.
- Edmonds, M., Cashman, K.V., Holness, M., Jackson, M., 2019. *Architecture and dynamics of magma reservoirs*. The Royal Society Publishing.
- Elardo, S.M., Shearer, C.K., 2014. Magma chamber dynamics recorded by oscillatory zoning in pyroxene and olivine phenocrysts in basaltic lunar meteorite Northwest Africa 032. *American Mineralogist* 99, 355-368.
- Elliott, T., Plank, T., Zindler, A., White, W., Bourdon, B., 1997. Element transport from slab to volcanic front at the Mariana arc. *Journal of Geophysical Research B: Solid Earth* 102, 14991-15019.
- England, P.C., Katz, R.F., 2010. Melting above the anhydrous solidus controls the location of volcanic arcs. *Nature* 467, 700-703.
- Erdmann, S., Martel, C., Pichavant, M., Kushnir, A., 2014. Amphibole as an archivist of magmatic crystallization conditions: problems, potential, and implications for inferring magma storage prior to the paroxysmal 2010 eruption of Mount Merapi, Indonesia. *Contributions to Mineralogy and Petrology* 167, 1016.
- Ernst, W.G., 1998. Experimental phase-equilibrium study of Al- and Ti-contents of calcic amphibole in MORB-A semiquantitative thermobarometer. *American Mineralogist* 83, 952-969.
- Errázuriz-Henao, C., Gómez-Tuena, A., Duque-Trujillo, J., Weber, M., 2019. The role of subducted sediments in the formation of intermediate mantle-derived magmas from the Northern Colombian Andes. *Lithos* 336-337, 151-168.
- Ersoy, Y., Helvacı, C., 2010. FC–AFC–FCA and mixing modeler: a Microsoft® Excel® spreadsheet program for modeling geochemical differentiation of magma by crystal fractionation, crustal assimilation and mixing. *Computers & Geosciences* 36, 383-390.
- Féménias, O., Mercier, J.C.C., Nkono, C., Diot, H., Berza, T., Tatu, M., Demaiffe, D., 2006. Calcic amphibole growth and compositions in calc-alkaline magmas:

- Evidence from the Motru Dike Swarm (Southern Carpathians, Romania). *American Mineralogist* 91, 73-81.
- First, E.C., Hammer, J.E., Ruprecht, P., Rutherford, M., 2021. Experimental constraints on dacite magma storage beneath Volcán Quizapu, Chile. *Journal of Petrology*.
- Foden, J.D., Green, D.H., 1992. Possible role of amphibole in the origin of andesite: some experimental and natural evidence. *Contributions to Mineralogy and Petrology* 109, 479-493.
- Frost, C., Coombs, D., 1989. Nd isotope character of New Zealand sediments; implications for terrane concepts and crustal evolution. *American Journal of Science* 289, 744-770.
- Funnell, R., Chapman, D., Allis, R., Armstrong, P., 1996. Thermal state of the Taranaki Basin, New Zealand. *Journal of Geophysical Research: Solid Earth* (1978–2012) 101, 25197-25215.
- Furlong, K.P., Kamp, P.J.J., 2009. The lithospheric geodynamics of plate boundary transpression in New Zealand: Initiating and emplacing subduction along the Hikurangi margin, and the tectonic evolution of the Alpine Fault system. *Tectonophysics* 474, 449-462.
- Ganne, J., Bachmann, O., Feng, X., 2018. Deep into magma plumbing systems: Interrogating the crystal cargo of volcanic deposits. *Geology* 46, 415-418.
- Garcia, M.O., Jacobson, S.S., 1979. Crystal clots, amphibole fractionation and the evolution of calc-alkaline magmas. *Contributions to Mineralogy and Petrology* 69, 319-327.
- Gaylord, D.R., Neall, V.E., Palmer, A.S., 2014. The Middle Pleistocene Maitahi Formation, Taranaki, New Zealand: a new formal lithostratigraphic unit. *New Zealand Journal of Geology and Geophysics* 57, 369-377.
- Genareau, K., Clarke, A.B., 2010. In situ measurements of plagioclase growth using SIMS depth profiles of $7\text{Li}/30\text{Si}$: A means to acquire crystallization rates during short-duration decompression events. *American Mineralogist* 95, 592-601.
- Genareau, K., Clarke, A.B., Hervig, R.L., 2009. New insight into explosive volcanic eruptions: Connecting crystal-scale chemical changes with conduit-scale dynamics. *Geology* 37, 367-370.
- Genareau, K., Cronin, S.J., Lube, G., 2015. Effects of volatile behaviour on dome collapse and resultant pyroclastic surge dynamics: Gunung Merapi 2010 eruption. Geological Society, London, Special Publications 410, 199-218.
- Gerya, T.V., Yuen, D.A., 2003. Rayleigh - Taylor instabilities from hydration and melting propel 'cold plumes' at subduction zones. *Earth and Planetary Science Letters* 212, 47-62.
- Giba, M., Nicol, A., Walsh, J.J., 2010. Evolution of faulting and volcanism in a back-arc basin and its implications for subduction processes. *Tectonics* 29.
- Giggenbach, W.F., 1995. Variations in the chemical and isotopic composition of fluids discharged from the Taupo Volcanic Zone, New Zealand. *Journal of Volcanology and Geothermal Research* 68, 89-116.
- Giletti, B.J., Casserly, J.E.D., 1994. Strontium diffusion kinetics in plagioclase feldspars. *Geochimica et Cosmochimica Acta* 58, 3785-3793.
- Giletti, B.J., Shanahan, T.M., 1997. Alkali diffusion in plagioclase feldspar. *Chemical Geology* 139, 3-20.
- Gill, J.B., 1981. Orogenic Andesites and Plate Tectonics. *Orogenic Andesites and Plate Tectonics*.
- Ginibre, C., Kronz, A., Wörner, G., 2002a. High-resolution quantitative imaging of plagioclase composition using accumulated backscattered electron images: New

- constraints on oscillatory zoning. *Contributions to Mineralogy and Petrology* 142, 436-448.
- Ginibre, C., Wörner, G., Kronz, A., 2002b. Minor- and trace-element zoning in plagioclase: Implications for magma chamber processes at Parinacota volcano, northern Chile. *Contributions to Mineralogy and Petrology* 143, 300-315.
- Ginibre, C., Wörner, G., Kronz, A., 2007. Crystal zoning as an archive for magma evolution. *Elements* 3, 261-266.
- Giuffrida, M., Viccaro, M., Ottolini, L., 2018. Ultrafast syn-eruptive degassing and ascent trigger high-energy basic eruptions. *Scientific reports* 8, 1-7.
- Gómez-Tuena, A., Cavazos-Tovar, J.G., Parolari, M., Straub, S.M., Espinasa-Pereña, R., 2018. Geochronological and geochemical evidence of continental crust 'relamination' in the origin of intermediate arc magmas. *Lithos* 322, 52-66.
- Gómez-Tuena, A., Straub, S.M., Zellmer, G.F., 2014. An introduction to orogenic andesites and crustal growth. Geological Society, London, Special Publications 385, 1-13.
- Gonnermann, H.M., Manga, M., 2013. Dynamics of magma ascent. *Modeling volcanic processes: The physics and mathematics of volcanism* 55.
- Gow, A.J., 1968. Petrographic and petrochemical studies of MT Egmont andesites. *New Zealand Journal of Geology and Geophysics* 11, 166-190.
- Graham, I.J., Hackett, W.R., 1987. Petrology of calc-alkaline lavas from ruapehu volcano and related vents, taupo volcanic zone, New Zealand. *Journal of Petrology* 28, 531-567.
- Grant-Taylor, T.L., 1964. Volcanic history of Western Taranaki. *New Zealand Journal of Geology and Geophysics* 7, 78-86.
- Green, R.M., Bebbington, M.S., Cronin, S.J., Jones, G., 2013. Geochemical precursors for eruption repose length. *Geophysical Journal International* 193, 855-873.
- Grove, T.L., Donnelly-Nolan, J.M., Housh, T., 1997. Magmatic processes that generated the rhyolite of Glass Mountain, Medicine Lake volcano, N. California. *Contributions to Mineralogy and Petrology* 127, 205-223.
- Grove, T.L., Kinzler, R.J., Bryan, W.B., 1992. Fractionation of mid-ocean ridge basalt (MORB). *Mantle Flow and Melt Generation at Mid-Ocean Ridges* 71, 281-310.
- Grove, T.L., Till, C.B., Lev, E., Chatterjee, N., Médard, E., 2009. Kinematic variables and water transport control the formation and location of arc volcanoes. *Nature* 459, 694-697.
- Gruender, K., Stewart, R.B., Foley, S., 2010. Xenoliths from the sub-volcanic lithosphere of Mt Taranaki, New Zealand. *Journal of Volcanology and Geothermal Research* 190, 192-202.
- Gualda, G.A.R., Ghiorso, M.S., Lemons, R.V., Carley, T.L., 2012. Rhyolite-MELTS: A modified calibration of MELTS optimized for silica-rich, fluid-bearing magmatic systems. *Journal of Petrology* 53, 875-890.
- Hammarstrom, J.M., Zen, E., 1986. Aluminum in hornblende: an empirical igneous geobarometer. *American Mineralogist* 71, 1297-1313.
- Hammer, J.E., Rutherford, M.J., 2002. An experimental study of the kinetics of decompression-induced crystallization in silicic melt. *Journal of Geophysical Research: Solid Earth* 107, 8-1 - 8-24.
- Hammer, J.E., Rutherford, M.J., Hildreth, W., 2002. Magma storage prior to the 1912 eruption at Novarupta, Alaska. *Contributions to Mineralogy and Petrology* 144, 144-162.
- Hao, L.-L., Wang, Q., Wyman, D.A., Ou, Q., Dan, W., Jiang, Z.-Q., Yang, J.-H., Li, J., Long, X.-P., 2016. Andesitic crustal growth via mélange partial melting: Evidence

- from Early Cretaceous arc dioritic/andesitic rocks in southern Qiangtang, central Tibet. *Geochemistry, Geophysics, Geosystems* 17, 1641-1659.
- Hart, S.R., 1984. A large-scale isotope anomaly in the Southern Hemisphere mantle. *Nature* 309, 753-757.
- Hawthorne, F.C., Oberti, R., Harlow, G.E., Maresch, W.V., Martin, R.F., Schumacher, J.C., Welch, M.D., 2012. Nomenclature of the amphibole supergroup. *American Mineralogist* 97, 2031-2048.
- Heiken, G., Eichelberger, J.C., 1980. Eruptions at Chaos Crags, Lassen Volcanic National Park, California. *Journal of Volcanology and Geothermal Research* 7, 443-481.
- Herzer, R.H., 1995. Seismic stratigraphy of a buried volcanic arc, Northland, New Zealand and implications for Neogene subduction. *Marine and Petroleum Geology* 12, 511-531.
- Higgins, M.D., 1996. Crystal size distributions and other quantitative textural measurements in lavas and tuff from Egmont volcano (Mt. Taranaki), New Zealand. *Bulletin of Volcanology* 58, 194-204.
- Higgins, O.J., Sheldrake, T., Caricchi, L., 2021. Machine learning thermobarometry and chemometry using amphibole and clinopyroxene: a window into the roots of an arc volcano (Mount Liamuiga, Saint Kitts).
- Hildreth, W., Moorbath, S., 1988. Crustal contributions to arc magmatism in the Andes of Central Chile. *Contributions to Mineralogy and Petrology* 98, 455-489.
- Hirose, K., 1997. Melting experiments on lherzolite KLB-1 under hydrous conditions and generation of high-magnesian andesitic melts. *Geology* 25, 42-44.
- Holland, T., Blundy, J., 1994. Non-ideal interactions in calcic amphiboles and their bearing on amphibole-plagioclase thermometry. *Contributions to Mineralogy and Petrology* 116, 433-447.
- Hollister, L.S., Gancarz, A.J., 1971. Compositional sector-zoning in clinopyroxene from the Narce area, Italy. *Am. Mineral.* 56, 959-979.
- Hollister, L.S., Grissom, G.C., Peters, E.K., Stowell, H.H., Sisson, V.B., 1987. Confirmation of the empirical correlation of Al in hornblende with pressure of solidification of calc-alkaline plutons. *American Mineralogist* 72, 231-239.
- Holness, M.B., Anderson, A.T., Martin, V.M., MacLennan, J., Passmore, E., Schwindinger, K., 2007a. Textures in partially solidified crystalline nodules: A window into the pore structure of slowly cooled mafic intrusions. *Journal of Petrology* 48, 1243-1264.
- Holness, M.B., Stock, M.J., Geist, D., 2019. Magma chambers versus mush zones: Constraining the architecture of sub-volcanic plumbing systems from microstructural analysis of crystalline enclaves. *Philosophical Transactions of the Royal Society A: Mathematical, Physical and Engineering Sciences* 377.
- Holness, M.B., Tegner, C., Nielsen, T.F.D., Stripp, G., Morse, S.A., 2007b. A textural record of solidification and cooling in the skaergaard intrusion, East Greenland. *Journal of Petrology* 48, 2359-2377.
- Holt, W.E., Stern, T.A., 1994. Subduction, platform subsidence, and foreland thrust loading: The late Tertiary development of Taranaki Basin, New Zealand. *Tectonics* 13, 1068-1092.
- Humphreys, M.C.S., Blundy, J.D., Sparks, R.S.J., 2006. Magma evolution and open-system processes at Shiveluch Volcano: Insights from phenocryst zoning. *Journal of Petrology* 47, 2303-2334.
- Hutton, F.W., 1889. The eruptive rocks of New Zealand. *Journal of the Royal Society NSW* 23, 102-156.

- Ishizuka, O., Uto, K., Yuasa, M., 2003. Volcanic history of the back-arc region of the Izu-Bonin (Ogasawara) arc, Geological Society Special Publication, pp. 187-205.
- Jackson, M.D., Cheadle, M.J., Atherton, M.P., 2003. Quantitative modeling of granitic melt generation and segregation in the continental crust. *Journal of Geophysical Research: Solid Earth* 108, 3-1 - 3-21.
- Jacoby, W.R., 1973. Model experiment of plate movements. *Nature Physical Science* 242, 130-134.
- James, M.R., Robson, S., 2012. Straightforward reconstruction of 3D surfaces and topography with a camera: Accuracy and geoscience application. *Journal of Geophysical Research: Earth Surface* 117.
- Jarosewich, E., Nelen, J.A., Norberg, J.A., 1980. Reference Samples for Electron Microprobe Analysis. *Geostandards Newsletter* 4, 43-47.
- Jeffery, A., Gertisser, R., Troll, V., Jolis, E., Dahren, B., Harris, C., Tindle, A., Preece, K., O'Driscoll, B., Humaida, H., 2013. The pre-eruptive magma plumbing system of the 2007–2008 dome-forming eruption of Kelut volcano, East Java, Indonesia. *Contributions to Mineralogy and Petrology* 166, 275-308.
- Jiao, R., Herman, F., Seward, D., 2017. Late Cenozoic exhumation model of New Zealand: Impacts from tectonics and climate. *Earth-Science Reviews* 166, 286-298.
- Johannes, W., Koepke, J., Behrens, H., 1994. Partial melting reactions of plagioclases and plagioclase-bearing systems. *Feldspars and Their Reactions*, 161-194.
- Johnson, M.C., Rutherford, M.J., 1989. Experimental calibration of the aluminum-in-hornblende geobarometer with application of Long Valley caldera (California) volcanic rocks. *Geology* 17, 837-841.
- Kahl, M., Chakraborty, S., Costa, F., Pompilio, M., 2011. Dynamic plumbing system beneath volcanoes revealed by kinetic modeling, and the connection to monitoring data: An example from Mt. Etna. *Earth and Planetary Science Letters* 308, 11-22.
- Kahl, M., Viccaro, M., Ubide, T., Morgan, D.J., Dingwell, D.B., 2017. A branched magma feeder system during the 1669 eruption of Mt Etna: Evidence from a time-integrated study of zoned olivine phenocryst populations. *Journal of Petrology* 58, 443-472.
- Karig, D.E., 1970. Kermadec arc—new zealand tectonic confluence. *New Zealand Journal of Geology and Geophysics* 13, 21-29.
- Kelemen, P.B., Hanghoj, K., Hacker, B., 2005. Melt of subducting sediment and basalt is a component in arc magmas worldwide, pp. V34A-08.
- Kent, A.J., Blundy, J., Cashman, K.V., Cooper, K.M., Donnelly, C., Pallister, J.S., Reagan, M., Rowe, M.C., Thornber, C.R., 2007. Vapor transfer prior to the October 2004 eruption of Mount St. Helens, Washington. *Geology* 35, 231-234.
- Kent, A.J.R., 2014. Preferential eruption of andesitic magmas: Implications for volcanic magma fluxes at convergent margins, Geological Society Special Publication, pp. 257-280.
- Kilgour, G., Blundy, J., Cashman, K., Mader, H.M., 2013. Small volume andesite magmas and melt-mush interactions at Ruapehu, New Zealand: Evidence from melt inclusions. *Contributions to Mineralogy and Petrology* 166, 371-392.
- Kilgour, G., Mader, H., 2014. Rheological controls on the eruption style and size of historical eruptions from Mt. Ruapehu, New Zealand. *EGUGA*, 4677.
- Kimbrough, D., Tulloch, A., Coombs, D., Landis, C., Johnston, M., Mattinson, J., 1994. Uranium-lead zircon ages from the median tectonic zone, New Zealand. *New Zealand Journal of Geology and Geophysics* 37, 393-419.

- King, P.R., 2000. Tectonic reconstructions of New Zealand: 40 Ma to the Present. *New Zealand Journal of Geology and Geophysics* 43, 611-638.
- King, P.R., Thrasher, G.P., 1996. Cretaceous-Cenozoic geology and petroleum systems of the Taranaki Basin, New Zealand. *Monogr.* 13.
- Kiss, B., Harangi, S., Ntaflos, T., Mason, P.R., Pál-Molnár, E., 2014. Amphibole perspective to unravel pre-eruptive processes and conditions in volcanic plumbing systems beneath intermediate arc volcanoes: a case study from Ciomadul volcano (SE Carpathians). *Contributions to Mineralogy and Petrology* 167, 986.
- Knox, G.J., 1982. Taranaki Basin, structural style and tectonic setting. *New Zealand Journal of Geology and Geophysics* 25, 125-140.
- Krawczynski, M.J., Grove, T.L., Behrens, H., 2012. Amphibole stability in primitive arc magmas: Effects of temperature, H₂O content, and oxygen fugacity. *Contributions to Mineralogy and Petrology* 164, 317-339.
- Lamarche, G., Lebrun, J.F., 2000. Transition from strike-slip faulting to oblique subduction: Active tectonics at the Puysegur Margin, South New Zealand. *Tectonophysics* 316, 67-89.
- Lange, A.E., Nielsen, R.L., Tepley, F.J., Kent, A.J.R., 2013. The petrogenesis of plagioclase-phyric basalts at mid-ocean ridges. *Geochemistry, Geophysics, Geosystems* 14, 3282-3296.
- Larrea, P., França, Z., Lago, M., Widom, E., Galé, C., Ubide, T., 2013. Magmatic processes and the role of antecrysts in the genesis of corvo island (azores archipelago, portugal). *Journal of Petrology* 54, 769-793.
- Larsen, J.F., Nye, C.J., Coombs, M.L., Tilman, M., Izbekov, P., Cameron, C., 2010. Petrology and geochemistry of the 2006 eruption of Augustine Volcano. *US Geological Survey Professional Paper*, 335-371.
- Le Maitre, R.W., 1989. *A Classification of Igneous Rocks and Glossary of Terms*.
- Le Maitre, R.W., 2002. *Igneous Rocks: A Classification and Glossary of Terms*. 236.
- Lerner, G.A., Cronin, S.J., Bebbington, M.S., Platz, T., 2019a. The characteristics of a multi-episode volcanic regime: the post-AD 960 Maero Eruptive Period of Mt. Taranaki (New Zealand). *Bulletin of Volcanology* 81, 1-24.
- Lerner, G.A., Cronin, S.J., Turner, G.M., Rowe, M.C., 2019b. Paleomagnetic determination of the age and properties of the 1780–1800 AD dome effusion/collapse episode of Mt. Taranaki, New Zealand. *Bulletin of Volcanology* 81, 15.
- Leung, I.S., 1974. Sector-zoned titanite: Morphology, crystal chemistry, and growth. *Am. Mineral.* 59, 127-138.
- Lewis, K., Pantin, H., 1984. Intersection of a marginal basin with a continent: structure and sediments of the Bay of Plenty, New Zealand. *Geological Society, London, Special Publications* 16, 121-135.
- Lissenberg, C.J., MacLeod, C.J., 2016. A reactive porous flow control on mid-ocean ridge magmatic evolution. *Journal of Petrology* 57, 2195-2220.
- Liu, Y., Anderson, A.T., Wilson, C.J.N., 2007. Melt pockets in phenocrysts and decompression rates of silicic magmas before fragmentation. *Journal of Geophysical Research: Solid Earth* 112.
- Locke, C.A., Cassidy, J., 1997. Egmont Volcano, New Zealand: three-dimensional structure and its implications for evolution. *Journal of Volcanology and Geothermal Research* 76, 149-161.
- Locke, C.A., Cassidy, J., MacDonald, A., 1993. Three-dimensional structure of relict stratovolcanoes in Taranaki, New Zealand: evidence from gravity data. *Journal of Volcanology and Geothermal Research* 59, 121-130.

- Locke, C.A., Cassidy, J., MacDonald, A., 1994. Constraints on the evolution of the Taranaki volcanoes, New Zealand, based on aeromagnetic data. *Bulletin of Volcanology* 56, 552-560.
- Locock, A.J., 2014. An Excel spreadsheet to classify chemical analyses of amphiboles following the IMA 2012 recommendations. *Computers & Geosciences* 62, 1-11.
- Lofgren, G.E., Huss, G.R., Wasserburg, G.J., 2006. An experimental study of trace-element partitioning between Ti-Al-clinopyroxene and melt: Equilibrium and kinetic effects including sector zoning. *American Mineralogist* 91, 1596-1606.
- Longhi, J., Fram, M.S., Vander Auwera, J., Montieth, J.N., 1993. Pressure effects, kinetics, and rheology of anorthositic and related magmas. *American Mineralogist* 78, 1016-1030.
- Lormand, C., Zellmer, G., Kilgour, G., Németh, K., Palmer, A., Sakamoto, N., Yurimoto, H., Kuritani, T., Iizuka, Y., Moebis, A., 2020. Slow ascent of unusually hot intermediate magmas triggering Strombolian to sub-Plinian eruptions. *Journal of Petrology*.
- Marschall, H.R., Schumacher, J.C., 2012. Arc magmas sourced from mélange diapirs in subduction zones. *Nature Geoscience* 5, 862.
- Marshall, P., 1908. geology of centre and north of North Island. *Transactions of the Royal Society of New Zealand* 40, 79-98.
- Martel, C., Brooker, R., Andújar, J., Pichavant, M., Scaillet, B., Blundy, J., 2017. Experimental simulations of magma storage and ascent. *Volcanic Unrest*, 101-110.
- Masotta, M., Mollo, S., 2019. A new plagioclase-liquid hygrometer specific to trachytic systems. *Minerals* 9, 375.
- Masotta, M., Pontesilli, A., Mollo, S., Armienti, P., Ubide, T., Nazzari, M., Scarlato, P., 2020. The role of undercooling during clinopyroxene growth in trachybasaltic magmas: Insights on magma decompression and cooling at Mt. Etna volcano. *Geochimica et Cosmochimica Acta* 268, 258-276.
- Mastin, L.G., Ghiorso, M.S., 2001. Adiabatic temperature changes of magma-gas mixtures during ascent and eruption. *Contributions to Mineralogy and Petrology* 141, 307-321.
- Matthews, N., Pyle, D., Smith, V., Wilson, C., Huber, C., Van Hinsberg, V., 2012. Quartz zoning and the pre-eruptive evolution of the ~ 340-ka Whakamaru magma systems, New Zealand. *Contributions to Mineralogy and Petrology* 163, 87-107.
- McCanta, M.C., Rutherford, M.J., Hammer, J.E., 2007. Pre-eruptive and syn-eruptive conditions in the Black Butte, California dacite: Insight into crystallization kinetics in a silicic magma system. *Journal of Volcanology and Geothermal Research* 160, 263-284.
- McGlone, M.S., Neall, V.E., Clarkson, B.D., 1988. The effect of recent volcanic events and climatic changes on the vegetation of Mt Egmont (Mt Taranaki), New Zealand. *New Zealand Journal of Botany* 26, 123-144.
- Melekhova, E., Annen, C., Blundy, J., 2013. Compositional gaps in igneous rock suites controlled by magma system heat and water content. *Nature Geoscience* 6, 385-390.
- Miller, J., Matzel, J., Miller, C., Burgess, S., Miller, R., 2007. Zircon growth and recycling during the assembly of large, composite arc plutons. *Journal of Volcanology and Geothermal Research* 167, 282-299.
- Mojtaba, R., Moritz, Z., Mark, T., Oliver, H., Scott, R., 2016. Contemporary tectonic stress pattern of the Taranaki Basin, New Zealand. *Journal of Geophysical Research: Solid Earth* 121, 6053-6070.

- Molina, J.F., Moreno, J.A., Castro, A., Rodríguez, C., Fershtater, G.B., 2015. Calcic amphibole thermobarometry in metamorphic and igneous rocks: New calibrations based on plagioclase/amphibole Al-Si partitioning and amphibole/liquid Mg partitioning. *Lithos* 232, 286-305.
- Mollo, S., Blundy, J.D., Giacomoni, P., Nazzari, M., Scarlato, P., Coltorti, M., Langone, A., Andronico, D., 2017. Clinopyroxene-melt element partitioning during interaction between trachybasaltic magma and siliceous crust: Clues from quartzite enclaves at Mt. Etna volcano. *Lithos* 284-285, 447-461.
- Mollo, S., Blundy, J.D., Iezzi, G., Scarlato, P., Langone, A., 2013a. The partitioning of trace elements between clinopyroxene and trachybasaltic melt during rapid cooling and crystal growth. *Contributions to Mineralogy and Petrology* 166, 1633-1654.
- Mollo, S., Del Gaudio, P., Ventura, G., Iezzi, G., Scarlato, P., 2010. Dependence of clinopyroxene composition on cooling rate in basaltic magmas: Implications for thermobarometry. *Lithos* 118, 302-312.
- Mollo, S., Giacomoni, P.P., Coltorti, M., Ferlito, C., Iezzi, G., Scarlato, P., 2015. Reconstruction of magmatic variables governing recent Etnean eruptions: Constraints from mineral chemistry and P-T-fO₂-H₂O modeling. *Lithos* 212-215, 311-320.
- Mollo, S., Hammer, J., 2017. Dynamic crystallization in magmas. *EMU Notes Mineral* 16, 373-418.
- Mollo, S., Putirka, K., Misiti, V., Soligo, M., Scarlato, P., 2013b. A new test for equilibrium based on clinopyroxene-melt pairs: Clues on the solidification temperatures of Etnean alkaline melts at post-eruptive conditions. *Chemical Geology* 352, 92-100.
- Mollo, S., Ubide, T., Di Stefano, F., Nazzari, M., Scarlato, P., 2020. Polybaric/polythermal magma transport and trace element partitioning recorded in single crystals: A case study of a zoned clinopyroxene from Mt. Etna. *Lithos* 356-357.
- Morgan, P.M.G., W., 1927. The geology of Egmont subdivision, Taranaki. *New Zealand Geological Survey Bulletin* 65, 1007-1032.
- Morimoto, N., 1988. Nomenclature of Pyroxenes. *Mineralogy and Petrology* 39, 55-76.
- Mortazavi, M., Sparks, R.S.J., 2004. Origin of rhyolite and rhyodacite lavas and associated mafic inclusions of Cape Akrotiri, Santorini: The role of wet basalt in generating calcalkaline silicic magmas. *Contributions to Mineralogy and Petrology* 146, 397-413.
- Mortimer, N., Campbell, H.J., Tulloch, A.J., King, P.R., Stagpoole, V.M., Wood, R.A., Rattenbury, M.S., Sutherland, R., Adams, C.J., Collot, J., 2017. Zealandia: Earth's hidden continent. *GSA Today* 27, 27-35.
- Mortimer, N., Gans, P., Calvert, A., Walker, N., 1999a. Geology and thermochronometry of the east edge of the Median Batholith (Median Tectonic Zone): A new perspective on Permian to Cretaceous crustal growth of New Zealand. *Island Arc* 8, 404-425.
- Mortimer, N., Gans, P.B., Palin, J.M., Meffre, S., Herzer, R.H., Skinner, D.N.B., 2010. Location and migration of Miocene-Quaternary volcanic arcs in the SW Pacific region. *Journal of Volcanology and Geothermal Research* 190, 1-10.
- Mortimer, N., Tulloch, A.J., Ireland, T.R., 1997. Basement geology of Taranaki and Wanganui Basins, New Zealand. *New Zealand Journal of Geology and Geophysics* 40, 223-236.

- Mortimer, N., Tulloch, A.J., Spark, R.N., Walker, N.W., Ladley, E., Allibone, A., Kimbrough, D.L., 1999b. Overview of the Median Batholith, New Zealand: A new interpretation of the geology of the Median Tectonic Zone and adjacent rocks. *Journal of African Earth Sciences* 29, 257-268.
- Moune, S., Sigmarsson, O., Schiano, P., Thordarson, T., Keiding, J., 2012. Melt inclusion constraints on the magma source of Eyjafjallajökull 2010 flank eruption. *Journal of Geophysical Research: Solid Earth* 117.
- Müntener, O., Kelemen, P.B., Grove, T.L., 2001. The role of H₂O during crystallization of primitive arc magmas under uppermost mantle conditions and genesis of igneous pyroxenites: An experimental study. *Contributions to Mineralogy and Petrology* 141, 643-658.
- Müntener, O., Ulmer, P., 2018. Arc crust formation and differentiation constrained by experimental petrology. *American Journal of Science* 318, 64-89.
- Murphy, M.D., Sparks, R.S.J., Barclay, J., Carroll, M.R., Brewer, T.S., 2000. Remobilization of andesite magma by intrusion of mafic magma at the Soufriere Hills volcano, Montserrat, West Indies. *Journal of Petrology* 41, 21-42.
- Mutch, E., Blundy, J., Tattitch, B., Cooper, F., Brooker, R., 2016. An experimental study of amphibole stability in low-pressure granitic magmas and a revised Al-in-hornblende geobarometer. *Contributions to Mineralogy and Petrology* 171, 85.
- Myers, M.L., Wallace, P.J., Wilson, C.J., Watkins, J.M., Liu, Y., 2018. Ascent rates of rhyolitic magma at the onset of three caldera-forming eruptions. *American Mineralogist* 103, 952-965.
- Nakamura, M., 1995a. Continuous mixing of crystal mush and replenished magma in the ongoing Unzen eruption. *Geology* 23, 807-810.
- Nakamura, M., 1995b. Residence time and crystallization history of nickeliferous olivine phenocrysts from the northern Yatsugatake volcanoes, Central Japan: Application of a growth and diffusion model in the system Mg-Fe-Ni. *Journal of Volcanology and Geothermal Research* 66, 81-100.
- Nakamura, M., Shimakita, S., 1998. Dissolution origin and syn-entrapment compositional change of melt inclusion in plagioclase. *Earth and Planetary Science Letters* 161, 119-133.
- Namur, O., Charlier, B., Toplis, M.J., Vander Auwera, J., 2012. Prediction of plagioclase-melt equilibria in anhydrous silicate melts at 1-atm. *Contributions to Mineralogy and Petrology* 163, 133-150.
- Nandedkar, R.H., Ulmer, P., Müntener, O., 2014. Fractional crystallization of primitive, hydrous arc magmas: An experimental study at 0.7 GPa. *Contributions to Mineralogy and Petrology* 167, 1-27.
- Neall, V.E., 1971. Volcanic domes and lineations in Egmont national park. *New Zealand Journal of Geology and Geophysics* 14, 71-81.
- Neall, V.E., 1972. Tephrochronology and tephrostratigraphy of western Taranaki (N108-109), New Zealand. *New Zealand Journal of Geology and Geophysics* 15, 507-545.
- Neall, V.E., 1979. Sheets P19, P20, and P21. New Plymouth, Egmont and Maniaia. 1st ed. Geological map of New Zealand 1:50,000. New Zealand Geological Survey.
- Neall, V.E., Stewart, R.B., Smith, I.E.M., 1986. History and petrology of the Taranaki volcanoes. *Late Cenozoic volcanism in New Zealand*, Vol. 23, 251-263.
- Neave, D.A., Bali, E., Guðfinnsson, G.H., Halldórsson, S.A., Kahl, M., Schmidt, A.S., Holtz, F., 2019a. Clinopyroxene-Liquid Equilibria and Geothermobarometry in Natural and Experimental Tholeiites: The 2014-2015 Holuhraun Eruption, Iceland. *Journal of Petrology* 60, 1653-1680.

- Neave, D.A., MacLennan, J., 2020. Clinopyroxene Dissolution Records Rapid Magma Ascent. *Frontiers in Earth Science* 8, 188.
- Neave, D.A., Namur, O., Shorttle, O., Holtz, F., 2019b. Magmatic evolution biases basaltic records of mantle chemistry towards melts from recycled sources. *Earth and Planetary Science Letters* 520, 199-211.
- Neave, D.A., Putirka, K.D., 2017. A new clinopyroxene-liquid barometer, and implications for magma storage pressures under Icelandic rift zones. *American Mineralogist* 102, 777-794.
- Nelson, S.T., Montana, A., 1992. Sieve-textured plagioclase in volcanic rocks produced by rapid decompression. *American Mineralogist* 77, 1242-1249.
- Nicholis, M.G., Rutherford, M.J., 2004. Experimental constraints on magma ascent rate for the Crater Flat volcanic zone hawaiite. *Geology* 32, 489-492.
- Nicol, A., Mazengarb, C., Chanier, F., Rait, G., Uruski, C., Wallace, L., 2007. Tectonic evolution of the active Hikurangi subduction margin, New Zealand, since the Oligocene. *Tectonics* 26.
- Nicol, A., Seebeck, H., Wallace, L., 2017. Quaternary Tectonics of New Zealand.
- Nicol, A., Wallace, L.M., 2007. Temporal stability of deformation rates: Comparison of geological and geodetic observations, Hikurangi subduction margin, New Zealand. *Earth and Planetary Science Letters* 258, 397-413.
- Nielsen, R.L., Ustunisik, G., Lange, A.E., Tepley, F.J., Kent, A.J.R., 2020. Trace Element and Isotopic Characteristics of Plagioclase Megacrysts in Plagioclase Ultraphyric Basalts (PUB). *Geochemistry, Geophysics, Geosystems* 21.
- Nielsen, S.G., Marschall, H.R., 2017. Geochemical evidence for mélange melting in global arcs. *Science Advances* 3.
- Nimis, P., 1995. A clinopyroxene geobarometer for basaltic systems based on crystal-structure modeling. *Contributions to Mineralogy and Petrology* 121, 115-125.
- Nixon, G.T., 1988. Petrology of the Younger Andesites and Dacites of Iztaccíhuatl Volcano, Mexico: II. Chemical Stratigraphy, Magma Mixing, and the Composition of Basaltic Magma Influx. *Journal of Petrology* 29, 265-303.
- Nixon, G.T., Pearce, T., 1987. Laser-interferometry study of oscillatory zoning in plagioclase; the record of magma mixing and phenocryst recycling in calc-alkaline magma chambers, Iztaccíhuatl Volcano, Mexico. *American Mineralogist* 72, 1144-1162.
- Nodder, S.D., 1994. Characterizing potential offshore seismic sources using high-resolution geophysical and seafloor sampling programs: An example from Cape Egmont fault zone, Taranaki shelf, New Zealand. *Tectonics* 13, 641-658.
- O'Brien, H.E., Irving, A.J., McCallum, I.S., 1988. Complex zoning and resorption of phenocrysts in mixed potassic mafic magmas of the Highwood Mountains, Montana. *American Mineralogist* 73, 1007-1024.
- Otten, M.T., 1984. The origin of brown hornblende in the Artfjället gabbro and dolerites. *Contributions to Mineralogy and Petrology* 86, 189-199.
- Palme, H., O'Neill, H., 2013. Cosmochemical Estimates of Mantle Composition, *Treatise on Geochemistry: Second Edition*, pp. 1-39.
- Palmer, B.A., Alloway, B.V., Neall, V.E., 1991. Volcanic-debris-avalanche deposits in New Zealand - lithofacies organization in unconfined, wet-avalanche flows. *Sedimentation in volcanic settings*, 89-98.
- Palmer, B.A., Neall, V.E., 1991. Contrasting lithofacies architecture in ring-plain deposits related to edifice construction and destruction, the Quaternary Stratford and Opunake Formations, Egmont Volcano, New Zealand. *Sedimentary Geology* 74, 71-88.

- Pan, S., Zheng, J., Yin, Z., Griffin, W.L., Xia, M., Lin, A., Zhang, H., 2018. Spongy texture in mantle clinopyroxene records decompression-induced melting. *Lithos* 320-321, 144-154.
- Papale, P., Dobran, F., 1994. Magma flow along the volcanic conduit during the Plinian and pyroclastic flow phases of the May 18, 1980, Mount St. Helens eruption. *Journal of Geophysical Research* 99, 4355-4373.
- Parolari, M., Gómez-Tuena, A., Errázuriz-Henao, C., Cavazos-Tovar, J.G., 2021. Orogenic andesites and their link to the continental rock cycle. *Lithos* 382, 105958.
- Parson, L.M., Wright, I.C., 1996. The Lau-Havre-Taupo back-arc basin: A southward-propagating, multi-stage evolution from rifting to spreading. *Tectonophysics* 263, 1-22.
- Paton, C., Hellstrom, J., Paul, B., Woodhead, J., Hergt, J., 2011. Iolite: Freeware for the visualisation and processing of mass spectrometric data. *Journal of Analytical Atomic Spectrometry* 26, 2508-2518.
- Pearce, J.A., Peate, D.W., 1995. Tectonic implications of the composition of volcanic arc magmas. *Annual Review of Earth & Planetary Sciences* 23, 251-285.
- Perugini, D., Petrelli, M., Poli, G., 2006. Diffusive fractionation of trace elements by chaotic mixing of magmas. *Earth and Planetary Science Letters* 243, 669-680.
- Petford, N., Atherton, M., 1996. Na-rich partial melts from newly underplated basaltic crust: The Cordillera Blanca Batholith, Peru. *Journal of Petrology* 37, 1491-1521.
- Petrelli, M., Caricchi, L., Perugini, D., 2020. Machine Learning Thermo-Barometry: Application to Clinopyroxene-Bearing Magmas. *Journal of Geophysical Research: Solid Earth* 125, e2020JB020130.
- Petrelli, M., Zellmer, G.F., 2020. Rates and timescales of magma transfer, storage, emplacement, and eruption. *Dynamic Magma Evolution*, 1-41.
- Pichavant, M., Martel, C., Bourdier, J.L., Scaillet, B., 2002. Physical conditions, structure, and dynamics of a zoned magma chamber: Mount Pelée (Martinique, Lesser Antilles Arc). *Journal of Geophysical Research: Solid Earth* 107, ECV 2-1 -ECV 2-30.
- Pinkerton, H., Wilson, L., Macdonald, R., 2002. The transport and eruption of magma from volcanoes: A review. *Contemporary Physics* 43, 197-210.
- Plank, T., 2013. The Chemical Composition of Subducting Sediments, *Treatise on Geochemistry: Second Edition*, pp. 607-629.
- Platz, T., 2007. Aspects of Dome-forming Eruptions from Andesitic Volcanoes through the Maero Eruptive Period (1000 yrs BP to Present) Activity at Mt. Taranaki.
- Platz, T., Cronin, S.J., Cashman, K.V., Stewart, R.B., Smith, I.E.M., 2006. Transition from effusive to explosive phases in andesite eruptions - A case-study from the AD1655 eruption of Mt. Taranaki, New Zealand. *Journal of Volcanology and Geothermal Research* 161, 15-34.
- Platz, T., Cronin, S.J., Cashman, K.V., Stewart, R.B., Smith, I.E.M., 2007. Transition from effusive to explosive phases in andesite eruptions - A case-study from the AD1655 eruption of Mt. Taranaki, New Zealand. *Journal of Volcanology and Geothermal Research* 161, 15-34.
- Platz, T., Cronin, S.J., Procter, J.N., Neall, V.E., Foley, S.F., 2012. Non-explosive, dome-forming eruptions at Mt. Taranaki, New Zealand. *Geomorphology* 136, 15-30.
- Plechov, P.Y., Tsai, A.E., Shcherbakov, V.D., Dirksen, O.V., 2008. Opacitization conditions of hornblende in Bezymyannyi volcano andesites (March 30, 1956 eruption). *Petrology* 16, 19-35.

- Pontesilli, A., Masotta, M., Nazzari, M., Mollo, S., Armienti, P., Scarlato, P., Brenna, M., 2019. Crystallization kinetics of clinopyroxene and titanomagnetite growing from a trachybasaltic melt: New insights from isothermal time-series experiments. *Chemical Geology* 510, 113-129.
- Price, R., Cronin, S., Smith, I., Ukstins, I., Zernack, A., 2021. Formation of crystal-rich, mixed, intermediate lavas at Pouakai Volcano and the evolution of the Taranaki volcanic lineament, western North Island, New Zealand. *Lithos* 380, 105850.
- Price, R.C., Gamble, J.A., Smith, I.E.M., Maas, R., Waight, T., Stewart, R.B., Woodhead, J., 2012. The anatomy of an andesite volcano: A time-stratigraphic study of andesite petrogenesis and crustal evolution at Ruapehu Volcano, New Zealand. *Journal of Petrology* 53, 2139-2189.
- Price, R.C., Gamble, J.A., Smith, I.E.M., Stewart, R.B., Eggins, S., Wright, I.C., 2005. An integrated model for the temporal evolution of andesites and rhyolites and crustal development in New Zealand's North Island. *Journal of Volcanology and Geothermal Research* 140, 1-24.
- Price, R.C., McCulloch, M.T., Smith, I.E.M., Stewart, R.B., 1992. Pb-Nd-Sr isotopic compositions and trace element characteristics of young volcanic rocks from Egmont Volcano and comparisons with basalts and andesites from the Taupo Volcanic Zone, New Zealand. *Geochimica et Cosmochimica Acta* 56, 941-953.
- Price, R.C., Mortimer, N., Smith, I.E.M., Maas, R., 2015. Whole-rock geochemical reference data for Torlesse and Waipapa terranes, North Island, New Zealand. *New Zealand Journal of Geology and Geophysics* 58, 213-228.
- Price, R.C., Smith, I.E.M., Stewart, R.B., Gamble, J.A., Gruender, K., Maas, R., 2016. High-K andesite petrogenesis and crustal evolution: Evidence from mafic and ultramafic xenoliths, Egmont Volcano (Mt. Taranaki) and comparisons with Ruapehu Volcano, North Island, New Zealand. *Geochimica et Cosmochimica Acta* 185, 328-357.
- Price, R.C., Stewart, R.B., Woodhead, J.D., Smith, I.E.M., 1999. Petrogenesis of high-K arc magmas: Evidence from Egmont Volcano, North Island, New Zealand. *Journal of Petrology* 40, 167-197.
- Prior, D.J., Boyle, A.P., Brenker, F., Cheadle, M.C., Day, A., Lopez, G., Peruzzi, L., Potts, G., Reddy, S., Spiess, R., 1999. The application of electron backscatter diffraction and orientation contrast imaging in the SEM to textural problems in rocks. *American Mineralogist* 84, 1741-1759.
- Procter, J.N., Cronin, S.J., Platz, T., Patra, A., Dalbey, K., Sheridan, M., Neall, V., 2010. Mapping block-and-ash flow hazards based on Titan 2D simulations: A case study from Mt. Taranaki, NZ. *Natural Hazards* 53, 483-501.
- Procter, J.N., Cronin, S.J., Zernack, A.V., 2009. Landscape and sedimentary response to catastrophic debris avalanches, western Taranaki, New Zealand. *Sedimentary Geology* 220, 271-287.
- Prouteau, G., Scaillet, B., 2003. Experimental constraints on the origin of the 1991 Pinatubo dacite. *Journal of Petrology* 44, 2203-2241.
- Putirka, K., 2016. Amphibole thermometers and barometers for igneous systems and some implications for eruption mechanisms of felsic magmas at arc volcanoes. *American Mineralogist* 101, 841-858.
- Putirka, K., Johnson, M., Kinzler, R., Longhi, J., Walker, D., 1996. Thermobarometry of mafic igneous rocks based on clinopyroxene-liquid equilibria, 0- 30 kbar. *Contributions to Mineralogy and Petrology* 123, 92-108.
- Putirka, K.D., 2008. Thermometers and barometers for volcanic systems, *Reviews in Mineralogy and Geochemistry*, pp. 61-120.

- Rajabi, M., Ziegler, M., Tingay, M., Heidbach, O., Reynolds, S., 2016. Contemporary tectonic stress pattern of the Taranaki Basin, New Zealand. *Journal of Geophysical Research: Solid Earth* 121, 6053-6070.
- Reilly, C., Nicol, A., Walsh, J.J., Seebeck, H., 2015. Evolution of faulting and plate boundary deformation in the Southern Taranaki Basin, New Zealand. *Tectonophysics* 651-652, 1-18.
- Reubi, O., Blundy, J., 2009. A dearth of intermediate melts at subduction zone volcanoes and the petrogenesis of arc andesites. *Nature* 461, 1269-1273.
- Reyners, M., 1980. A microearthquake study of the plate boundary, North Island, New Zealand. *Geophysical Journal of the Royal Astronomical Society* 63, 1-22.
- Reyners, M., 1989. New Zealand seismicity 1964–87: An interpretation. *New Zealand Journal of Geology and Geophysics* 32, 307-315.
- Reyners, M., Cowan, H., 1993. The transition from subduction to continental collision: crustal structure in the North Canterbury region, New Zealand. *Geophysical Journal International* 115, 1124-1136.
- Reyners, M., Eberhart-Phillips, D., Stuart, G., 2007. The role of fluids in lower-crustal earthquakes near continental rifts. *Nature* 446, 1075.
- Reyners, M., Eberhart-Phillips, D., Stuart, G., Nishimura, Y., 2006. Imaging subduction from the trench to 300 km depth beneath the central North Island, New Zealand, with Vp and Vp/Vs. *Geophysical Journal International* 165, 565-583.
- Reyners, M., Webb, T., 2002. Large earthquakes near doubtful sound, New Zealand, 1989–93. *New Zealand Journal of Geology and Geophysics* 45, 109-120.
- Ridolfi, F., Renzulli, A., 2012. Calcic amphiboles in calc-alkaline and alkaline magmas: Thermobarometric and chemometric empirical equations valid up to 1,130°C and 2.2 GPa. *Contributions to Mineralogy and Petrology* 163, 877-895.
- Ridolfi, F., Renzulli, A., Puerini, M., 2010. Stability and chemical equilibrium of amphibole in calc-alkaline magmas: An overview, new thermobarometric formulations and application to subduction-related volcanoes. *Contributions to Mineralogy and Petrology* 160, 45-66.
- Rubin, A., Pollard, D., 1987. Origins of blade-like dikes in volcanic rift zones. *US Geological Survey Professional Paper* 1350, 1449-1470.
- Rutherford, M.J., 2008. Magma Ascent Rates. *Reviews in Mineralogy and Geochemistry* 69, 241-271.
- Rutherford, M.J., Devine, J.D., 2003. Magmatic conditions and magma ascent as indicated by hornblende phase equilibria and reactions in the 1995-2002 Soufrière Hills magma. *Journal of Petrology* 44, 1433-1454.
- Rutherford, M.J., Devine, J.D., Barclay, J., 1998. Changing magma conditions and ascent rates during the Soufriere Hills eruption on Montserrat. *GSA Today* 8, x1-7.
- Rutherford, M.J., Hill, P.M., 1993. Magma ascent rates from amphibole breakdown: an experimental study applied to the 1980-1986 Mount St. Helens eruptions. *Journal of Geophysical Research* 98, 19667-19685.
- Sakyi, P.A., Tanaka, R., Kobayashi, K., Nakamura, E., 2012. Inherited Pb isotopic records in olivine antecryst-hosted melt inclusions from Hawaiian lavas. *Geochimica et Cosmochimica Acta* 95, 169-195.
- Scaillet, B., Evans, B.W., 1999. The 15 June 1991 eruption of Mount Pinatubo. I. Phase equilibria and pre-eruption P-T-fO₂-fH₂O conditions of the dacite magma. *Journal of Petrology* 40, 381-411.
- Schmidt, M.W., 1992. Amphibole composition in tonalite as a function of pressure: an experimental calibration of the Al-in-hornblende barometer. *Contributions to Mineralogy and Petrology* 110, 304-310.

- Schmidt, M.W., Poli, S., 1998. Experimentally based water budgets for dehydrating slabs and consequences for arc magma generation. *Earth and Planetary Science Letters* 163, 361-379.
- Schoneveld, L., Barnes, S.J., Makkonen, H.V., Le Vaillant, M., Paterson, D.J., Taranovic, V., Wang, K.-Y., Mao, Y.-J., 2020. Zoned Pyroxenes as prospectivity indicators for magmatic Ni-Cu sulfide mineralization. *Frontiers in Earth Science* 8, 256.
- Schwandt, C.S., McKay, G.A., 2006. Minor- and trace-element sector zoning in synthetic enstatite. *American Mineralogist* 91, 1607-1615.
- Scott, B.J., 2013. A revised catalogue of Ruapehu volcano eruptive activity: 1830-2012. GNS Science Report 2013/45.
- Scott, J.A.J., Mather, T.A., Pyle, D.M., Rose, W.I., Chigna, G., 2012. The magmatic plumbing system beneath Santiaguito Volcano, Guatemala. *Journal of Volcanology and Geothermal Research* 237-238, 54-68.
- Seebeck, H., Nicol, A., Giba, M., Pettinga, J., Walsh, J., 2014. Geometry of the subducting Pacific plate since 20 Ma, Hikurangi margin, New Zealand. *Journal of the Geological Society* 171, 131-143.
- Shane, P., 2005. Towards a comprehensive distal andesitic tephrostratigraphic framework for New Zealand based on eruptions from Egmont volcano. *Journal of Quaternary Science* 20, 45-57.
- Sheldrake, T.E., Sparks, R.S.J., Cashman, K.V., Wadge, G., Aspinall, W.P., 2016. Similarities and differences in the historical records of lava dome-building volcanoes: Implications for understanding magmatic processes and eruption forecasting. *Earth-Science Reviews* 160, 240-263.
- Sherburn, S., White, R.S., 2005. Crustal seismicity in Taranaki, New Zealand using accurate hypocentres from a dense network. *Geophysical Journal International* 162, 494-506.
- Sherburn, S., White, R.S., Chadwick, M., 2006. Three-dimensional tomographic imaging of the Taranaki volcanoes, New Zealand. *Geophysical Journal International* 166, 957-969.
- Shore, M., Fowler, A.D., 1996. Oscillatory zoning in minerals: A common phenomenon. *Canadian Mineralogist* 34, 1111-1126.
- Sisson, T.W., Grove, T.L., 1993. Experimental investigations of the role of H₂O in calc-alkaline differentiation and subduction zone magmatism. *Contributions to Mineralogy and Petrology* 113, 143-166.
- Smith, D.R., Leeman, W.P., 1987. Petrogenesis of Mount St. Helens dacitic magmas (USA). *Journal of Geophysical Research* 92, 10,313-310,334.
- Smith, E.G.C., Stern, T., Reyners, M., 1989. Subduction and back-arc activity at the Hikurangi convergent Margin, New Zealand. *Pure and Applied Geophysics PAGEOPH* 129, 203-231.
- Sobolev, A.V., Hofmann, A.W., Kuzmin, D.V., Yaxley, G.M., Arndt, N.T., Chung, S.L., Danyushevsky, L.V., Elliott, T., Frey, F.A., Garcia, M.O., Gurenko, A.A., Kamenetsky, V.S., Kerr, A.C., Krivolutskaya, N.A., Matvienkov, V.V., Nikogosian, I.K., Rocholl, A., Sigurdsson, I.A., Sushchevskaya, N.M., Teklay, M., 2007. The amount of recycled crust in sources of mantle-derived melts. *Science* 316, 412-417.
- Solano, J., Jackson, M., Sparks, R., Blundy, J., Annen, C., 2012. Melt segregation in deep crustal hot zones: a mechanism for chemical differentiation, crustal assimilation and the formation of evolved magmas. *Journal of Petrology* 53, 1999-2026.

- Sollas, J.W., 1894. On the volcanic district of Carlingford and Slieve Gullion, Part I. On the relation of the granite to the gabbro of Barnavave, Carlingford. *Trans. R. Ir. Acad* 30, 477-512.
- Sparks, R., 2003. Dynamics of magma degassing. Geological Society, London, Special Publications 213, 5-22.
- Sparks, R.S.J., Annen, C., Blundy, J.D., Cashman, K.V., Rust, A.C., Jackson, M.D., 2019. Formation and dynamics of magma reservoirs. *Philosophical Transactions of the Royal Society A: Mathematical, Physical and Engineering Sciences* 377.
- Sparks, R.S.J., Baker, L., Brown, R.J., Field, M., Schumacher, J., Stripp, G., Walters, A., 2006. Dynamical constraints on kimberlite volcanism. *Journal of Volcanology and Geothermal Research* 155, 18-48.
- Sparks, R.S.J., Cashman, K.V., 2017. Dynamic magma systems: Implications for forecasting volcanic activity. *Elements* 13, 35-40.
- Stagpoole, V., Nicol, A., 2008. Regional structure and kinematic history of a large subduction back thrust: Taranaki Fault, New Zealand. *Journal of Geophysical Research: Solid Earth* 113.
- Stern, R.J., 2002. Subduction zones. *Reviews of Geophysics* 40, 3-1 - 3-38.
- Stern, T.A., 1987. Asymmetric back-arc spreading, heat flux and structure associated with the Central Volcanic Region of New Zealand. *Earth and Planetary Science Letters* 85, 265-276.
- Stern, T.A., Stratford, W.R., Salmon, M.L., 2006. Subduction evolution and mantle dynamics at a continental margin: Central North Island, New Zealand. *Reviews of Geophysics* 44.
- Stewart, M.L., Pearce, T.H., 2004. Sieve-textured plagioclase in dacitic magma: Interference imaging results. *American Mineralogist* 89, 348-351.
- Stewart, R., 2010. Andesites as magmatic liquids or liquid-crystal mixtures; insights from Egmont and Ruapehu Volcanoes, New Zealand. *Central European Journal of Geosciences* 2, 329-338.
- Stewart, R.B., Price, R.C., Smith, I.E.M., 1996. Evolution of high-K arc magma, Egmont volcano, Taranaki, New Zealand: Evidence from mineral chemistry. *Journal of Volcanology and Geothermal Research* 74, 275-295.
- Stewart, R.B., Zernack, A., Price, R.C., 2006. Slab or Crust—K₂O enrichment at Egmont volcano, New Zealand. *Geochimica et Cosmochimica Acta* 70, A614.
- Straub, S.M., Gomez-Tuena, A., Stuart, F.M., Zellmer, G.F., Espinasa-Perena, R., Cai, Y., Iizuka, Y., 2011. Formation of hybrid arc andesites beneath thick continental crust. *Earth and Planetary Science Letters* 303, 337-347.
- Straub, S.M., Gómez-Tuena, A., Vannucchi, P., 2020. Subduction erosion and arc volcanism. *Nature Reviews Earth & Environment* 1, 574-589.
- Straub, S.M., LaGatta, A.B., Martin-Del Pozzo, A.L., Langmuir, C.H., 2008. Evidence from high-Ni olivines for a hybridized peridotite/pyroxenite source for orogenic andesites from the central Mexican Volcanic Belt. *Geochemistry, Geophysics, Geosystems* 9.
- Streck, M.J., 2008. Mineral textures and zoning as evidence for open system processes, *Reviews in Mineralogy and Geochemistry*, pp. 595-622.
- Tatsumi, Y., Eggins, S., 1995. Subduction zone magmatism. *Subduction zone magmatism*.
- Tatsumi, Y., Ishizaka, K., 1982. Origin of high-magnesian andesites in the Setouchi volcanic belt, southwest Japan, II. Melting phase relations at high pressures. *Earth and Planetary Science Letters* 60, 305-317.

- Taylor, S.R., McLennan, S.M., 1985. The continental crust: its composition and evolution.
- Timm, C., Davy, B., Haase, K., Hoernle, K.A., Graham, I.J., de Ronde, C.E.J., Woodhead, J., Bassett, D., Hauff, F., Mortimer, N., Seebeck, H.C., Wysoczanski, R.J., Caratori-Tontini, F., Gamble, J.A., 2014. Subduction of the oceanic Hikurangi Plateau and its impact on the Kermadec arc. *Nature Communications* 5, 4923.
- Timm, C., Hoernle, K., Werner, R., Hauff, F., den Bogaard, P.v., White, J., Mortimer, N., Garbe-Schönberg, D., 2010. Temporal and geochemical evolution of the Cenozoic intraplate volcanism of Zealandia. *Earth-Science Reviews* 98, 38-64.
- Tomiya, A., Takahashi, E., 2005. Evolution of the magma chamber beneath Usu Volcano since 1663: a natural laboratory for observing changing phenocryst compositions and textures. *Journal of Petrology* 46, 2395-2426.
- Topping, W.W., 1972. Burrell Lapilli eruptives, Mount Egmont, New Zealand. *New Zealand Journal of Geology and Geophysics* 15, 476-490.
- Torres-Orozco, R., Cronin, S., Pardo, N., Palmer, A., 2017a. New insights into Holocene eruption episodes from proximal deposit sequences at Mt. Taranaki (Egmont), New Zealand. *Bulletin of Volcanology* 79, 1-25.
- Torres-Orozco, R., Cronin, S.J., Damaschke, M., Pardo, N., 2017b. Diverse dynamics of Holocene mafic-intermediate Plinian eruptions at Mt. Taranaki (Egmont), New Zealand. *Bulletin of Volcanology* 79.
- Tsuchiyama, A., 1985. Dissolution kinetics of plagioclase in the melt of the system diopside-albite-anorthite, and origin of dusty plagioclase in andesites. *Contributions to Mineralogy and Petrology* 89, 1-16.
- Tsune, A., Toramaru, A., 2007. A simple model of oscillatory zoning in magmatic plagioclase: Development of an isothermal undercooling model. *American Mineralogist* 92, 1071-1079.
- Turner, G.M., Alloway, B.V., Dixon, B.J., Atkins, C.B., 2018. Thermal history of volcanic debris flow deposits on the eastern flanks of Mt. Taranaki, New Zealand: Implications for future hazards. *Journal of Volcanology and Geothermal Research* 353, 55-67.
- Turner, M.B., 2008. Eruption Cycles and Magmatic Processes at a Reawakening Volcano, Mt. Taranaki, New Zealand: A Thesis Presented in Partial Fulfilment of the Requirements for the Degree of Doctor of Philosophy in Earth Science at Massey University, Palmerston North, New Zealand. *Eruption Cycles and Magmatic Processes At a Reawakening Volcano*.
- Turner, M.B., Bebbington, M.S., Cronin, S.J., Stewart, R.B., 2009a. Merging eruption datasets: Building an integrated Holocene eruptive record for Mt Taranaki, New Zealand. *Bulletin of Volcanology* 71, 903-918.
- Turner, M.B., Cronin, S.J., Bebbington, M.S., Platz, T., 2008a. Developing probabilistic eruption forecasts for dormant volcanoes: A case study from Mt Taranaki, New Zealand. *Bulletin of Volcanology* 70, 507-515.
- Turner, M.B., Cronin, S.J., Bebbington, M.S., Smith, I.E.M., Stewart, R.B., 2011a. Integrating records of explosive and effusive activity from proximal and distal sequences: Mt. Taranaki, New Zealand. *Quaternary International* 246, 364-373.
- Turner, M.B., Cronin, S.J., Bebbington, M.S., Smith, I.E.M., Stewart, R.B., 2011b. Relating magma composition to eruption variability at andesitic volcanoes: A case study from Mount Taranaki, New Zealand. *Bulletin of the Geological Society of America* 123, 2005-2015.

- Turner, M.B., Cronin, S.J., Smith, I.E., Stewart, R.B., Neall, V.E., 2008b. Eruption episodes and magma recharge events in andesitic systems: Mt Taranaki, New Zealand. *Journal of Volcanology and Geothermal Research* 177, 1063-1076.
- Turner, M.B., Cronin, S.J., Stewart, R.B., Bebbington, M., Smith, I.E.M., 2008c. Using titanomagnetite textures to elucidate volcanic eruption histories. *Geology* 36, 31-34.
- Turner, S., Handler, M., Bindeman, I., Suzuki, K., 2009b. New insights into the origin of O–Hf–Os isotope signatures in arc lavas from Tonga–Kermadec. *Chemical Geology* 266, 187-193.
- Turner, S.J., Izbekov, P., Langmuir, C., 2013. The magma plumbing system of Bezymianny Volcano: Insights from a 54 year time series of trace element whole-rock geochemistry and amphibole compositions. *Journal of Volcanology and Geothermal Research* 263, 108-121.
- Turner, S.J., Langmuir, C.H., Dungan, M.A., Escrig, S., 2017. The importance of mantle wedge heterogeneity to subduction zone magmatism and the origin of EM1. *Earth and Planetary Science Letters* 472, 216-228.
- Ubide, T., Galé, C., Larrea, P., Arranz, E., Lago, M., 2014. Antecrysts and their effect on rock compositions: The Cretaceous lamprophyre suite in the Catalonian Coastal Ranges (NE Spain). *Lithos* 206-207, 214-233.
- Ubide, T., McKenna, C.A., Chew, D.M., Kamber, B.S., 2015. High-resolution LA-ICP-MS trace element mapping of igneous minerals: In search of magma histories. *Chemical Geology* 409, 157-168.
- Ubide, T., Mollo, S., Zhao, J.X., Nazzari, M., Scarlato, P., 2019. Sector-zoned clinopyroxene as a recorder of magma history, eruption triggers, and ascent rates. *Geochimica et Cosmochimica Acta* 251, 265-283.
- Ui, T., Kawachi, S., Neall, V.E., 1986. Fragmentation of debris avalanche material during flowage - Evidence from the Pungarehu Formation, Mount Egmont, New Zealand. *Journal of Volcanology and Geothermal Research* 27, 255-264.
- Umino, S., Horio, A., 1998. Multistage magma mixing revealed in phenocryst zoning of the Yunokuchi Pumice, Akagi Volcano, Japan. *Journal of Petrology* 39, 101-124.
- Van Gerve, T., Neave, D., Almeev, R., Holtz, F., Namur, O., 2020. Zoned crystal records of transcrustal magma transport, storage and differentiation: insights from the Shatsky Rise oceanic plateau. *Journal of Petrology* 61, ega080.
- Vance, J.A., 1962. Zoning in igneous plagioclase: Normal and oscillatory zoning. *American Journal of Science* 260, 746-760.
- Viccaro, M., Giuffrida, M., Nicotra, E., Cristofolini, R., 2016. Timescales of magma storage and migration recorded by olivine crystals in basalts of the March-April 2010 eruption at Eyjafjallajökull volcano, Iceland. *American Mineralogist* 101, 222-230.
- Villiger, S., Ulmer, P., Müntener, O., 2007. Equilibrium and fractional crystallization experiments at 0–7 GPa; the effect of pressure on phase relations and liquid compositions of tholeiitic magmas. *Journal of Petrology* 48, 159-184.
- Villiger, S., Ulmer, P., Müntener, O., Thompson, A.B., 2004. The liquid line of descent of anhydrous, mantle-derived, tholeiitic liquids by fractional and equilibrium crystallization—an experimental study at 1–0 GPa. *Journal of Petrology* 45, 2369-2388.
- Wager, L.R., Brown, G.M., Wadsworth, W.J., 1960. Types of igneous cumulates. *Journal of Petrology* 1, 73-85.
- Walcott, R.I., 1978. Present tectonics and Late Cenozoic evolution of New Zealand. *Geophysical Journal International* 52, 137-164.

- Walcott, R.I., 1984. The kinematics of the plate boundary zone through New Zealand: a comparison of short-and long-term deformations. *Geophysical Journal of the Royal Astronomical Society* 79, 613-633.
- Walcott, R.I., 1998. Modes of oblique compression: Late cenozoic tectonics of the South Island of New Zealand. *Reviews of Geophysics* 36, 1-26.
- Wallace, L.M., Beavan, J., McCaffrey, R., Berryman, K., Denys, P., 2007. Balancing the plate motion budget in the South Island, New Zealand using GPS, geological and seismological data. *Geophysical Journal International* 168, 332-352.
- Wallace, L.M., Beavan, J., McCaffrey, R., Darby, D., 2004. Subduction zone coupling and tectonic block rotations in the North Island, New Zealand. *Journal of Geophysical Research: Solid Earth* 109, 1-21.
- Wallace, P.J., Carmichael, I.S., 1994. Petrology of Volcán Tequila, Jalisco, Mexico: disequilibrium phenocryst assemblages and evolution of the subvolcanic magma system. *Contributions to Mineralogy and Petrology* 117, 345-361.
- Waters, L.E., Lange, R.A., 2015. An updated calibration of the plagioclase-liquid hygrometer-thermometer applicable to basalts through rhyolites. *American Mineralogist* 100, 2172-2184.
- Welsch, B., Faure, F., Bachèlery, P., Famin, V., 2009. Microcrysts record transient convection at Piton de la Fournaise volcano (La Réunion hotspot). *Journal of Petrology* 50, 2287-2305.
- Welsch, B., Hammer, J., Baronnet, A., Jacob, S., Hellebrand, E., Sinton, J., 2016. Clinopyroxene in postshield Haleakala ankaramite: 2. Texture, compositional zoning and supersaturation in the magma. *Contributions to Mineralogy and Petrology* 171, 1-19.
- Westoby, M.J., Brasington, J., Glasser, N.F., Hambrey, M.J., Reynolds, J.M., 2012. 'Structure-from-Motion' photogrammetry: A low-cost, effective tool for geoscience applications. *Geomorphology* 179, 300-314.
- Wild, A.J., Wilson, T.M., Bebbington, M.S., Cole, J.W., Craig, H.M., 2019. Probabilistic volcanic impact assessment and cost-benefit analysis on network infrastructure for secondary evacuation of farm livestock: A case study from the dairy industry, Taranaki, New Zealand. *Journal of Volcanology and Geothermal Research* 387, 106670.
- Wilson, C., Gravley, D.M., Leonard, G.S., Rowland, J., 2009. Volcanism in the central Taupo Volcanic Zone, New Zealand: Tempo, styles and controls.
- Wilson, C.J.N., Houghton, B.F., McWilliams, M.O., Lanphere, M.A., Weaver, S.D., Briggs, R.M., 1995. Volcanic and structural evolution of Taupo Volcanic Zone, New Zealand: a review. *Journal of Volcanology and Geothermal Research* 68, 1-28.
- Wilson, C.J.N., Rowland, J.V., 2016. The volcanic, magmatic and tectonic setting of the Taupo Volcanic Zone, New Zealand, reviewed from a geothermal perspective. *Geothermics* 59, 168-187.
- Wright, I.C., 1990. Late quaternary faulting of the offshore whakatane graben, taupo volcanic zone, new zealand. *New Zealand Journal of Geology and Geophysics* 33, 245-256.
- Wright, I.C., 1992. Shallow structure and active tectonism of an offshore continental back-arc spreading system: the Taupo Volcanic Zone, New Zealand. *Marine Geology* 103, 287-309.
- Wu, F., Turner, S., Schaefer, B.F., 2020. Mélange versus fluid and melt enrichment of subarc mantle: A novel test using barium isotopes in the Tonga-Kermadec arc. *Geology* 48, 1053-1057.

- Yavuz, F., Döner, Z., 2017. WinAmptb: A Windows program for calcific amphibole thermobarometry.
- Zellmer, G.F., 2021. Gaining acuity on crystal terminology in volcanic rocks. *Bulletin of Volcanology* 83, 78.
- Zellmer, G.F., Blake, S., Vance, D., Hawkesworth, C., Turner, S., 1999. Plagioclase residence times at two island arc volcanoes (Kameni Islands, Santorini, and Soufriere, St. Vincent) determined by Sr diffusion systematics. *Contributions to Mineralogy and Petrology* 136, 345-357.
- Zellmer, G.F., Pistone, M., Iizuka, Y., Andrews, B.J., Gomez-Tuena, A., Straub, S.M., Cottrell, E., 2016. Petrogenesis of antecryst-bearing arc basalts from the Trans-Mexican Volcanic Belt: Insights into along-Arc variations in magma-mush ponding depths, H₂O contents, and surface heat flux. *American Mineralogist* 101, 2405-2422.
- Zellmer, G.F., Sparks, R.S.J., Hawkesworth, C.J., Wiedenbeck, M., 2003. Magma emplacement and remobilization timescales beneath Montserrat: Insights from Sr and Ba zonation in plagioclase phenocrysts. *Journal of Petrology* 44, 1413-1431.
- Zemeny, A., Procter, J., Németh, K., Zellmer, G.F., Zernack, A.V., Cronin, S.J., 2021. Elucidating stratovolcano construction from volcanoclastic mass-flow deposits: The medial ring-plain of Taranaki Volcano, New Zealand. *Sedimentology* n/a.
- Zernack, A.V., Cronin, S.J., Neall, V.E., Procter, J.N., 2011. A medial to distal volcanoclastic record of an andesite stratovolcano: Detailed stratigraphy of the ring-plain succession of south-west Taranaki, New Zealand. *International Journal of Earth Sciences* 100, 1937-1966.
- Zernack, A.V., Price, R.C., Smith, I.E.M., Cronin, S.J., Stewart, R.B., 2012. Temporal evolution of a high-K andesitic magmatic system: Taranaki volcano, New Zealand. *Journal of Petrology* 53, 325-363.
- Zernack, A.V., Procter, J.N., 2021. *Cyclic Growth and Destruction of Volcanoes, Volcanic Debris Avalanches*. Springer, pp. 311-355.
- Zernack, A.V., Procter, J.N., Cronin, S.J., 2009. Sedimentary signatures of cyclic growth and destruction of stratovolcanoes: A case study from Mt. Taranaki, New Zealand. *Sedimentary Geology* 220, 288-305.

Appendix A

List of all major oxide element data analysed during this study using XRF (Massey University) and EPMA (Victoria University of Wellington and Academia Sinica) for whole rock, groundmass, and mineral phases. Provided as electronic supplement.

Appendix B

Trace and minor element data obtained from LA-ICP-MS analyses for whole rock (University of Waikato) and mineral phases (University of Queensland). Provided as electronic supplement.

Appendix C

Supplementary data for published paper “Nessa G. D’Mello, Georg F. Zellmer, Marianne Negrini, Gabor Kereszturi, Jonathan Procter, Robert Stewart, David Prior, Masako Usuki, Yoshiyuki Iizuka (2021) Deciphering magma storage and ascent processes of Taranaki, New Zealand, from the complexity of amphibole breakdown textures. *Lithos*, article number 106264”. Provided as electronic supplement.

Appendix D

Isotopic data from literature used to model for subduction melanges in Taranaki. Provided as electronic supplement.

Appendix E

DRC forms for each chapter intended for or already submitted for publication

STATEMENT OF CONTRIBUTION DOCTORATE WITH PUBLICATIONS/MANUSCRIPTS

We, the candidate and the candidate's Primary Supervisor, certify that all co-authors have consented to their work being included in the thesis and they have accepted the candidate's contribution as indicated below in the *Statement of Originality*.

Name of candidate:	
Name/title of Primary Supervisor:	
In which chapter is the manuscript /published work:	
<p>Please select one of the following three options:</p> <p>The manuscript/published work is published or in press</p> <ul style="list-style-type: none"> • Please provide the full reference of the Research Output: <p>The manuscript is currently under review for publication – please indicate:</p> <ul style="list-style-type: none"> • The name of the journal: • The percentage of the manuscript/published work that was contributed by the candidate: • Describe the contribution that the candidate has made to the manuscript/published work: <p style="text-align: center;">It is intended that the manuscript will be published, but it has not yet been submitted to a journal</p>	
Candidate's Signature:	Nessa D'Mello <small>Digitally signed by Nessa D'Mello Date: 2021.11.29 22:31:44 +13'00'</small>
Date:	
Primary Supervisor's Signature:	Georg F. Zellmer <small>Digitally signed by Georg F. Zellmer DN: cn=Georg F. Zellmer, c=NZ, o=Massey University, ou=School of Agriculture and Environment, email=g.f.zellmer@massey.ac.nz Date: 2021.11.30 10:31:25 +13'00'</small>
Date:	

This form should appear at the end of each thesis chapter/section/appendix submitted as a manuscript/ publication or collected as an appendix at the end of the thesis.

STATEMENT OF CONTRIBUTION DOCTORATE WITH PUBLICATIONS/MANUSCRIPTS

We, the candidate and the candidate's Primary Supervisor, certify that all co-authors have consented to their work being included in the thesis and they have accepted the candidate's contribution as indicated below in the *Statement of Originality*.

Name of candidate:	
Name/title of Primary Supervisor:	
In which chapter is the manuscript /published work:	
Please select one of the following three options:	
<p>The manuscript/published work is published or in press</p> <ul style="list-style-type: none"> • Please provide the full reference of the Research Output: 	
<p>The manuscript is currently under review for publication – please indicate:</p> <ul style="list-style-type: none"> • The name of the journal: • The percentage of the manuscript/published work that was contributed by the candidate: • Describe the contribution that the candidate has made to the manuscript/published work: 	
It is intended that the manuscript will be published, but it has not yet been submitted to a journal	
Candidate's Signature:	<p>Nessa D'Mello <small>Digitally signed by Nessa D'Mello Date: 2021.08.16 10:44:12 +12'00'</small></p>
Date:	
Primary Supervisor's Signature:	<p>Georg F. Zellmer <small>Digitally signed by Georg F. Zellmer DN: cn=Georg F. Zellmer, c=NZ, o=Massey University, ou=School of Agriculture and Environment, email=g.f.zellmer@massey.ac.nz Date: 2021.08.16 11:16:23 +12'00'</small></p>
Date:	

This form should appear at the end of each thesis chapter/section/appendix submitted as a manuscript/publication or collected as an appendix at the end of the thesis.

STATEMENT OF CONTRIBUTION DOCTORATE WITH PUBLICATIONS/MANUSCRIPTS

We, the candidate and the candidate's Primary Supervisor, certify that all co-authors have consented to their work being included in the thesis and they have accepted the candidate's contribution as indicated below in the *Statement of Originality*.

Name of candidate:	
Name/title of Primary Supervisor:	
In which chapter is the manuscript /published work:	
<p>Please select one of the following three options:</p> <p style="padding-left: 40px;">The manuscript/published work is published or in press</p> <ul style="list-style-type: none"> • Please provide the full reference of the Research Output: <p style="padding-left: 40px;">The manuscript is currently under review for publication – please indicate:</p> <ul style="list-style-type: none"> • The name of the journal: • The percentage of the manuscript/published work that was contributed by the candidate: • Describe the contribution that the candidate has made to the manuscript/published work: <p style="text-align: center; padding-top: 20px;">It is intended that the manuscript will be published, but it has not yet been submitted to a journal</p>	
Candidate's Signature:	Nessa D'Mello <small>Digitally signed by Nessa D'Mello Date: 2021.08.16 10:53:50 +12'00'</small>
Date:	
Primary Supervisor's Signature:	Georg F. Zellmer <small>Digitally signed by Georg F. Zellmer DN: cn=Georg F. Zellmer, c=NZ, o=Massey University, ou=School of Agriculture and Environment, email=g.f.zellmer@massey.ac.nz Date: 2021.08.16 11:16:50 +12'00'</small>
Date:	

This form should appear at the end of each thesis chapter/section/appendix submitted as a manuscript/publication or collected as an appendix at the end of the thesis.